UCGE Reports

Number 20354

Department of Geomatics Engineering

Coastal Sea Level Change from Satellite Altimetry and Tide Gauges

(URL: http://www.geomatics.ucalgary.ca/graduatetheses)

by

Feng Tang

April 12th, 2012

Coastal Sea Level Change from Satellite Altimetry and Tide Gauges

PhD Thesis

By

Feng Tang

April 12th

Abstract

Coastal regions around the world are places with advanced economy and almost half of the Earth's population. The change of coastal sea level is significant for living safely in the coastal regions of many countries. Satellite altimetry and tide gauges are two main techniques providing the direct sea surface height measurements. Although the application of satellite altimetry or tide gauge data on estimating the global or regional sea level change achieves great success, however, their utilities are limited in the coastal areas. Satellite altimetry data are degraded as approaching to the land due to the land contamination on altimeter and radiometer, and insufficient geophysical corrections. Tide gauge data are contaminated by the vertical land motion and their spatial distribution is sparse. In order to overcome these problems, special data processing methods are developed.

Residual ocean tides are analyzed and removed from the T/P and Jason-1 sea level anomalies. It reduces almost half variability of the data in our study areas. The linear trend of sea level at every altimetry or tide gauge site is estimated by a simple linear regression model. The power spectral density and maximum likelihood analyses are used to determine the noise model for both types of data. The white, and white and flicker noise model are found to be the best noise model for altimetry and tide gauge data respectively. The covariance matrix for each noise model is estimated and used in the linear regression model. In addition, the vertical land motion, which contaminates in tide gauge data, is monitored by GPS measurements. The rate estimates are in agreement with published values.

A joint analysis method is developed to combine satellite altimetry and tide gauge rate estimates together for estimating the regional sea level change. The variance component analysis is used to modify the weights for each type of data. Our results indicate that the contribution of tide

gauge data in the joint analysis method is limited by the accuracy of GPS-derived vertical land motion and the number of GPS sites used.

Table of Contents

List of Tables

List of Figures

Chapter One: Introduction

1.1 Introduction

Global mean sea level is believed to be rising since the late 19th century. The estimate for the 20th century indicates that global mean sea level rose at a rate close to 2 mm/year (Douglas and Peltier, 2002; Bindoff, 2007; Nicholls and Cazenave, 2010; Church and White, 2011). Compared with other geophysical phenomena like earthquakes, volcanoes, and hurricanes, sea level change is so benign (rate of only a few millimeters per year) that is hardly noticeable. However, the present-day sea level change draws much attention because global sea level change is a significant factor to global climate change and the local sea level change is more related to the stability of the coastal ecosystems and the safety of properties and people living in coastal regions and on islands. Almost half of the population lives within 100 km of the coastal areas around the world, with various levels of economic activity and significant ecosystems for our environment. The physical effects of the sea level rise on coastal areas were summarized in five categories by Douglas (2001): erosion of beaches and bluffs, increased flooding and storm damage, inundation of low-lying areas, salt intrusion into aquifers and surface waters, and higher water tables.

The reasons for sea level rise or fall are complex. The change can be seen as a result of the variety of the mass and volume of the ocean body, combined with the motions of the land. Thermal expansion and the exchange of water between oceans and other reservoirs (glaciers and ice caps, ice sheets, other land water reservoirs – including through anthropogenic change in land hydrology, and the atmosphere) are two major processes, mostly related to recent climate

change, that alter the volume of water in the global oceans (Bindoff, 2007). Climate models and oceanic observations show that sea level is not changing uniformly around the world. Sea level is rising in some regions but falling in others, which is mostly due to non-uniform changes in temperature and salinity. Vertical land movements also affect global mean sea level. They do not alter ocean water volume, but through their alteration of the shape and hence the volume of the ocean basins containing the water. The motion of land in uplift is composed of large-scale and local motions. The large-scale motion is the response of the crust to global scale changes in the mass loading of the Earth's surface, with the major part of the melting of ice sheets occurring through natural geological processes. The local motion is resulting from tectonics, subsidence and sedimentation. Subsidence and sedimentation are partly due to anthropogenic influences like groundwater withdrawal, oil and gas extraction, dam building and river flow alternations involved in the process of population explosion and urbanization (Bindoff, 2007).

Measurements of present-day sea level change mainly rely on two different techniques: tide gauge records and satellite altimetry. Tide gauges are traditionally employed for continuously measuring the sea level at a specific location in a relatively long time. One type of tide gauges is a float system operating in a stilling well, measuring the sea level relative to a nearby geodetic benchmark. There are other three types of gauges which are based on pressure, acoustics and radar. There are hundreds of tide gauge stations distributed in the oceans around the world. Figure 1.1 is an example showing the location of the tide gauge stations which are participating in the Permanent Service for Mean Sea Level (PSMSL). Most of them have decade-long records and some stations even have collected data for over a century. Tide gauges are the only measuring devices providing historical, precise, long-term sea level data.

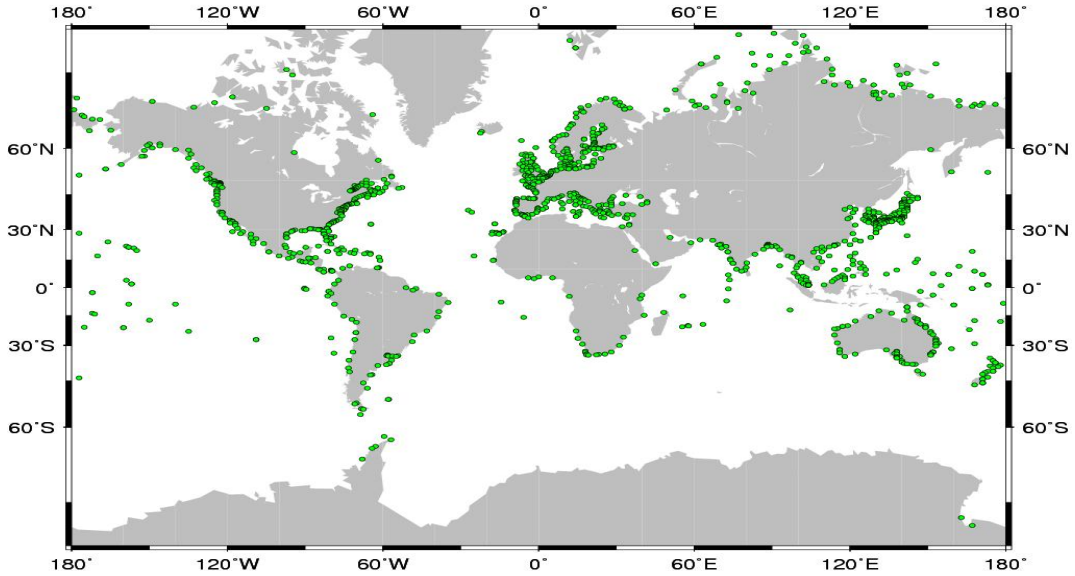

Figure 1.1: Distribution of tide gauge stations.

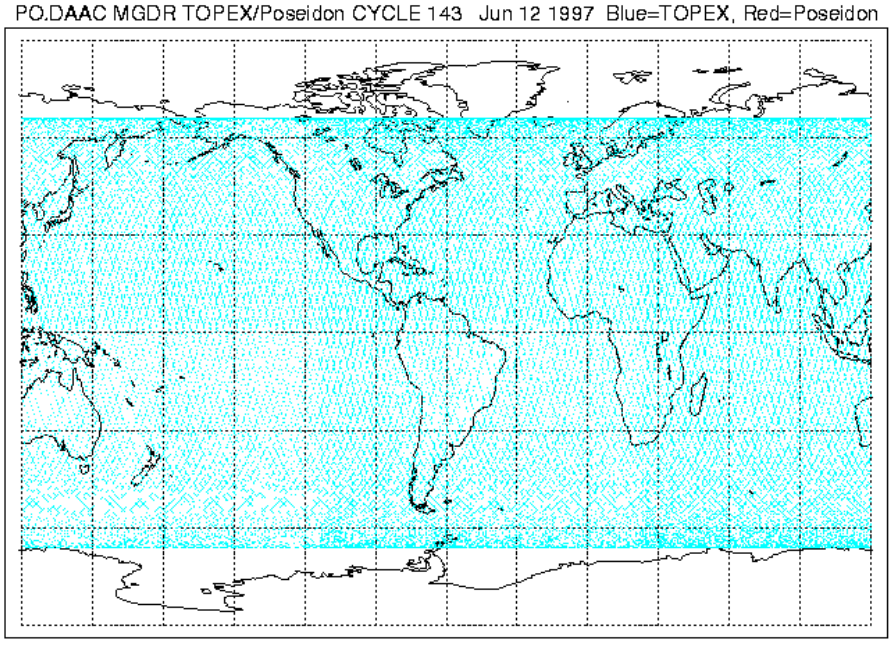

Figure 1.2: Ground track of TOPEX/POSEIDON on a world map (Benada, 1997).

Satellite altimetry data for Oceanography and Geodesy have been available for over forty years. Before the application of satellite altimetry, although it was relatively simple to collect a long

time series of sea surface heights (SSHs) at a specific location (e.g. a tide gauge), obtaining synoptic time series for a large region or globally has been impossible due to the vastness of the oceans. A shipborne campaign is one of the traditional methods for collecting geodetic and oceanographic observations in a region. It has obvious disadvantages as it is time-consuming and expensive, and provides inhomogeneous and limited coverage. Satellite altimetry enables of to monitor and model the mean sea level and its variation, gravity field, ocean circulation, temperature and pressure changes, tides, ocean bottom topography, tectonics, etc., on a global scale (Vergos, 2002). Satellite altimetry provides direct, continuous, homogeneous and repeated measurements of instantaneous ocean surface with high accuracy, high resolution and wide coverage (Figure 1.2).

1.2 Research Background and Open Problems

1.2.1 Global and regional sea level change estimated by tide gauge data

The global or regional trend results estimated by tide gauge data have been published in many papers. Douglas (1991) estimated the global sea level trend by averaging data from 21 tide gauge sites for the period from 1900 to 1980 and obtained the value of 1.8±0.4 mm/year. Then Douglas (1997) used 24 long tide gauge records, accounted for the post-glacial rebound (PGR) by the glacial isostatic adjustment (GIA) model ICE-3G (Tushingham and Peltier, 1991) to estimate the average rate of global sea level rise and obtained a value of 1.8±0.1 mm/year. Peltier applied a new model named ICE-4G (Peltier, 2001 and 2002) to the 24 tide gauge records used by Douglas (1997) and derived a global sea level rise rate as 1.84 to 1.91 mm/year. Church et al. (2004) analyzed more than 1000 records of monthly tide gauge data from PSMSL and obtained a rate estimate indicating a global sea level rise of 1.83±0.3 mm/year. Holgate and

Woodworth (2004) estimated the rate of global sea level rise over 55 years as 1.7±0.2 mm/year based on records from 177 tide gauges which were divided into 13 regions with near global coverage using the ICE-4G GIA model (Peltier, 2002) for correcting for the land movement. Church and White (2011) estimated the rise in global average sea level from tide gauge data for the period from 1880 to 2009. The linear trend was reported as 1.7±0.2 mm/year, 1.9±0.4 mm/year, and 2.8±0.8 mm/year for the period from 1900, 1960 and 1993 to 2009, respectively. It indicates a statistically significant acceleration of sea level rise in the last two decades.

In addition to estimating the global mean sea level trend, authors also used tide gauge data to analyze the regional sea level change. Douglas (1991) chose 22 tide gauge sites in 9 ocean regions, which are not at convergent tectonic plate boundaries and have more than 80% complete records from 1900 to 1980, to estimate the sea level trend for each region. In the west coast of North America, sea level was rising with the velocity 1.7 mm/year for the period from 1900 to 1980. During the same period, in the North East coast of North America, the trend of sea level change was 1.3 mm/year while in the South East coast of North America the value was 2.5 mm/year. Woodworth et al. (1999) worked on estimating the mean sea level in the British Isles Sea. They analyzed the effects of vertical land movement and tide-surge, and data length on the trend estimation. And they got a conclusion that one needs typically 30 years of data in order to determine a secular sea level trend with a standard error of the order of 0.5 mm/year, and 50 years for an error of the order of 0.3 mm/year. 1 mm/year sea level rise in the British Isles Sea was reported from their results. Church et al. (2004) used empirical orthogonal functions (EOFs) to reconstruct the global distribution of monthly sea level from 1950 to 2000. They found two maximum rates of rise, one in the central to eastern off-equatorial Pacific, and

one in the Northeast Indian Ocean. Snay et al. (2007) found that the mean rate of sea level change was equal to 1.8±0.18 mm/year for the period from 1900 to 1999 for North America. Their result was based on analyzing 37 North American tide gauge records and applying the velocity estimates of vertical land motion from continuous Global Positioning System (GPS) observations. Mazzotti et al. (2008) estimated the relative and absolute sea level rise in the Pacific coast of Canada and Northwest United Stated by combining tide gauge and GPS data. Their result indicated a 1.8±0.2 mm/year rise of sea level through the 20th century.

1.2.2 Global and regional sea level change estimated by satellite altimetry data

Wagner and Cheney (1992) used a collinear differencing scheme of 2.5 years Geodetic Satellite (Geosat) mission data to determine the rate of global sea level rise as -12±3 mm/year. Another rate estimate of 10 mm/year was obtained when combining Geosat data with a 17-day Seafaring Satellite (Seasat) dataset. The large uncertainty may be due to the large errors in orbit determination, the ionosphere and wet troposphere delay corrections, and unknown drift in the altimeter data. The TOPEX/POSEIDON (T/P) mission, launched in 1992, provided sea surface measurements with unprecedented accuracy. Nerem (1995) obtained a global rate of 5.8±0.7 mm/year by averaging two years of T/P data. He also evaluated the effects of altimeter corrections on the trend estimate. Cazenave et al. (1998) processed 4.5 years of T/P and 4 years of ERS1 data with updated environmental and geophysical corrections. Their global rate estimate was 1.4±0.2 mm/year and 0.3±0.3 mm/year, respectively. 6 years of T/P observations showed a 15 mm rise and fall in mean sea level, which accompanied the 1997–1998 El Ninõ–Southern Oscillation (ENSO) event (Nerem et al., 1999). Jason-1, which was launched in 2002, was the optimum continuation mission of T/P and the extension of accurate scientific data

records if provided could satisfy the requirement that multiple-decade records are needed to detect the climate signals well (Nerem et al., 1999). Leuliette et al. (2004) compared the satellite-dependent corrections of T/P and Jason-1, and analyzed their impacts on global mean sea level determination. Then a continuous record of sea level from T/P and Jason-1 was constructed (after accounting for the drifts present in each system) based on the results of inter-satellite and tide gauge calibrations; the rate estimate of global sea level rise was 2.8±0.4 mm/year. Nicholls and Cazenave (2010) published the mean rate of sea level rise amounts to 3.3±0.4 mm/year for the period from 1993 to 2009. They attributed two main factors to the rise: (1) thermal expansion of sea water due to ocean warming and (2) water mass input from land ice melt and land water reservoirs. They also predicted the sea level would rise between 30 and 180 cm by 2100.

Satellite altimetry data has also been used to analyze regional sea level changes. In the Mediterranean Sea, the mean rate of sea level rise, derived by averaging 6 years of T/P (1993 to 1998) and 4 years of ERS-1/2 data, was 7±1.5 mm/year, while in the Black Sea the rate reached 27±2.5 mm/year (Cazenave et al., 2002). The inter-annual/decadal variability of the upper ocean circulation and the increase of temperature and salinity are two factors affecting the estimate of sea level trend in the Mediterranean Sea. In the Black Sea, regional hydrology change could be one reason for the sea level rise. The Sea Level Research Group of University of Colorado (CU SLRGroup) published the regional sea level time series for 17 oceanic areas for the period from 1993 to 2011 on their website. A linear trend of 2.55±0.07 mm/year for the Pacific Ocean and 2.81±0.09 mm/year for the Atlantic Ocean were found in their corresponding sea level time series. Mazzotti et al.

(2008) stated an altimetry-derived sea level rate ranging between about 0 and -3 mm/year off the western United States and between -3 and -8 mm/year in the Gulf of Alaska from 1993 to 2003.

1.2.3 Problems in estimating the coastal sea level change

The problems we encounter when estimating the coastal sea level change come from two sources: the measurement itself and the estimation methods. Although the utilization of highly precise satellite altimetry data to estimate the global or regional sea level change achieves great success, using altimetry data in coastal areas presents great challenges. One major problem is the relatively poor sampling of data due to the special design of altimeters for capturing global observations. Because the satellite moves in a specific repeated orbit, the same point on the ground track is theoretically re-measured after a specific period (actually, “re-measured” within 1km). A one-second sampling interval corresponds to 6-7 km spatial resolution along the ground track for T/P and Jason-1. However, the inter-track gaps are not sampled by any repeating tracks. In principle, longer repeat period generates smaller interval between adjacent tracks and vice versa. In order to obtain global observations in a short period, the cross-track resolution is compromised. T/P has a repeat period of nearly 10 days, so the cross-track sample is 350 km in the equatorial areas, a little less in high latitudes. ERS has a 34 days repeat period with a cross-track sample of 80 km at the equator. Such inter-track spatial resolution, which is adequate in the open ocean, is insufficient to separate coastal sea level signals with shorter wavelengths.

Second limitation is that the footprint illuminated by the altimeter antenna is contaminated by land, making it hard for both the altimeter and the radiometer to retrieve stable measurements with satisfactory quality. Taking the range measurement as an example, the range between the

satellite and nadir sea surface is one half of the two-way travel time of the radar pulse transmitted and reflected multiplying the light speed. The altimeter receives the reflected radar returns and averages them to form the waveform which is used to estimate the transmitting and reflecting time. The shape of the returned waveform depends on the shape of the reflecting surface, which means the shape of the returned waveform reflected from the ocean is different from that reflected from the land. As a satellite ground track approaches, recedes, or runs parallel to the coastline, even though the altimeter's nadir point is over the sea, the altimeter will also track the off-nadir returns reflected from the higher land (Deng et al., 2002). The altimeter processes the radar return using a tracking algorithm basing on a special ocean statistics model. When the reflections are over land or continental ice sheets, the returned radar signal differs from that of the model. As a result, the derived waveform is different from the expected waveform over oceans. Hence the time estimate will shift with respect to its 'true' value and then the range measurement near the coast is spurious. Generally, a retracking process can be used to improve coastal altimeter data. Anzenhofer and Shum (1999) developed a retracking process and applied it to ERS-1 waveforms. They first used a developed radar waveform tracker, and then fitted the waveforms using the so-called beta retracker.

A similar problem occurs on radiometer measurements, which makes the derived wet troposphere corrections are spurious. A satellite-based downward-looking passive radiometer determines the columnar water vapor by measuring the brightness temperatures within the water vapor absorption band (Chelton et al., 2001). In the deep ocean, wet troposphere corrections determined by the on-board radiometer have very high accuracy. The accuracy of T/P's wet troposphere correction is 1.1 cm in rain-free conditions, even when heavy clouds and winds are

present in the radiometer footprint (Chelton et al., 2001). But in coastal areas where the footprint may contain both water and land surfaces, the wet troposphere correction is highly contaminated by the land effects, because the algorithms used to derive the wet tropospheric delay from the measured brightness temperatures are based on sea-surface emissivity models. Several methods may partly solve this problem. They are: (1) use of meteorological model values (e.g., water vapor from the European Center for Medium range Weather Forecasting (ECMWF) model); (2) propagation of the open-ocean radiometer-derived wet troposphere correction to the coastal area which is generally done by interpolation; (3) propagation but imposing a meteorological model as a constraint. Desportes et al. (2007) indicate that the latter two approaches yield comparable results which are better than those from the first method. Madsen et al. (2007) used the third method to generate wet troposphere corrections based on the ECMWF model and recovered satellite data as close as 10 km from the coast of the North Sea-Baltic Sea area.

Another limitation to the application of satellite altimetry in coastal areas is due to the complex dynamics of coastal seas and the irregular shape of the shorelines. Some geophysical corrections, especially the ocean tide which is responsible for more than 80% of the sea level variability (Koblinsky et al., 1999), are not appropriate any more. The coastal ocean encompasses an area extending from the near-shore to the continental shelf and slope (Vignudelli, 2006). The coastal area is also named as shallow water area because the water depth is relatively lower compared to that in the open ocean. When the tide waves travel through the shallow water, they are progressively distorted and damped by the effects of some dynamic processes. Le Provost (1991) discussed the major processes making the dynamics of the coastal sea complex. In the shallow

water, the instantaneous sea surface elevation is not negligible compared to the water depth. The velocity of the tide waves is greater at the tide crest than at the trough, leading to wave steepening. Steepening is one of the most important physical processes controlling tidal dynamics in shallow waters. Another affecting process is the bottom friction which decays the wave's propagation exponentially with a slight decrease of the wave velocity. Other affecting factors are the wave reflections along the coastline and the Earth rotation which influences the structure of the two dimensional tidal wave patterns over the coastal basins. Hence, in addition to the astronomical tides which may have extreme ranges and change rapidly in the coastal area, under the effects of the above physical processes, shallow water tides (overtides and compound tides) are generated. Overtides are generated as the astronomical constituents disturb with themselves while compound tides are generated as the major constituents disturb with others. For example, the interaction of the semidiurnal constituent M_2 with itself generates the overtide constituent M_4. So under the effects of the geophysical processes, the tidal patterns in the coastal area become very complex. In the deep ocean, the dynamics of barotropic tides are recognized to be linear. Eight major constituents, Q_1, O_1, P_1, K_1, N_2, M_2, S_2 and K_2, can represent the whole tidal spectrum well with only few discrepancies. Savcenko et al. (2011) compared global tide models, e.g., FES2004 (Lyard et al., 2006), EOT11a (Savcenko et al., 2011), TPXO7.2 (Dgbert and Erofeeva, 2002) and DTU10 (Cheng and Andersen, 2010), with pelagic or shallow coastal tide gauges. Their comparison result showed that in the deep ocean the discrepancy between global tide models and tide gauges is around 1 cm while in the coastal area, the discrepancy could reach up to several centimeters and even 10 cm for the constituent M_2. The inefficiency of global hydrodynamic tide models is mainly due to the

insufficient resolution of bathymetric features and the incorrect frictional dissipation, while the spatial resolutions of the empirical models is not high enough to capture the signals changing rapidly with short wavelengths in shallow water areas (Foreman, 1998). In addition, the shallow water tides, which are very small in the deep ocean, cannot be ignored in the coastal area. Foreman et al. (2000) found the amplitude of overtide constituent M_4 could exceed 20 cm in some locations in the west coast of Canada. In previous papers, the tide correction for satellite altimetry data in coastal areas was derived from a carefully selected global tide model (e.g., Cazenave et al., 2002; Mangiarotti 2007), or from a regional tide model for the study area (e.g., Foreman et al., 1998; Vignudelli et al., 2005), or from pointwise least-square harmonic fitting of the significant tidal constituents (e.g., Cherniawsky et al., 2001; Cherniawsky et al., 2004; Madsen et al., 2007).

The disadvantages of using global tide models are discussed above. Regional tide models generally perform better than global tide models in coastal areas but their utilization is constricted by the limited number of constituents involved and the spatial resolution. Similar to global tide models, regional tide models are mainly composed of major astronomical constituents (e.g., Ballantyne et al., 1996; Foreman and Thomson, 1997; Foreman et al., 2000; Dupont et al., 2002), and very few of them include the long term, minor astronomical, or shallow water constituents. Regional tide models are recorded as triangular or rectangular grids. Although the grids are smaller than those of global tide models, they are still too large to capture some tidal signals with very short wavelengths. Analyzing the tidal constituents pointwisely for the altimetry time series is a widely used method. But this method requires looking deep into the residual ocean tide signals and finding out the distinguishable residual

constituents. In this study, in order to overcome the problems of using satellite altimetry data in coastal areas, we focus on residual ocean tide analysis.

Two disadvantages of tide gauge data limit their utilization in estimating not only the coastal but also the global and regional sea level change. Firstly, tide gauges have sparse spatial distribution. Tide gauges are established along the coast of the continents or islands (see, e.g., Figure 1.1). However the available tide gauges which are established on stable bedrock, are in good conditions, have long data record (more than 20 years), and have intact, exact information about benchmarks, are not too many. For example, Fisheries and Oceans Canada (DFO) operates 220 coastal tide gauge stations in the Pacific Ocean, and only 9 stations satisfy the above conditions. And in the Atlantic Ocean, only 11 out of 272 coastal tide gauges are used in this thesis. The number of tide gauge sites is very small compared to the number of altimetry data in these two areas.

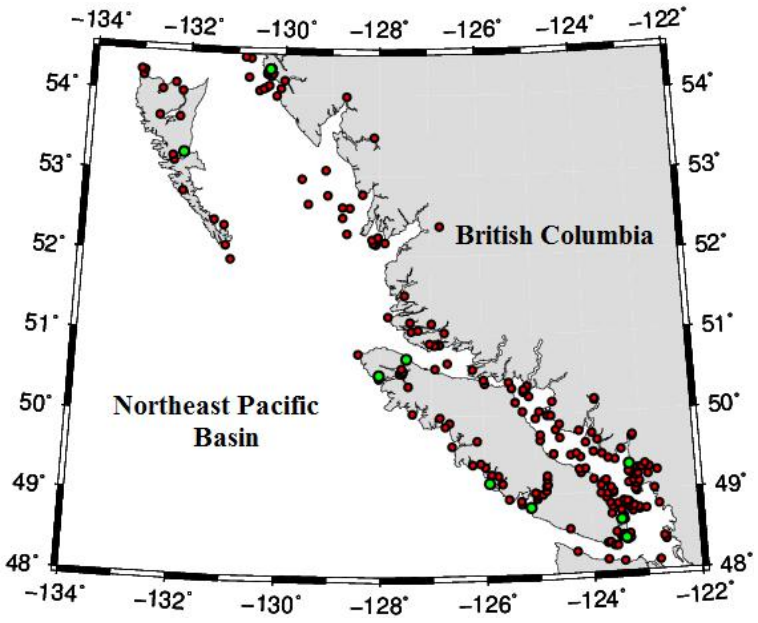

Figure 1.3: Tide gauge stations from Fisheries and Oceans Canada in the west coast of Canada. Red cycles are for the position of all available tide gauge stations. Green cycles are for the position of tide gauge stations used in this thesis.

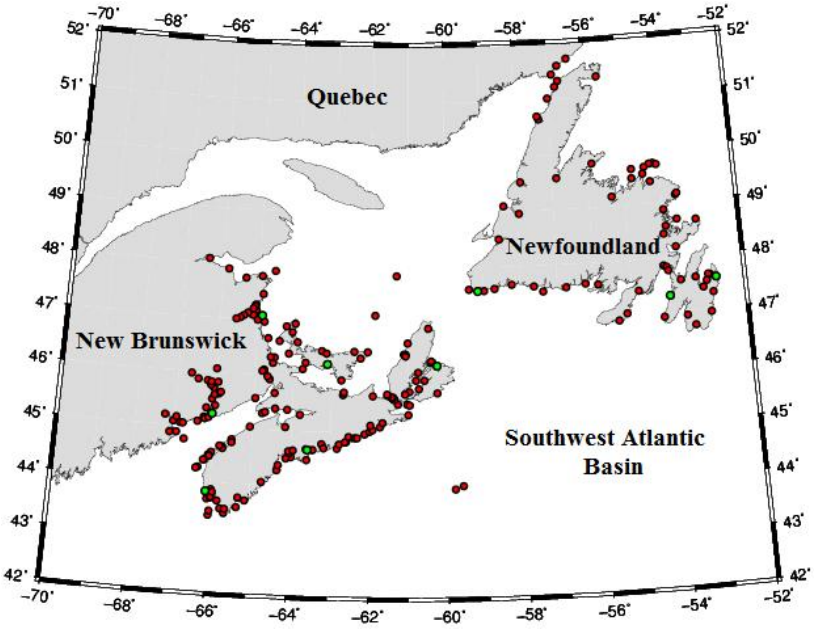

Figure 1.4: Tide gauge stations from Fisheries and Oceans Canada in the east coast of Canada. Red cycles are for the position of all available tide gauge stations. Green cycles are for the position of tide gauge stations used in this thesis.

Secondly, tide gauge measurements are contaminated by vertical land motion. Tide gauge measurements are referring to the nearby benchmarks (BM), which are established on bedrock. The position of a BM is not stable but varies as land is moving upward or downward. So sea level change estimated by tide gauge data is basically relative sea level (RSL) change. The vertical land movement, which is a kind of "geophysical noise" in the tide gauge data, increases the difficulty in obtaining a consensus on the value of sea level change. Concerning the vertical crustal movements, the most ubiquitous source of regional submergence or emergence at tide gauge sites is the PGR that continues since the last deglaciation period (Douglas, 1997). In or near formerly ice-covered regions, vertical land movements due to PGR have at most sites, approximately the same or even greater magnitude as the global sea level change. In areas far away from rebounding deglaciated areas and the adjacent collapsing peripheral bulge, the PGR is still a significant fraction of the sea level change (Bindoff, 2007). Besides PGR, there is

vertical land motion maybe caused by other processes, such as active tectonics, subsidence and sedimentation. Mazzotti et al. (2008) stated in their paper that, for the western Canada and the northwestern United States, postglacial rebound and tectonics are particularly significant. Global postglacial rebound models overpredict rebound velocities by 1 to 2 mm/year because they are not accounting for the low viscosity of the western North America upper mantle. Active tectonics lead to vertical velocities that are typically between -1 to 4 mm/yr. Many researches have used a GIA model to remove PGR from tide gauge data (e.g., Douglas (1997), Peltier (2001), Church et al. (2004), Holgate and Woodworth (2004)). But using a GIA model to correct for the vertical land motion leads to two main issues: first, GIA corrections vary depending on the GIA model used; second, GIA corrections do not account for other processes such as active tectonics. The real vertical land motion can be measured by continuous GPS stations at or near tide gauges; published results can be found in Wöppelmann et al. (2007), Snay et al. (2007), Mazzotti et al. (2003) and Mazzotti (2007). In this study, the velocity of the vertical land motion is obtained from continuous GPS data.

Satellite altimetry and tide gauge data are generally used to estimate the global or regional sea level trend separately. In the coastal areas, though, considering their respective advantages, it is better to combine them together. Tide gauges located along the coastline can provide accurate sea surface measurements as close as possible to the land, which are a good supplement to the altimetry data that are degraded near the coastline. Moreover, the dense sampling by satellite altimetry can overcome the limitation of the sparse distribution of tide gauges.

Not many combination methods have been developed to date. Church et al. (2004) combined T/P data from 1993 to 2001 with tide gauge data from 1950 to 2000 to estimate the spatial variations of sea level change between 1950 and 2000. They constructed the global distribution of monthly sea level between 1950 and 2000 by EOFs analysis. Satellite altimetry data was used to estimate the global covariance structure as expressed in EOFs. The amplitude of these EOFs was estimated by the tide gauge records. The spatial patterns derived by this method from the 9-year T/P data are not representative of interdecadal averages (Berge-Nguyen et al. 2008). Another combination method was proposed by Mangiarotti (2007). He used a general least-squares (GLS) model to extrapolate T/P data to 153 tide gauge locations in the Mediterranean Sea and then jointly analyzed altimetry and tide gauge data to construct the SSHs at each location. The difficulty of this method is the calculation of the covariance matrix used in the GLS and, moreover, the data extrapolation by the GLS could cause errors on the trend estimate. Mangiarotti (2007) estimated the effect of the error associated with the data extrapolation on the sea level trend estimate to be 0.84 mm/year on average. In this study, a different combination method has been developed in order to overcome these difficulties.

1.3 Objectives

Based on the above discussion about the problems of estimating the coastal sea level change, we can see that both the accuracy of altimetry data in coastal areas and the estimation methods should be developed. Accordingly the objectives of this thesis are categorized into three parts. The first objective is to improve the efficiency of altimetry data in coastal areas. We choose to improve the ocean tide corrections for altimetry data because ocean tides cause most of the variations of the sea surface, and signals with periods longer than 6 months in the residual ocean

tides could affect the accuracy of sea level trend estimates. The other two objectives are about the development of the estimation method and appropriate calculating strategies.

1) To estimate the residual ocean tides in the Pacific and Atlantic coasts of Canada and remove them from altimetry data. The residual ocean tides include the signals with periods from several hours to one year. Among them, annual or semiannual tidal constituents could impact significantly the uncertainty of the sea level trend estimate. Spectral analysis is used to detect the constituents of the residual ocean tides and the traditional harmonic analysis is used to estimate the amplitude and phase for every constituent that can be distinguished.

2) To estimate an accurate linear sea level trend with reliable uncertainty at every satellite altimetry or tide gauge site. The linear regression model for estimating the linear sea level trend is simple but the calculating strategies for processing the altimetry and tide gauge time series are complex. Firstly, appropriate data pre-processing, averaging and blunder detection methods are needed to convert the raw data from altimetry or tide gauges to the time series of sea surface measurements. These time series are the suitable observations for the regression model. Secondly, an appropriate covariance matrix for the measurement errors should be developed by the carefully designed methods. It is significant for determining reliably the uncertainty of the trend estimate. Thirdly, the least-squares estimate is used to fit the sea level observations to the linear regression model. For tide gauges, another step is required to compensate for the effects of vertical land motion.

3) To develop a new combination method for estimating the coastal sea level change using satellite altimetry and tide gauge data together. The combination method should not produce additional errors on sea level estimates.

The investigations will be carried out in two areas: the Pacific coast and Atlantic coast of Canada. These two areas have different shapes of the coastline, continental shelves, water bathymetries and ocean patterns.

1.4 Thesis Outline

This thesis consists of eight chapters, and the general structure and contents of each one are outlined below.

In Chapter 2, the satellite altimetry and tide gauge data used in this study and the pre-processing applied on them are presented. We first introduce the principle and definitions of altimetric systems and measurements. Then we describe the T/P and Jason-1 altimetric missions, the editing criteria and the various corrections used during the pre-processing. The following section shows examples of the continuous time series from T/P and Jason-1, which are generated by stacking and removing the bias between T/P and Jason-1 data. The next section of this chapter is about the measuring principle of tide gauges, error sources, and the pre-processing of tide gauge data. The last section will define the study coastal areas.

In Chapter 3, the linear regression model and calculating strategies for estimating the linear trend of sea level change at every altimetry or tide gauge site are explained theoretically. The

methods for deriving the annual seasonal and regional common mode corrections for altimetry and tide gauge data are also introduced in this chapter. Then the definitions of the power-law noises are reviewed. One specific section introduces the power spectral density and maximum likelihood analysis which are used to find appropriate noise model. The final section summarizes the standard estimation strategies.

In Chapter 4, residual ocean tides are analyzed by least-squares spectral analysis, and the amplitudes and phases of selected constituents are estimated by harmonic analysis. The second section introduces the local tide model Webtide and also examines the model accuracy. The third section describes two analysis methods: the harmonic analysis and least-squares spectral analysis. Section four and section five show the analyze results for the west coast and east coast of Canada, respectively.

In Chapter 5, sea surface time series from T/P and Jason-1 are processed under the estimation strategies defined in Chapter Three to determine the rate of absolute sea level change.

In Chapter 6, the estimated results of relative and absolute sea level change by tide gauge data under the processing strategies described in Chapter Three are presented. The GPS estimates of the vertical land motion are also presented.

In Chapter 7, altimetry-derived rates and tide-gauge-derived rates will be averaged alone or together to obtain the mean regional sea level rate. The first two sections will present the least-squares averaging method and associated regional rate estimates for each type of data

individually. The third section will exhibit the results from combining altimetry and tide gauge data together. The last section will explain the error sources affecting the regional rate estimates by the combination method.

In Chapter 8, the main conclusions of this thesis are presented, followed by recommendations for future research.

Chapter Two: Satellite Altimetry and Tide Gauge Data and Associated Pre-processing Methods

2.1 Introduction

Satellite altimetry and tide gauges are two main types of observing systems providing direct observations of the instantaneous sea surface (ISS). The main advantages of the satellite altimetry method are the dense coverage, repeatability and homogeneity of the data for almost the entire global oceans. On the other hand, the tide gauge technique is the only measuring method providing long data records (even more than one hundred years) and with high temporal resolution (e.g., 1 measurement per hour). Therefore satellite altimetry and tide gauge data are often utilized together to monitor the mean sea level changes effectively.

These data sets need to be edited to reject any spurious or degraded observations and must be corrected for various sources of errors. This process is called pre-processing of the data. The pre-processing of both altimetry and tide gauge data can convert the raw sea surface observations to the appropriate time series for estimating the sea level change. The altimetry data used in this thesis are from the T/P and Jason-1 missions which are provided by the Physical Oceanography Distributed Active Archive Center (PO.DAAC) of Jet Propulsion Laboratory (JPL). JPL uses its own editing criteria and models for the corrections. The pre-processing of the tide gauge data from DFO is not as complex as that of the satellite altimetry data.

In the following paragraphs we will first describe the T/P and Jason-1 altimetric missions. Then analyze the principle of altimetric system and measurements, the editing criteria and corrections used by JPL, and the modifications to some JPL corrections. The next section of this chapter is about the principle of tide gauges, error sources, and the pre-processing of tide gauge data. The last section is about the two research areas in this thesis.

2.2 Satellite Altimetry

2.2.1 Satellite altimetry definitions and principle

Before describing the pre-processing of satellite altimetry data, the satellite altimetry principle and the definition of terms used in subsequent sections are given. Figure 2.1 depicts the basic terms describing the altimetric system.

The main measurement provided by satellite altimetry is the range R in Figure 2.1, which is defined as the one-way distance from the mass-centre of the satellite to the nadir ISS. The altimeter with an accurate on-board time-tagging device measures the time for the short pulse of microwave radiation transmitted from the altimeter to the rough sea surface and back. Then the range R can be calculated as

$$R = \frac{c * t}{2}, \tag{2.1}$$

where t is the travel time of the radar pulse, and c is the speed of light.

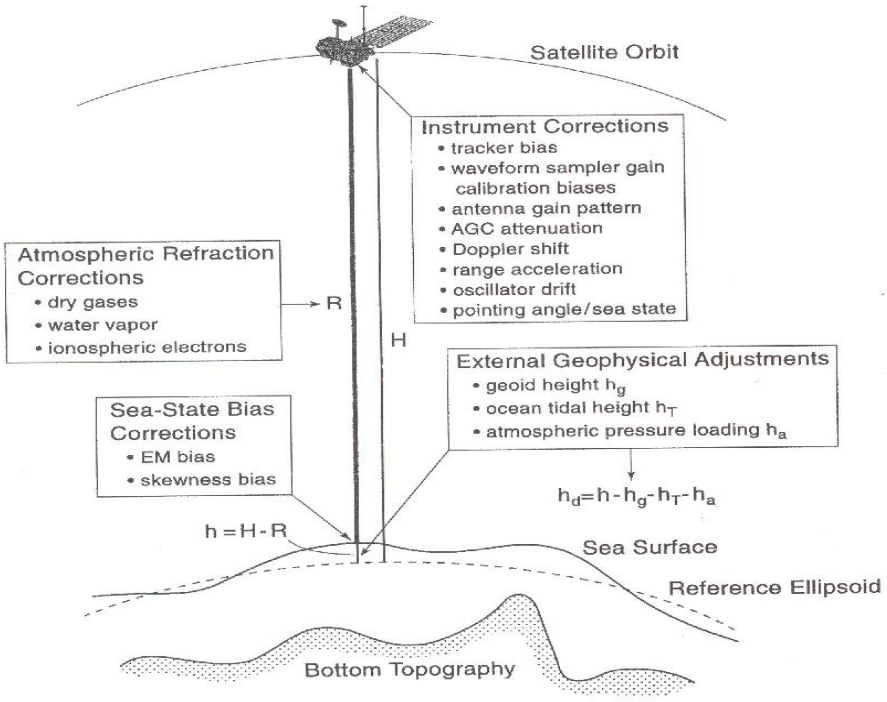

Figure 2.1: Principle of application of satellite altimetry on oceanographic research. (Figure 1 of Chelton, 2001)

In most cases, a dual-frequency radar altimeter operates at 13.5 GHz (Ku band) and 5.3 GHZ (C band) with its footprint radius varying between 1 to 12 km depending on the sea state. The choice of Ku and C band is due to the following three reasons: (1) at frequencies higher than 18 GHz, atmospheric attenuation rapidly increases, thus decreasing the power of the transmitted signal; (2) at lower frequencies, the refraction of electromagnetic radiation by the ionosphere increases and the interference from ground-based civilian and military sources of electromagnetic radiation related to communications, navigation, and radar increases; (3) the antenna footprint size on the sea surface is proportional to the wavelength of the electromagnetic radiation and inversely proportional to the antenna size (Chelton et al., 2001). The time estimate is derived by analyzing the returned pulse from the footprint. To achieve the

appropriate signal-to-noise ratio a specific number, which is determined by the pulse repetition frequency (PRF), of returned pulses are averaged. Then the averaged pulses are fitted to a smoothed curve and two consecutive curves are used to determine one range measurement every tenth of a second (0.1s). The shape of the fitted curve depends on the roughness of the sea surface. If the sea is calm, then the curve is steep while if the sea is rough, the curve is much smoother. The wave height is expressed by the term significant wave height (SWH), which is another important measurement provided by satellite altimetry. Thus, the measured R is actually a mean height of the sea surface that is covered by the radar footprint.

In practice, the range R estimated by Equation (2.1) is converted to the instantaneous height of the sea surface h_{isl} by the satellite altitude. Satellite altitude, denoted as H in Figure 2.1, is defined as the distance between the mass-center of the satellite and that of the reference ellipsoid in the normal direction. The equation is

$$h_{isl} = H - R \,. \tag{2.2}$$

As shown in Figure 2.1, both altitude and range measurements include errors. The errors of the range measurement are categorized into two groups: the instrumental errors ΔR_{ins} and the propagation delay ΔR_{delay}. Considering as well the radial orbit error ΔH, Equation (2.2) is rewritten as

$$h = H + \Delta H - (R + \Delta R_{ins} + \Delta R_{delay}) \,, \tag{2.3}$$

where h shown in Figure 2.1 is named as sea surface height (SSH).

The sea state bias mentioned in Figure 2.1 is considered as one part of the instrument errors in our definition. When we look deep into the propagation delay, the dry and wet troposphere and the ionosphere all affect the pulses during their traveling through the atmosphere. Accordingly, the corrections for the propagation delay are categorized into the corrections of the dry and wet troposphere ΔR_{dry}^{C}, ΔR_{wet}^{C} and the ionospheric delay ΔR_{iono}^{C}, respectively. So we can develop Equation (2.3) to

$$h = H + \Delta H - (R + \Delta R_{ins} + \Delta R_{dry}^{C} + \Delta R_{wet}^{C} + \Delta R_{iono}^{C} + \Delta\alpha), \tag{2.4}$$

where $\Delta\alpha$ is an error term that includes the residual instrumental errors and propagation delay, and the noise of the range measurement.

We will now discuss the orbit error ΔH. ΔH exists because of our insufficient knowledge of the true satellite orbit, which is mainly attributed to the inaccurate gravity field models and the sparse coverage of the tracking systems available all over the world. Following the improvements of the gravity models and global tacking systems, the radial orbit error decreased from 2-3 m for the SEASAT mission to 2-3 cm for T/P and 1.5 cm for Jason-1.

In Geodesy, h is generally converted to a physical surface, e.g., the geoid, which is a geopotential surface; the Geoid undulation N is shown in Figure 2.2. In Oceanography, the reference surface would be a geometric surface, e.g., the Mean Sea Surface (MSS) shown in Figure 2.2. This conversion is necessary because the ground tracks of exact repeat missions like T/P, Jason-1 are allowed to drift by ±1 km. This introduces a problem: on different cycles, the satellite will sample a different geoid profile. This effect is the so-called cross-track geoid

gradient, and Brenner and Koblinsky (1990) estimated it at about 2 cm/km over most of the ocean, larger over continental slopes, reaching 20 cm/km at trenches (T/P user handbook, 1997). Even if the passes repeated exactly, one would have to interpolate along the pass (say, to a fixed set of latitudes) because a 3 km mismatch in along-pass position would cause approximately a 6 cm difference in the geoid, which would mistakenly be interpreted as a change in oceanographic conditions (Benada, 1997). Both problems are simultaneously solved if the SSHs are referred to the MSS (SSH-MSS). Then the real geoid changes across the track are automatically accounted for because the MSS is spatially interpolated to the actual satellite latitude-longitude. All altimetry derived sea surface heights are referring to the MSS in this thesis.

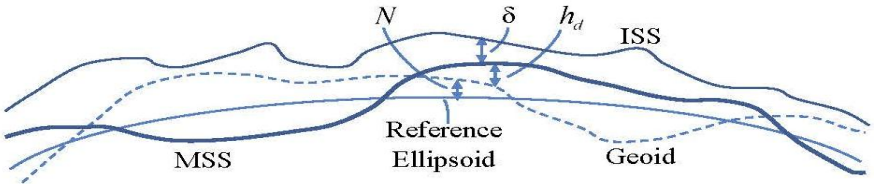

Figure 2.2: Relations between the ISS, MSS, Geoid and the reference ellipsoid.

The sea level anomaly (SLA) δ shown in Figure 2.2 can be derived by removing the effects of the tides and atmospheric loading from the SSH h by

$$\delta = h - h_{MSS} - h_T - h_a \tag{2.5}$$

where h_{MSS} is the height of the MSS referring to the ellipsoid, h_T is the tidal effect including the ocean, the loading, the Earth and the pole tides, and h_a is the inverse Barometer (IB) correction. h_T and h_a are called the geophysical correction for altimetry data. Using equations (2.3) to (2.5), we can get the final expression of the SLA as

$$\delta = H - R - \Delta R^C_{ins} - \Delta R^C_{dry} - \Delta R^C_{wet} - \Delta R^C_{iono} - h_{MSS} - h_T - h_a - \Delta\beta \tag{2.6}$$

where $\Delta\beta$ contains the residual errors and the noise of the range measurement and has a relation with $\Delta\alpha$ as

$$\Delta\beta = \Delta\alpha - \Delta H + \Delta h_T + \Delta h_a + \Delta h_{MSS} .$$

where Δh_T is the error of tide corrections, Δh_a is the error of inverse barometer corrections, and Δh_{MSS} is the error of the mean sea level model. All the corrections in Equation (2.6) are provided in the altimetry (M)GDR products. A brief overview of them will be given in the next section.

There are other terms used in this thesis defined below:

1) Revolution: a complete revolution of the satellite around the Earth.
2) Satellite pass: one half of a satellite revolution.
3) Ascending passes: passes that the satellite goes from South to North (North-going passes).
4) Descending passes: passes that the satellite goes from North to South (South-going passes).
5) The complete satellite repeat cycle: the time period until the satellite passes twice from the exact same point. This term is only found in ERM phases.

2.2.2 T/P and Jason-1 missions

T/P which is an altimetric mission jointly launched by NASA and CNES on August 10, 1992. It began to collect data on September 25 by the TOPEX-A altimeter. TOPEX-A worked until February, 1999 (cycle 235) and then was turned off because there was a degradation in the point target response which impacted the significant wave height. Then the backup altimeter TOPEX-

B was turned on and worked for the remaining period of T/P's life. T/P began a drift maneuver on August 15, 2002 and moved to a different orbit on September 16, 2002. T/P was operated on the new orbit for 3 years and stopped working on October 18, 2005. 481 cycles of data were collected by T/P, among which 368 to 481 cycles of data were obtained on the shifted orbit.

The six onboard scientific instruments contributed to the science and mission goals of T/P. These instruments can be categorized into two groups according to their functions. The dual-frequency radar altimeter (NRA) built by NASA and the solid state altimeter (SSALT) built by CNES measured the altimeter range and significant wave height, and shared the same antenna. As the main sensor, NRA took about 90% of the operating time while SSALT took 10%. The TOPEX Microwave Radiometer (TMR) measured the water vapor to provide the wet troposphere corrections for the range measurements.

T/P was orbiting the Earth at an altitude of 1336 km in a near circular orbit with an inclination of 66.039°. The repeat period of T/P was 9.9156 days and its repeated ground tracks were within approximate 1 km. The achieved orbit accuracy reached 3 cm, and benefited from the utilization of the onboard Precise Orbit Determination (POD) system as well as the JGM-3 gravity model (Tapley et al. 1996). The POD was composed of the Doppler Orbitography and Radiopositioning by Satellite (DORIS) transmitter and the Global Positioning System Demonstration Receiver (GPSDR). DORIS was used for all-weather global tracking and to calculate the orbit ephemeris in high accuracy. GPSDR used GPS differential ranging for the POD. T/P was the first mission to demonstrate that GPS could be used to determine the exact

location of a spacecraft and track it in an orbit. Another instrument the Laser Retroreflector Array (LRA), supported the calibration and validation of POD.

Jason-1 is the tandem mission of T/P and is also a joint mission operated by NASA and CNES. Jason-1 was launched on December 7, 2001 and began to collect the data on January 15, 2002. The orbit of Jason-1 is almost the same as that of T/P. After working for 7-year, Jason-1 began a maneuvering shift to a new orbit on January 26, 2009 (cycle 260) after the launch and operation of OSTM/Jason-2. The maneuver was completed on February 14, 2009 and the cycle 263 is the first complete cycle for the new orbit.

Jason-1 carries instruments very similar to those on T/P except that it has only one altimeter: Poseidon 2. Jason-1 Microwave Radiometer (JMR) measures the sea surface microwave brightness temperatures in three frequencies to provide the error estimate in the range measurement caused by pulse delay due to the atmosphere water vapor. The DORIS, LRA and GPS systems onboard determine the orbit of Jason-1 precisely; the accuracy of the radial component of the Jason-1 orbit is 2.5 cm.

The T/P and Jason-1 missions have made observations of the global oceans with unprecedented accuracy: 4.7 cm for the TOPEX system and 5.1 cm for the POSEIDON system (Fu et al., 1994) and 4.2 cm for the Jason-1 system (Jason-1 user handbook, 2008). The complete 481 cycles of T/P data (1992 to 2004) and 259 cycles of Jason-1 data (2002 to 2008), which are spanning almost 16 years, offer accurate, repeated and densely covered observations for the sea surface, making possible the study of MSL variations.

2.2.3 Altimetry corrections

This section will introduce the corrections listed in Equation (2.5) and their derivations for T/P and Jason-1 data.

2.2.3.1 Instrumental errors

Instrumental errors are related to the instrument itself and its mechanical and electronic characteristics. Vergos (2002) ranked the instrumental errors into (1) the real instrument noise which for T/P or Jason-1 is at the level of a few centimeters; (2) the antenna mispointing effect, due to the off-nadir excursions of the altimeter antenna; (3) the electronic altimeter bias, due to the deviation of the electronic center of the altimeter from the satellite center of mass; and (4) the sea state bias, due to the systematic deviation of the scattering surface of the radar pulse from the mean sea surface.

The sea state bias is an important correction for altimetry data. Because the sea surface is not state-stable and mirror-like, the surface located in the footprint illuminated by the altimeter, which has a large radius of 2-12 km, will have different characters influencing the back-scattered pulses. This bias is believed to be composed of three parts. (1) The electromagnetic bias (EM), which arises from the fact that the backscattered power per unit surface area from wave troughs is greater than that from wave crests. It happens because the power backscattered from a small wave facet is proportional to the local radius of curvature of the long-wavelength portion of the wave spectrum. Since ocean waves are generally skewed, the wave troughs have a larger radius of curvature than wave crests. Thus the centroid of the mean reflecting surface is shifted from the mean sea level towards the troughs of the waves. (2) The tracker bias, which is

a purely instrumental effect. (3) The skewness bias, which is due to the assumption in the onboard algorithms that the probability density function of heights is symmetric, while in reality it is skewed (T/P user handbook, 1997; Jason-1 user handbook, 2008).

The error sources 1 to 3 are estimated for each individual satellite during the initial calibration phase of the mission. But the theoretical understanding of the sea state bias remains limited. The current most accurate estimates are obtained using empirical models derived from analyses of the altimeter data. The sea state bias corrections are computed as a function of the significant wave height and wind speed, based on the parameters results of Gaspar et al. (1994) for T/P data and on the parameters results of Labroue (2002 and 2006) for Jason-1 data. The function is written as

$$SSB = SWH \cdot (a_0 + a_1 SWH + a_2 U + a_3 U^2), \tag{2.7}$$

where SWH is the significant wave height, U is the wind speed, and a_i are empirical estimated parameters.

2.2.3.2 Atmospheric delay

The radar pulse sent by an altimeter travels through the atmosphere twice during its transmission from the satellite and back-scatting from the sea surface. At a distance of 0-40 km from the Earth's surface, exists the troposphere with its dry and wet components. The propagation velocity of a radar pulse is slowed by the refractivity of the dry gases and the water vapour. The contribution of the dry gases is nearly constant and produces a height error of approximately -2.3 m (Benada, 1997). The dry tropospheric refractivity is proportional to the dry atmospheric pressure and inversely proportional to the temperature. When hydrostatic

equilibrium and the ideal gas law are assumed, the dry troposphere range delay can be calculated as a function of the surface pressure. There is no straight forward way to measure the nadir surface pressure from a satellite, but it is determined by the meteorological models. T/P and Jason-1 both use the surface pressure model of ECMWF (Benada, 1997; AVISO and PODAAC, 2008) to calculate the surface pressure, and the uncertainty on the derived dry troposphere delay is about 0.7 cm over 1000-3000 km.

The wet troposphere produces a height calculation error of -6 cm to -40 cm (T/P user handbook, 1997). Both the water vapor and the cloud liquid water droplet contribute to the atmospheric refraction. The effects of water vapor on atmospheric refraction are 1-2 orders of magnitude larger than the effects of cloud liquid water droplets (Chelton et al., 2001). The amount of water vapor present along the path in the troposphere is quite variable and unpredictable. Thereby the range delay can vary from just a few millimeters in dry, cold air to more than 40 cm in hot, wet air. In the early missions, the column of water vapor along the path was determined through empirical models. But for the missions T/P and Jason-1, the vertically integrated densities of water vapor and cloud liquid water droplet can be determined by the passive microwave radiometer which is part of the payload on the satellites (Chelton et al. 2001). The wet tropospheric delay for T/P is derived from the brightness temperature measurements given by the three-channel TMR in frequencies 18, 21 and 37 GHz. The water vapor signal is sensed by the 21 GHz channel, while the 18 GHz removes the surface emission (wind speed influence), and the 37 GHz removes other atmospheric contributions (cloud cover influence). The JMR of Jason-1 is almost the same as the TMR but has three channels in frequencies 18.7, 23.8 and 34.0

GHz. The uncertainty of wet troposphere delay determined by the radiometer is $\pm$1.2 cm over 100-2000 km (Chelton et al. 2001).

At a distance of 60-1000 km above the Earth's surface, it is the ionosphere. The ionospheric refraction occurs due to the free electrons and ions in the upper atmosphere. Unlike in the troposphere, the transmitting speed of the radar pulse in the ionosphere is faster than the free-space speed of light. The ionosphere delay relies on the frequency of the signal and the electron density. For the early missions, the electron density was calculated from the models but since the T/P mission, every mission carries a dual-frequency altimeter to estimate the ionosphere refraction delay for the range measurement directly. When two microwave pulses in different frequencies transmitted by the altimeter at the same time propagate through the atmosphere, they will suffer the same tropospheric refraction but different ionospheric refraction because only ionospheric refraction is sensitive to the frequency. Hence measurement of the ranges at two frequencies reveals the ionospheric delay. The ionospheric range delay computed from TOPEX or Jason-1 data has an expected accuracy of 0.5 cm over 150-2000 km (Benada, 1997; AVISO; Koblinsky et al., 1999; and PODAAC, 2008). DORIS also provides the ionospheric corrections with an accuracy of 2 cm for one-frequency altimeters such as POSEIDON.

2.2.3.3 Tide corrections

The tide correction on altimetry measurements is composed of the ocean tide, the loading tide, the Earth tide and the pole tide corrections. In this section, every component of the tide correction will be described briefly.

Ocean tides are by far the largest geophysical corrections to altimetry data, as they account for up to 80% of the sea surface height variability of the world ocean (Koblinsky, 1999; Cherniawsky, 2001). The effects of ocean tides are removed from altimetry measurements by either using large-scale hydrodynamic models, or empirical models determined by satellite altimetry or tide gauge data, or assimilated models. Global tide models CSR3.0 and FES95.2 (Le Provost et al., 1995) are provided for T/P while GOT00.2 (Ray, 1999) and FES2004 (Le Provost, 2001) are provided for Jason-1. Although global tide models are accurate enough in the deep oceans, they show high disagreement in the coastal areas. The solution may come from developing the local tide models, which seem to perform better in certain regions (Shum et al., 1997) and analyzing the ocean tide by satellite altimetry data. The T/P and Jason-1 data are corrected for the ocean tides from a local tide model for the west and east coast of Canada. Specific methods are also used to analyze the residual ocean tides. Details are described in Chapter Four.

The load tide is the deformation of the lithosphere caused by the variation of the bottom pressure of the ocean due to the ocean tides. The sum of the ocean tide and the loading tide is the elastic ocean tide. Conveniently, the load tide can be expressed in terms of a sequence of load-Love numbers multiplied with the spherical harmonics of the ocean tide (Schrama, 1997). Unfortunately, we lack information about the loading tide associated with the local tide model used for Canada. So no load tide correction is applied to the altimetry data.

The solid Earth tide is the purely elastic responses of the solid-Earth itself to the astronomical tidal forces. It can be considered to be in equilibrium with the tide-generating forces. The

vertical displacement of the solid Earth tide depends on the adopted Love numbers (Koblinsky, 1999). Corrections of the solid Earth tide for T/P and Jason-1 data are from the results of Cartwright and Tayler (1971) and Cartwright and Edden (1973). This correction is believed accurate enough, not in excess of a couple of millimeters for the altimetric experiment (Schrama, 1997).

The pole tide is a tide-like motion of the ocean surface that is a response of both the solid Earth and oceans to the centrifugal potential that is generated by small perturbations to the Earth's rotation axis. The perturbations primarily occur at periods of 14 months and annual. The pole tide corrections for T/P and Jason-1 data are computed as described in Wahr (1985) using the knowledge of the Love numbers, and time series of perturbations to the Earth's rotation axis which is measured routinely with space techniques.

2.2.3.4 Effect of atmospheric loading

The sea surface elevation is inversely proportional to the atmosphere pressure loading on the sea surface. Such variations of sea surface are unrelated to sea surface topographic features associated with geostrophic currents and therefore must be removed (Chelton et al., 2001). The effect of atmospheric loading can be corrected by the inverse barometer (IB) correction. Generally, a 1 mbar increment in the atmospheric pressure depresses the sea surface by about 1 cm. An equation derived by Fu and Pihos (1994) is used to provide the IB correction for T/P and Jason-1:

$$IB = -9.948 \times (SLP - 1013.3), \tag{2.8}$$

where SLP is the sea level pressure (SLP), 1013.3 is the nominal value of mid latitude average atmospheric pressure and -9.948 is a scale factor which is based on the theoretical value of the static inverted barometer at mid-latitudes. The SLP is extracted from the sea level pressure product of ERA-40 Data Archive (http://www.ecmwf.int/products/data/archive/descriptions/e4/index.html).

2.2.3.5 Radial orbit error

As stated previously, this error is attributed to the inaccurate determination of the true satellite orbit. With the improvement of the gravity models and the global tracking system, especially the application of the POD technique, which stands for the Precise Orbit Determination, the accuracy of satellite orbits has been improved from meter-level to centimeter-level. POD is the procedure for determining the three-dimensional location of a satellite's centre-of-mass (called the orbit ephemeris) at regularly spaced time intervals in a specified reference frame with high accuracy (Chelton et al., 2001). The basic philosophy of POD is to fit the initial dynamic model of the satellite to the empirical tracking observations to correct the estimates of initial state of the satellite and the estimates of various parameters in the force or measurement model. An iterative least-squares estimation is the most general method to use. The dynamic model of the satellite is determined by analyzing the forces acting on the satellite, which are the gravitational and the non-gravitational forces like atmospheric drag and radiation pressure. The tracking data known as the observations of the satellite's motion are obtained from different tracking systems with different measurement characteristics, temporal coverage, geographic coverage and accuracy levels. The main present altimeter satellite tracking systems are SLR, DORIS, GPS, and Data Relay Satellite System (TDRSS). The POD of T/P achieves a significant improvement

with extremely high accuracy, and the radial orbit accuracy is in the range of 2-3 cm. The POD for Jason-1 obtains an accuracy of .5 cm for the radial element.

In Section 2.2.3, we have described the error sources of satellite altimetry and their derivations briefly. The altimetric error budgets for T/P and Jason-1 are summarized in Table 2.1.

Table 2.1 T/P and Jason-1 error budget (after Fu et al., 1994; T/P MGDR user handbook, 1997; Jason-1 GDR user handbook, 2008)

	TOPEX	POSEIDON	Jason-1
Altimeter noise (cm) 1Hz	1.7	2	1.6
Sea State Bias (% of SWH)	2.3	2.3	2.0
Ionosphere (cm)	0.5	1.7	0.5
Dry Troposphere (cm)	0.7	0.7	0.7
Wet Troposphere (cm)	1.1	1.1	1.2
Corrected Range (RSS, cm) 1Hz	3.2	3.7	3.0
Orbit (radial component) (cm)	3.0	3.0	2.5
Corrected Sea Surface Height (RSS, cm) 1Hz	4.7	5.1	4.2

2.2.4 Altimetry data pre-processing

The pre-processing of altimetry data is composed of reading the raw data from MGDR files, editing the raw data under special criteria to delete spurious measurements, and applying the required corrections.

2.2.4.1 Geophysical data records

The raw altimetric range measurements collected from the on-board satellite recording devices are received by the ground stations and then forwarded to special processing centers with the measuring time and the instrumental corrections in digital form. The processing centers apply more processing on the altimetric data, during which the precise orbit is computed, some instrumental errors are removed and other corrections are added. Then the altimetric data are

stored in digital form and provided to the users as the product of Geophysical Data Records (GDRs). The GDRs product is post processed, e.g., two months after receiving the raw measurements. There are also real or near real altimetry products named as Interim Geophysical Data Records (IGDRs) which are generated two days for T/P and 2-3 hours for Jason-1 after receiving the raw measurements. IGDRs do not include the precise orbit ephemerides for the orbit determination but an initial estimate of it. IGDRs products from different agencies have different contents and formats, which constitutes one of the main problems for the data user.

The T/P data used for the numerical investigations come from the Merged GDRs (MGDRs) products in version B released by PO.DAAC of JPL. One cycle MGDR data are organized in a cycle header file and a maximum of 254 pass-files. A pass-file which contains altimeter data from a satellite pass is composed of a header part, which provides organization and data product identifications, and the data part which is a record per second consisting of satellite measurements of sea level, all corrections applied to the data, the precise orbit of the satellite, as well as the altimeter measurements of wave height, wind speed, and ionospheric electron content, and the microwave radiometer observations of brightness temperatures. The header file is recorded in ASCII code, while the data part is written in a VAX binary integer format. PO.DAAC provides the programs for dumping the MGDR data in FORTRAN or C. T/P measurements are referring to an ellipsoid of revolution with equatorial radius of 6378.1363 km and a flattening coefficient of 1/298.257. The time system for T/P is UTC and the reference time is January 1, 1958 00:00:00.00, sometimes abbreviated UTC58. The unit for all distances and distance corrections is millimeters.

Jason-1 GDRs are also downloaded from PO.DAAC. Like T/P MGDRs, a pass-file of Jaosn-1 is composed of a header (73 records) and a data part with 3360 scientific data records maximum. The header is encoded in ASCII and contains the information about the generation of the product, sensors, processing information, data flow of the product, product confidence data and the reference of the auxiliary data used to generate the product. The data part is written in a Unix binary format and includes the information of the time tag, the location and surface type, the quality information and sensors status, the orbit, the altimetry range and range corrections, the Significant Wave Height (SWH) and SWH corrections, the backscatter coefficients and associating corrections, the off nadir angle, the brightness temperatures, the geophysical parameters, the environmental parameters and flags. Jason1 GDRs use the same reference ellipsoid and time system as T/P but one tenth of a millimeter as the unit for all distances and distance corrections.

2.2.4.2 Editing and correcting altimetry data

The correction and validation of T/P or Jason-1 data is a significant aspect of the pre-processing step. Any data record with inaccurate measurements, insufficient corrections and over land surface rather than ocean surface requires to be removed. Such a removal can be realized by editing procedures which follow some specific criteria. The editing criteria are satellite and agency dependent, and the user is advised to apply them in accordance to the specific needs of the study. The editing criteria for T/P and Jason1 are well documented in the literature (JPL, 1997; JPL and AVISO, 2008) and the common criteria for them are summarized into three principles.

The first principle is that any data that refer to continental regions, sea ice or ice caps is removed. GDRs have one or more flags that reflect the measurement location. Sometimes data bathymetry masks are used with depth values that are interpolated on the sub-satellite points and then those corresponding to shallow water and land areas are removed. In this study, all the calculations are done in coastal areas, so this bathymetry validation is not used because the water bathymetry in coastal areas is generally small.

Another principle is to remove all records not containing accurate range measurements or SSHs estimates. The 1s range measurements recorded in GDRs are averaged by the raw measurements taken in the higher rate (principally 10 times per second for TOPEX or Jason-1 and 20 times per second for POSEIDON). If the number of the raw measurements is not sufficient to provide a representative mean (the threshold value is 5 for TOPEX and 15 for POSEIDON by the JPL criteria), then the corresponding data record is removed. Additionally, when the RMS of the mean value is larger than a certain number, i.e., 100 mm for TOPEX and 175 mm for POSEIDON (Benada, 1997) then the data record is rejected.

The last principle is based on the characteristics of the retrieved signal through the significant wave heights (SWH) and the standard deviation of the backscatter coefficient. Measurements with big SWH values (11000 mm for T/P defined by the JPL criteria) are rejected as blunders. If the backscatter coefficient has big values, i.e., above 36dB, then it means that the measurement is over a non-oceanic surface, which can be either land or ice covered. In general, for the measurement not to be removed the standard devition values should range between 7-25dB (Benada, 1997).

After applying the JPL editing criteria, for example, the data pool for the west coast of Canada is composed of 305898 T/P records and 211413 Jason-1 records (Figure 2.3), while for the east coast of Canada 566468 T/P records and 398403 Jason-1 records (Figure 2.4) consist of the data pool. It indicates that even after rejecting some of the measurements, the number of remaining data is still very high. The corrections in the MGDR products of T/P and Jason-1 which were stated in Section 2.2.3 are applied to the edited data except for the ocean tide correction which will be discussed in Chapter Four and the inverse barometer correction which will be presented in Chapter Five. Corrections for the ionospheric delay for TOPEX and Jason-1 data, sea state bias and wet tropospheric delay for T/P data are modified to improve their accuracy or remove the bias. These modifications are discussed in the following sections.

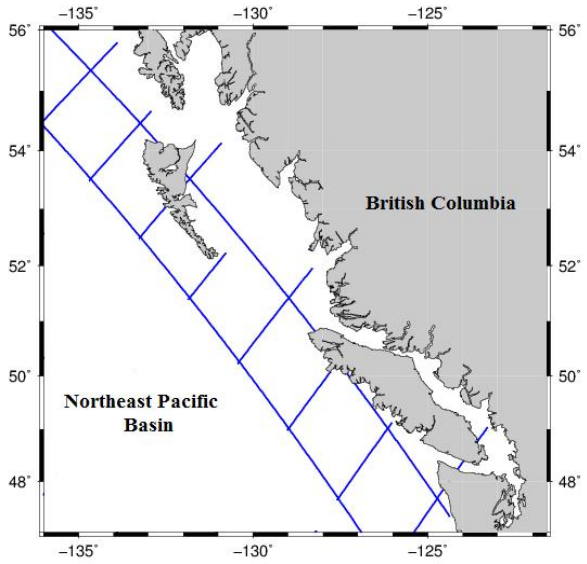

Figure 2.3: Ground tracks of satellite altimetry data in the west coast of Canada

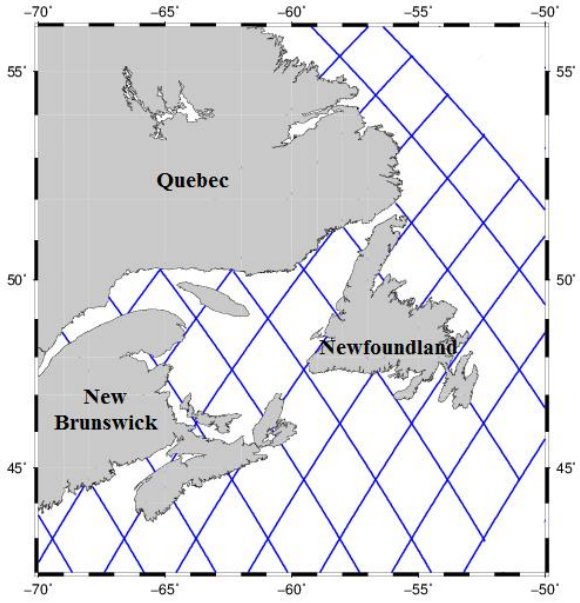

Figure 2.4: Ground tracks of satellite altimetry data in the west coast of Canada

2.2.4.2.1 Smoothness of the ionospheric correction for TOPEX and Jason-1 data

The ionospheric correction for TOPEX and Jason-1 data is from two frequency observations. The 1-s ionospheric correction should be negative, but sometimes it is positive up to 40 mm for accommodating instrument noise effects. In order to reduce the noise, Imel (1994) suggests averaging the ionospheric correction over 20s in order to increase its precision to 2 mm RMS without loss of accuracy even in the most rapidly varying regions of the ionosphere. In this study, following Imel's advice, the ionospheric correction for both TOPEX and Jason-1 data is averaged over 20s, but the correction for POSEIDON data is not because it has been smoothed as a result of the DORIS model used. Figure 2.5 shows an example of smoothed ionospheric correction for TOPEX data on pass 19 of cycle 18. From the blue line to the green line, we can see that, the editing process has removed large variations or spurious peaks of the raw ionospheric correction. Most of the edited ionospheric corrections in the middle and high

latitude areas vary between -50 and 0 mm along the track but a few locations have positive value. The red line indicates the smoothed ionospheric correction with smoother value less than 0. Figure 2.6 shows the example for Jason-1 data on pass 124 of cycle 1.

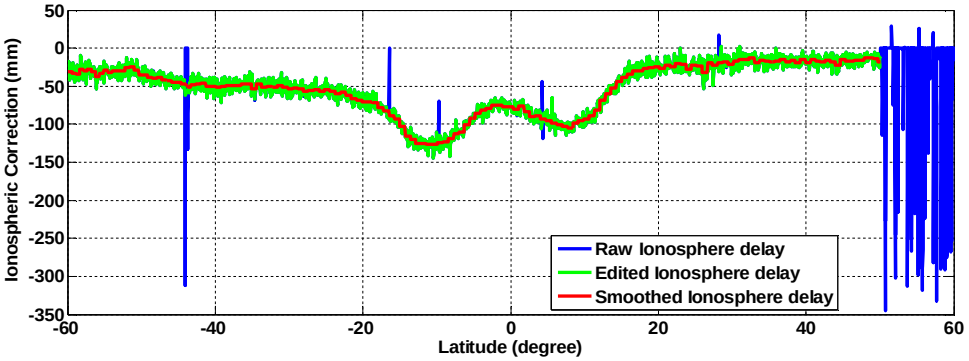

Figure 2.5: The ionospheric correction for TOPEX data on pass 19 of cycle 18.

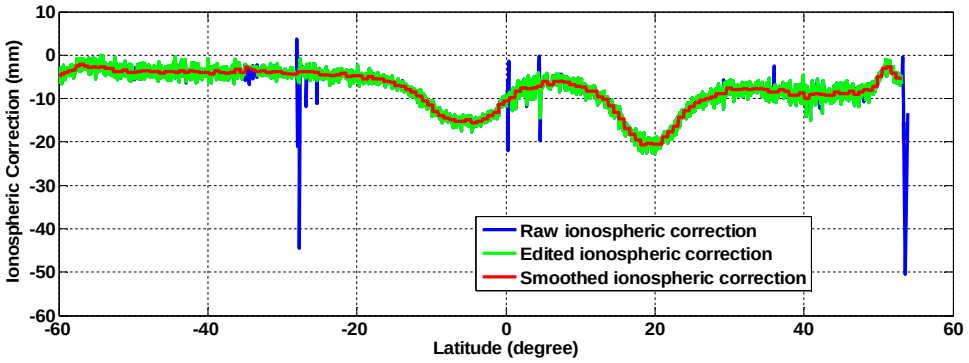

Figure 2.6: The ionospheric correction for Jason-1 data on pass 124 of cycle 1

2.2.4.2.2 Modification to the sea state bias of T/P

As stated in section 2.2.1, TOPEX altimetric measurements of cycles 1 to 235 were obtained by TOPEX_A altimeter while the data of cycles 236 to 481 were measured by TOPEX_B. Gasper et al. (1994) estimated the values of the coefficients a_0, a_1, a_2, and a_3 in Equation (2.7) by fitting TOPEX_A SSHs crossover measurements of cycles 1-110 to Equation (2.7) as a second-order power series in significant wave height (SWH) (in m) and wind speed U (in m/sec). Their

result is called BM4 model and the values of these four parameters are listed in the first column of Table 2.2. SSB corrections derived using the BM4 coefficients for T/P data of entire cycles are provided in the MGDR product as the standard correction.

Table 2.2. Estimated coefficients of BM4 (Gasper et al., 1994), CRS_A and CRS_B SSB models (Chambers et al., 2003). The coefficients for MGDR are total coefficients, while the coefficients for TOPEX_A and TOPEX_B are correcting coefficients relative to the original MGDR model.

Coefficients	BM4	CRS_A-BM4	CRS_B-BM4
a_0 (Δa_0)	**0.0203**	**0.00179**	**-0.00317**
a_1 (Δa_1)	**-0.00265**	**0.0000364**	**0.000251**
a_2 (Δa_2)	**0.00369**	**-0.000456**	**0.000153**
a_3 (Δa_3)	**-0.000149**	**0.0000178**	**-0.0000244**

Chambers et al. (2003) estimated new models for TOPEX_A and TOPEX_B by their full dataset, which are CSR_A and CSR_B, respectively. The differences of coefficients between BM4 and CSR_A or between BM4 and CSR_B are listed in the third and fourth column of Table 2.2. Figure 2.7 shows an example with both BM4 and CRS_A SSB corrections. The SSB correction is for the data on pass 19 of cycle 18. From the figure, we can see that the BM4 and CRS_A SSB corrections are in very good agreement. The small difference is due to the short TOPEX_A dataset used to estimate the BM4 model. Figure 2.8 shows the BM4 and CRS_B SSB corrections for the data on pass 19 of cycle 237. In the figure, the green line (BM4) is significantly different from the red line (CRS_B). It indicates that the BM4 model is not appropriate for TOPEX_B data because it is determined by only TOPEX_A data. In this study, SSB corrections for TOPEX_A and TOPEX_B data are recalculated by the CRS_A and CRS_B models, respectively.

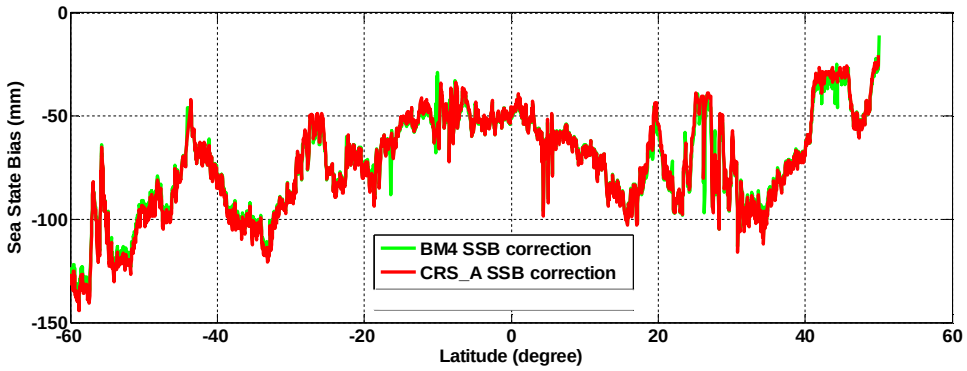

Figure 2.7: The SSB correction for TOPEX_A pass 19 of cycle 18. The green line shows the variation of the BM4 SSB corrections, and the red line indicates the SSB corrections from the CSR_A model.

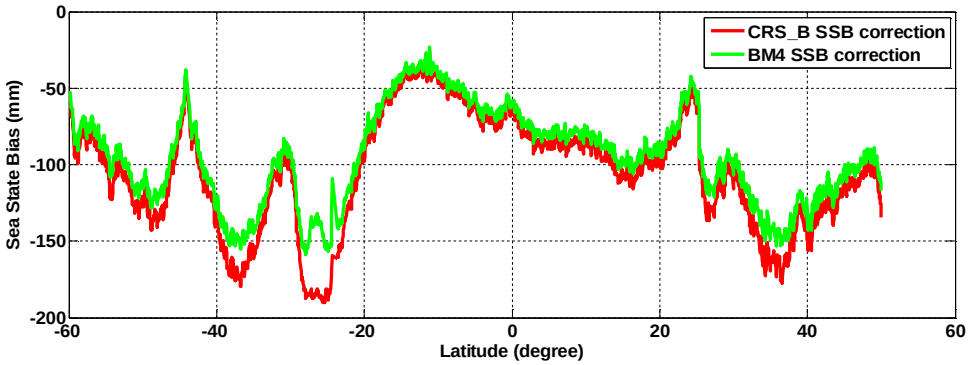

Figure 2.8: The SSB correction for TOPEX_B pass 19 of cycle 237. The green line shows the variation of the BM4 SSB corrections, and the red line indicates the SSB corrections from the CSR_A model.

2.2.4.2.3 Modification to the wet troposphere correction of T/P

A drift of the T/P wet troposphere correction which was generated by the drift in one channel of the TMR is corrected by the method of Leuliette et al. (2004):

$$h_{wetC} = h_{wetM} + \begin{cases} (1.2mm/yr)\cdot(t-1992.75) & t<1997.0 \\ 5.2mm & t>1997.0 \end{cases} \quad (2.9)$$

where t is the year, h_{wetM} is the wet troposphere correction from the T/P MGDRs, and h_{wetC} represents the wet troposphere correction corrected for the effect of the TMR drift. Figure 2.9

shows an example of the wet tropospheric correction for T/P data on pass 19 of cycle 18. The blue, green and red lines indicate the raw, the edited, and the edited and bias removed wet tropospheric corrections, respectively. After editing, some spurious corrections are removed. The difference between the green and red lines is very tiny because the bias is small. It is equivalent to applying an instrumental correction from September 1992 to January 1997 of -1.2 mm/yr followed by a constant -5.2 mm bias.

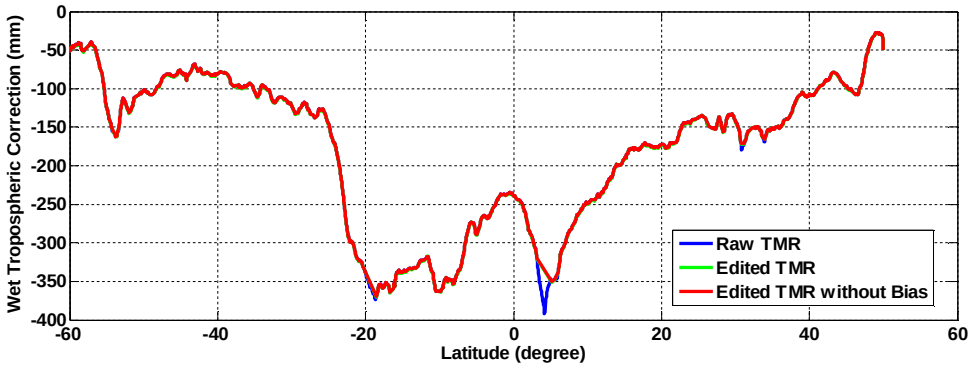

Figure 2.9: The wet tropospheric correction for T/P data on pass 19 of cycle 18. The blue line is the raw wet tropospheric correction, the green line is the edited correction, and the red line is the edited correction with the bias removed.

2.2.4.3 Stacking of T/P and Jason-1 data

To study sea level changes between two dates, it is necessary to have the sea surface observations from different cycles at the exact same coordinates, in another word to have the time series of sea surface measurements. In this study, the sea surface measurement is the SLA which is derived by removing the geophysical effects and MSS from SSHs. After differencing the SLAs from the time series, the unknown geoid automatically cancels out. However, the MGDR samples of T/P or Jason-1 are not given at the same locations on different cycles. They are measured approximately 6 km along the ground track, which is allowed to drift by ±1 km. So SLAs on different cycles require to be interpolated along a reference track. The reference

track is generally an actual pass with maximum data and/or minimum gaps. In this study, for the two study areas which are in the west and east coasts of Canada, the reference passes are from the T/P cycles 234 and 114, respectively. The detail description about the along track interpolation can be found in the T/P MGDR user handbook (Benada, 1997) and in Jason-1 GDRs user handbook (AVISO and JPL, 2008).

In addition to the along track SLA time series, crossover SLA time series is another type of observations being useful in altimetry data validation and calibration, and in studying sea level changes and ocean tides. One cycle of satellite altimetry is composed of the ascending and descending passes, e.g., one T/P cycle has 254 passes among which the odd ones are the ascending passes and the even ones are the descending passes. The ground tracks of the ascending and descending passes intersect with each other to generate the crossover point. On the crossover point, sea surface variations can be measured twice by the ascending and descending pass separately for one cycle, while on the along track one point has only one observation. So the crossover SLA time series samples the sea level more densely than the along track time series does. Because there are seldom direct observations on the crossover points, a crossover time series is generated by the interpolation; see details in Vergos (2002).

The time series from T/P is from 1993 to 2002 in this study. In order to extend the observation time series as long as possible, Jason-1 data are also stacked to the same reference pass as T/P. The time series from T/P and Jason-1 is from 1993 to 2008. During the period for the last 20 cycles of T/P (344 to 364) on the original orbit, Jason-1 was flying after T/P just several seconds. These 20 cycles of T/P data and the associating 20 cycles of Jason-1 data help us to

determine the bias between the T/P and Jason-1 time series. For the west coast of Canada, we compute the RMS of 20 cycle-by-cycle differences in SLA from Jason-1 and T/P (see Figure 2.10) to determine a mean relative bias of 120 mm with Jason-1. For the east coast of Canada, the RMS results are shown in Figure 2.11, and the relative bias with Jason-1 is 123 mm on average.

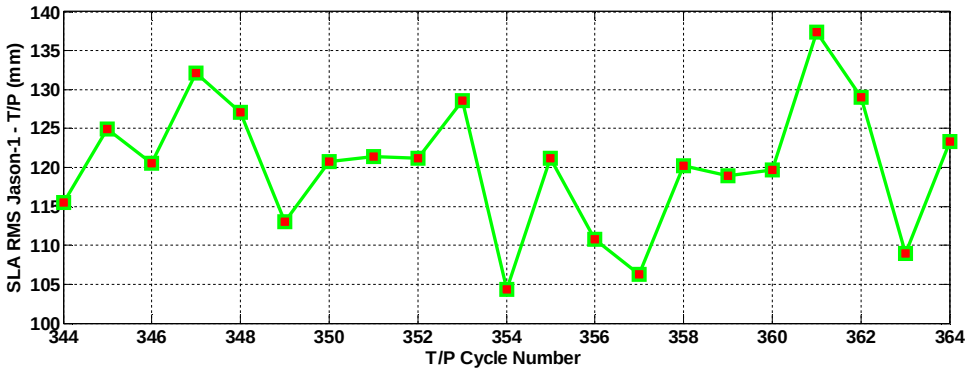

Figure 2.10: Ten-day RMS of differences in SLA from Jason-1 and T/P for the west coast of Canada.

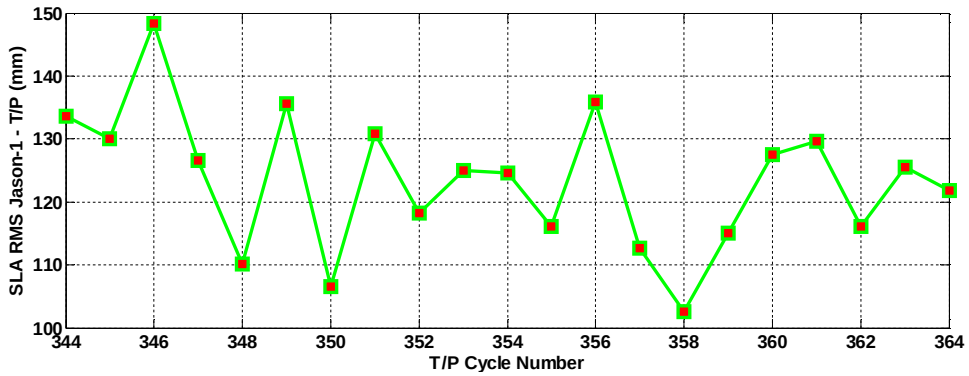

Figure 2.11: Ten-day RMS of differences in SLA from Jason-1 and T/P for the east coast of Canada.

For every along-track or crossover SLA time series from 1993 to 2008, the relative bias with Jason-1 is estimated by the data from T/P and Jason-1 on the overlapping cycles. Figure 2.12 shows an example of the along-track SLA time series. From the top figure, it is obvious that there exists a bias between the T/P and Jason-1 SLAs. The bias is estimated to be 130 mm.

After removing this bias from the Jason-1 SLAs, the bottom of Figure 2.12 shows a continuous and reliable SLA time series. Figure 2.13 shows an example of the crossover SLA time series. The estimated bias between T/P and Jason-1 SLAs is 115 mm on average.

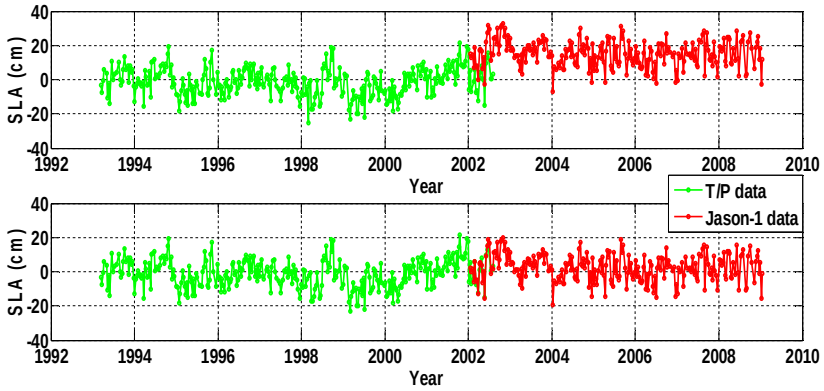

Figure 2.12: SLA time series at the location with latitude 45.0955° and longitude -132.8476°. The top of the figure shows the raw T/P and Jason-1 SLAs, while the bottom shows the time series after removing the bias from Jason-1 SLAs.

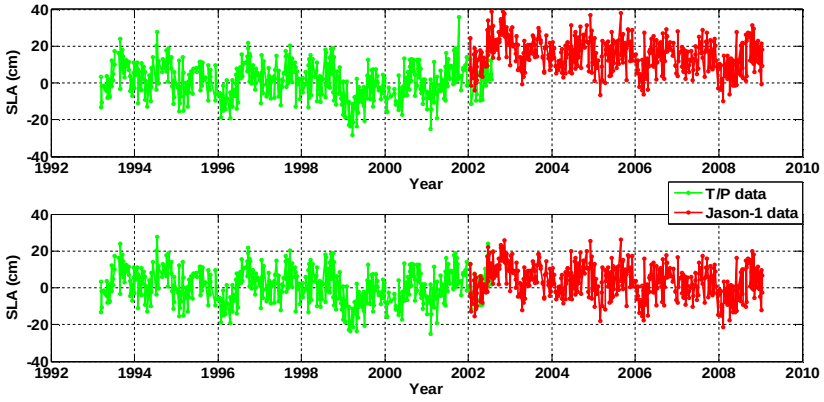

Figure 2.13: SLA time series at the crossover interacted by the pass 28 and pass 19. The top of the figure shows the raw T/P and Jason-1 SLAs, while the bottom shows the time series after removing the bias from Jason-1 SLAs.

In Section 2.2, we introduced the working principle of satellite altimetry, various error sources and the two altimetry missions T/P and Jason-1 which are used in this study. We focus on the pre-processing steps applied to altimetry data. After pre-processing, the raw range

measurements are converted to the along-track or crossover SLA time series which are the preliminary observations used in the sea level estimation.

2.3 Tide Gauge Measurements

2.3.1 Tide gauge definitions and principles

As shown in Figure 2.14, the most commonly used tide gauge system is a float operating in a stilling well, which is measuring the sea level relative to a nearby benchmark. A stilling well is a vertical enclosure with only limited access to the outside water; it can damp out most of the rapid vertical oscillation of the water surface to prevent the suspension cable of a float gauge slipping over, or even jumping off, the pulley wheel (Forrester, 1983). The float is flowing on the sea surface in the stilling well; the water level information is transmitted from the float to the recorder by a thin cable attached at one end to the float. Another type of gauges, which needs to be placed inside a stilling well, is the electrical tape gauges. The sea level is sensed by bouncing an electronic signal off the water surface to an associated sensor unit either above or below. Both of the mechanical float and electrical tape gauges measure the sea level directly. Another type of gauges measures the hydrostatic pressure and then converts the pressure to the corresponding depth; they are the pressure gauges. Use of pressure sensors instead of float gauges to measure water levels at temporary locations for the control of hydrographic surveys has become almost standard practice. This is because installation of the pressure gauge is much easier; a stilling well is not normally required with a pressure sensor (Forrester, 1983). Besides above types of gauges, there is another type of gauges namely staff gauges. A staff gauge is

simply graduated staff mounted vertically in the water with its zero below the lowest anticipated water level. A staff gauge is used as a check on the operation of the other types of tide gauges.

Sea level heights from tide gauges are identified of a local datum by using nearby benchmarks. Tide gauge data can also be converted from one datum to the other by tying the benchmarks into a geodetic network during a Geodetic Survey by leveling. The benchmarks should be solidly set in stable structures, bedrock, or firm ground within a radius of half a kilometer of the gauge (Forrester, 1983). For comparison purposes, tide gauge data which are referring to a local datum through benchmarks need to be converted to regional or global vertical datum, which is used by satellite altimetry data. Datum transformation is very significant in pre-processing steps.

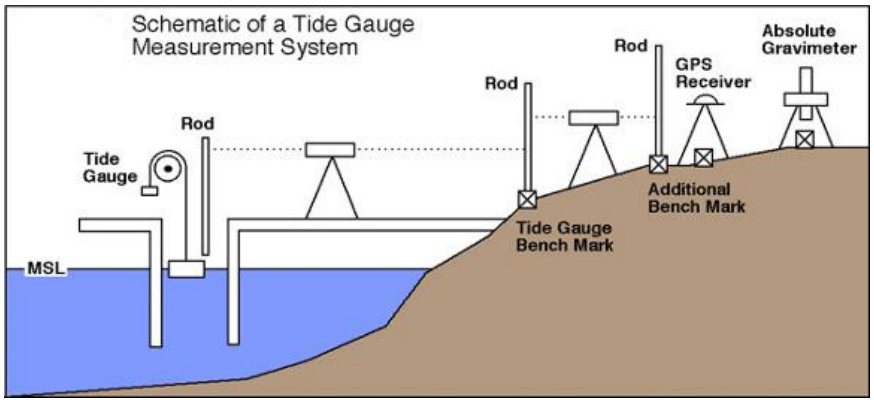

Figure 2.14: Principle of a tide gauge measurement system (CU SLRGroup website).

2.3.2 Tide gauge errors

2.3.2.1 Instrument and calibration errors

The error sources of the float gauges are categorized into three groups. (1) Sediment collecting in the bottom of the stilling well. The float would sit on sediment at or near low water and fail to

delineate the change in the low water tide. (2) Friction in the float mechanism. Excess friction in the float mechanism can cause an arbitrary flattening of the tidal curves at both high and low tides. (3) Clock errors. This problem arises either when the clock has been set incorrectly or because it drifts with time. These time errors could affect the tidal observations but have little influence on the monthly and annual sea level means that are used in long-term sea level trend studies. (4) Gauge setting errors. Gauge setting errors can also be named as the calibration errors. A float gauge is calibrated in a regular interval, e.g., monthly. The setting error could be little better than 6 cm. Assuming the setting error for a gauge of 7.6 cm and a setting interval of one month, then the contribution of this error to the standard deviation associated with an annual MSL could be expected to be in the order of 2.2 cm (Hannah, 2010). The calibration problem remains with the electronic and pressure gauges. The above errors can be greatly reduced by maintaining the gauges carefully and averaging the data.

2.3.2.2 Datum Errors

In addition, datum errors, generally arising from anthropological factors, are by far the most important effects to the estimation of a long-term sea level trend. Unlike the above errors, datum errors are subtle, tend to be systematic and, if not correctly resolved, will completely invalidate a sea level record. Datum errors arise (1) when tide gauge are shifted from their original positions and the new gauge zero differs from the previous zero; (2) when a tide pole is replaced and the new pole is set at a different level than the previous one; (3) when there is no consistent history of leveling from stable benchmarks to the tide pole; (4) when the setting of the gauge datum changes. More discussions about datum errors can be found in Hannah (2010).

2.3.2.3 Geophysical effects

Like satellite altimetry, tide gauge data are affected by some geophysical processes. Two significant factors are the vertical land motion and atmosphere loading. Because tide gauge data are referring to nearby benchmarks, which are not stable but vary as the land moving uplift. So tide gauge data are contaminated by vertical land motion. The vertical land motion is resulted from tectonic motion at plate boundaries and GIA. GIA models and continuous GPS measurements are two proposed methods for solving these effects and published results are reviewed in Chapter One. In this thesis, the vertical land motion is not removed from original tide gauge directly, but compensated by removing its trend from the estimated sea level trend.

Similar to satellite altimetry data, tide gauge data need the IB corrections for compensating the effects of atmospheric loading. The IB corrections are also calculated by Equation (2.8) with sea level pressure products from NCEP Reanalysis data provided by the NOAA/OAR/ESRL PSD, Boulder, Colorado, USA, from their Web site at http://www.esrl.noaa.gov/psd/.

2.3.3 Tide gauge data

The tide gauge stations which are operated by the Department of Fisheries and Oceans Canada provide the hourly or daily water heights used in this study. In our two study areas, 9 out of 225 and 9 out of 272 DFO tide gauge stations constitute the dataset used in this thesis; they are shown in Table 2.3. The selected tide gauge sites should have relative long dataset (minimum 20 years), minimum data gaps and be located along the coastline. In the west coast of Canada, the longest records are from Tofino (1948-2008) and Prince Rupert (1941-2008). The average series length is 46.0 years. The data gaps at every tide gauge site do not exceed 5% of the entire

measurements. In the east coast of Canada, the station Halifax has the longest record (1918-2008) among the 11 stations used in this thesis. The average series length in this area is 59.0 years. The data gaps at every tide gauge site vary between 2.3% to 10.4% of the entire measurements.

2.3.4 Pre-processing

DFO tide gauge data undergo two levels of quality control and are adjusted if there is a change in the reference datum at the station. In particular, corrections for tide gauge relocations, site stability, and instrumental problems are commonly applied. The hourly data is used for the residual ocean tides analysis, and the daily data is utilized to derive the monthly mean sea level. Both utilizations are not sensitive to the data gaps. So no specific processing is carried out to fill out the gaps for the hourly or daily data. The pre-processing on tide gauge data comprises removing the effect of local atmospheric loading and the datum transformation.

Similar to altimetry data, sea surface measurements from tide gauge include the direct response of coastal sea level to local atmospheric pressure forcing. In order to reduce the effects of atmospheric loading, the IB correction is applied to the tide gauge data. Daily sea level atmospheric pressure (SLP) series from NCEP Reanalysis data provided by the NOAA/OAR/ESRL PSD, Boulder, Colorado, USA, from their Web site at http://www.esrl.noaa.gov/psd/ are used to calculate the inverse barometer corrections for each tide gauge site. NCEP/NCAR data are continuous between January 1948 and now, thus the earliest data record of tide gauges used in this thesis is starting from January 1948, if available. The inverse barometer corrections are calculated using Equation (2.8).

Table 2.3 Tide gauge stations used in this study.

Station ID	Station Name	Record Length (year)	Latitude (N)	Longitude (W)	Data Gap
		West Coast of Canada			
7120	Victoria Harbour	47	48.424	123.371	0.6%
7277	Patricia Bay	34	48.654	123.452	1.1%
7795	Point Atkinson	49	49.337	123.253	2.3%
8408	Port Hardy	47	50.722	127.489	1.9%
8545	Bamfield	40	48.836	125.136	1.2%
8615	Tofino	60	49.154	125.913	4.2%
8735	Winter Harbour	22	50.513	128.029	1.0%
9354	Prince Rupert	67	54.317	130.324	2.4%
9850	Queen Charlotte City	46	53.252	132.072	3.0%
		East Coast of Canada			
65	Saint John	65	45.251	66.063	6.8%
365	Yarmouth	44	43.833	66.117	7.3%
490	Halifax	91	44.667	63.583	2.3%
612	North Sydney	40	46.217	60.250	2.8%
665	Port Aux Basques	51	47.567	59.133	10.4%
835	Argentia	38	47.300	53.983	8.3%
905	St Johns	53	47.567	52.717	4.1%
1700	Charlottetown	72	46.233	63.117	4.6%
2000	Lower Escuminac	37	47.083	64.883	7.2%

DFO tide gauge data h_{tg} are referring to the chart datum, which is the datum to which depths on a published chart, all tide height predictions, and most water level measurements are referred. On most Canadian coastal charts the surface of lower low water, large tide (derived by averaging all the lower low waters from 19 years of tide gauge data), has been adopted as chart datum (Forrester, 1983). Water level rarely goes below chart datum. DFO establishes a chart datum at each tide gauge, which is independent unless tide gauges are tied by leveling or GPS surveys. So we cannot compare the tide gauge data with the altimetry data which are referring to a vertical datum e.g. the MSS in this study directly. The tide gauge is referring it to a series of benchmarks in close proximity having heights known above the chart datum to maintain its

stability. If one of the benchmarks is known above a vertical datum e.g. the MSS or geoid, tide gauge data can be transformed from the chart datum to the vertical datum. H_{BM} denotes the height of the benchmark above the MSS ,which is also the vertical datum for satellite altimetry data, and CD expresses the height of the benchmark above the char datum, SLA from the tide gauge can be determined by

$$SLA = h_{tg} + H_{BM} - CD \tag{2.10}$$

(shown in Figure 2.15). The heights information of the reference benchmarks are provided by Dr. Véronneau.

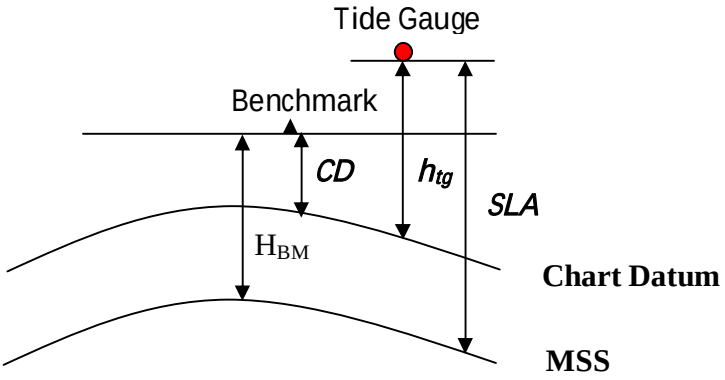

Figure 2.15: Principle of vertical datum transformation of tide gauge data

2.4 Definition of the of the coastal region

The term ‘coastal region’ used in this study indicates the oceanic area off the shoreline within a limited distance. There is no predetermined value for this distance for most coastal states. In this study, the extend of the coastal region is determined by the extension of the continental shelf, which is the underwater extension perimeter of the continent and associated coastal plain, whose boundary is the dividing line between the coastal region and the open ocean (Figure 2.16).

The width and depth of the continental shelf vary in different regions and generally the average width of the continental shelf is about 80 km and the limit for depth is 150 m. The continental margin of Canada's west coast is described by Macdonald and Pedersen (1990) and also can be found in Figure 2.17 which shows maps of the Atlas of Canada provided by Natural Resources Canada (http://atlas.nrcan.gc.ca/site/english/maps/environment/geology/geologicalprovi nces/1). The southern portion of the western shelf from the Strait of Juan de Fuca to Barkley Sound is about 75 km wide. The topography further north is more regular and the shelf narrows to a width of about 5 km at Brooks Peninsula. Queen Charlotte Sound and Hecate Strait form part of a large north-trending trough. It makes the west shoreline of Queen Charlotte Islands almost coinciding with the boundary of the continental shelf there. In the Atlantic coast of Canada, the width of the continental shelf from the east coast of Nova Scotia to that of Newfoundland and Labrador is increasing from roughly 150 km to 440 km. The whole Gulf of ST. Lawrence is also included in this study. The bathymetry of these continental regions is generally less than 500 m.

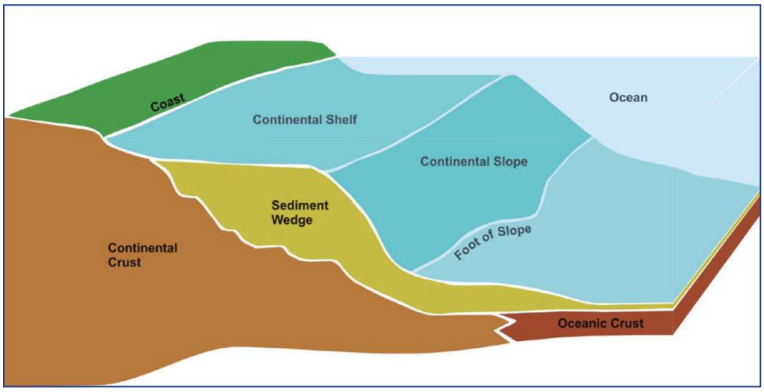

Figure 2.16**:** Example of an Atlantic-style continental margin including the continental shelf, slop and rise (NRCan, http://www.nrcan.gc.ca/earth-sciences/about/organization/organization-structure/geological-survey-of-canada/8335).

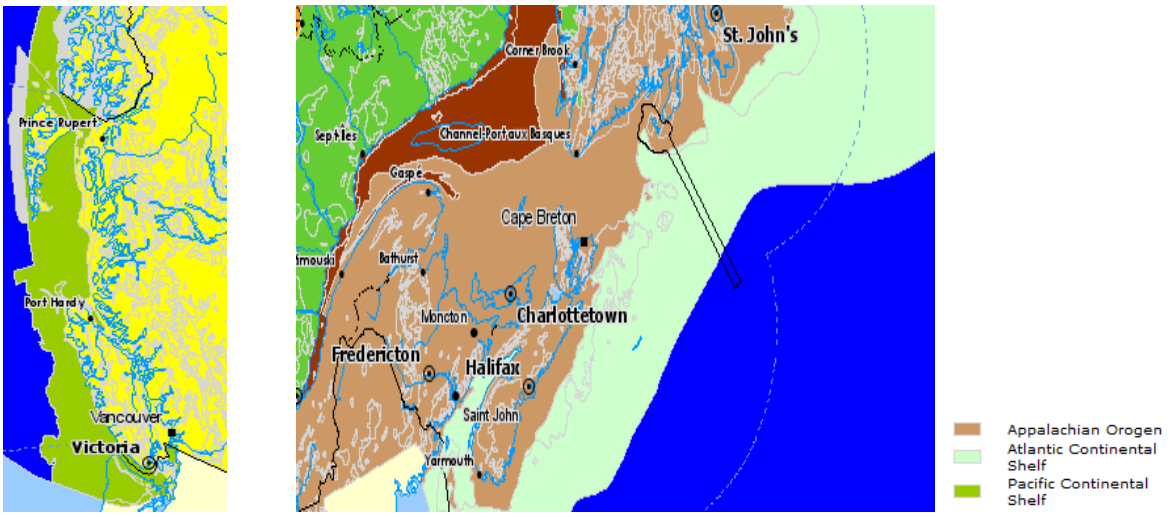

Figure 2.17: Continental shelf of Canada. The left figure is for the west coast and the right figure is for the east coast.

2.5 Summary

In this chapter, definitions and principles, data missions, error sources of satellite altimetry and tide gauge data are presented. The dry tropospheric, solid earth tide, pole tide, IB corrections and the radial orbit heights, which were applied to T/P and Jason-1 data, are standard errors provided in the data products. We applied modifications to the standard corrections of the ionospheric, wet tropospheric and sea state bias errors, provided in the data products, and then applied the modified corrections to altimetry data. We used a local tide model namely Webtide, which is different from the global models provided in the data products, to correct for the ocean tides in the pre-processing steps. Then we utilized special analysis methods to remove the residual ocean tides, which will be discussed in Chapter Four. Continuous SLA time series from T/P and Jason-1 were constructed at along-track or crossover points by removing biases between two missions.

For tide gauge data, the instrument, calibration and datum errors are controlled and removed by the provider Fisheries and Oceans Canada. We calculated the IB corrections by Equation (2.8) using sea level pressure products from NCEP Reanalysis data and applied them to the hourly and daily data. Vertical land motion which contaminates in tide gauge data is not accounted for in the pre-processing steps. This effect will be removed directly from the estimate of a sea level trend, which will be discussed in Chapter Six. The tide gauge data were converted from the chart datum to the mean sea level through the vertical heights of associating benchmarks in two datum systems. The hourly sea level time series from tide gauge are used to analyze the ocean tides, which are the comparing values to the results of residual ocean tides from satellite altimetry data in Chapter Four. The daily sea level time series will be averaged to the monthly mean sea level time series, which will be used in the trend estimation.

Chapter Three: Method for estimating the rate of sea level change

3.1 Introduction

In this chapter, the linear regression model and calculating strategies for estimating the linear trend of sea level change at every altimetry or tide gauge site are projected. The 10-day altimetry SLA and daily tide gauge SLA derived from the pre-processing steps are averaged to the monthly mean sea level (MMSL) which is the observation of the regression model. Additional processing, which is applied on MMSL to remove the annual, semiannual and regional common signals, is introduced. Then the definitions of the power-law noises are reviewed. One specific section introduces the power spectral density and maximum likelihood analysis that are used to detect the noise model. The final section summarizes the standard estimation strategies.

3.2 Linear regression model

The sea level observations are generally analyzed using a linear regression model to derive the rate of sea level change. The linear regression model is expressed as:

$$S(t_i) = a + bt_i + \varepsilon_i , \tag{3.1}$$

where $S(t_i)$ is the sea level measurement from altimetry or tide gauge at time t_i, a is the offset, b is the linear trend of sea level change, and ε_i is the error of the i^{th} observation. This model is linear with respect to the coefficients

$$\boldsymbol{x} = [a \quad b]^T , \tag{3.2}$$

so Equation (3.1) becomes to

$$\boldsymbol{s} = \boldsymbol{A}\boldsymbol{x} + \boldsymbol{\varepsilon}\,, \tag{3.3}$$

where $\boldsymbol{A}$ is the design matrix. If the covariance matrix $\boldsymbol{C}_S$ of measurements $\boldsymbol{s}$ is given, then the least-squares estimate of the unknown parameters is obtained from

$$\hat{\boldsymbol{x}} = (\boldsymbol{A}^T\boldsymbol{C}_S^{-1}\boldsymbol{A})^{-1}\boldsymbol{A}^T\boldsymbol{C}_S^{-1}\boldsymbol{s}\,, \tag{3.4}$$

with the parameter covariance matrix

$$\hat{\boldsymbol{C}}_{\hat{x}} = (\boldsymbol{A}^T\boldsymbol{C}_S^{-1}\boldsymbol{A})^{-1}\,. \tag{3.5}$$

From Equation (3.3), the post-fit residuals are

$$\hat{\boldsymbol{\varepsilon}} = \boldsymbol{s} - \boldsymbol{A}\hat{\boldsymbol{x}}\,. \tag{3.6}$$

The a-posteriori variance factor $\hat{\sigma}_0^2$ corresponding to the a-priori variance factor σ_0^2 is

$$\hat{\sigma}_0^2 = \frac{\hat{\boldsymbol{\varepsilon}}^T\boldsymbol{C}_S^{-1}\hat{\boldsymbol{\varepsilon}}}{\sigma_0^2(N-m)}\,. \tag{3.7}$$

where N is the number of observations and m is the number of model parameters.

Solving the linear regression model (3.3) requires two conditions. Firstly, we need very "clean" sea level observations. Equation (3.1) is a simple function relating our sea level observations to two model parameters; there are no other periodic signals estimated. So in order to estimate the rate of sea level change as accurate as possible, we need to ensure that the sea level observations are only composed of the trend and the noise. We know however that the SLA time series from satellite altimetry and tide gauges are affected by a variety of physical processes over timescales ranging from a few minutes to decades. Besides the trend and the noise, there are other signals with different periods in the SLA time series. This requires accurate corrections and an

appropriate processing strategy to remove or decrease these signals. We will discuss these corrections and the derivation methods in section 3.3.

Secondly, in order to resolve this regression model under the least-square criterion, we need to know the covariance matrix of $\boldsymbol{\varepsilon}$, which is known as the stochastic model. In practical computations, $\boldsymbol{\varepsilon}$ is always assumed to be white noise but real sea level time series may be temporally or spatially correlated and have a pronounced "colored" frequency dependence, with the highest power in the long periods (Nikolaidis, 2002; Mazzotti et al., 2008; Santamaría-Gómez et al., 2011). It is important to select an appropriate stochastic model for altimetry and tide gauge data separately. Different noise models and methods for testing the models will be introduced in section 3.4.

3.3 Data cleaning processing

3.3.1 Corrections for raw monthly mean sea level

The sea level observation used to estimate the rate of sea level change is the monthly mean sea level (MMSL). 10-day altimetry SLA time series and daily tide gauge data are averaged to monthly mean. For tide gauge data, the use of MMSL effectively filters out signals with periods shorter than about one week, such as the main diurnal and semi-diurnal tidal constituents. However, this is not the case for satellite altimetry data. The tidal constituents with semi-diurnal, diurnal or shorter periods would be aliased to the signals with longer periods due to the 10-day sampling period of T/P and Jason1. These tidal constituents with large amplitudes cannot be removed by monthly averaging. Ocean tides should be treated carefully and corrected by an

accurate ocean tide model or by applying an appropriate method for analyzing satellite altimetry data. Ocean tide corrections for satellite altimetry will be discussed in Chapter Four.

In the MMSL time series, longer-period signals (including fortnightly, monthly and semiannual variations) remain evident, with the annual cycle signal accounting for most of the signal variance. Interannual to decadal-scale processes such as the El Niño-southern Oscillation (ENSO) and the Pacific Decadal Oscillation (PDO) are also evident in some series. Long-period signals can significantly bias the linear trend estimate, especially if the time series is not substantially longer than the dominant low-frequency oscillations or if it ends midway through a major decadal-scale event (Mazzotti et al., 2008). The two corrections applied to the MMSL time series for compensating the effects of longer-period signals are introduced in the following two sections.

3.3.1.1 Annual seasonal correction

Annual and semi-annual variations maybe two strong signals showing two peaks in the sea level spectra, which may even overpower the rest of the spectrum by a factor of 100 (Mazzotti et al., 2008) (Shown in Figure 3.1f). The generation of these signals is due to a combination of several effects, including seasonal variations in air and water temperature, predominant wind direction, and fresh water influx resulting in local density variations (Larsen et al., 2003). Although such short-period signals are unlikely to affect the estimation of long-term rates, they impact significantly the uncertainties of the rates. Instead of detailed analysis involving wind, temperature, precipitation and runoff data, annual seasonal signals can be removed by applying an empirical correction. In this thesis, the annual seasonal correction is calculated by the method

used by Mazzotti et al. (2008). For a given MMSL time series $s(t)$, which has already been corrected for IB, average monthly water level anomalies are calculated by stacking 1-year data slices over the whole time series:

$$AVEma_i = \frac{\sum_{j=1}^{N} s_{ij}}{N}, \tag{3.8}$$

where $AVEma_i$ denotes average monthly water level anomalies, the suffix i indicates i^{th} month from 1 to 12, and the suffix j indicates the j^{th} year. These average monthly anomalies are subtracted from each matching month throughout the record, thus getting the annual seasonal corrected sea level SC_{ij}:

$$SC_{ij} = s_{ij} - AVEma_i, \tag{3.9}$$

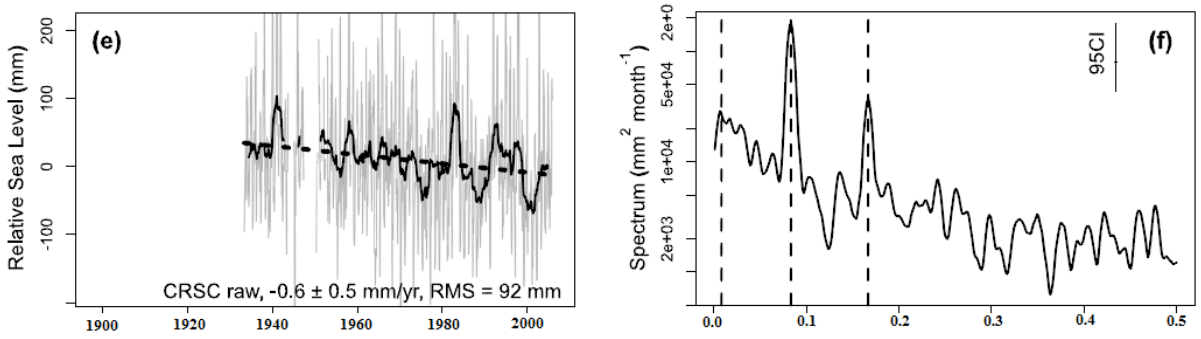

Figure 3.1: Monthly mean sea level data for Crescent City (California). (e) MMSL time series. Thin gray lines show raw (Figure 3.1e) MMSL data for Crescent City tide gauge. Thick solid lines show 2-year moving averages. Thick dashed lines show linear RSL trends. (f) Power spectra of raw detrended MMSL data (Figure from Mazzotti et al., 2008).

3.3.1.2 Regional common mode noise correction

The regional common mode noise correction is used to remove sea level variations which are caused by large-scale oceanographic variations and are spatially coherent on a local basin scale. The calculating method used in this thesis is similar to the methods of Larsen et al. (2003) and Mazzotti et al. (2008). Sea level time series at different locations in the study area are required to be divided into several groups. In each group, the correlation coefficient between any two time series should be greater than 0.6 indicating that they are highly correlated. In one specific group, suppose these is a set of time series $s_1(t)\cdots s_n(t)$. Sea level data are first corrected for IB, annual seasonal variations and detrended. We get residual time series $sr_1(t)\cdots sr_n(t)$. Then the regional common mode noise is calculated as:

$$RCMN_{ij} = \frac{\sum_{s=1}^{n} sr_{sij}}{n}. \tag{3.10}$$

Then corrected sea level H_{ij} can be derived as

$$H_{ij} = SC_{ij} - RCMN_{ij}. \tag{3.11}$$

3.3.2 Outlier detection

MMSL time series corrected by the above three corrections are also cleaned using a robust outlier detection algorithm applied to the postfit residuals $\hat{\varepsilon}$. The outlier detection algorithm used in this thesis is the same as Nikolaidis (2002). The algorithm is based on the median and interquartile range (IQR) statistics to describe the central value and spread of the data. The IQR of a data sample is the difference between its 75^{th} and 25^{th} percentiles. The detection algorithm is

$$\left|\hat{\varepsilon}_i - median(\hat{\varepsilon})\right| > (3 \times IQR(\hat{\varepsilon})). \quad (3.12)$$

3.4 Stochastic model

3.4.1 Power-law noises

For many types of geophysical signals, their noises may be described as a power-law process. The one-dimensional time or space-domain behavior of this power-law process is such that its power spectrum has the form

$$P(f) = P_0(\frac{f}{f_0})^{\kappa}, \quad (3.13)$$

where f is the spatial or temporal frequency, P_0 and f_0 are normalizing constants, and κ is the spectral index lying within the range -3 to 1 and is the slop of the spectra in log-log space (Williams, 2006). A subdivided process with $-3 < \kappa < -1$ is "fractional Brownian motion". This process indicates that the process is strongly correlated (also called autoregressive) and has higher energy at low frequencies (Mazzotti et al., 2008). Another subdivided process with $-1 < \kappa < 1$ is "fractional white noise". There are three kinds of commonly used noises depending on the value of κ. At $\kappa = 0$, we get $P(f) = P_0$, which is the white noise (WH). At $\kappa = -1$, we have $P(f) = P_0(\frac{f}{f_0})^{-1}$, which is the flicker noise (Pink noise) and, at $\kappa = -2$, we get $P(f) = P_0(\frac{f}{f_0})^{-2}$, which is the random walk noise (also called Brownian or Red noise). The latter two are also called colored noises. In order to describe the frequency-dependent noise and standard error of rate in the MMSL time series, an assumption is made that their power spectrum can be described by one of the special cases describing the noise amplitudes as a

function of the spectrum parameters. Noise models tested here were formed by combining white and colored noise components. The testing noise models are chosen as: white (WH), white and flicker (WF), white and random walk (WR) noise.

3.4.2 Power-law noise covariance matrix

In order to introduce the uncorrelated or colored noises or their combination to the least-squares regression problem, it is necessary to determine the covariance matrix of the noise. For the combined noise model, ε for a specific time t_i can be written as:

$$\boldsymbol{\varepsilon}(t_i) = c\alpha(t_i) + d_{-1}\beta(t_i) + d_{-2}\gamma(t_i), \tag{3.14}$$

where $\alpha(t_i)$ is the white noise, $\beta(t_i)$ is the flicker noise, $\gamma(t_i)$ is the random walk noise, c is the amplitude of white noise and d_κ is the amplitude of the colored noise of spectral index κ (-1 or -2). Based on Equation (3.14), we can derive the covariance matrix of the measurements S as:

$$\boldsymbol{C_S} = c^2\boldsymbol{I} + \sum_{\kappa=-2}^{-1} d_\kappa^2 \boldsymbol{J_\kappa}, \tag{3.15}$$

where $\boldsymbol{I}$ is the identity matrix and $\boldsymbol{J_\kappa}$ is the covariance matrix for the colored noise. The derivation of $\boldsymbol{J_\kappa}$ for the power-law noise with any spectral index $-3 < \kappa < 1$ can be found in Zhang et al., 1997; Mao et al., 1999; and Williams (2006). In the following section, we will cite their derivations to introduce the covariance matrix $\boldsymbol{C_\varepsilon}$ for different noise models and we will also introduce the formulas for estimating the standard errors for the rate of sea level change a.

3.4.2.1 Covariance matrix of the white noise

Williams (2003) provides a formula for the covariance matrix, which is based on using a transformation matrix. A transformation matrix $\boldsymbol{T}$ is used to express a sequence of random variables $\boldsymbol{x}$ by a vector $\boldsymbol{g}$ of identically distributed unit-variance random variables as $\boldsymbol{x} = \boldsymbol{T}\boldsymbol{g}$. By propagation of errors, the covariance matrix of power-law noise $\boldsymbol{J}_{\kappa}$ can be expressed by the transformation matrix $\boldsymbol{T}$ by

$$\boldsymbol{J}_{\kappa} = \boldsymbol{T}\boldsymbol{T}^{\boldsymbol{T}}, \tag{3.16}$$

The transformation matrix is derived using the method of fractional differencing/integrating (Hosking, 1981) with the form:

$$\boldsymbol{T} = \Delta T^{-\kappa/4} \begin{bmatrix} \psi_0 & 0 & 0 & \cdots & 0 \\ \psi_1 & \psi_0 & 0 & \cdots & 0 \\ \psi_2 & \psi_1 & \psi_0 & \cdots & 0 \\ \vdots & \vdots & \vdots & \ddots & \vdots \\ \psi_n & \psi_{n-1} & \psi_{n-2} & \cdots & \psi_0 \end{bmatrix}, \tag{3.17}$$

where

$$\psi_n = \frac{-\frac{\kappa}{2}\left(1-\frac{\kappa}{2}\right)\cdots\left(n-1-\frac{\kappa}{2}\right)}{n!} = \frac{\Gamma\left(n-\frac{\kappa}{2}\right)}{N!\Gamma\left(-\frac{\kappa}{2}\right)} \tag{3.18}$$

and ΔT is the sampling interval.

Equation (3.17) and Equation (3.18), for white noise with $\kappa = 0$, $\psi_0 = 1$, $\psi_n = 0$ $(n > 0)$ yield $\boldsymbol{T} = \boldsymbol{I}$ and $\boldsymbol{J_0} = \boldsymbol{I}$. Since $\Delta T_j^{-\kappa/4} = 1$, it is obvious that the white noise is independent of time.

3.4.2.2 Covariance matrix of the random walk noise

For the random walk noise with $\kappa = -2$, $\psi_n = 1$ for any n. Based on Equation (3.17) and (3.18) the transformation matrix is:

$$T = \Delta T^{-\kappa/4} \begin{bmatrix} 1 & 0 & 0 & \cdots & 0 \\ 1 & 1 & 0 & \cdots & 0 \\ 1 & 1 & 1 & \cdots & 0 \\ \vdots & \vdots & \vdots & \ddots & \vdots \\ 1 & 1 & 1 & \cdots & 1 \end{bmatrix}. \tag{3.19}$$

If the data are not equally spaced, then the covariance matrix is equal to

$$J_{-2} = \begin{bmatrix} \Delta T_1 & \Delta T_1 & \Delta T_1 & \cdots & \Delta T_1 \\ \Delta T_1 & \Delta T_2 & \Delta T_2 & \cdots & \Delta T_2 \\ \Delta T_1 & \Delta T_2 & \Delta T_3 & \cdots & \Delta T_3 \\ \vdots & \vdots & \vdots & \ddots & \vdots \\ \Delta T_1 & \Delta T_2 & \Delta T_3 & \cdots & \Delta T_n \end{bmatrix} \tag{3.20}$$

where $\Delta T_i = \left| t_j - t_0 \right|$. This means if the data are not equally spaced, then each column of the transformation matrix T is scaled by the individual ΔT_i. This formula can also been found in Zhang et al. (1997) or Mao et al. (1999).

3.4.2.3 Covariance matrix of the flicker noise

For the flicker noise with $\kappa = -1$, the covariance matrix is approximated by Zhang et al. (1997). The approximate formula for the elements r_{ij} of J_{-1} is:

$$r_{ij} = \begin{cases} \left(\frac{3}{4}\right)^2 \times \left(2 - \frac{\log\left|t_i - t_j\right| / \log 2 + 2}{12}\right) & t_i \neq t_j \\ \left(\frac{3}{4}\right)^2 \times 2 & t_i = t_j \end{cases} \tag{3.21}$$

The constants in Equation (3.14) are chosen such that the flicker noise and random walk noise, with equal variance and a sampling interval of one day, have equivalent power levels over a period of one year (Mao et al., 1999). The covariance matrix computed by Equation (3.21) is similar to that computed by Equation (3.17) except for a major difference in the scaling of the amplitude of d_{-1}. Williams 2003 verified that when the sampling frequency is once per day (in Hz) then d_{-1} of Williams (2003) is equal to 1.774 times d_{-1} of Zhang et al. (1997).

3.4.3 Noise modelling

Several methods are used to figure out the characteristics of the noise. The methods used are described in detail in the following sections.

3.4.3.1 Power spectral density

The power spectral density of the postfit residuals $\hat{\varepsilon}$ calculated by Equation (3.6) is estimated per measuring site using the periodogram. The periodogram estimator is of the form:

$$P_\varepsilon(f) = \frac{1}{N}\left|\sum_{j=0}^{N-1} \varepsilon_i \exp(-2\pi i j f)\right|^2 \tag{3.22}$$

where N is the number of MMSL records and ε_i denotes the i^{th} element of the post-fit residuals, $\hat{\boldsymbol{\varepsilon}}$. For the individual measuring site spectra, Welch's method is used to reduce the variance of the individual power spectra and protect against bias. Welch's method splits the data into overlapping segments, computes modified periodograms of the overlapping segments, and averages the resulting periodograms to produce the power spectral density estimate. The data $\hat{\boldsymbol{\varepsilon}}$ is segmented into eight sections of equal length, each with 50% overlap. Each segment is

windowed with a Hamming window that is the same length as the segment. The spectra for each window then are averaged to estimate the periodograms. The noise power is plotted in dB as

$$P(f) = 10\log_{10}\left(\frac{2P_{\varepsilon}(f)}{f_s}\right) \tag{3.23}$$

where f_s is the sampling frequency. The spectral index κ of Equation (3.13) is estimated as the slope of the spectra in log-log space (Nikolaidis, 2002) as

$$\kappa = \frac{P(f)}{10\log_{10} f}. \tag{3.24}$$

3.4.3.2 Maximum likelihood analysis

The estimation of the white and colored noise components can be realized by a maximum likelihood (MLE) estimator. The maximum likelihood estimator maximizes the probability function by adjusting the data covariance. The probability function is

$$lik(\hat{\boldsymbol{\varepsilon}}, \boldsymbol{C}_{\varepsilon}) = \frac{1}{(2\pi)^{N/2}(\det \boldsymbol{C}_{\varepsilon})^{1/2}} \exp\left(-0.5\hat{\boldsymbol{\varepsilon}}^{T}\boldsymbol{C}_{\varepsilon}^{-1}\hat{\boldsymbol{\varepsilon}}\right), \tag{3.25}$$

or

$$\ln\left[lik(\hat{\boldsymbol{\varepsilon}}, \boldsymbol{C}_{\varepsilon})\right] = -0.5\left[\ln(\det \boldsymbol{C}_{\varepsilon}) + \hat{\boldsymbol{\varepsilon}}^{T}\boldsymbol{C}_{\varepsilon}^{-1}\hat{\boldsymbol{\varepsilon}} + N\ln(2\pi)\right], \tag{3.26}$$

where ln is the natural logarithm and det is the matrix determinant. This analysis is applied on the residuals $\hat{\boldsymbol{\varepsilon}}$ calculated by Equation (3.6). $\boldsymbol{C}_{\varepsilon}$ is expressed by Equation (3.15) and is composed of both white and power-law noise with amplitudes c and d_{κ} ($\kappa = -1$ or $\kappa = -2$), respectively. The covariance of white or colored noise can be determined by Equation (3.17), (3.20) or (3.21). c and d_{κ} are the parameters estimated by MLE.

The problem of finding the maximum or minimum value can be solved by an optimization algorithm. There are many types of optimization algorithms, e.g., the gradient descent, Newton's method, Levenberg-Marquardt, etc. In this thesis, the Downhill Simplex method (Nelder and Mead, 1997) is used to solve the MLE problem. This method requires only function evaluations, not derivatives. The downhill simplex method relies on the use of simplices, i.e., in two dimensions, a simplex is a triangle with 3 vertices; in three dimensions, a simplex is a pyramid. In our MLE problem, for the white and color noise combination model, two parameters c and d_κ ($\kappa = -1$ or $\kappa = -2$) need to be estimated by MLE. So the triangle simplex in two-dimensional space is characterized by three distinct vectors (two elements for one vector) that are its vertices. The downhill simplex is a successive searching progress. It starts from an initial simplex. At each step of the search, a new point in or near the current simplex is generated. The function value at the new point is compared with the function's values at the vertices of the simplex and, usually, one of the vertices is replaced by the new point, giving a new simplex. This step is repeated until the diameter of the simplex is less than the specified tolerance. These updates of vertices are carried out using four operations: reflection, expansion, contraction, and multiple contractions. Let x denote the parameter vector (c, d_κ) and write f_i for the value of Equation (3.25) for at x_i. Let $\{x_0, \ldots, x_n\}$ be the current simplex ($x_i \in R^n$ for all $i \in [0, n]$ where $n = 2$ in our case). Let us define h as the suffix such that $f_h = \max_i(f_i)$ and l as the suffix such that $f_l = \min_i(f_i)$. The complete method is given in a flow diagram in Figure 3.2.

In order to test whether either or both of the colored noise models, WF and WR, fit the data better than the WN model, the maximum log-likelihood-ratio test statistic (Zhang et al., 1997) is used. The ratio is calculated by

$$\Lambda = \frac{\max likelihood1}{\max likelihood2} = \exp\left[\left(\max - \log - likelihood - WF/WR\right) - \left(\max - \log - likelihood - WN\right)\right], \quad (3.27)$$

where the max-log-*likelihood*-*WF/WR* is the maximum value of the log-likelihood function (3.26) for WF or WR model and the max-log-*likelihood*-WN is the maximum value of Equation (3.26) for WN model. Zhang et al. (1997) simulated 100 GPS time series to test whether the null hypothesis that white noise model best fits the time series can be rejected in favor of the alternative hypothesis that the colored noise model better fits the data. They concluded that if the value of Λ is equal to 1.0, it implies that WN model is better than the color noise model and if the value of Λ is equal to 0.0, WF or WR model describes the MMSL data better than WN model.

3.4.4 Rate error estimates for equally spaced data

During the calculation of sea level rates and their uncertainties, first we need to estimate the type and amplitude of the noise present in the time series, and then the rates and their uncertainties at different measuring sites are estimated using linear regression Equation (3.1) with the appropriate covariance matrix derived from the first step. Sections 3.4.1 to 3.4.3 are about the estimation of the noise. Besides linear regression, the rate uncertainties can also be approximately estimated by some formulas. In this section, these formulas for estimating the uncertainties of the estimated sea level rates are discussed. These formulas are adopted from Zhang et al. (1997); Williams (2003) and Mazzotti et al. (2008). They are derived under two assumptions: first, the estimated rates are not significantly affected by the assumed

measurement model, and second, the rate uncertainties are not overly sensitive to uneven spacing or small gaps in the time series (Williams 2003).

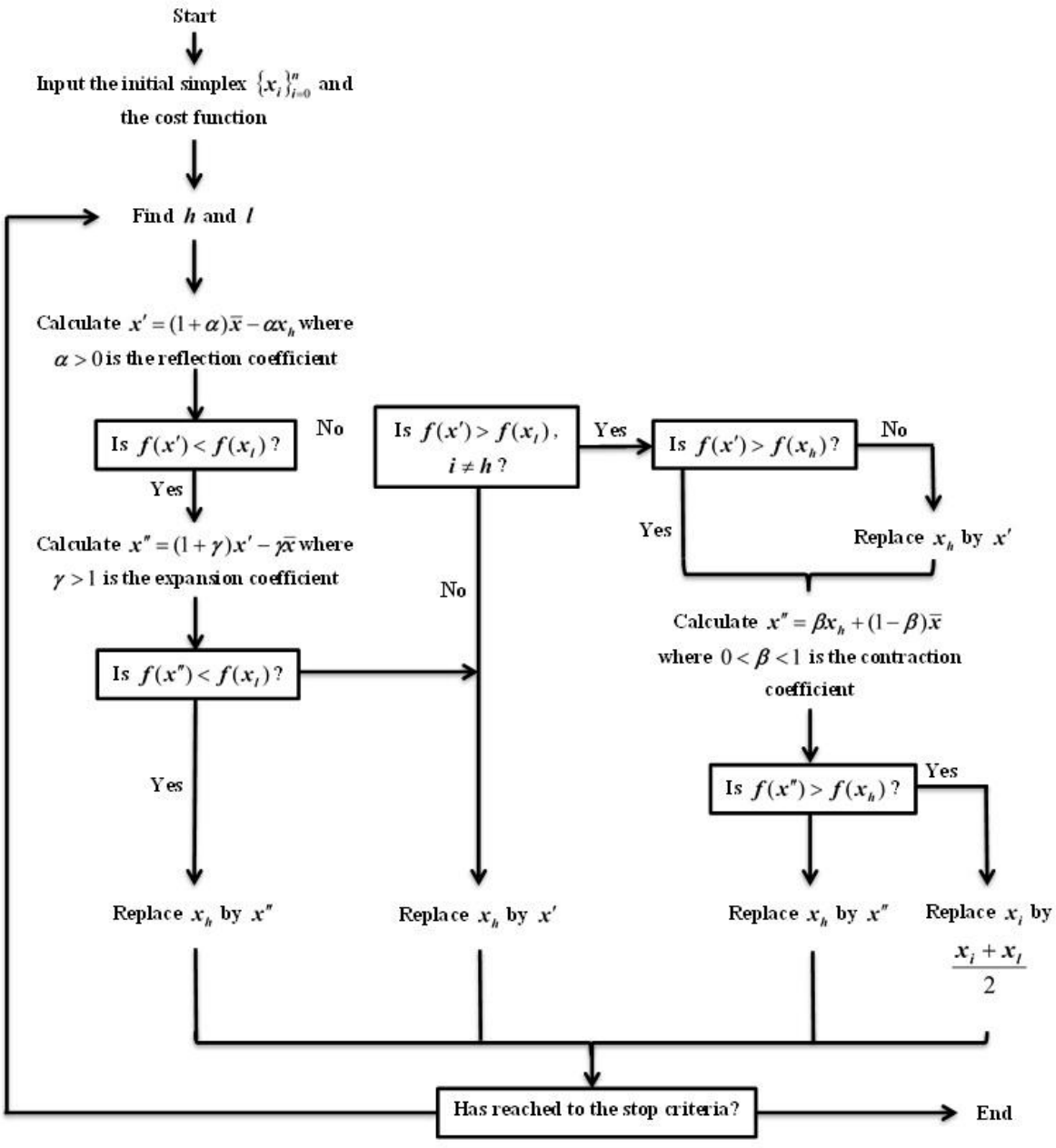

Figure 3.2: Flow chart of downhill simplex method (Nelder and Mead, 1997).

3.4.4.1 Rate uncertainty for white noise

If the uncertainties in the measurements are all equal and if the residuals $\hat{\boldsymbol{\varepsilon}}(t_i)$ consist of white noise only ($\kappa = 0$), then the inverse covariance matrix $\boldsymbol{C}_{\hat{x}}$ of the estimated parameters which is determined by Equation (3.5) can be written as

$$\boldsymbol{C}_{\hat{x}}^{-1} = c^{-2}\begin{bmatrix} N & \sum_{i=1}^{N} t_i \\ \sum_{i=1}^{N} t_i & \sum_{i=1}^{N} t_i^2 \end{bmatrix}, \tag{3.28}$$

where c is the amplitude of white noise which is defined in Equation (3.15). Based on the definition of the estimated parameters Equation (3.2), Equation (3.28) can be written as

$$\boldsymbol{C}_{\hat{x}} = \begin{bmatrix} \sigma_a^2 & \sigma_{ab} \\ \sigma_{ba} & \sigma_b^2 \end{bmatrix} = c^2 \frac{\begin{bmatrix} \sum_{i=1}^{N} t_i^2 & -\sum_{i=1}^{N} t_i \\ -\sum_{i=1}^{N} t_i & N \end{bmatrix}}{N\sum_{i=1}^{N} t_i^2 - \left[\sum_{i=1}^{N} t_i\right]^2}. \tag{3.29}$$

The variance of the estimated intercept which indicates the mean sea level a for white noise (WN) is then

$$\left(\sigma_{\hat{a}}^2\right)_{WN} = c^2 \frac{\sum_{i=1}^{N} t_i^2}{N\sum_{i=1}^{N} t_i^2 - \left[\sum_{i=1}^{N} t_i\right]^2}. \tag{3.30}$$

The variance of the estimated slope, which indicates the sea level rate b, is

$$\left(\sigma_{\hat{b}}^2\right)_{WN} = \frac{Nc^2}{N\sum_{i=1}^{N} t_i^2 - \left[\sum_{i=1}^{N} t_i\right]^2}. \tag{3.31}$$

If the data are equally spaced, i.e.,

$$t_i = (i-1)\Delta T\,, \tag{3.32}$$

where ΔT is the sampling interval, and

$$T = (N-1)\Delta T\,, \tag{3.33}$$

where T is the total observation length, then substituting Equation (3.32) into Equation (3.31) yields

$$\left(\sigma_{\hat{b}}^2\right)_{WN} = \frac{Nc^2}{\Delta T^2\left\{N\sum_{i=1}^{N-1} i^2 - \left(\sum_{i=1}^{N-1} i\right)^2\right\}}. \tag{3.34}$$

Using the identities

$$\sum_{i=1}^{n-1} k = \frac{n(n-1)}{2}; \quad \sum_{i=1}^{n-1} k^2 = \frac{n(n-1)(2n-1)}{6}, \tag{3.35}$$

Equation (3.34) can be expressed as

$$\left(\sigma_{\hat{b}}^2\right)_{WN} = \frac{Nc^2}{\Delta T^2\left\{\frac{N^2(N-1)(2N-1)}{6} - \left(\frac{N(N-1)}{2}\right)^2\right\}}, \tag{3.36}$$

which can be reduced to

$$\sigma_{\hat{b}}^2 = \frac{c^2}{\Delta T^2}\frac{12}{N^3 - N}; \quad \mathrm{N} \geq 2\,. \tag{3.37}$$

Or, using Equation (3.33),

$$\left(\sigma_{\hat{b}}^2\right)_{WN} = \frac{c^2}{T^2}\frac{12(N-1)}{N(N+1)}; \quad \mathrm{N} \geq 2\,. \tag{3.38}$$

Similarly, Zhang et al. 1997 derived an expression for the variance of a

$$\left(\sigma_{\hat{a}}^2\right)_{WN} = \frac{2c^2(2N-1)}{N(N+1)}; \quad \mathrm{N} \geq 2\,. \tag{3.39}$$

For large N, Equation (3.38) and Equation (3.39) can reduce to

$$\left(\sigma_{\hat{b}}^2\right)_{WN} \cong \frac{12c^2}{NT^2}. \tag{3.40}$$

and

$$\left(\sigma_{\hat{a}}^2\right)_{WN} \cong \frac{4c^2}{N}. \tag{3.41}$$

3.4.4.2 Rate uncertainty for Random walk and white and random walk noise

If the uncertainties in measurements are all equal and if the residuals $\hat{\boldsymbol{\varepsilon}}(t_i)$ consist of random walk errors only ($\kappa = -2$), then the inverse covariance matrix $\boldsymbol{C}_{\hat{x}}$ of the estimated parameters is

$$\boldsymbol{C}_{\hat{x}}^{-1} = d_{-2}^{-2}\frac{N-1}{T}\begin{bmatrix} 1 & t_1 \\ t_1 & \boldsymbol{C}_{22} \end{bmatrix}. \tag{3.42}$$

where

$$\boldsymbol{C}_{22} = t_N^2 + 2\sum_{i=1}^{N-1} t_i^2 - 2\sum_{i=1}^{N-1}\left(t_i t_{i+1}\right). \tag{3.43}$$

Using Equation (3.32) and (3.35), $\boldsymbol{C}_{22}$ can be simplified to

$$\begin{aligned} \boldsymbol{C}_{22} &= \Delta T^2\left[(N-1)^2 + 2\sum_{i=1}^{N-1}(i-1)^2 - 2\sum_{i=1}^{N-1} i(i-1)\right] \\ &= (N-1)\Delta T^2 \end{aligned} \tag{3.44}$$

and hence

$$\boldsymbol{C}_{\hat{x}}^{-1} = d_{-2}^{-2}\begin{bmatrix} \dfrac{1}{\Delta T} & 0 \\ 0 & (N-1)\Delta T \end{bmatrix}. \tag{3.45}$$

Inverting Equation (3.45) yields

$$\boldsymbol{C}_{\hat{x}} = \frac{d_{-2}^2}{N-1}\begin{bmatrix} (N-1)\Delta T & 0 \\ 0 & \dfrac{1}{\Delta T} \end{bmatrix}. \tag{3.46}$$

So

$$\left(\sigma_{\hat{b}}^2\right)_{RW} = \frac{d_{-2}^2}{(N-1)\Delta T} = \frac{d_{-2}^2}{T}; \quad N \geq 2. \tag{3.47}$$

and

$$\left(\sigma_{\hat{a}}^2\right)_{RW} = d_{-2}^2 \Delta T = \frac{d_{-2}^2 T}{(N-1)}; \quad N \geq 2. \tag{3.48}$$

For white and random walk noise the variance of the sea level rate would be

$$\left(\sigma_{\hat{a}}^2\right)_{WR} = \left(\sigma_{\hat{a}}^2\right)_{WN} + \left(\sigma_{\hat{a}}^2\right)_{RW} = \frac{12c^2}{NT^2} + \frac{d_{-2}^2}{T}. \tag{3.49}$$

3.4.4.3 Rate uncertainty for flicker and white and flicker noise

There is no exact analytical expression for the variance of the sea level rate $\sigma_{\hat{a}}^2$. The knowledge of the covariance $\boldsymbol{J}_{-1}$ could help to calculate $\sigma_{\hat{a}}^2$ numerically. Williams (2003) derived a reasonable approximation based on the Zhang et al. (1997) covariance matrix, which is in the form

$$\left(\sigma_{\hat{a}}^2\right)_F \cong \frac{9d_{-1}^2}{16\Delta T^2\left(N^2-1\right)}. \tag{3.50}$$

For large number of samples (N>1000)

$$\left(\sigma_{\hat{a}}^2\right)_F \cong \frac{9d_{-1}^2}{16T^2}. \tag{3.51}$$

Hence the variance for white and flicker noise is

$$\left(\sigma_{\hat{a}}^2\right)_{WF} \cong \frac{12c^2}{NT^2} + \frac{9d_{-1}^2}{16\Delta T^2\left(N^2-1\right)}. \tag{3.52}$$

or

$$\left(\sigma_{\hat{a}}^2\right)_{WF} \cong \frac{12c^2}{NT^2} + \frac{9d_{-1}^2}{16T^2}. \tag{3.53}$$

The white noise expression for the standard error shows the classical "square root of N" increase in precision for a non-correlated series (Mazzotti et al., 2008). $\left(\sigma_{\hat{a}}^2\right)_{RW}$ is proportional to $1/N$ for random-walk noise. The largest difference between $\left(\sigma_{\hat{a}}^2\right)_F$ predicted by Equation (3.50) and $\left(\sigma_{\hat{a}}^2\right)_F$ predicted using the covariance matrix is only 2.5% (Williams, 2003). So although Equation (3.50) is not exact, the difference is not large.

3.5 Calculation strategies

The linear regression calculations in this thesis include the determination of errors and the least-squares calculations. So the estimation of sea level rates and their uncertainties should follow several basic strategies.

First step, 10-day T/P and Jason-1 and daily tide gauge SLA time series are averaged to the monthly mean sea level time series. Then the original MMSL time series are corrected for the annual seasonal (Equations (3.8) and (3.9)) and the regional common mode noise corrections (Equations (3.10) and (3.11)).

Second step, the corrected MMSL time series are modeled to create the post-fit residuals that are used in identifying outliers (Equations (3.3), (3.4), and (3.6)). In this step, the error in measurements is assumed to be white noise.

Third step, the cleaned time series are modeled to create new post-fit residuals by Equations (3.3), (3.4), and (3.6) that are used for the noise analysis. In this step, the error in measurements is assumed to be white noise. The post-fit residuals are then substituted to Equations (3.22), (3.23) and (3.24), and Equations (3.26) and (3.27) to test WN, WR and WF models. From Equation (3.26) we can also determine the amplitudes of white noise parameter c and of color noise d_κ, which are defined in Equation (3.14). After finding the better noise model among WN, WR and WF models, the full data covariance matrix can be constructed by Equations (3.17), (3.20) or (3.21).

Forth step, the weighted least-squares algorithm (Equations (3.3), (3.4), (3.5), and (3.6)) is executed again using the new covariance matrix to estimate the parameters with more realistic uncertainties.

After applying above four steps, we can get the estimates of the sea level trend and the uncertainty at each satellite altimetry and tide gauge site.

3.6 Summary

In this chapter, the linear regression method for estimating the sea level rates and their uncertainties is introduced. The calculation is composed of three parts: original data corrections

and outlier detection; error model testing; and rates and uncertainties estimations. The calculating strategies are shown in Figure 3.3.

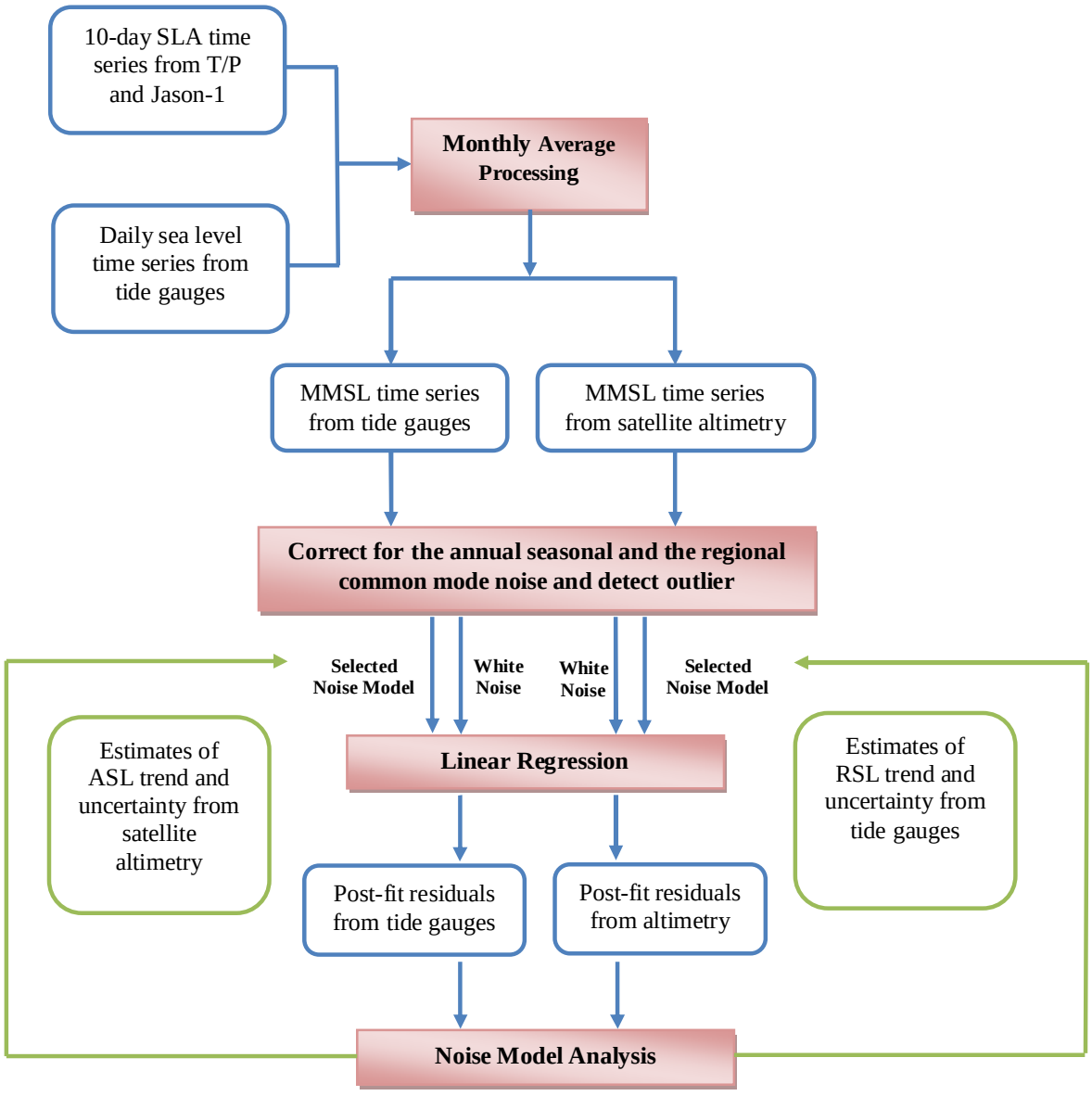

Figure 3.3: Flow chart of the calculating strategies

The three corrections of inverse barometer, annual seasonal and regional common mode can largely decrease the variation of signals in the sea level observations by 70% to 80% (see results in Chapter five and Chapter six) and make our data satisfy as far as possible the requirement for estimating the rate of sea level change and associating uncertainties by the linear regression model. Practice, besides the above three processes, other phenomena such as large earthquakes may affect the tide gauge data by shifting the datum. In the west coast of Canada, there were four earthquakes of magnitude larger than 7: the 1918 M = 7.0 and 1946 M = 7.3 in the central Vancouver Island, the 1949 M = 8.1 and 1972 M = 7.6 earthquakes off the Queen Charlotte, Alaska Panhandle margin. In the east coast of Canada, the earthquake larger than 7 was the 1929 M = 7.3 earthquake in Newfoundland. For all events, the potential earthquake-related offsets in the MMSL time series are smaller than the data resolution and should not affect the long-term trend estimates by more than a few tenths of mm/yr (Larsen et al., 2003; Mazzotti, et al., 2008). For satellite altimetry data, besides the above three corrections, the ocean tide is another significant signal required to be removed. Its correction will be discussed in detail in Chapter four. In Chapter five and Chapter six, the corrected sea level observations from satellite altimetry and tide gauges are treated separately.

Error model testing is very important for the least-squares method. That is because our linear regression model is very simple, using only two parameters: the intercept a indicating the mean sea level and the slope b indicating the rate of sea level change to describe the data. Hence the measurement errors ε are composed of not only the observation errors but also some signals (e.g., the long term signals with periods longer than 10 years) which cannot be removed by the correcting methods. In this case it is not appropriate to assume the errors to be white noise only

whose power spectrum is constant over all frequencies. The color noise (random walk or flicker noise) may be better to describe the measurement error at the low frequencies because the powers of the color noise concentrate at the low frequencies. So a white and color noise combination model is suggested in least-squares estimation (Zhange et al., 1997; Mao et al., 1999; Williams 2003; Mazzotti et al., 2008). The testing and determination of the error model is realized by spectral analysis and maximum likelihood analysis. The results of data corrections, error testing and rate estimations will be shown in Chapter four and Chapter five for satellite altimetry data and, in Chapter six for tide gauge data.

Chapter Four: Residual Ocean Tides Analysis

4.1 Introduction

Ocean tides are responsible for 92% of the variations of the sea surface (Koblinsky et al., 1999). Correcting the ocean tides accurately is especially important for altimetry data because they cannot be filtered out during the monthly averaging processing, which is due to the 10-day T/P and Jason-1 repeat period. Ocean tides were preliminary corrected by a local tide model for Canada, named Webtide. In this chapter, sea level anomalies are analyzed by least-squares spectral analysis to explore the residual tidal signals included in the observations. Then the amplitudes and phases of these residual tidal signals are determined by the traditional harmonic analysis. Detected residual tidal signals are removed from our sea level anomaly observations to decrease their effects further. This chapter is composed of five sections. The first section states the basic information about the tide generation and tidal constituents. The second section introduces the local tide model Webtide and also exam the model accuracy. The third section describes those two analysis methods: harmonic analysis and Least-square spectral analysis. Section four and section five show the results of the analysis for the west coast and east coast of Canada, respectively.

4.2 Local ocean tide model --- Webtide

Actually Webtide is the name of a graphical user interface for the tidal prediction program which is operated by DFO (Figure 4.1), but in this thesis Webtide is used as the name of the whole tide model which is composed of 10 data sets for the predicted areas (Figure 4.2). Predictions can be obtained for any point inside a selected model domain by analyzing the corresponding data set.

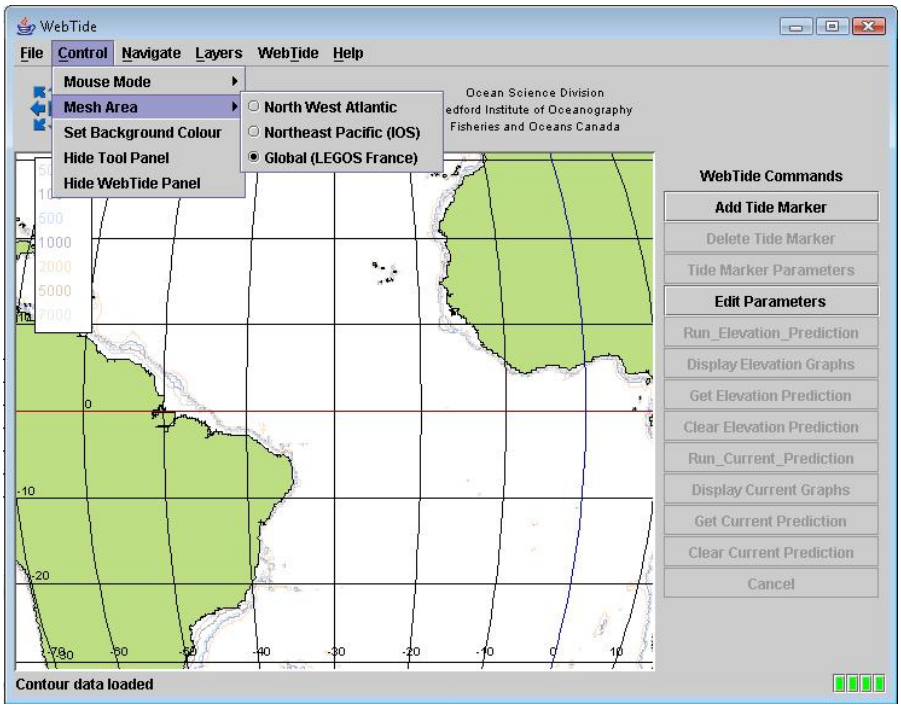

Figure 4.1: The interface of Webtide.

Webtide of Northeast Pacific (hereafter Webtide-NP) and Webtide of Northwest Atlantic (hereafter Webtide-NA) are used in this thesis. The harmonic data of 8 major semi-diurnal and diurnal constituents (M_2, S_2, N_2, K_2, K_1, O_1, P_1, Q_1) for the Northeast Pacific were derived by assimilating the amplitudes and phases computed by Cherniawsky et al. (2001) using 5-year T/P time series at crossover locations along the tracks by harmonic analysis to the finite element model FUNDY5SP, with boundary forcing from the Oregon State University global tide model, TPXO.3 (Foreman et al., 2000). It covers the Pacific Ocean northward of $30^{\circ}N$ and eastward of $180^{\circ}W$, excluding the Bering Sea (Figure 4.2).

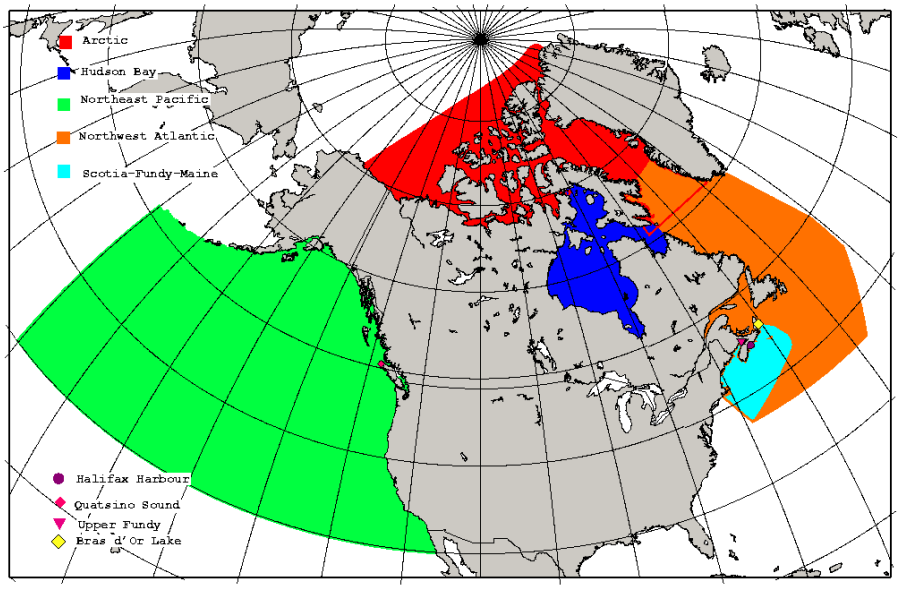

Figure 4.2: Model domain of Webtide (DFO website).

Webtide-NA is composed of 5 major astronomical, namely M_2, S_2, N_2, K_1, O_1. Harmonics of these five constituents were derived by a data assimilation system. This system consists of two numerical models, one that is a nonlinear time-stepping model that computes the water levels and currents from specified elevation boundary conditions and one that is a linear inverse model that computes the elevation boundary conditions that minimize the difference between the selected observations and the model predictions. The assimilated data was the tidal harmonics computed at T/P crossover points from 7 years of data. Two coastal tide gauges in the Saint Lawrence estuary were another source of input data used to constrain the open boundary condition there. The model domain for Northwest Atlantic extends from Cape Cod to Greenland, part of Baffin Island, Northern Quebec, Labrador, Newfoundland and Nova Scotia, corresponding to the latitude band from $35^{\circ}S$ to $67^{\circ}N$ and to the longitude band from $75^{\circ}W$ to $35^{\circ}W$ (Figure 4.2).

In order to assess the performance of Webtide, three global tide models, FES2004, EOT11a and DTU10, are used for comparisons. The comparisons are carried out in two ways: (1) spatial resolution comparisons and (2) harmonic accuracy comparisons.

All of these three global tide models are in rectangular grids with spacing of 0.125° in latitude and 0.125° in longitude. Their horizontal spatial resolution is approximate 9 km. Both Webtide-NP and Webtide-NA are in triangular grids. The mesh of the former (Figure 4.3) has 51330 nodes and 93272 elements. The mesh of the latter (Figure 4.6) has 17055 modes and 30839 elements. Their horizontal resolution varies from approximately 80 km in the deep ocean to about 100 m in the coastal areas. Grid sizes of 80 km are adequate in the deep ocean where tidal harmonics do not exhibit great variability (Foreman et al., 2000). In the coastal areas, the spatial resolution of Webtide is much higher than that of the three global models. The 0.125° grid spacing of these three global models is not sufficiently fine to permit precise interpolation and accuracy evaluation at any of the coastal locations.

In order to assess the accuracy of Webtide in the coastal areas, we first compare the complex tidal elevation amplitude for each of the major constituents of Webtide and the global models FES2004, EOT11a and DTU10 with harmonics from the coastal tide gauge sites (Figure 4.4 and Figure 4.5 show the positions of these tide gauge stations). We then compare the harmonics of the largest constituents derived by Webtide with the values estimated from tide gauge data. The complex tidal elevation amplitude difference between model-derived harmonics and tide gauge estimated harmonics is calculated by:

$$D_{rms} = (C_{rms}^2 + S_{rms}^2)^{1/2}, \tag{4.1}$$

where

$$C_{rms} = [\sum_{1}^{N} (A_T \cos G_T - A_m \cos G_m)^2 / N]^{1/2}, \tag{4.2}$$

$$S_{rms} = [\sum_{1}^{N} (A_T \sin G_T - A_m \sin G_m)^2 / N]^{1/2}, \tag{4.3}$$

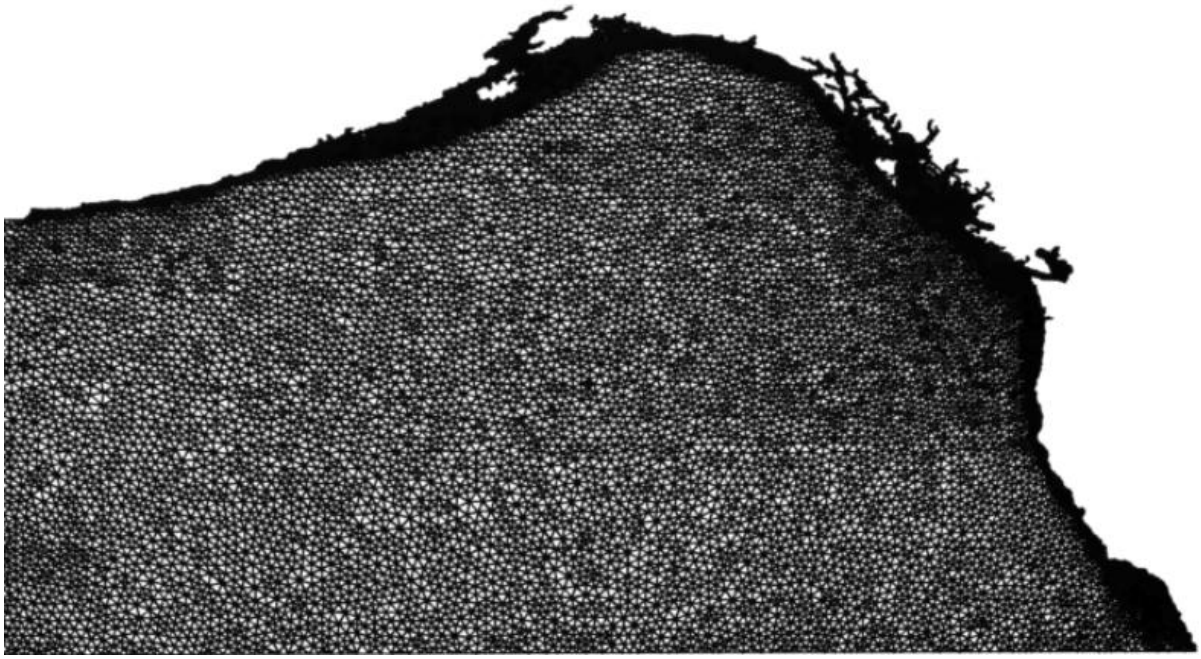

Figure 4.3: The triangular grid for Webtide-NP

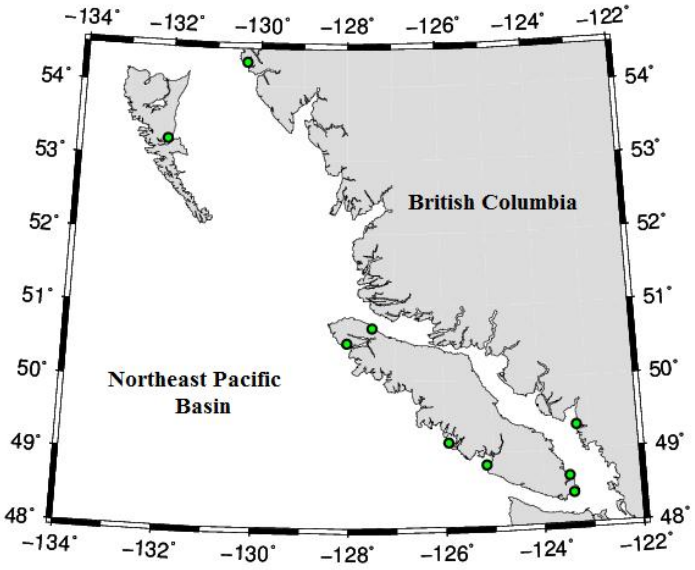

Figure 4.4: Position of tide gauge stations in the west coast of Canada used for comparing with tide models

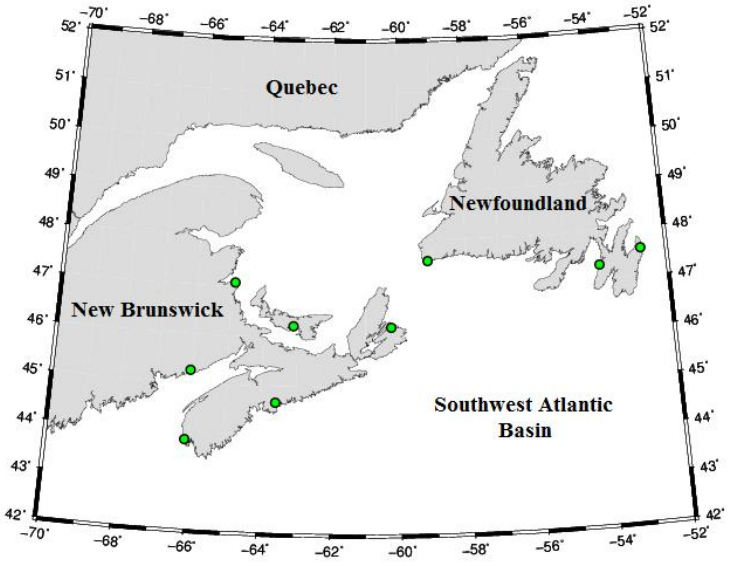

Figure 4.5: Position of tide gauge stations in the east coast of Canada used for comparing with tide models

Figure 4.6: The triangular grid for Webtide-NA

N is the number of tide gauge sites, and A_T, G_T and A_m, G_m are the tide gauge and modeled amplitudes and phases lags, respectively. The comparison results are listed in Table 4.1 and Table 4.2. In the Northeast Pacific coastal area, for all constituents except M_2, Webtide-NP is seen to be more accurate than FES2004, EOT11a and DTU10. For M_2, Webtide-NP has comparable accuracy with FES2004 and EOT11a but is much more accurate than DTU10. In

the Northwest Atlantic coastal area, 3 out of 5 major constituents of Webtide-NA have higher accuracy than the other global tide models, while for the constituents N_2 and M_2, the RMS of Webtide-NA is 2 cm larger than the RMS of the global tide models.

Table 4.1 The RMS differences between the complex tidal elevation amplitudes at the 9 coastal tide gauge stations and those computed by the four tide models. Differences are in centimeters (D_{rms})

Constituents	Q_1	O_1	P_1	K_1	N_2	M_2	S_2	K_2
Webtide-NP	**0.30**	**1.47**	**0.81**	**2.45**	**1.07**	**5.86**	**2.34**	**0.68**
EOT11a	**0.82**	**3.22**	**2.07**	**4.13**	**3.83**	**5.31**	**6.06**	**1.89**
FES2004	**0.83**	**2.99**	**2.19**	**4.10**	**3.68**	**5.04**	**5.51**	**2.30**
DTU10	**1.59**	**7.51**	**5.23**	**14.68**	**7.23**	**32.06**	**10.15**	**3.47**

Table 4.2 The RMS differences between the complex tidal elevation amplitudes at the 10 coastal tide gauge stations and those computed by the four tide models. Differences are in centimeters (D_{rms})

Constituents	O_1	K_1	N_2	M_2	S_2
Webtide-NP	**0.84**	**1.71**	**5.28**	**7.18**	**2.62**
EOT11a	**1.69**	**2.43**	**2.40**	**4.07**	**2.77**
FES2004	**1.65**	**2.20**	**2.74**	**5.13**	**3.05**
DTU10	**3.41**	**4.48**	**3.26**	**13.04**	**2.59**

The observation-estimated harmonics of M_2, the largest semi-diurnal constituent and K_1, the largest diurnal constituent, and the Webtide-derived harmonics at 9 tide gauge locations in the west coast of Canada and at 10 locations in the east coast of Canada are listed in Table 4.3 and Table4.4. Differences between the two sets of harmonic constants are expressed as distances in the complex plane:

$$D = [(C_T - C_m)^2 + (S_T - S_m)^2]^{1/2}, \tag{4.4}$$

Table 4.3 Tide gauge estimated and Webtide-NP derived M_2 and K_1 amplitudes and phases at selected coastal locations

Sites	M_2					K_1				
	TG Estimates		Webtide-NP			TG Estimates		Webtide-NP		
	Amplitude cm	Phase deg UTC	Amplitude cm	Phase deg UTC	D Cm	Amplitude cm	Phase deg UTC	Amplitude cm	Phase deg UTC	D cm
Victoria Harbour 7120	37.22	317.56	31.69	323.97	6.74	63.63	271.26	63.05	269.59	1.94
Patricia Bay 7277	60.61	13.51	64.70	21.44	9.58	76.20	280.78	77.54	282.18	2.30
Point Atkinson 7795	92.11	31.02	90.92	31.00	1.18	86.39	286.33	86.05	286.01	0.59
Port Hardy 8408	133.59	253.42	126.49	254.49	7.51	50.13	250.59	49.03	252.97	2.34
Bamfield 8545	94.37	234.61	92.47	235.23	2.15	39.29	245.94	36.97	243.21	2.94
Tofino 8615	98.76	240.85	96.93	237.98	5.24	38.90	241.33	41.17	234.95	5.00
Winter Harbour 8735	100.85	243.55	97.65	244.41	3.53	43.60	246.52	44.34	245.62	1.01
Prince Rupert 9354	195.50	267.36	191.42	266.25	5.53	51.27	259.712	50.58	258.59	1.22
Queen Charlotte City 9850	199.16	271.77	193.92	270.77	6.26	51.43	262.13	49.72	261.83	1.73

Table4.4 Tide gauge estimated and Webtide-NA derived M_2 and K_1 amplitudes and phases at selected coastal locations

Sites	M_2					K_1				
	TG Estimates		Webtide-NP			TG Estimates		Webtide-NP		
	Amplitude cm	Phase deg UTC	Amplitude cm	Phase deg UTC	D Cm	Amplitude cm	Phase deg UTC	Amplitude cm	Phase deg UTC	D cm
Saint John 65	303.48	98.27	300.08	97.94	3.80	15.20	194.46	15.05	188.44	1.60
Yarmouth 365	165.97	63.24	170.88	60.04	10.61	13.917	183.82	13.57	175.93	1.92
Halifax 490	62.53	350.55	62.69	350.62	0.18	10.38	121.63	11.27	122.46	0.90
North Sydney 612	36.67	353.99	36.12	350.32	2.39	7.50	324.15	6.32	328.53	1.29
Port Aux Basques 665	43.58	13.95	45.59	12.49	2.310	7.72	251.17	7.314	238.27	1.74
Argentia 835	69.40	338.82	68.72	337.69	1.53	7.73	181.45	7.08	173.02	1.27
St Johns 905	35.17	315.40	35.98	314.19	1.11	7.83	160.85	7.31	161.70	0.53
Charlottetown 1700	71.52	63.17	69.10	49.32	17.12	24.87	326.68	21.71	328.52	3.24
Shediac Bay 1805	14.93	56.92	16.47	24.31	8.93	24.87	314.06	22.98	315.86	2.04
Lower Escuminac 2000	25.65	239.32	25.68	242.53	1.44	20.42	295.30	19.54	295.64	0.89

where C and S are calculated by the form $C = A\cos G$ and $S = A\sin G$. C_T, S_T, C_m and S_m are the tide gauge estimated and model derived C and S values, respectively. In general, D values for sites along the open coast are small, while those from inland seas and inlets are larger. This suggests a need for finer grid resolution, more accurate bathymetry, and perhaps additional forms of dissipation (Foreman et al., 2000).

According to the comparison results, Webtide-NP and Webtide-NA have greater accuracy than FES2004, EOT11a and DTU10 for most of the major constituents in the coastal areas. Hence Webtide-NP and Webtide-NA were chosen to provide the ocean tide corrections to satellite altimetry data in this thesis. However, there exist three limitations in Webtide. First, based on the comparison results, we found there are larger discrepancies for M_2 and N_2 in Webtide-NA. Hence after we remove the tide corrections from satellite altimetry data, the data still contain relative large residual M_2 and N_2 tidal patterns. Additional analysis is required to determine the residual M_2 and N_2 tides and then we should remove them from satellite altimetry data. Second, Webtide-NP and Webtide-NA were developed and published in 2000 and 2002, respectively. After almost 10 years since their development, more satellite altimetry data have been obtained which can be used to update the original models. In addition, Webtide consists of limited tidal spectrum lines, 8 constituents for Northeast Pacific and 5 constituents for Northwest Atlantic, whereas the other three global tide models are composed of not only the same constituents as Webtide has but also of other constituents, e.g., the minor astronomical, long term, and even nonlinear constituents. Hence although Webtide has higher accuracy at the major astronomical constituents in common, it is lacking information about the minor

astronomical, long term and nonlinear constituents. The major constituents can represent the entire tide very well in the deep ocean where the major constituents make 92% of the entire ocean tide signal, however, in coastal areas, because of the complex dynamics of the tidal patterns, the effects of other constituents cannot be ignored. Hence it is required to analyze the sea level anomalies data from satellite altimetry after correcting the ocean tide by Webtide to derive the harmonic estimates for the residual major constituents and selected minor, long term and nonlinear constituents. Traditional harmonic analysis and least-squares spectral analysis are used to do the estimation and are introduced in the following sections.

4.3 Analysis methods

Traditional spectral analysis, such as, Fourier analysis, requires the observational time series to be stationary and sampled at equal interval but in practice, the real measurements cannot fulfill these two requirements. In addition, there are data gaps in every time series due to altimeter failures or environmental effects. Therefore, more robust methods must be selected.

4.3.1 Choice of estimated constituents

Before applying any method to analyze the tidal measurements, a very important process is to choose the constituents involved in the estimation. Foreman (1996) suggested there is a maximum of 146 possible tidal constituents that can be included in the tidal analysis; 45 of these are astronomical in origin while the remaining 101 are shallow water constituents. Taking the computation time and the levels of significances of these constituents into account, he created a smaller package of constituents, with an additional 6 long term constituents and 24 shallow water constituents. In this study, a set of 57 constituents is chosen based on the choice

of Foreman (1996). In addition, in order to be consistent with Webtide-NP, the 8 main astronomical constituents M_2, S_2, N_2, K_2, K_1, O_1, Q_1 and P_1 are involved and another 19 minor astronomical constituents are included as suggested by Foreman (1998). This set of 57 constituents is chosen for tide gauge hourly data, which are listed in the first column of Table 4.5 and Table 4.6.

The choice of T/P and Jason-1 data is a little more complex. The T/P repeat period is 10 days which is much longer than the periods of most of the tidal constituents. It is well known that aliasing problem will occur when the sampling interval is longer than one half of the signal period. The original signal period will be thus aliased to a longer period. The calculation of the alias period is straightforward. For two measurements of the signal with frequency f separated by a time interval Δt (10 days for T/P) the corresponding phase difference is:

$$\delta\varphi = 2\pi\left| f\Delta t - [\, f\Delta t + 0.5]\right|, \tag{4.5}$$

where $|x|$ is the operator taking the absolute value of x and $[x]$ is the operator taking the largest integer less than x. Then the alias period would be:

$$T_{alias} = P \cdot 2\pi\Delta t / \delta\varphi, \tag{4.6}$$

where P is an arbitrary integer. The smallest alias period would be $T_a = 2\pi\Delta t / \delta\varphi$. Original and alias periods of every selected constituent are listed in the second and third column of Table 4.5 and Table 4.6.

In practical calculation, the Rayleigh criterion is usually used to determine if two constituents can be separated by the data or to determine the minimum length of the data that can separate

two constituents. Two constituents whose frequencies are f_i and f_j respectively, can be separated only if the time span T of the data record satisfies the condition:

$$\left| f_i - f_j \right| T \geq RAY \,, \tag{4.7}$$

RAY is commonly given the value 1. In this study, two constituents which have the minimum difference between their aliasing frequencies compose a Rayleigh comparison pair. Applying the condition (4.7 on every Rayleigh pair can help to determine the minimum duration of observations which is needed to separate them. The Rayleigh pairs among the 57 constituents and their required record length are listed in Table 4.5 and Table 4.6.

There are 5 pairs (χ_1 and SN_4, ν_2 and $2MS_6$, L_2 and M_6, SO_3 and MK_4, M_8 and MM) whose required record length is pretty close to or much longer than the T/P and Jason-1 data duration that cannot be separated. So SN_4, $2MS_6$, M_6, M_8, MK_4 are removed. The rest of the 52 constituents form the constituents set for the T/P and Jason-1 data.

Table 4.5 Original periods and alias periods of selected long term, astronomical diurnal and semi-diurnal constituents. Their Rayleigh comparison pairs and corresponding minimum record length required for constituents separation.

Constituent	Period (day/cycle)	Alias Period T/P (day/cycle)	Rayleigh Comparison Pair		Record Length Required for Constituents Separation (days)
			Long Term Constituent		
SA	**365.260**	**365.260**	SA	MN_4	**741**
SSA	**182.621**	**182.621**	SSA	K_1	**3355**
MSM	**31.8119**	**31.8119**	MSM	M_4	**1303**
MM	**27.5546**	**27.5546**	MM	M_8	**6445**
MSF	**14.7653**	**30.1889**	MSF	OO_1	**3355**

MF	**13.6608**	**36.1677**	MF	SK_4	**1084**
			Astronomical Diurnal Constituent		
$2Q_1$	**1.16693**	**19.9430**	$2Q_1$	μ_2	**1091**
σ_1	**1.16035**	**21.8096**	σ_1	$2N_2$	**675**
Q_1	**1.11951**	**69.3645**	Q_1	π_1	**2331**
ρ_1	**1.11346**	**104.606**	ρ_1	MK_3	**1303**
O_1	**1.07581**	**45.7142**	O_1	MKS_2	**3355**
NO_1	**1.03472**	**23.7724**	NO_1	$3MK_7$	**2156**
χ_1	**1.02954**	**26.8755**	χ_1	SN_4	**180547**
π_1	**1.00551**	**71.4923**	π_1	Q_1	**2331**
P_1	**1.00275**	**88.8909**	P_1	K_2	**3355**
S_1	**1.00000**	**117.485**	S_1	ρ_1	**955**
K_1	**0.99727**	**173.192**	K_1	SSA	**3355**
φ_1	**0.99185**	**3354.44**	φ_1	MS_4	**1602**
θ_1	**0.96695**	**38.9699**	θ_1	$2MK_5$	**1303**
J_1	**0.96243**	**32.7679**	J_1	MSM	**1091**
OO_1	**0.92942**	**29.9196**	OO_1	MSF	**3355**
			Astronomical Semidiurnal Constituent		
ε_2	**0.54697**	**77.3140**	ε_2	MSK_6	**2160**
$2N_2$	**0.53772**	**22.5383**	$2N_2$	σ_1	**675**
μ_2	**0.53632**	**20.3145**	μ_2	L_2	**1304**
N_2	**0.52743**	**49.5282**	N_2	T_2	**2331**
ν_2	**0.52608**	**65.2162**	ν_2	$2MS_6$	**6450**
M_2	**0.51753**	**62.1075**	M_2	ν_2	**1303**
λ_2	**0.50924**	**21.0367**	λ_2	M_6	**1304**
L_2	**0.50798**	**20.6362**	L_2	M_6	**6444**
T_2	**0.50069**	**50.6036**	T_2	N_2	**2331**

S_2	**0.50000**	**58.7417**	S_2	$2MS_6$	**1084**
K_2	**0.49864**	**86.5961**	K_2	P_1	**3355**
η_2	**0.48977**	**40.4142**	η_2	θ_1	**1091**

Table 4.6 Periods and alias periods of selected nonlinear constituents as well as their Rayleigh comparison pairs and corresponding minimum record length required for constituents separation.

Constituent	Period (day/cycle)	Alias Period: T/P (day/cycle)	Rayleigh Comparison Pair		Record Length Required for Constituents Separation (days)
SO_1	**0.934174**	**25.7078**	SO_1	$2SK_5$	**1084**
MKS_2	**0.516063**	**46.3458**	MKS_2	O_1	**3355**
MSN_2	**0.491089**	**51.8996**	MSN_2	T_2	**2027**
MO_3	**0.349429**	**26.3323**	MO_3	SN_4	**1313**
SO_3	**0.341351**	**206.127**	SO_3	MK_4	**3355**
MK_3	**0.340714**	**96.8318**	MK_3	ρ_1	**1303**
SK_3	**0.333029**	**43.8642**	SK_3	O_1	**1084**
MN_4	**0.261216**	**244.534**	MN_4	MK_4	**2156**
M_4	**0.258763**	**31.0537**	M_4	MSM	**1303**
SN_4	**0.256675**	**26.8715**	SN_4	χ_1	**180547**
MS_4	**0.254306**	**1083.94**	MS_4	SA	**551**
MK_4	**0.253952**	**219.623**	MK_4	SO_3	**3355**
S_4	**0.250000**	**29.3709**	S_4	OO_1	**1602**
SK_4	**0.249658**	**34.9999**	SK_4	MF	**1084**
$2MK_5$	**0.205453**	**37.8382**	$2MK_5$	θ_1	**1303**
$2SK_5$	**0.199891**	**25.1122**	$2SK_5$	SO_1	**1084**
$2MN_6$	**0.173595**	**83.2521**	$2MN_6$	MSK_6	**2180**
M_6	**0.172508**	**20.7025**	M_6	L_2	**6444**
$2MS_6$	**0.170516**	**65.8824**	$2MS_6$	ν_2	**6450**
$2MK_6$	**0.170357**	**48.4159**	$2MK_6$	N_2	**2156**

$2SK_6$	**0.168569**	**55.7220**	$2SK_6$	S_2	**1084**
MSK_6	**0.168414**	**80.1897**	MSK_6	$2MN_6$	**2180**
$3MK_7$	**0.147068**	**23.5131**	$3MK_7$	NO_1	**2156**
M_8	**0.129381**	**27.4373**	M_8	MM	**6446**

4.3.2 Harmonic analysis

The tidal signal can be expressed as a sinusoidal function:

$$P(t) = A_0 + \sum_{i=1}^{M} A_i \cos(\omega_i t + \theta_i), \tag{4.8}$$

with $P(t)$ the tidal measurement, A_i the amplitude of the i^{th} constituent, θ_i the phase of the i^{th} constituent, ω_i the angular frequency of the i^{th} constituent, t the measuring time and M the number of analyzed constituents. Equivalently, Equation (4.8) can be written as

$$P(t) = A_0 + \sum_{i=1}^{M} (U_i \cos(\omega_i t) + V_i \sin(\omega_i t)), \tag{4.9}$$

where U_i is the i^{th} cosine constituent and V_i is the i^{th} sine constituent. The relations between A_i, θ_i and U_i, A_i are:

$$A_i = \sqrt{(U_i^2 + V_i^2)}, \tag{4.10}$$

$$\theta_i = \tan^{-1}(\frac{V_i}{U_i}), \tag{4.11}$$

Equation (4.9) can be written in a matrix form as:

$$\boldsymbol{p} = \begin{bmatrix} \boldsymbol{u} & \boldsymbol{v} \end{bmatrix} \begin{bmatrix} \boldsymbol{C} \\ \boldsymbol{D} \end{bmatrix}, \tag{4.12}$$

where

$$\boldsymbol{p}^T = \{P(t_1)\cdots P(t_n)\}, \tag{4.13}$$

$$\boldsymbol{u} = [U_1 \quad \cdots \quad U_M], \tag{4.14}$$

$$\boldsymbol{v} = [V_1 \quad \cdots \quad V_M], \tag{4.15}$$

$$\boldsymbol{C} = \begin{bmatrix} \cos\omega_1 t_1 & \cdots & \cos\omega_1 t_n \\ \vdots & \ddots & \vdots \\ \cos\omega_M t_1 & \cdots & \cos\omega_M t_n \end{bmatrix}, \tag{4.16}$$

$$\boldsymbol{D} = \begin{bmatrix} \sin\omega_1 t_1 & \cdots & \sin\omega_1 t_n \\ \vdots & \ddots & \vdots \\ \sin\omega_M t_1 & \cdots & \sin\omega_M t_n \end{bmatrix}, \tag{4.17}$$

and n is the dimension of the time series.

In Equation (4.9) or Equation (4.12), the unknown parameters are U_i and V_i. Harmonic analysis is a method that can be used to determine the unknown parameters by fitting the Equation (4.9) to a given time series of sea surface measurements $S(t)$ from tide gauge or satellite altimetry data under the least-squares criterion.

In practical calculations, there are two modifications to Equation (4.9). For a harmonic analysis, we analyze at the frequency of the main constituent and obtain an apparent amplitude and phase. However, every main constituent has a set of minor constituents, which have very similar frequencies and tidal patterns to the main constituent. Hence harmonic results for one main constituent are actually due to the cumulative effect of all associating constituents (Godin, 1972;

Foreman et al., 1977). In order to remove the effects of these minor constituents, the nodal modulation f and u are applied. Equation (4.9) with the nodal modulation is written as:

$$P(t) = A_0 + \sum_{i=1}^{M} (f \cdot U_i \cos(\omega_i t + u) + f \cdot V_i \sin(\omega_i t + u)), \quad (4.18)$$

A second modification to the least-squares solution is the astronomical argument correction. Foreman et al. (1977) defined the astronomical argument in the following way. Instead of regarding each tidal constituent as the result of some particular component of the tidal potential, an artificial causal agent can be attributed to each constituent in the form of a fictitious star which travels around the equator with an angular speed equal to that of its corresponding constituent. Making use of this conceptual aid, the astronomical argument, $B(L,t)$, of a tidal constituent can then be viewed as the angular position of this fictitious start relative to longitude, L, and at time, t. L is generally assumed to be the Greenwich meridian, and B is reduced to a function of one variable. After introducing the definition of the astronomical argument, the phase θ can be expressed as $\theta = B + g$, where g, the Greenwich phase lag, is the difference between this Greenwich astronomical argument and the phase of the observed constituent signal. The value of g is dependent upon the time zone in which the hourly heights of the record are taken. This means that when phases at various stations, not necessarily in the same time zone, are compared, they must be reduced to a common zone in order to avoid spurious differences due to different relative time. So it would be better to record in, or convert all the observations to GMT. Introducing the astronomical argument A and Greenwich phase lag g into Equation (4.18), the final expression of harmonic analysis for practical calculation is derived as:

$$P(t) = A_0 + \sum_{i=1}^{M} (f \cdot U_i \cos(\omega_i t + B(t) + g) + f \cdot V_i \sin(\omega_i t + B(t) + g)), \quad (4.19)$$

4.3.3 Least-squares spectral analysis

The principle of least-squares spectral analysis will be introduced with the help of the functional analysis and the projection theorem.

$\Phi' = \cos\omega_i t$ and $\Phi'' = \sin\omega_i t$ are considered as the basis to form a manifold L and orthogonal with each other (see Figure 4.7). $\boldsymbol{p}$ is a vector in the manifold L and generated by two basis with nonzero coefficients U_i and V_i:

$$\boldsymbol{p}(\omega_i) = U_i \cos\omega_i t + V_i \sin\omega_i t, \quad (4.20)$$

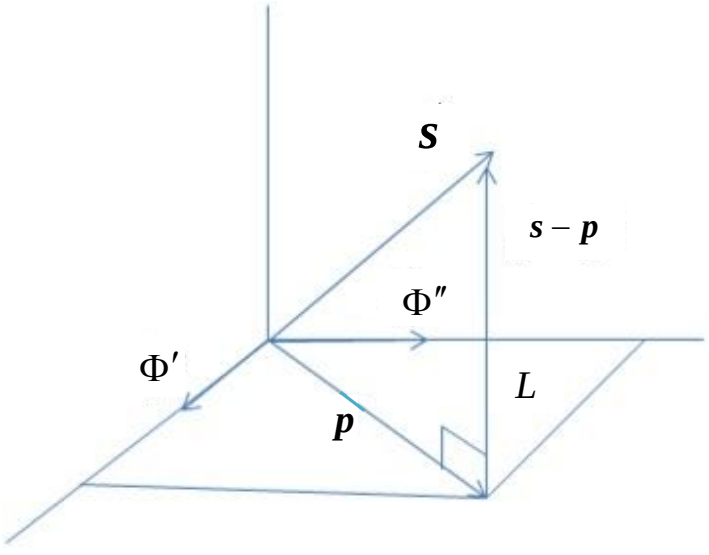

Figure 4.7: Projection theorem.

Least-squares spectral analysis is a method to find the best fitting approximant $\boldsymbol{p}$ to $\boldsymbol{s}$. As shown in Figure 4.7, using the projection theorem, best fitting means vector $\boldsymbol{s}$ has the shortest distance to $\boldsymbol{p}$, i.e., $\boldsymbol{s}-\boldsymbol{p}$ is minimum. $\boldsymbol{s}-\boldsymbol{p}$ is minimum only when $\boldsymbol{s}-\boldsymbol{p}$ is perpendicular to the manifold L so as to $\boldsymbol{p}$. Using the functional analysis, if $(\boldsymbol{s}-\boldsymbol{p}) \perp \boldsymbol{p}$, that means the scalar product between $\boldsymbol{s}-\boldsymbol{p}$ and $\boldsymbol{p}$ is going to be zero. Their scalar product is written as:

$$\langle \boldsymbol{s}-\boldsymbol{p},\ \boldsymbol{p} \rangle = 0, \tag{4.21}$$

From Equation (4.21) we can get

$$\langle \boldsymbol{p},\quad \boldsymbol{p} \rangle = \langle \boldsymbol{s},\quad \boldsymbol{p} \rangle, \tag{4.22}$$

We will now rewrite the expressions above in matrix form. Let $\boldsymbol{\Phi} = [\Phi' \quad \Phi''] = [\cos\omega_i t \quad \sin\omega_i t]$ and $\boldsymbol{c}^T = [U_i \quad V_i]$ Equation (4.20) is converted to

$$\boldsymbol{p} = \boldsymbol{\Phi c}, \tag{4.23}$$

Submitting Equation (4.23) into Equation (4.22) we get:

$$\boldsymbol{\Phi}^T \boldsymbol{\Phi c} = \boldsymbol{\Phi}^T \boldsymbol{s}, \tag{4.24}$$

Then

$$\boldsymbol{c} = (\boldsymbol{\Phi}^T \boldsymbol{\Phi})^{-1} \boldsymbol{\Phi}^T \boldsymbol{s}, \tag{4.25}$$

In order to assess if $\boldsymbol{p}(\omega_i)$ fits $\boldsymbol{s}$ well, we need to do the second orthogonal projection: project $\boldsymbol{p}(\omega_i)$ to $\boldsymbol{s}$ (shown in Figure 4.8). The length of this projection is

$$\frac{\langle \boldsymbol{s},\quad \boldsymbol{p} \rangle}{\|\boldsymbol{s}\|}, \tag{4.26}$$

The ratio of the length of this orthogonal projection to the length of $\boldsymbol{s}$ is

$$f(\omega_i) = \frac{\langle \boldsymbol{s}, \quad \boldsymbol{p}(\omega_i) \rangle}{\langle \boldsymbol{s}, \quad \boldsymbol{s} \rangle} = \frac{\boldsymbol{s}^T \boldsymbol{p}(\omega_i)}{\boldsymbol{s}^T \boldsymbol{s}}, \tag{4.27}$$

where f is the fractional content of $\boldsymbol{s}$ represented by $\boldsymbol{p}(\omega_i)$. If $\boldsymbol{p}(\omega_i)$ fits $\boldsymbol{s}$ very well, then f is 1 (all of $\boldsymbol{s}$ is represented by $\boldsymbol{p}(\omega_i)$). In general, $f(\omega_i)$ is defined as the spectrum of one special ω_i.

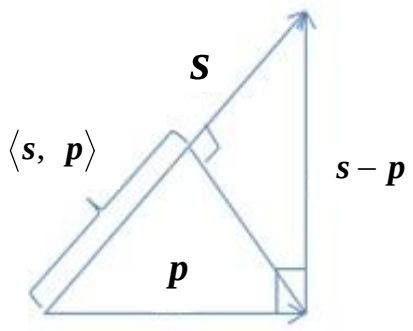

Figure 4.8: Definition of the spectrum.

4.3.4 Consistency between harmonic analysis and least-squares spectral analysis results

It is obvious that $\boldsymbol{p}(\omega_i)$ expressed by Equation (4.20) is one component of $P(t)$ expressed by Equation (4.9). By harmonic analysis, each component of $P(t)$ is determined at the same time whereas by least-squares spectral analysis, $\boldsymbol{p}(\omega_i)$ is estimated separately. The polynomial consisting of $\boldsymbol{p}(\omega_i)$, which is estimated by least-squares spectral analysis, is called $P^*(t)$. Generally $P^*(t)$ differs from $P(t)$ unless the frequencies ω_i are integers so that the matrix of the system of normal equations for such frequencies is diagonal and the system degenerates into $2M-1$ independent linear equations for individual coefficients. Hence it is required to examine if the results of harmonic analysis and least-squares spectral analysis are consistent.

We calculate the mean, maximum and minimum complex tidal elevation difference, which is determined by Equation (4.1), for 8 major constituents between the results derived by the two methods. In Northeast Pacific, results from 9 tide gauge sites are used and the comparison results can be found in Table 4.7. The comparison results of 9 tide gauge sties in the Northwest Atlantic are listed in Table 4.8.

Table 4.7 The mean, maximum and minimum complex tidal elevation differences between harmonic results derived by harmonic analysis and least square spectral analysis at 9 tide gauge stations in Northeast Pacific. Unit is centimeter.

Constituents	Q_1	O_1	P_1	K_1	N_2	M_2	S_2	K_2
D_{mean}	**0.046**	**0.042**	**0.250**	**0.079**	**0.118**	**0.036**	**0.093**	**0.140**
$D_{\max}$	**0.081**	**0.082**	**0.435**	**0.140**	**0.250**	**0.136**	**0.339**	**0.262**
$D_{\min}$	**0.016**	**0.021**	**0.133**	**0.028**	**0.017**	**0.009**	**0.016**	**0.043**

Table 4.8 The mean, maximum and minimum complex tidal elevation differences between results derived by harmonic analysis and least square spectral analysis at 9 tide gauge stations in Northwest Atlantic. Unit is centimeter

Constituents	Q_1	O_1	P_1	K_1	N_2	M_2	S_2	K_2
D_{mean}	**0.056**	**0.050**	**0.215**	**0.077**	**0.231**	**0.102**	**0.263**	**0.190**
$D_{\max}$	**0.212**	**0.228**	**0.648**	**0.299**	**0.928**	**0.448**	**0.288**	**0.500**
$D_{\min}$	**0.003**	**0.004**	**0.023**	**0.005**	**0.020**	**0.016**	**0.027**	**0.039**

We can see that the mean complex tidal elevation differences of every constituent are smaller than 0.5 cm for both areas. Most of the maximum differences are smaller than 0.5 cm while most of the minimum differences are smaller than 0.05 cm. The comparison results indicate that the estimations by these two methods are consistent with each other. Hence the spectra

estimated by least-squares spectral analysis truly reflect the power distribution of the tidal signal. In this thesis, least-squares spectral analysis is used to analyze the residual sea surface measurements from satellite altimetry and tide gauge data to make clear the composition of the tidal signal. Based on its results, we can determine the constituents whose contributions to the residual measurements are relative large. After that, we estimate the amplitudes and the phases of these constituents by harmonic analysis, and then remove their effects from the residual sea surface measurements.

4.4 Residual ocean tide estimates from T/P and Jason1 data in the West coast of Canada

The data pool for the west coast of Canada is composed of the SLA time series that are located in the area enclosed by the coastline and the ground track of data pass 28 (shown in Figure 4.9). The distance between the altimetry tracks and the coastline varies from 26 km to 188 km.

Firstly, least-squares spectral analysis is applied to the SLA time series at 9 crossover points from T/P and Jason-1. Spectral summation of 52 constituents at every location is plotted in Figure 4.10. Figure 4.10 also shows the water bathymetry. The maximum spectral summation, reaching 92.57%, is obtained at the crossover of passes 223 and 104. This is an extremely high value indicating that almost the whole signal is the residual ocean tide. The tide correction from Webtide-NP works very badly at this point, which may be because it has the second smallest bathymetry (450 m) and the shortest distance to the coast line (26 km) among the 9 crossover points. The effects of the shallow water and the coast line at this point are very large resulting in very complex dynamics of the ocean tide. Webtide-NP fails to capture such complex tide signals. The spectral summations of the crossover of 121 and 28, 147 and 104, as well as 197

and 104 are nearly the same. These points have almost the same distances to the coast line, whereas their bathymetries are -2500m, -281m and -531m, respectively.

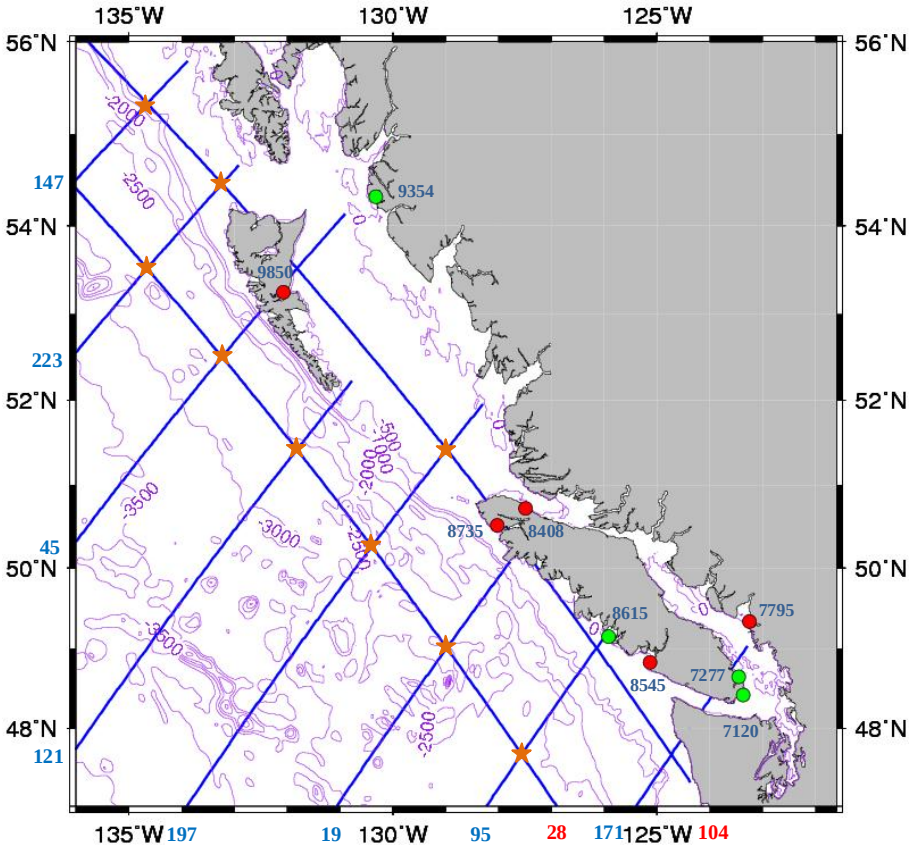

Figure 4.9: Locations of satellite altimetry ground tracks and tide gauge sites in the west coast of Canada. Blue lines are the ground tracks of T/P (Jason-1). The associated pass numbers are plotted the frame in blue for the ascending passes and in red for the descending passes. Circles indicate the locations of tide gauge stations. A green circle means the tidal prediction from Webtide-NP is valid whereas a red circle means no tide estimates came from Webtide-NP. Orange five-pointed stars indicate the position of the crossover points applying the spectral analysis.

The analysis results at these crossover points indicate that the SLA data contain very large residual ocean tides in this coastal area. The resulting a preliminary conclusion is that it is required to estimate the residual ocean tides at each point.

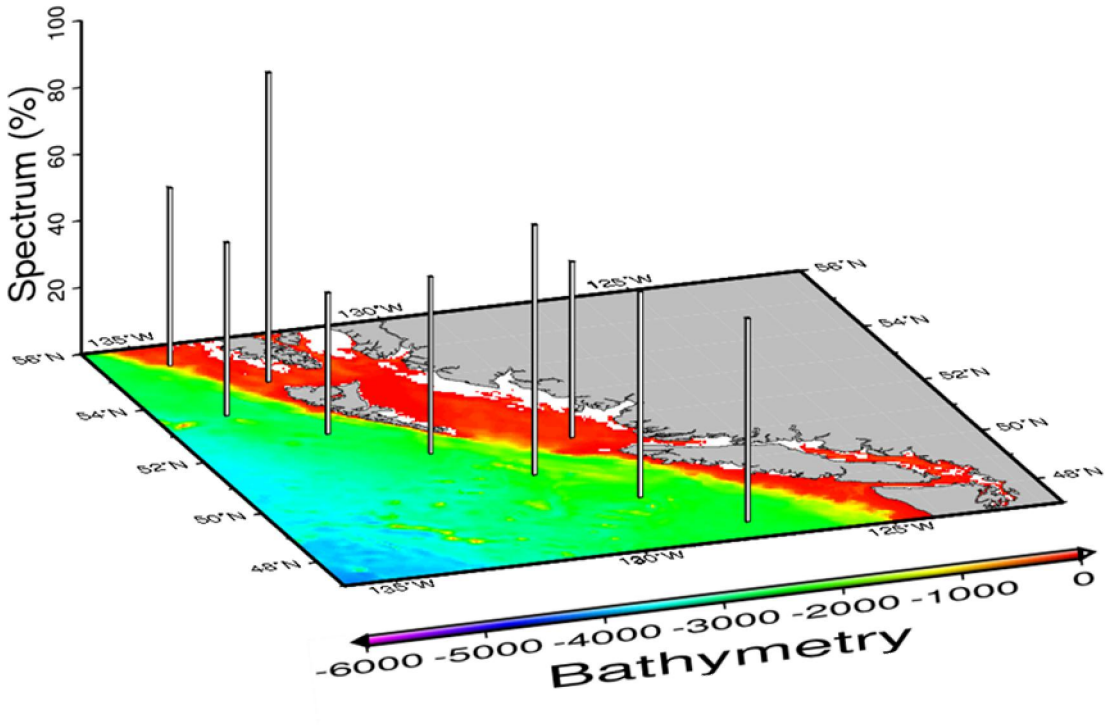

Figure 4.10: Spectral summations of 52 constituents at crossover points in the west coast of Canada. The bathymetry data plotted are from the global model DNSC08.

Then the least-squares spectral analysis is applied on 587 along-track time series of T/P and Jason-1 SLA by submitting the data to Equations (4.25), (4.23), and (4.27) to estimate the spectrums of 52 constituents. Table 4.9 lists the mean spectral summation over 587 spectrum results for every group of constituents. The mean spectral summation of main, minor diurnal, minor semi-diurnal, and long term constituents is about 15%, respectively. However, the shallow water constituents only account for 3.75% of the variations of the SLA time series. The total mean spectral summation of 52 constituents over 587 time series is 67%, which indicates again the requirement of analyzing the residual ocean tides.

Table 4.9 Mean spectral summation for every group of constituents over 587 altimetry time series in the west coast of Canada

	Residual Main constituents*	Long terms constituents	Shallow water constituents	Minor diurnal constituents	Minor semi-diurnal constituents	All constituents
Mean Spectral Summation (%)	14.79	15.43	3.75	15.96	17.67	67.61
Standard deviation (%)	4.76	5.41	1.31	2.69	4.18	7.08

Main constituents* include Q_1, O_1, P_1, K_1, N_2, M_2, S_2 **and** K_2,

Now let us look into the spectrums from individual time series. Figure 4.11 plots the spectral lines for a selected time series. From the figure, we can see that, most of the residual tidal power concentrates at the diurnal and semi-diurnal constituents, and there is also a peak at the long terms constituents. However, the power from the third diurnal to eighth diurnal constituents is very small. The three constituents that contribute to the spectrum over 7%, are ν_2, M_2 and SA. After removing the residual ocean tides of 52 constituents from the raw SLA time series, their variation decreases from ±20 cm to ±10cm (shown in Figure 4.12).

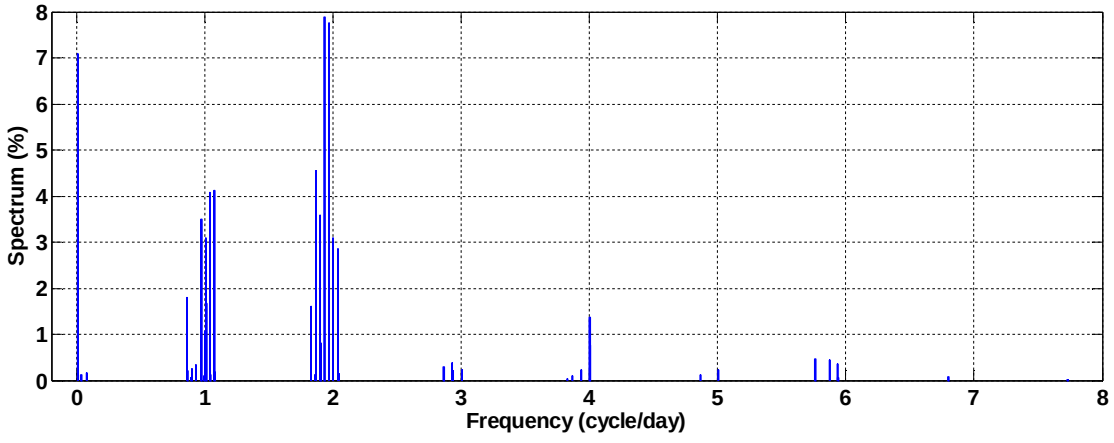

Figure 4.11: Spectral lines of 52 tidal constituents from the time series at the location closest to the coastline on the ground track of data pass 19.

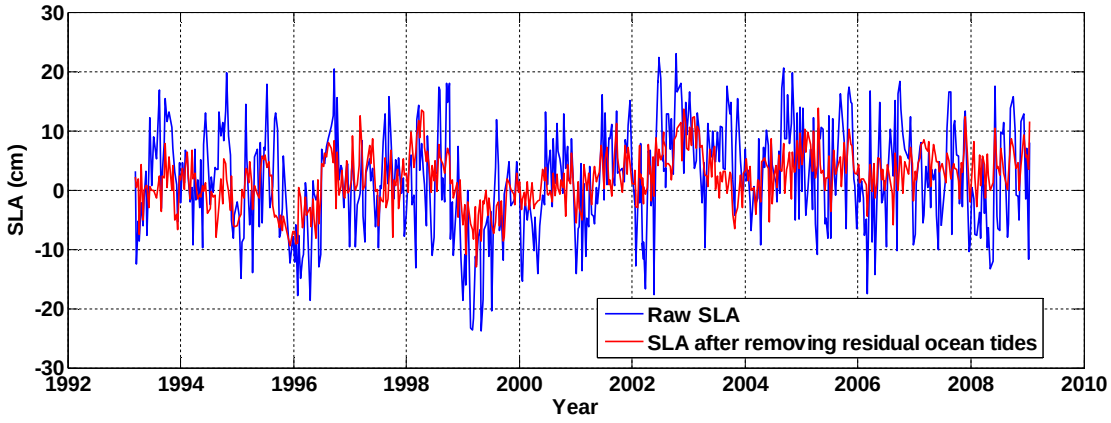

Figure 4.12: Raw SLA whose spectral lines are plotted in Figure 4.11: Spectral lines of 52 tidal constituents from the time series at the location closest to the coastline on the ground track of data pass 19. (the blue line) and SLA after corrected for the residual ocean tides (the red line).

Based on the least-squares spectral analysis results, we obtain a final conclusion that the residual ocean tides are too large to ignore and removing them can greatly reduce the variations of the SLA time series. Then we used harmonic analysis to estimate the amplitudes and phase lags for 52 tidal constituents at each point along the tracks. The tidal corrections were calculated by Equation (4.19) from the amplitudes and phases of 52 constituents and removed from the raw SLA time series. The variations of SLA reduce from 9.6 cm to 5.2 cm on average over the entire region.

4.5 Residual ocean tide estimates by T/P and Jason1 data in the East coast of Canada

The data pool for the east coast of Canada is composed of the SLA time series which are located in the area enclosed by the coastline and the ground tracks of passes 39, 124, 200, and 217 (shown in Figure 4.13). The distance between the altimetry tracks and the coastline varies from 6 km to 270 km.

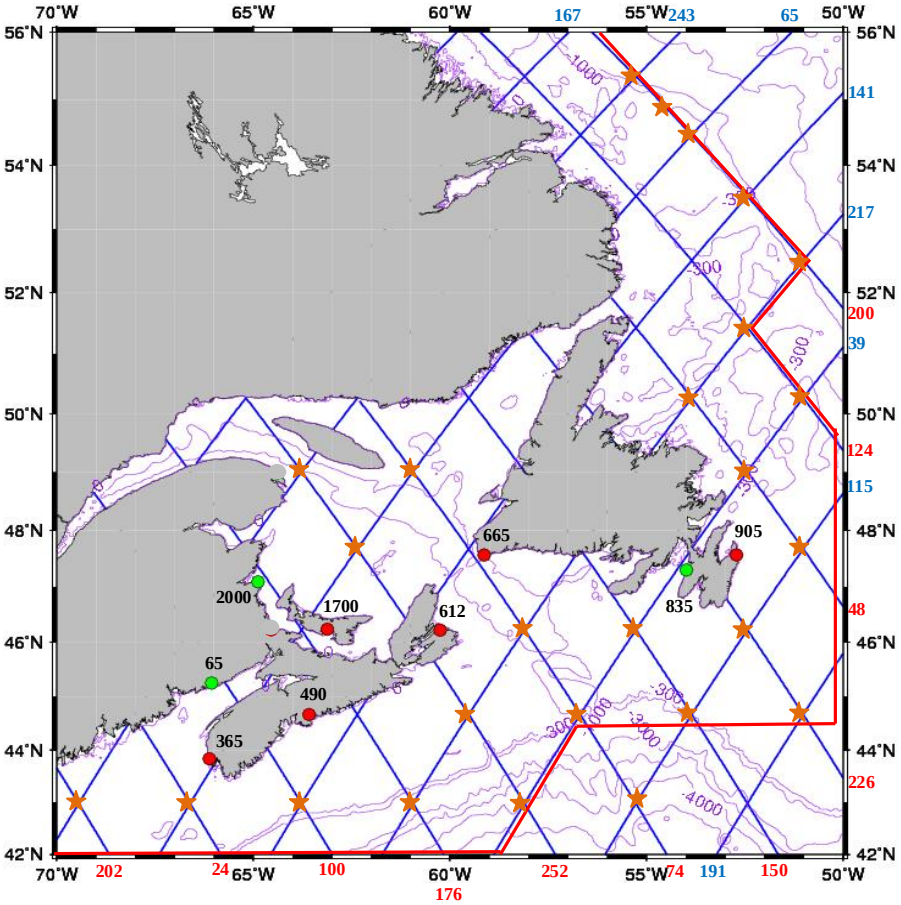

Figure 4.13: Locations of satellite altimetry ground tracks and tide gauge sites in the east coast of Canada. Blue lines are the ground tracks of T/P (Jason-1). The associating pass numbers are plotted in the frame in blue for the ascending passes and in red for the descending passes. Circles indicate the locations of tide gauge stations. A green circle means the tidal prediction from Webtide-NA is valid whereas the red circle means no tide estimates come from Webtide-NA, Orange five-pointed stars indicate the position of the crossover points applying the spectral analysis

The same process was applied as what we do for the west coast of Canada. Firstly, least-squares spectral analysis is applied to SLA time series at 25 crossover points from T/P and Jason-1. The spectral summation of 52 constituents at every location is plotted in Figure 4.14 which also shows the water bathymetry. Almost all the crossover points are located in the area with bathymetry less than 500 m. In contrast to the spectrum distribution in the west coast of Canada,

the spectral summations of 52 constituents at every crossover point are close with each other, with the residual ocean tides around 50% of the entire sea level anomalies.

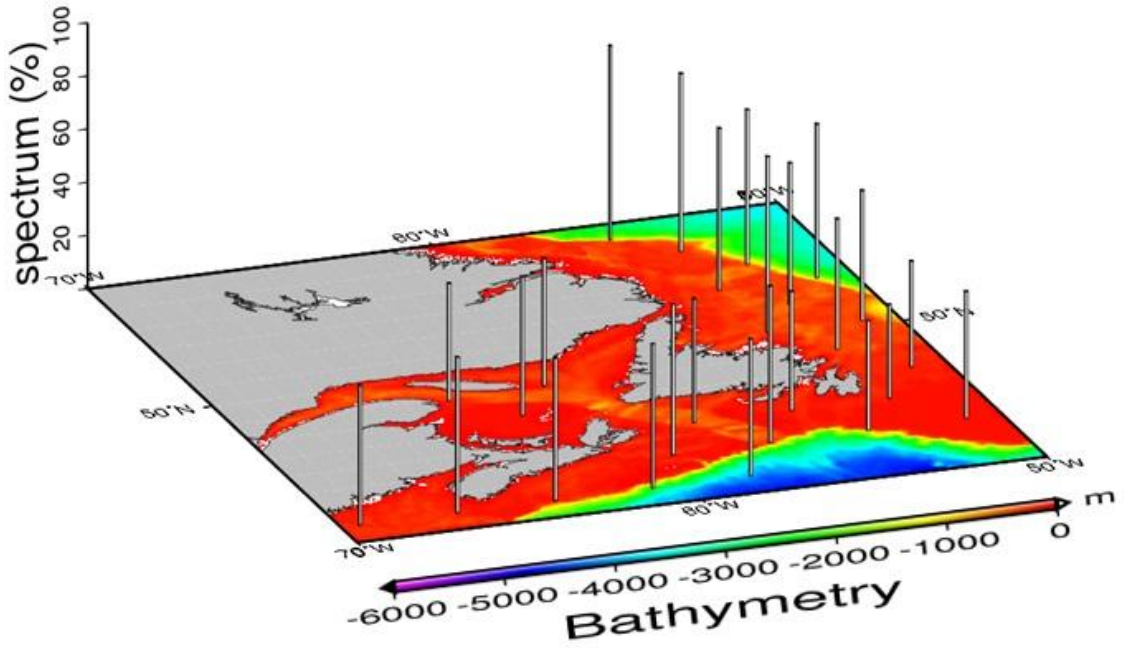

Figure 4.14: Spectral summations of 52 constituents of crossover points in the east coast of Canada. The bathymetry data plotted are from the global model DNSC08.

The analysis results at crossover points indicate that the SLA data contain very large residual ocean tides in the coastal area, which motivate us to estimate the residual ocean tides. The least-squares spectral analysis is applied to 1582 along-track time series of T/P and Jason-1 SLA to estimate the spectrums of the 52 constituents. Table 4.10 lists the mean spectral summation over 1582 time series for every group of constituents. The group of residual main constituents has the maximum mean spectral summation up to 19.96%, which is larger than that in the west coast of Canada. That is because Webtide-NA is composed of O_1, K_1, N_2, M_2, and S_2, but Webtide-NP has three more constituents. The long term constituents account for 12.58% of the variations of the SLA time series. More power concentrates at the shallow water constituents than that in

the west coast of Canada. The mean spectral summation of total constituents over 1582 time series is 51.78%. It indicates that half of the variations of the SLA time series are due to residual ocean tides.

Table 4.10 Mean spectral summation for every group of constituents

	Residual Main constituents	Long terms constituents	Shallow water constituents	Minor diurnal constituents	Minor semi-diurnal constituents	Total constituents
Mean spectral summation (%)	**19.96**	**12.58**	**6.07**	**3.71**	**9.46**	**51.78**
Standard deviation (%)	**6.53**	**6.73**	**3.38**	**1.74**	**6.57**	**7.33**

Main constituents* include O_1, K_1, N_2, M_2, **and** S_2

Figure 4.15 plots the spectral lines from the time series at data pass 176. The total spectrum is equal to 50.31%. The constituent *SA* has the maximum spectrum of over 16%. Another peak appears at the constituent M_4. Diurnal and semi-diurnal constituents also have obvious spectral lines. After removing the residual ocean tides from the raw SLA time series, the variation decreases from ±20 cm to ±10cm (shown in Figure 4.16).

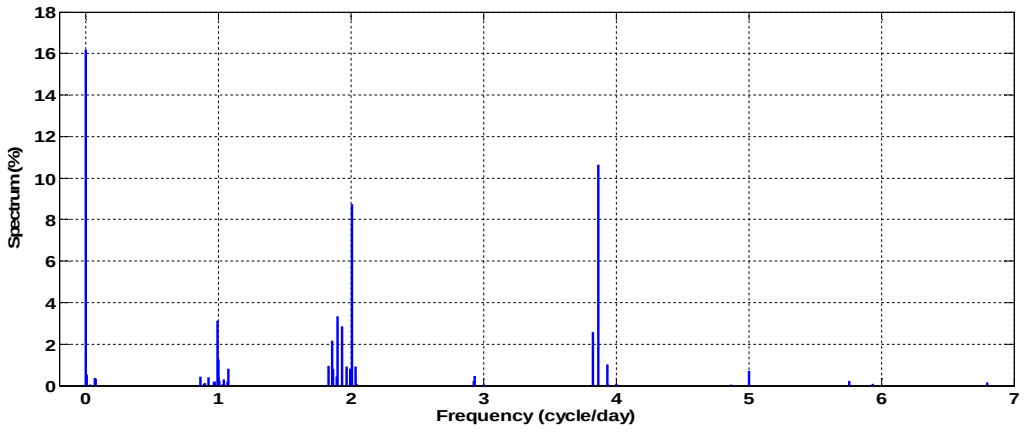

Figure 4.15: Spectral lines of 52 tidal constituents from the time series at the data pass 176.

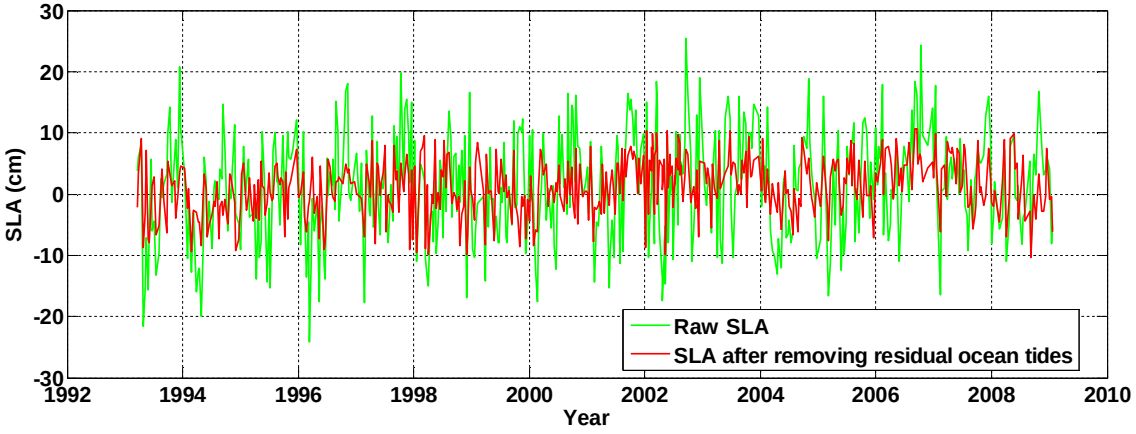

Figure 4.16: Raw SLA whose spectral lines are plotted in Figure 4.15 (the green line) and SLA after corrected for the residual ocean tides (the red line).

Based on the least-squares spectral analysis results, we find again that residual ocean tides cannot be ignored. The amplitudes and phase lags for 52 tidal constituents are estimated by the traditional harmonic analysis for every dataset. Then the tidal corrections are calculated by Equation (4.19) and removed from the raw SLA time series. The variations of SLA reduce from 8.7 cm to 5.1 cm on average over the entire region.

4.6 Summary

There are three contributions in this chapter.

(1) We assessed the accuracy of the local tide model namely Webtide. Webtide is considered the best current local model in the Pacific coast of Canada (Foreman, personal communication). In order to further verify it and simultaneously assess the accuracy of Webtide in the Atlantic coast of Canada, we compared the harmonics of major astronomical constituents from Webtide, FES2004, ETO11a and DTU10 with the harmonic estimates of the same constituents from coastal tide gauge data. We found the

Webtide model in the Pacific coast of Canada performs better than these three global models and have comparable accuracy in the Atlantic coast of Canada. The conclusions support our choice of using the Webtide model to correct T/P and Jason-1 data for the ocean tides in the pre-processing steps.

(2) We used least-squares spectral analysis to detect the magnitude of residual ocean tides in altimetry SLA time series. Spectra results indicate that in the west coast of Canada, average 67% variations of SLA time series are due to the residual ocean tides, and value is 51% in the east coast of Canada. The long term, residual main astronomical and minor astronomical constituents are the largest three groups. Under the 10-day sampling interval of T/P and Jason-1, the diurnal and semi-diurnal constituents have been aliased to signals with periods close to semi-annual or annual periods. They will affect the estimate of the rate uncertainty. Spectra results tell us it is truly necessary to analyze the residual ocean tides and remove them.

(3) We used harmonic method to estimate the amplitudes and phases of 52 selected constituents. After than we calculated the residual ocean tides by substituting the harmonics of these 52 constituents to Equation (4.19) and remove them from altimetry SLA time series. The reduction of residual ocean tides achieves great success. The variations of SLA reduce from 9.6 cm to 5.2 cm on average over the entire coastal area of west Canada. And in the east coast of Canada, the variations of SLA reduce from 8.7 to 5.1 cm on average.

Chapter Five: Absolute Sea Level and its variations

5.1 Introduction

In geodesy, Mean Sea Level (MSL) height is usually defined as the local height of the global Mean Sea Surface (MSS) above a 'level' reference surface, or datum, called the geoid. MSL (the local height of the MSS above the geoid) is a complicated quantity, which depends not only on the volume of water in the oceans, and the shape of the ocean basins, but also on the Earth's gravitational field and rotation rate (which determine the shape of the geoid), and on patterns of currents within the oceans.

Satellite altimeters provide the measurements of absolute sea level relative to a precise reference frame realized through the satellite-tracking stations whose origin coincides with the Earth's center of mass. In this chapter, SLA time series from T/P and Jason-1 are processed under the calculation strategies defined in Chapter Three to determine the rate of ASL change. Firstly, annual, seasonal and regional common mode corrections are applied to the MMSL time series averaged from 10-day altimetry data. Because the IB corrections have a large effect on the rate estimate, so they are also discussed in this Chapter. Secondly, the measurement noise model is detected by Power Spectral Density and MLE analysis using the post-fit residuals. Then the rate of ASL change at every altimetry site is determined by fitting the corrected MMSL time series to the linear regression model using the selected noise model under the least-squares criterion. The results are shown in the last section.

5.2 Satellite altimetry data corrections

10-day sampling T/P and Jason-1 data from March 1993 to December 2008 have been corrected for instrumental, propagation path delay and geophysical errors, and biases, which are described in Chapter two. Then these SLA time series are averaged to MMSL time series, which are the observations of the linear regression model. Two additional corrections: annual seasonal variations and regional common mode corrections, which are discussed in Chapter Three, are applied to MMSL. In addition, the IB correction applied to the 10-day time series has very large effect on the rate estimate, so it will be presented in this Chapter.

The number of altimetry time series is much higher than that of tide gauge time series. It is impossible and unnecessary to show all of them. 3 altimetry time series in the west coast of Canada and 3 in the east coast are used as examples, whose locations are listed in Table 5.1, Figure 5.1 and Figure 5.2. They are chosen because they are very close to the coastline.

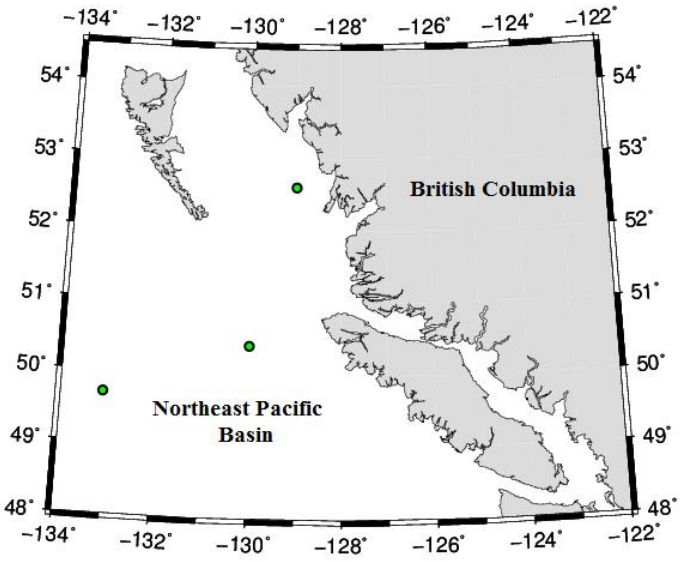

Figure 5.1: Position of example altimetry time series in the west coast of Canada

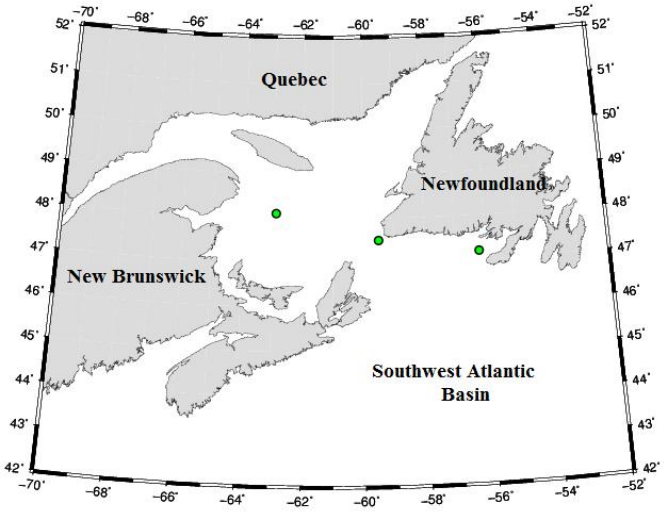

Figure 5.2: Position of example altimetry time series in the east coast of Canada

Table 5.1 Examples of altimetry time series

ID	Longitude (W°)	Latitude (N°)	ID	Longitude (W°)	Latitude (N°)
Pacific Coast of Canada			Atlantic Coast of Canada		
SA-45-57	133.1	49.7	SA-252-32	62.9	48.1
SA-104-70	130.0	50.4	SA-74-61	59.5	47.5
SA-197-144	129.0	52.6	SA-150-33	56.2	47.2

5.2.1 Inverse barometer corrections

The IB correction for satellite altimetry data is calculated by Equation (2.8) in Chapter Two using the nadir surface pressure determined from the model assimilated weather data from ECMWF (Benada, 1997; AVISO and JPL, 2008). The uncertainty of the ECMWF atmospheric pressure products is somewhat dependent on location. Typical errors vary from 1 mbar in the northern Atlantic Ocean to a few mbars in the southern Pacific Ocean. A 1-mbar error in the pressure translates into a 10 mm error in the computation of the IB correction. The IB correction for every chosen altimetry time series is shown in Figure 5.3. A negative linear trend is obvious

at every IB time series. The average linear trend of the IB correction for the west coast of Canada is -2.7 mm/year and the value is -2.1 mm/year for the east. It is of the same magnitude as the sea level trend. In order to avoid such bias of the sea level trend estimate, the IB correction is detrended before being applied to the 10-day SLA time series.

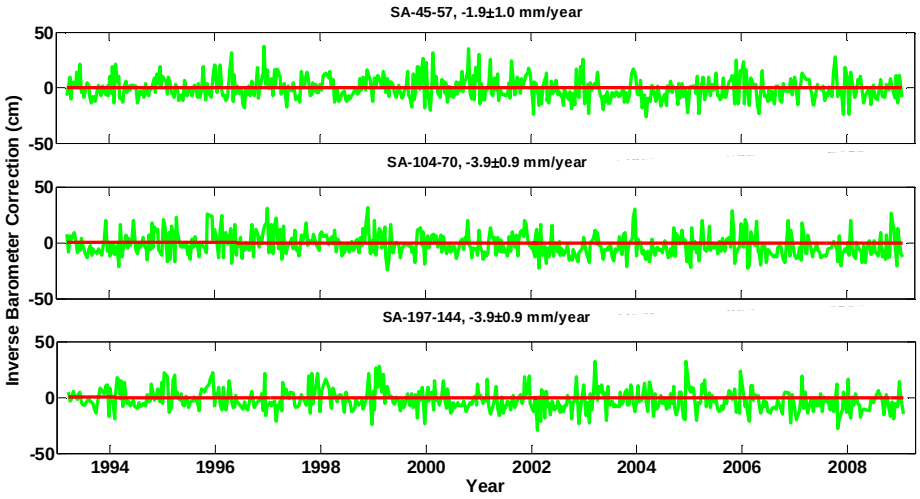

Figure 5.3: Inverse Barometer Correction for the chosen satellite altimetry time series in the west coast of Canada. The green line is the inverse barometer time series and the red line is the associated linear trend.

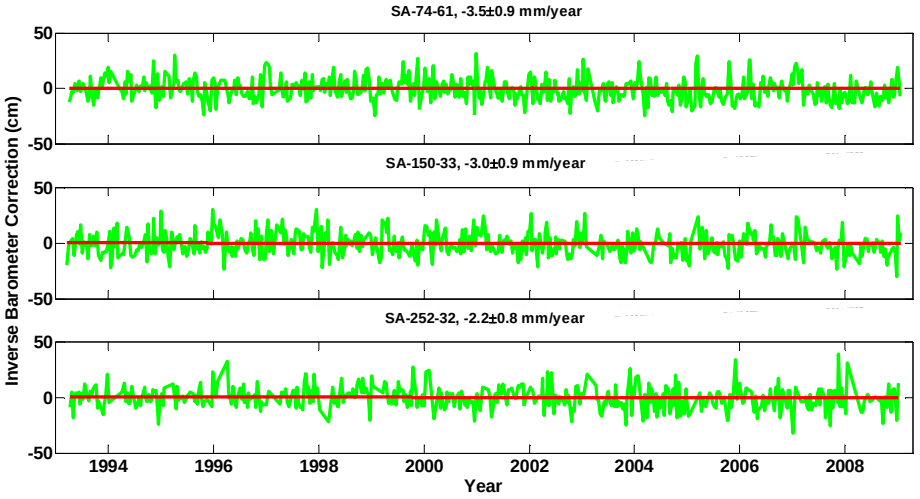

Figure 5.4: Continued. Inverse Barometer Correction for the chosen satellite altimetry time series in the east coast of Canada.

5.2.2 Annual seasonal variation correction

As stated in Chapter Three, the first correction to monthly altimetry time series is the annual seasonal variation correction which is used to remove annual or semi-annual signals. Before using the empirical method to estimate this correction, it is better to look into the altimetry time series to see if there exist annual seasonal variations. The spectrum of the altimetry time series is plotted by the periodogram analysis. The detrended MMSL and associated power spectral densities of the time series shown in Table 5.1 are plotted in Figure 5.5 and Figure 5.6. Annual and seasonal variations are not obvious at these MMSL time series of satellite altimetry except at SA-104-70 where the time series has a large seasonal signal with a period of 6 months. The dominant signals vary in different altimetry time series. The signals with period shorter than 1 year (e.g., the peaks at frequency 0.35 cycles/month, which are shown in Figure 5.5 and Figure 5.6) can be successfully removed by the annual seasonal variation correction. But for the signals with period longer than 1 year, e.g., 1.5 years or 5 years, the above correction cannot fully remove their effects on sea level trend estimate.

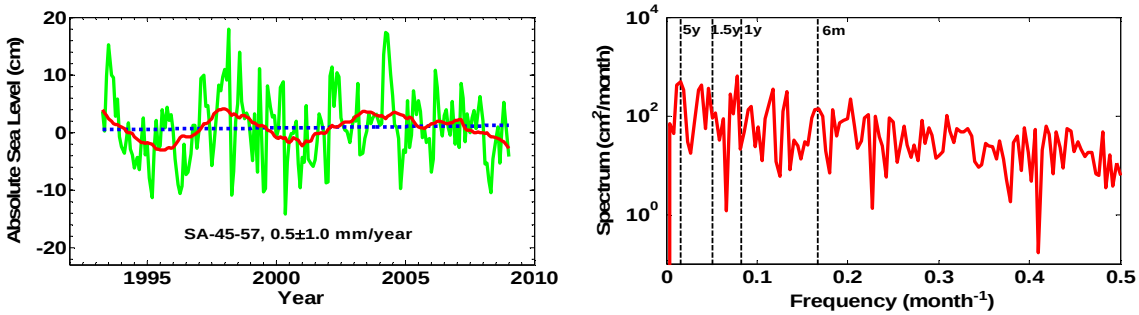

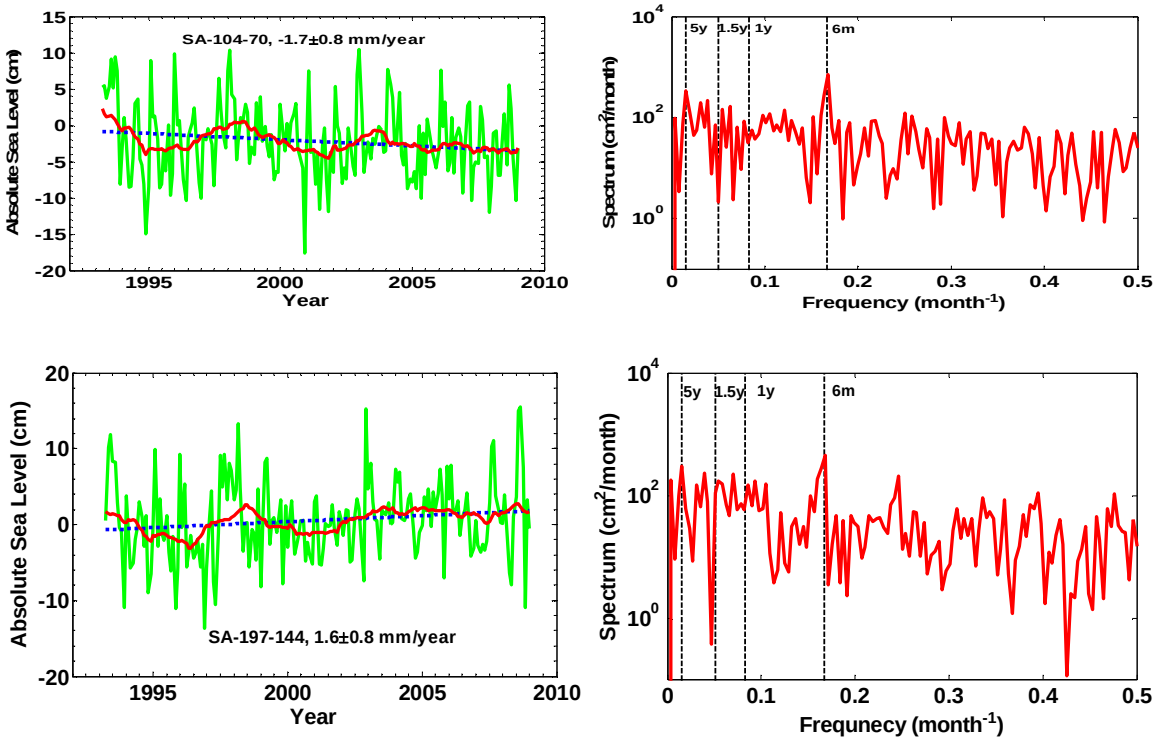

Figure 5.5: Monthly mean sea level data for satellite altimetry time series in the west coast of Canada. In the left figure the green line shows the raw MMSL, the red line shows 1-year moving averages and the blue line shows the linear ASL trend. The right figure shows the power spectral of detrended MMSL data.

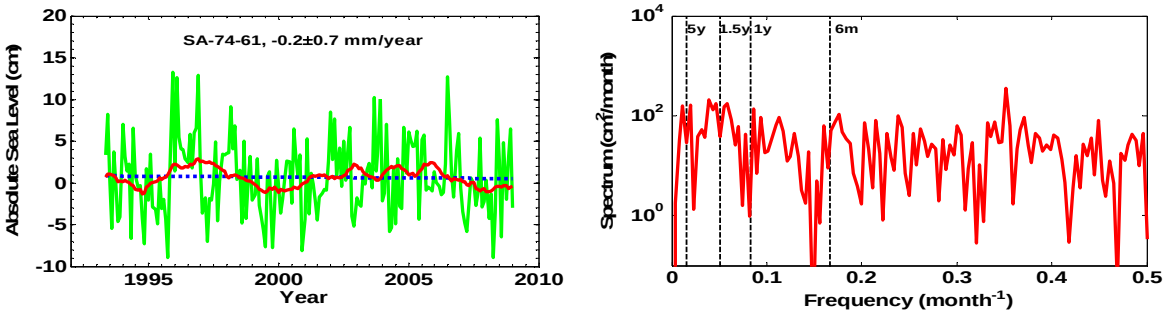

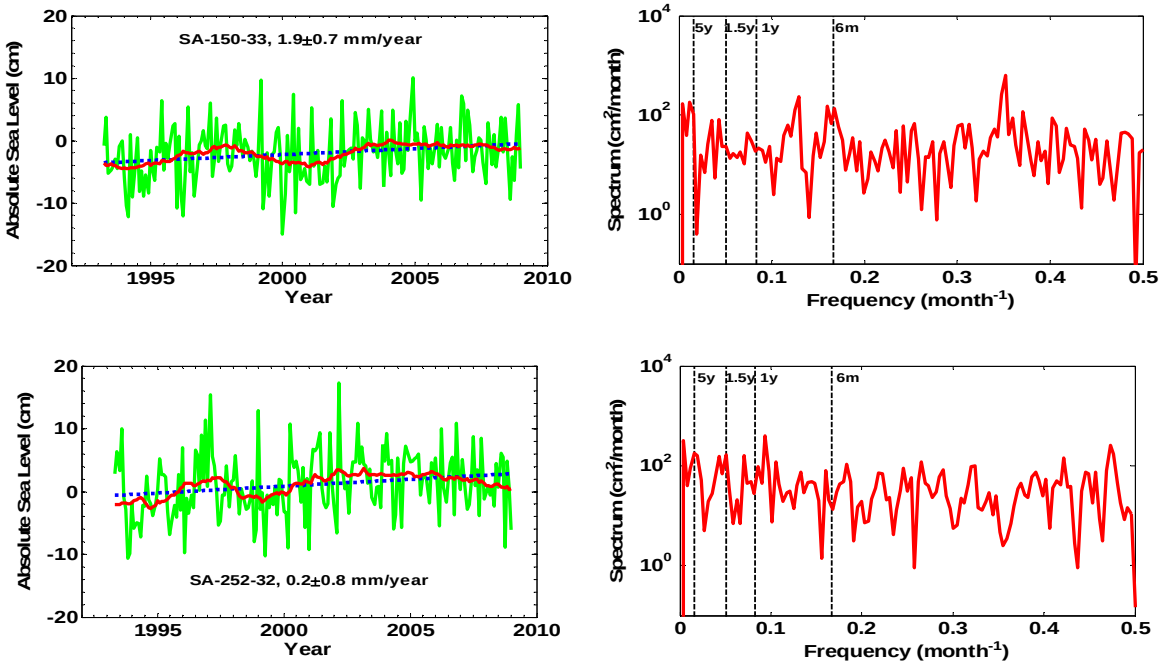

Figure 5.6 Monthly mean sea level data for satellite altimetry time series in the east coast of Canada. In the left figure the green line shows the raw MMSL, the red line shows 1-year moving averages and the blue line shows the linear ASL trend. The right figure shows the power spectral of detrended MMSL data.

5.2.3 Regional common mode correction

A high correlation can be found between altimetry MMSL time series in both west and east coast of Canada, which is caused by large-scale (interannual) oceanographic variations. This correlation is illustrated by two examples shown in Figure 5.7 and Figure 5.8. For the calculation of correlation coefficient, MMSL time series are first corrected for the IB correction and annual seasonal effects and detrended. Then a correlation coefficient is determined between the residuals for each site on each ground track and the residuals for SA-104-70. The correlation coefficients between the residuals of SA-74-61 and of other points are also calculated. The correlation coefficients between SA-104-70 and the other measuring points which are less than

41 km away is greater than 0.8. The maximum distance between SA-74-61 and the other measuring point, whose correlation coefficient is greater than 0.8 is 48 km.

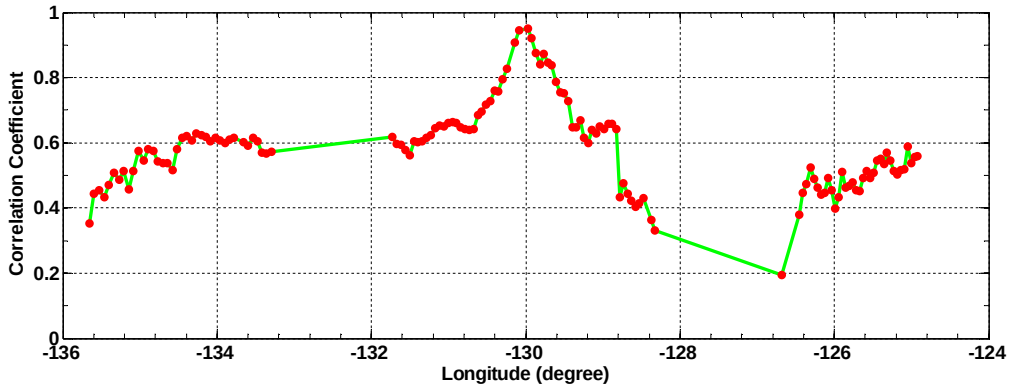

Figure 5.7: Correlation coefficients between time series on pass 104 and on SA-104-70.

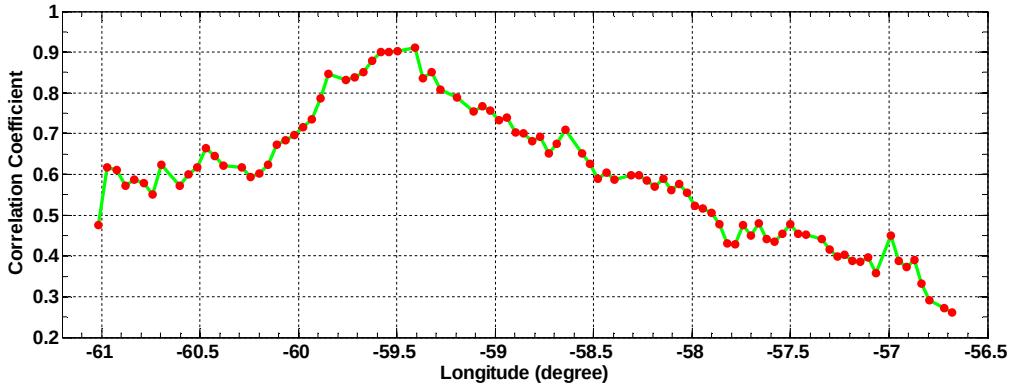

Figure 5.8: Correlation coefficients between time series on pass 74 and on SA-74-61.

The common mode correction is used to remove the regional sea level variations that are common to all sites. After applying the regional common mode corrections, correlations between nearby time series are greatly decreased. The standard procedure to calculate this correction is discussed in Chapter three in detail. The significant thing for the calculation is the choice of the sites forming a coherent region. For an individual site, its corresponding coherent site is determined by the correlation coefficient between them. The choice of the threshold value

of correlation coefficient is an iterative process based on the coherence of MMSL series and on the length restrictions versus the effectiveness of the common mode correction. The threshold value of correlation coefficient is chosen as 0.8.

5.2.4 Outlier detection

After correcting the altimetry MMSL time series for inverse barometer, annual seasonal and regional common mode variations, we need to detect and remove the outliers to obtain the final clean data set. Outliers are detected using the algorithm based on the median and IQR statistics, which was introduced in Chapter three. The detection results for the example altimetry time series are listed in Table 5.2. 0.54% and 0.88% of the MMSL time series in the west and east coast of Canada respectively are discarded after blunder detection.

Table 5.2 Number of monthly mean sea level time series, number of blunders and the blunder rate for the example time series

Data Point	Number of MMSL	Number of blunders	Blunder rate (%)	Data Point	Number of MMSL	Number of blunders	Blunder rate (%)
SA-45-57	190	2	1.05	SA-252-32	190	3	1.58
SA-104-70	190	0	0.00	SA-74-61	190	2	1.05
SA-197-144	190	2	1.05	SA-150-33	190	4	2.11

5.2.5 Corrected altimetry time series

The raw altimetry MMSL time series is cleaned by applying the inverse barometer, annual seasonal and regional common mode corrections and the outlier detection to obtain the final time series used for estimating the sea level trend. The cleaned and detrended time series and associated power spectrum for each example altimetry data are shown in Figure 5.9 and Figure 5.10. The power spectrum is plotted by the periodograms analysis. The linear trend of the cleaned altimetry time series is estimated by the linear regression analysis with unit weight

matrix. In the comparison with Figure 5.5 and Figure 5.6, we can find that after applying the above two corrections to the example time series in the west coast of Canada, the data variance reduces by 69% and for the series in the east coast of Canada, the data variance reduces by 71%. For all altimetry data in the west or east coast, the value is 70% or 68%, respectively. The spectrum shown in the right figure of Figure 5.9 or Figure 5.10 exhibits much less variation compared with that of the raw data shown in the right figure of Figure 5.5 or Figure 5.6. In addition, the strong peaks in amplitude of the raw MMSL power spectra corresponding to periods less than 1 year (e.g., 6-month peak at SA-45-57, 3-month peak at SA-74-61 and SA-150-33) disappear in the corrected MMSL power spectra. And in the corrected MMSL power spectra, long term signals become dominant. The trend uncertainties from cleaned time series are much smaller than those from raw data, which indicates the efficiency of the annual seasonal and regional common mode corrections.

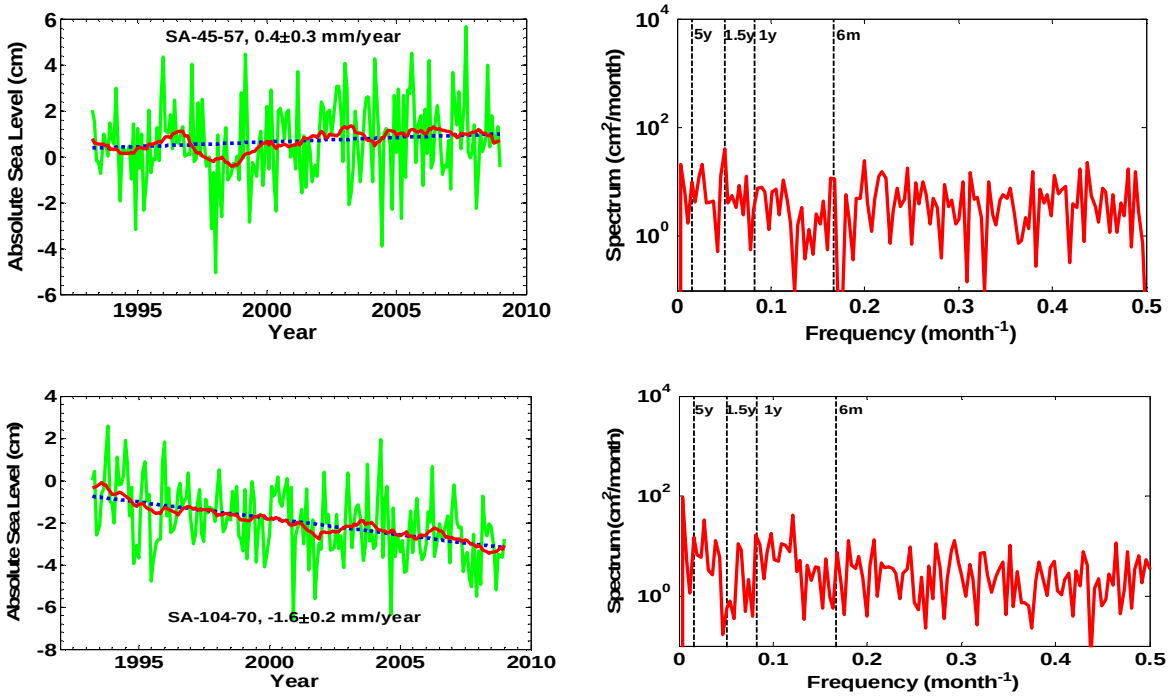

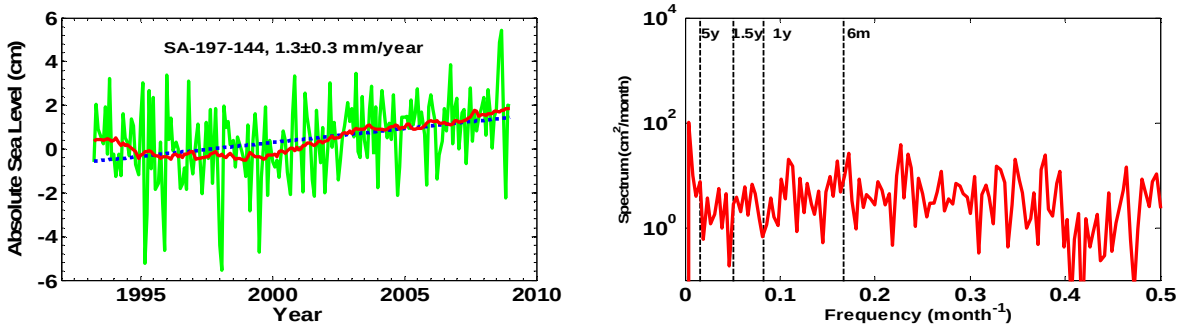

Figure 5.9: Corrected monthly mean sea level data for satellite altimetry time series in the west coast of Canada. In the left figure the green line shows the corrected MMSL, the red line shows 1-year moving averages and the blue line shows the linear ASL trend. The right figure shows the power spectral of corrected and detrended MMSL data.

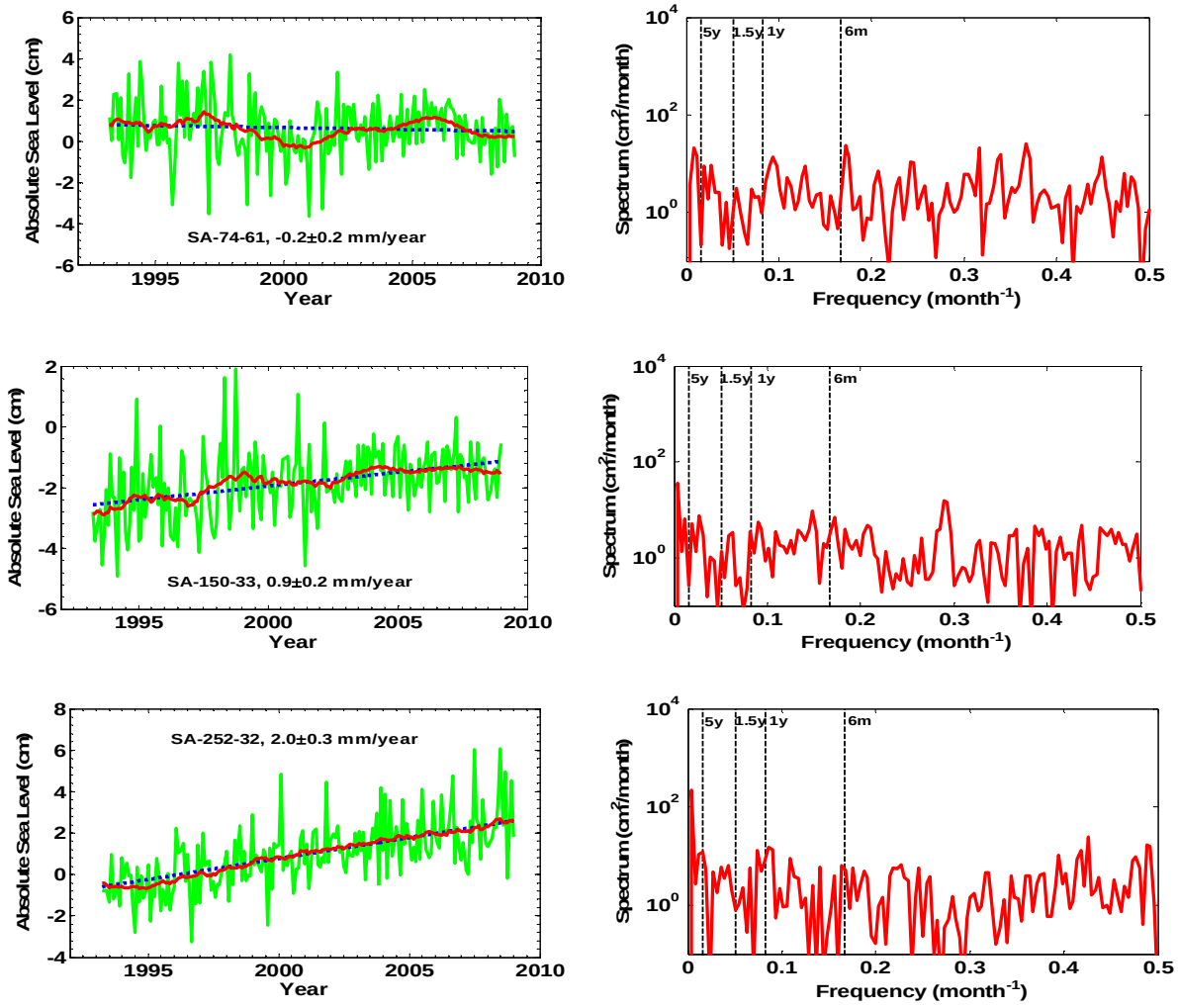

Figure 5.10: Corrected monthly mean sea level data for satellite altimetry time series in the east coast of Canada. In the left figure the green line shows the corrected MMSL, the red line shows 1-year moving averages and the blue line shows the linear ASL trend. The right figure shows the power spectral of corrected and detrended MMSL data.

5.3 Absolute sea level change

The rate of ASL and its uncertainty at each altimetry measuring point are estimated by the linear regression model

$$MMSL(t_i) = a_{ASL} t_i + b + \varepsilon_i, \tag{5.1}$$

Equation (5.1) is in the exact same form as Equation (3.1) but has the parameter a_{ASL} specific for the rate of ASL. As discussed in Chapter Three, in order to solve this model under the least-squares criterion, an appropriate noise model for MMSL should be found. Corrected altimetry MMSL time series are used with the assumption that the noise of MMSL is white with a variance of 1 cm^2 to obtain the post-fit residuals which are the "measurements" for testing the noise model.

5.3.1 Noise model testing

Power spectral density and maximum likelihood analysis, which are discussed in Chapter Three, are the two methods for testing the noise model for altimetry MMSL. The latter method can also estimate the noise amplitude.

5.3.1.1 Power spectral density analysis

The power spectra for the individual altimetry time series are calculated by analyzing the post-fit residuals using the formulas in Chapter Three and the spectra are plotted in log10-log10 scale. The power spectra for the example time series are shown in Figure 5.11 and Figure 5.12. The trends of the power spectra are approximate zero. The power is distributed almost equally to

every frequency and no obvious time-dependent noise can be found, which indicates that the noise of altimetry MMSL time series is white instead of colored noise. The power spectral density results give us a preliminary idea about on the noise model of altimetry MMSL time series. Maximum likelihood analysis will provide a further test on the noise model.

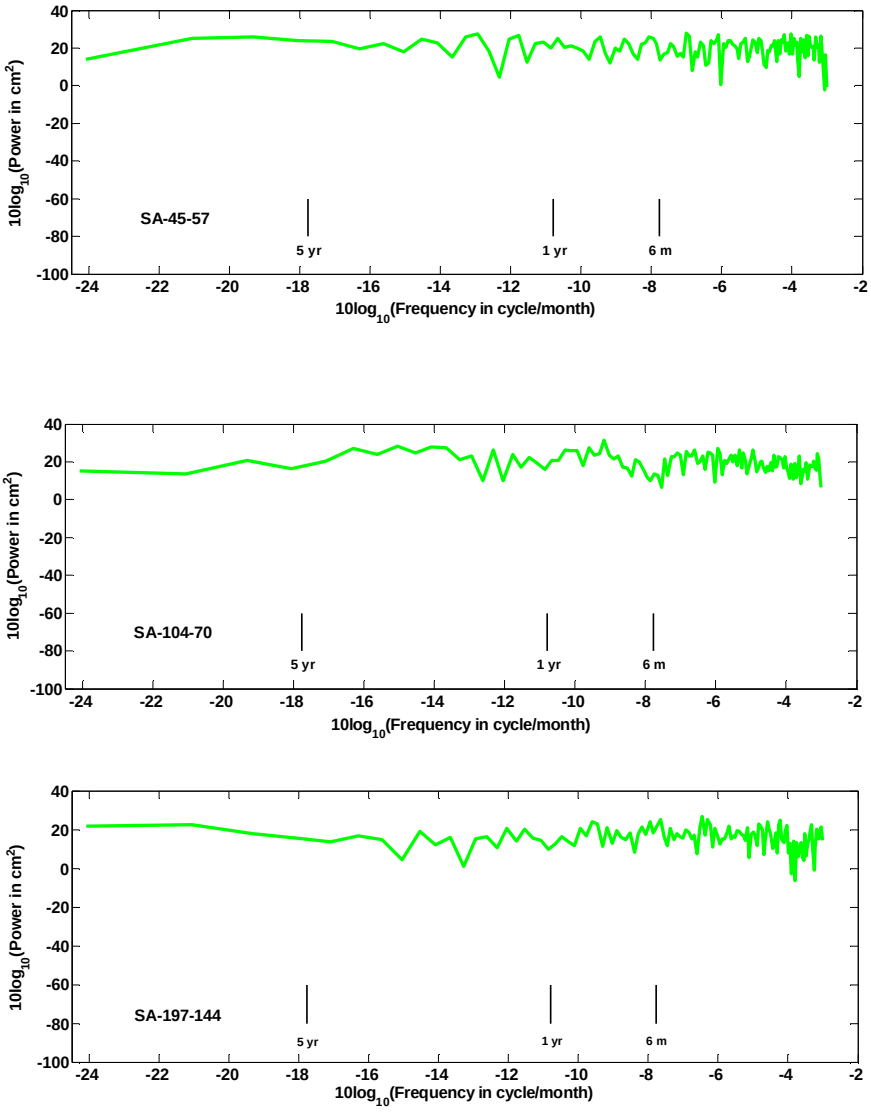

Figure 5.11: Power spectral density estimate at altimetry time series in the west coast of Canada in units of dB relative to cycle/month.

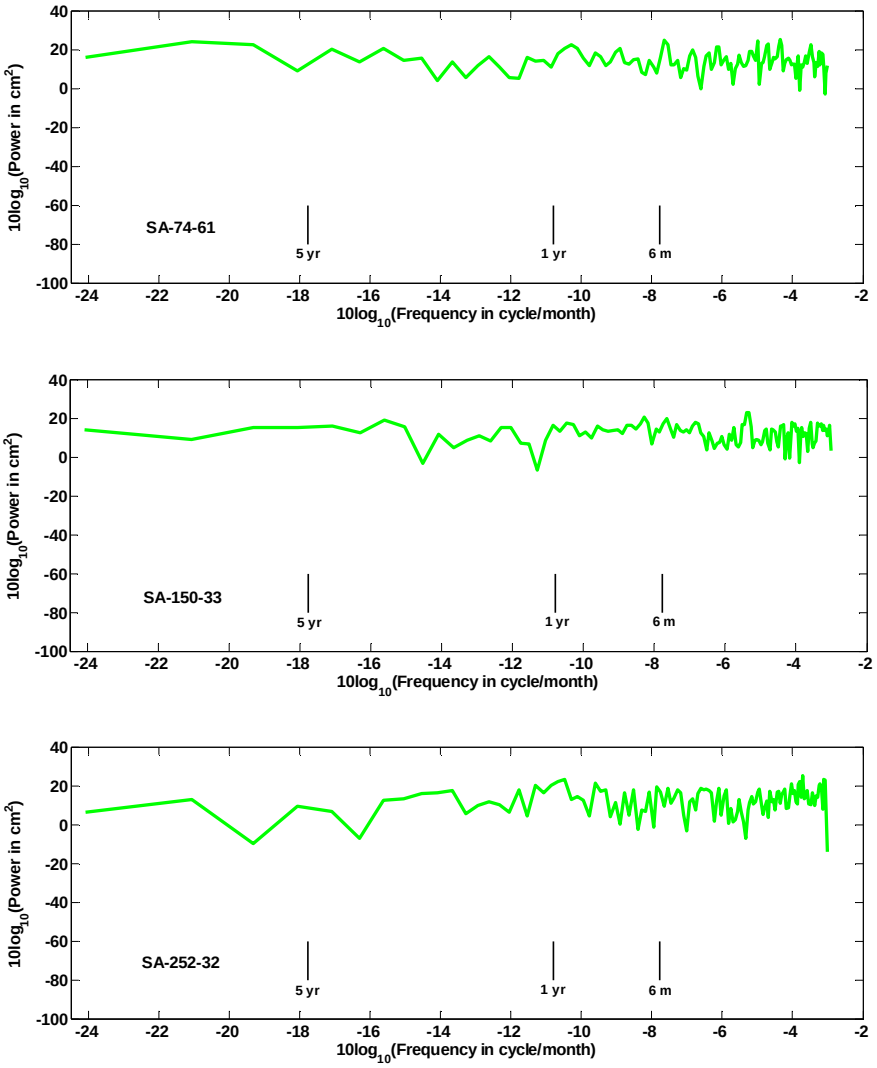

Figure 5.12: Power spectral density estimate at altimetry time series in the east coast of Canada in units of dB relative to cycle/month.

5.3.1.2 Maximum likelihood analysis

The WN, WF and WR noise models are the candidate ones for testing. As shown in Equation (3.15), the covariance of the combined noise model is the summation of the covariance of white and color noise multiplied with their associated noise amplitude, which is denoted as a for the white noise and $d_{-\kappa}$ for the color noise. d_{-1} is the amplitude of flicker noise and d_{-2} is the

amplitude of random walk noise. The values of a^2 and $d^2_{-\kappa}$ are estimated by maximizing the probability function (Equation (3.26) or Equation (3.27)) using the downhill simplex method.

Let us discuss the test results for the altimetry MMSL time series in the west coast of Canada. Assuming the noise model for MMSL to be the WF model for our altimetry data pool for the west coast of Canada which is composed of 417 time series, the MLE method finds the amplitude of flicker noise for only 40 time series successfully. Only 9.6% of the MMSL noise exhibits a time-dependent feature. a and d_{-1} estimates for these 40 altimetry time series are shown in Figure 5.13. The best fitting line indicates an amplitude ratio between d_{-1} and a of value 1.43. 18 out of 40 time series have an amplitude rate greater than 1.0.

Assuming the noise model for MMSL to be the WR model, only 11 MMSL time series among 417 in the west coast of Canada have an estimate of the amplitude of random walk noise derived by MLE. Figure 5.14 shows the estimates of a and d_{-1} for all 11 altimetry time series. The ratio between d_{-1} and a varies between 0.40 and 0.96.

Assuming the noise model to be the WN model, MLE analysis determines the white noise amplitude a for all the MMSL time series. Although the MLE method fails to estimate the flicker or random walk noise amplitude for most of the data, it is still an efficient method to estimate the white noise amplitude for each combined noise model. The comparisons between the white noise amplitude of the WN model and of each combined model are shown in Figure 5.15 and Figure 5.16 for 417 time series. The slope of the best fitting line to the white noise amplitude of the WF model and of the WN model data set is equal to 0.95, which indicates the

white noise components are well determined in both cases. The mean amplitude ratio between the white noise amplitude of the WR and of the WN model is 0.85.

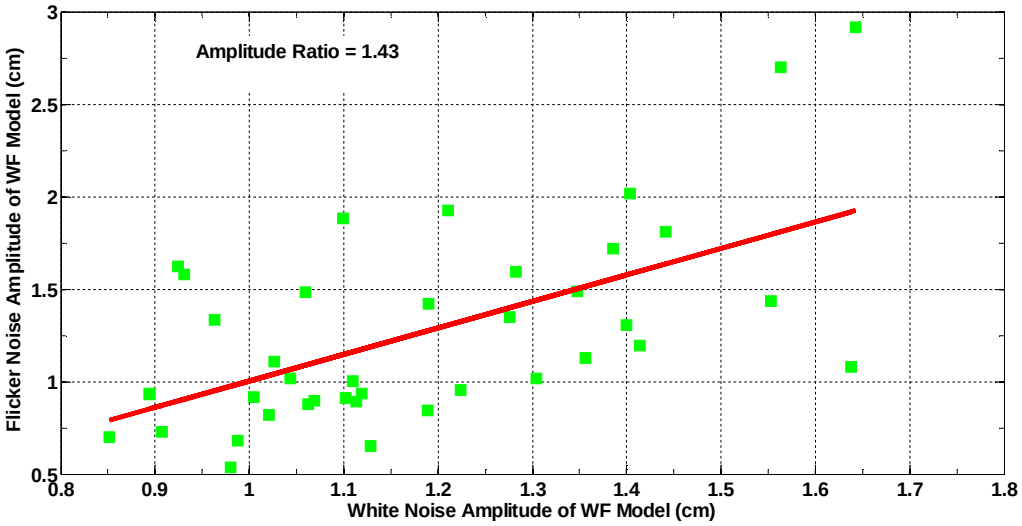

Figure 5.13: Comparison between a and d_{-1} estimates of WF model for 40 altimetry time series in the west coast of Canada.

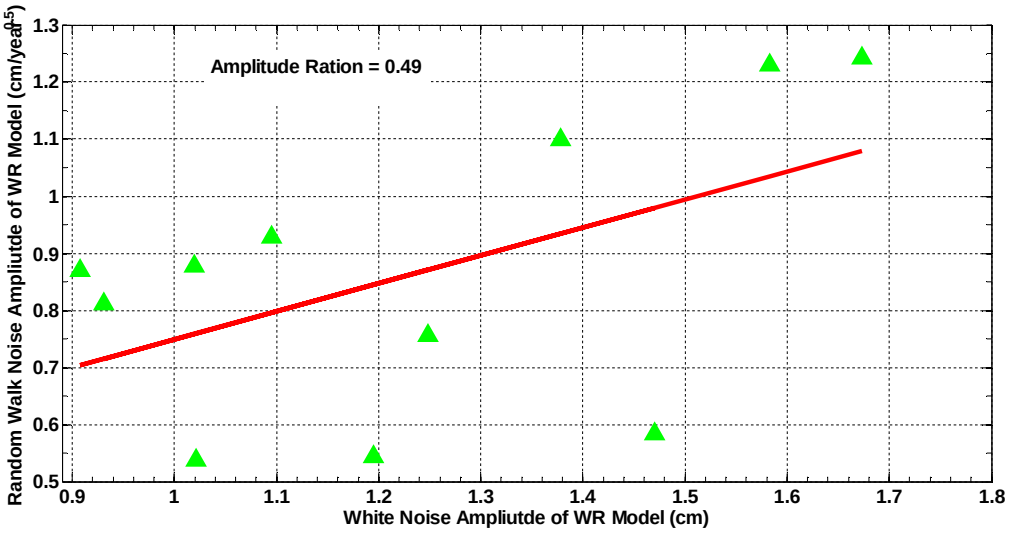

Figure 5.14: Comparison between a and d_{-2} estimates of WR model for 11 altimetry time series in the west coast of Canada.

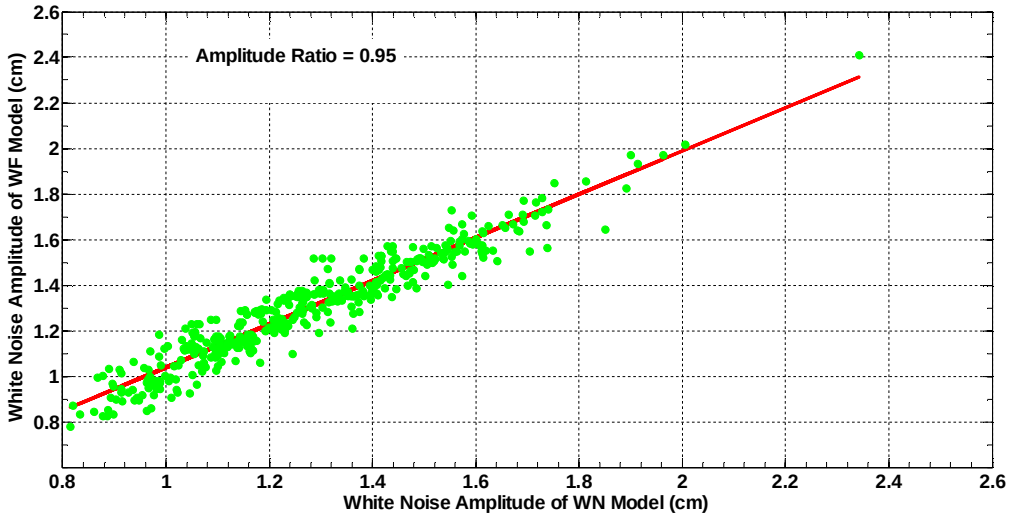

Figure 5.15: Comparison between *a* estimates of WF model and *a* estimates of WN model for 471 altimetry time series in the west coast of Canada.

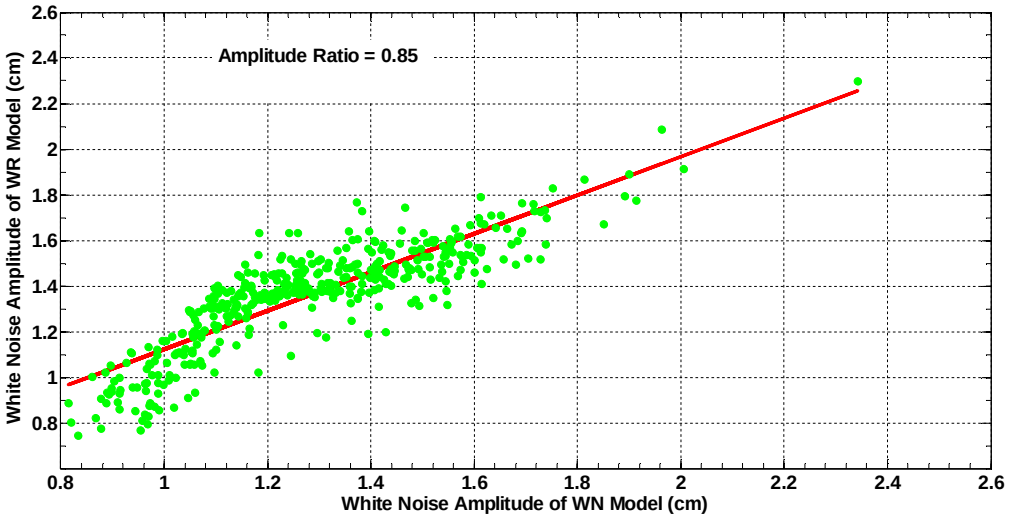

Figure 5.16: Comparison between *a* estimates of WR model and *a* estimates of WN model for 471 altimetry time series in the west coast of Canada.

In the east coast of Canada, the altimetry data pool is composed of 1110 MMSL time series. We can find the flicker noise components only in 175 time series (15.8%). Figure 5.17 shows the *a* and d_{-1} estimates for these 175 time series. The amplitude rate between d_{-1} and *a* is also

calculated, which varies from 0.40 to 1.70 with the mean value of 0.53. The amplitude ratio on 56 time series is greater than 1.0.

In the east coast of Canada, only 3.6% (40 out of 1110) of the MMSL noise exhibits the random walk noise feature. Figure 5.18 shows the estimates of d_{-2} and a for these 40 time series. The amplitude ratio between d_{-2} and a ranges from 0.29 to 0.87 and the mean value is equal to 0.43.

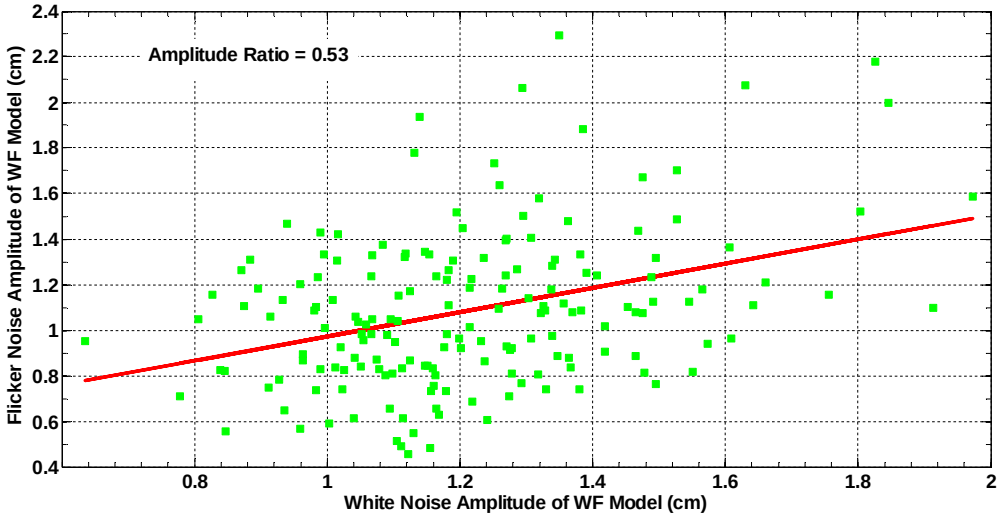

Figure 5.17: Comparison between a and d_{-1} estimates of WF model for 175 altimetry time series in the west coast of Canada

The white noise amplitude of the WN model is also estimated by MLE analysis. Estimated white noise component of the WN model for 1110 time series versus that of the WF model is plotted in Figure 5.19 and the mean amplitude ratio is 0.97. Figure 5.20 shows the comparison between the WN and WR model, which shows the mean amplitude ratio to be 0.86. The comparison results are similar to the results in the west coast of Canada.

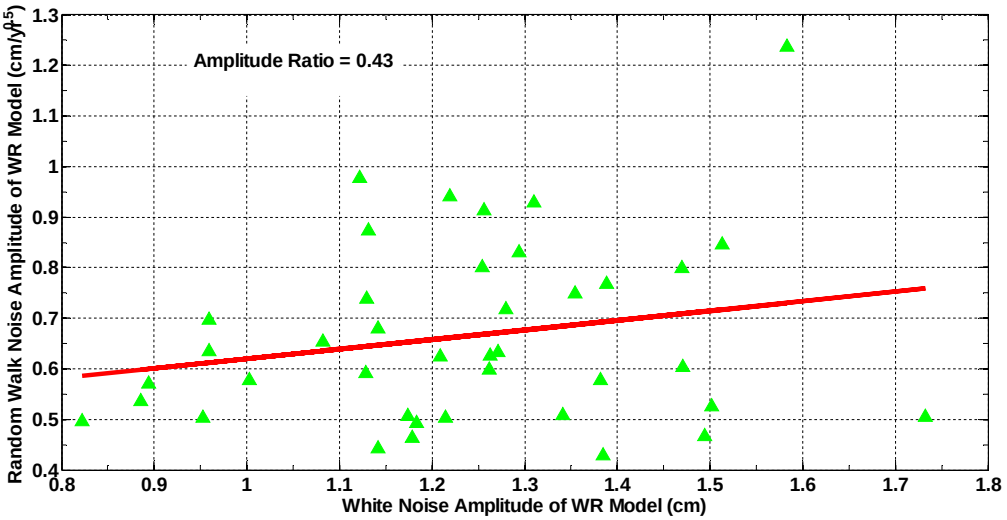

Figure 5.18 Comparison between a and d_{-2} estimates of WR model for 40 altimetry time series in the east coast of Canada.

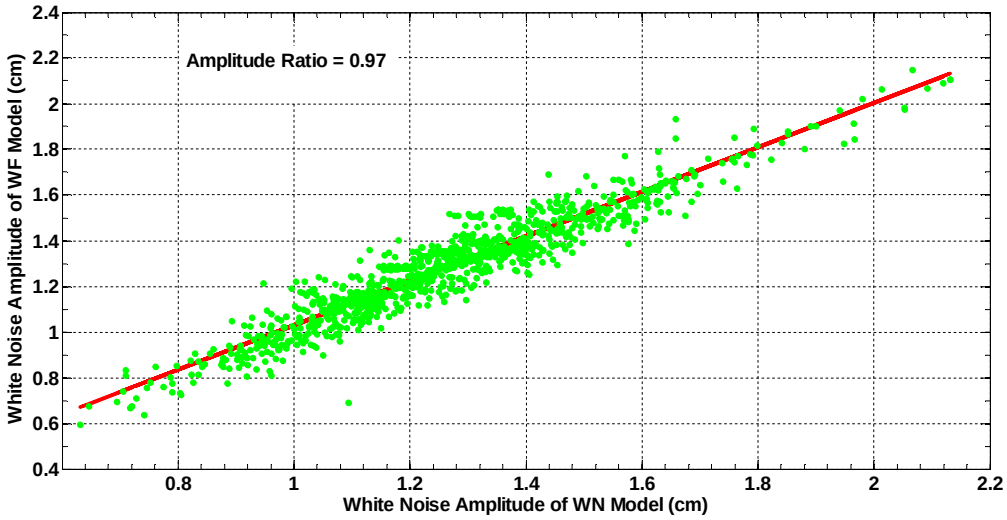

Figure 5.19: Comparison between a estimates of WF model and a estimates of WN model for 1110 altimetry time series in the east coast of Canada.

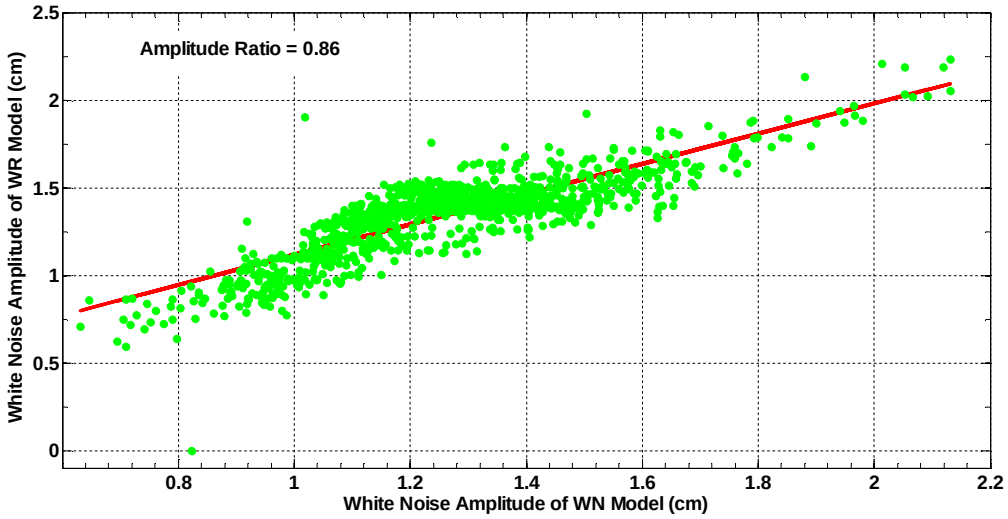

Figure 5.20: Comparison between *a* estimates of WR model and *a* estimates of WN model for 1110 altimetry time series in the east coast of Canada.

Based on the above results, we can make the following conclusions. First, time-dependent noise is very weak in altimetry time series. Among altimetry data, the number of time series exhibiting the color noise feature is less than 16%. Moreover, the amplitude ratio between the flicker white noise and for most of them is less than 1.0. The ratio between the random walk and white noise for all of the time series is less than 1.0. Johnson and Agnew (1995) and Zhang et al. (1997) confirm that if the amplitude ratio is less than 1.0, the temporally-dependent noise is not visually evident in the time series especially for short series and they nevertheless can have a significant detrimental effect on the uncertainties of sea level velocities. Automatically another conclusion comes out that the white noise is dominant in altimetry time series. The results of the power spectral density analysis also support this conclusion. The comparison between the white noise amplitude of the WN model and WF or WR model indicates that the white noise components are well determined and are statistically equivalent for the three models. The magnitudes of WN coefficients *a* are about 0.3-5.3 cm in the west coast of Canada and 0.4-4.5

cm in the east coast. In addition, for the time series which have an amplitude ratio between the flicker noise and white noise component greater than 1.0, the effect of temporally-dependent noise on the estimated uncertainty of sea level trend cannot be ignored (Johnson and Agnew, 1995). Based on above results, we can see that white noise is dominant in most of the time series. Very small numbers of time series exhibit flicker noise and there is no time series showing random walk noise. Hence WN model is used for almost all time series except for those that exhibiting flicker noise, which are using WF model.

5.4 Estimates of absolute sea level trend

The covariance matrix of altimetry measurements is denoted as $a^2 I$ where a is the white noise amplitude and I is the identity matrix. The value of a for every altimetry time series is estimated by MLE analysis discussed in Section 5.3.1. The sea level trend and associating uncertainty for each time series are estimated by the linear regression model (5.1.

Figure 5.21 and Figure 5.22 show the rates estimated from satellite altimetry data. The estimated rate varies at different points but is generally in the range of -2 to 2 mm/year. For 1993 to 2008, the rate of ASL is -1.27±0.28 mm/year for the west coast and 1.12±0.27 mm/year for the east coast. The rate error accounts for not only the random measuring errors but also the systematic errors, e.g., the T/P calibration error, which is common to all satellite data in the open ocean as well as in the coastal areas. The T/P calibration error can cause a bias of 0.27 mm/year on the rate estimation (Mangiarotti, 2006). The ASL fall for the west coast of Canada is in agreement with the published satellite altimetry results (Mazzotti 2008; CU SLRGroup), which indicate ASL rates varying between 0 and -5 mm/year. The estimate is close to the low

end, which might be related to shallow water effects. Our ASL rate for the east coast of Canada coincides with the results of the CU SLRGroup which vary between 0 and 3 mm/year. When comparing the west coastal rate for the period 1993 to 2008 between satellite altimetry and tide gauges (see e.g., Mazzotti et al., 2008), we find an opposite estimation, which may be due to the sparse distribution of tide gauge sites.

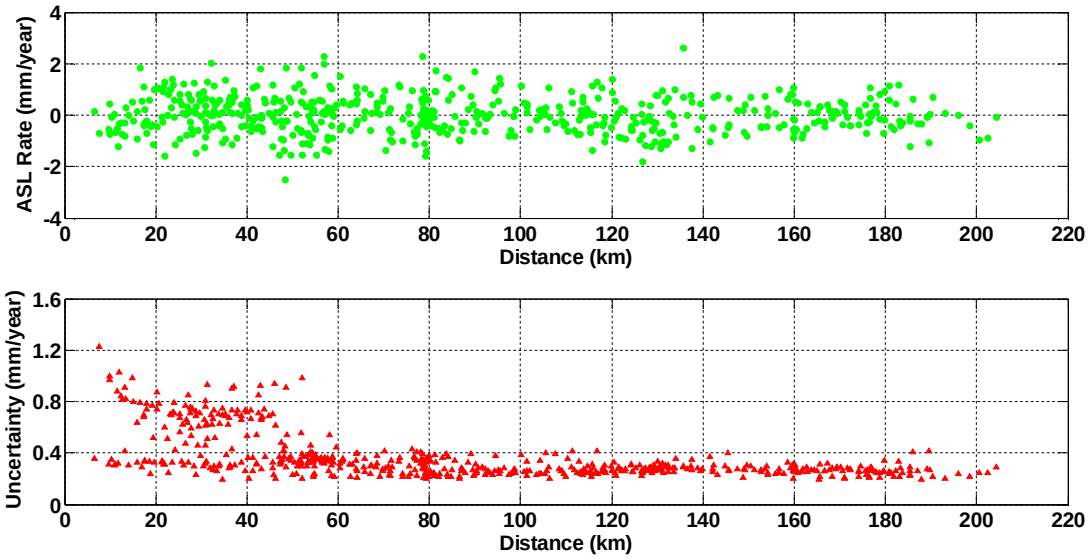

Figure 5.21: The rate and uncertainty estimation at every satellite altimetry measuring location in the west coast of Canada, which is plotted as a function of distance to the coastline.

5.5 Summary

There are three contributions in this chapter.

(1) We generated the cleaned MMSL time series from satellite altimetry data for the west and east coasts of Canada. In Chapter Four, 10-day T/P and Jason-1 SLA time series, which were created by the pre-processing described in Chapter Two, were corrected for the residual ocean tides. Then they were averaged to MMSL time series. Altimetry MMSL time series were then corrected for the seasonal annual (calculated by Equations

(3.8) and (3.9)) and regional common mode effects (derived by Equations (3.8) and (3.9)). Outlier detection which is defined by Equation (3.12) was used to detect the suspicious MMSL data, which were removed afterward. The cleaned MMSL data vary between -10 cm and 10 cm.

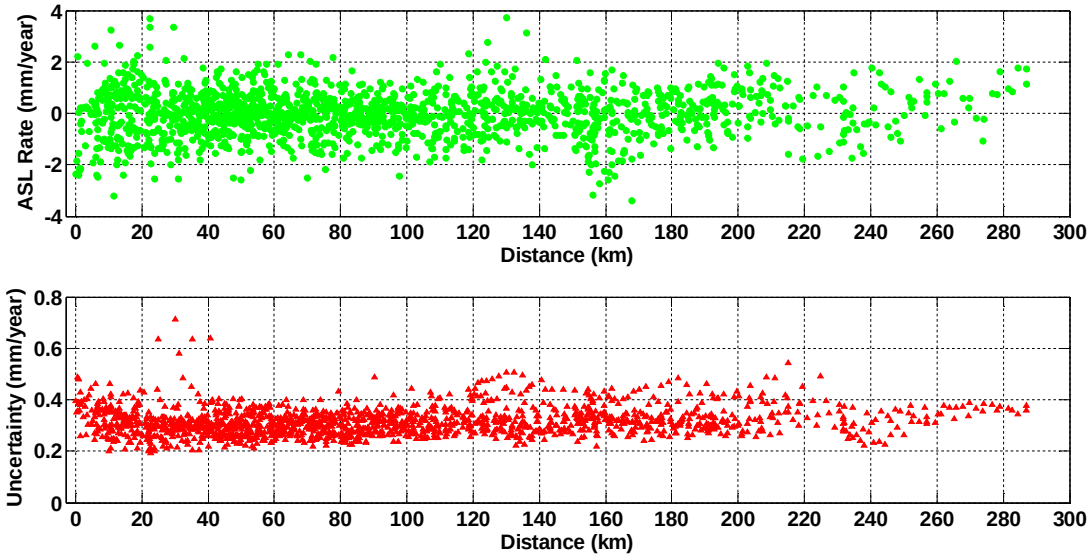

Figure 5.22: The rate and uncertainty estimation at every satellite altimetry measuring location in the east coast of Canada, which is plotted as a function of distance to the coastline.

(2) We tested WN, WR and WF models for altimetry MMSL time series by power spectral density (Equations (3.22), (3.23) and (3.24)) and maximum likelihood analysis (Equations (3.26) and (3.27)), and found that WN model is appropriate for most of the time series in the west and east coasts of Canada and very few data show obvious flicker noise. The covariance matrix of WN model for each altimetry site was constructed by Equation (3.17). The covariance matrix of WF model for those time series showing flicker noise was generated by Equation (3.21).

(3) We derived the rate and uncertainty of ASL change at every altimetry site. Cleaned MMSL time series were substituted to Equations (3.3), (3.4), (3.5) and (3.6) to solve the linear regression model using the generated covariance matrix. These estimates of ASL trend will be the observations for computing the rate of coastal sea level change in Chapter Seven.

Chapter Six: Relative sea level change and vertical land movement

6.1 Introduction

This chapter presents the estimated results of relative and absolute sea level change by tide gauge data under the processing strategy described in Chapter three. In the first section, the processing for correcting the MMSL tide gauge time series for the annual seasonal and regional common mode effects is described. The IB corrections for the daily data are also presented in this chapter because negative linear trends are found in the IB corrections which would affect the rate estimate greatly. Then the proposed method for estimating the rate of RSL change is presented. As suggested in Chapter Three, the appropriate measurement noise model is selected. Then the method is applied to the data to derive the rate estimates. In the following section, the vertical land motion and its effects on the determination of the absolute sea level change are discussed. Velocity estimates of the vertical land motion from GPS data and the corresponding ASL rate estimates are presented in this section.

6.2 Monthly mean sea level corrections

The tide gauge daily data from Fisheries and Oceans Canada are used to calculate the monthly mean sea level (MMSL). During the calculation of MMSL from daily data, if the number of daily data is less than 24 for one month, the value of MMSL is not averaged from these daily data but interpolated from nearby available MMSL. This is used to minimize possible biases arising from inaccurate resolution of fortnightly variability associated with the strong spring neap and anomalistic tides (Mazzotti et al., 2008). The gaps of MMSL time series were also filled. The water level measured by tide gauges is affected by a variety of physical processes

over timescales ranging from a few minutes to decades. The use of monthly mean sea levels effectively filters out signals with periods shorter than about one week, such as the main diurnal and semi-diurnal tidal constituents. However, longer-period signals (including fortnightly, monthly and semiannual variations) remain present in the MMSL time series, with the annual cycle signal accounting for most of the signal variance. Interannual to decadal-scale processes such as the El Niño-southern Oscillation (ENSO) and the Pacific Decadal Oscillation (PDO) are also evident in most series. Long-period signals can significantly bias long-term trend estimates, especially if the time series is not substantially longer than the dominant low-frequency oscillations or if it ends midway through a major decadal-scale event (Mazzotti et al., 2008). Hence special care must be taken to account for the effects of these long-period signals.

Two types of corrections, which are described in detail in Chapter Three, are applied to the original MMSL data to remove transient signals and noise that can bias long-term trend estimations. The IB corrections for the daily data are presented in Section 6.2.1 and the two corrections for MMSL data and their calculations are discussed in, 6.2.2 and 6.2.3. Section 6.2.4 presents the original, corrected time series and corresponding spectra on every tide gauge station.

6.2.1 Inverse barometric correction

The inverse barometer corrections for 8 tide gauge sites in the west and east coast of Canada are shown in Figure 6.1 and

Figure 6.2.

Table 6.1 Tide Gauges and Associated GPS Stations

site	ID	Latitude deg N	Longitude deg W	Start	End	*T* year	GPS station ID	Latitude deg N	Longitude deg W	*T* year	Distance from Gauge to GPS station, km
West Coast of Canada											
Victoria Harbour (BC)	7120	48.424	123.371	1963	2008	46	BCES	48.390	123.487	6.6	4
Patricia Bay (BC)	7277	48.654	123.452	1977	2008	32	PGC5	48.649	123.451	7.1	1
Point Atkinson (BC)	7795	49.337	123.253	1961	2008	48	BCVC	49.276	123.089	3.8	14
Port Hardy (BC)	8408	50.722	127.489	1964	2008	45	BCPH	50.686	127.375	5.5	9
Bamfield (BC)	8545	48.836	125.136	1970	2008	39	BAMF	48.835	125.135	4.5	0.1
Tofino (BC)	8615	49.154	125.913	1949	2008	60	UCLU	48.926	125.542	10.8	37
Winter Harbour (BC)	8735	50.513	128.029	1989	2008	20	HOLB	50.640	128.135	10.8	16
Prince Rupert (BC)	9354	54.317	130.324	1948	2008	61	BCPR	54.277	130.435	2.0	8
Queen Charlotte City (BC)	9850	53.252	132.072	1964	2008	45	BCSS	53.254	131.870	1.8	18
East Coast of Canada											
Saint John (NS)	65	45.251	66.063	1948	2008	61	EPRT	44.909	66.992	13	56
Halifax (NS)	490	44.667	63.583	1948	2008	61	HLFX	44.684	63.611	9	2
St Johns (NL)	905	47.567	52.717	1957	2008	52	STJO	47.595	52.678	16	4
Lower Escuminac (NS)	2000	47.083	64.883	1973	2008	36	ESCU	47.073	64.799	7	4

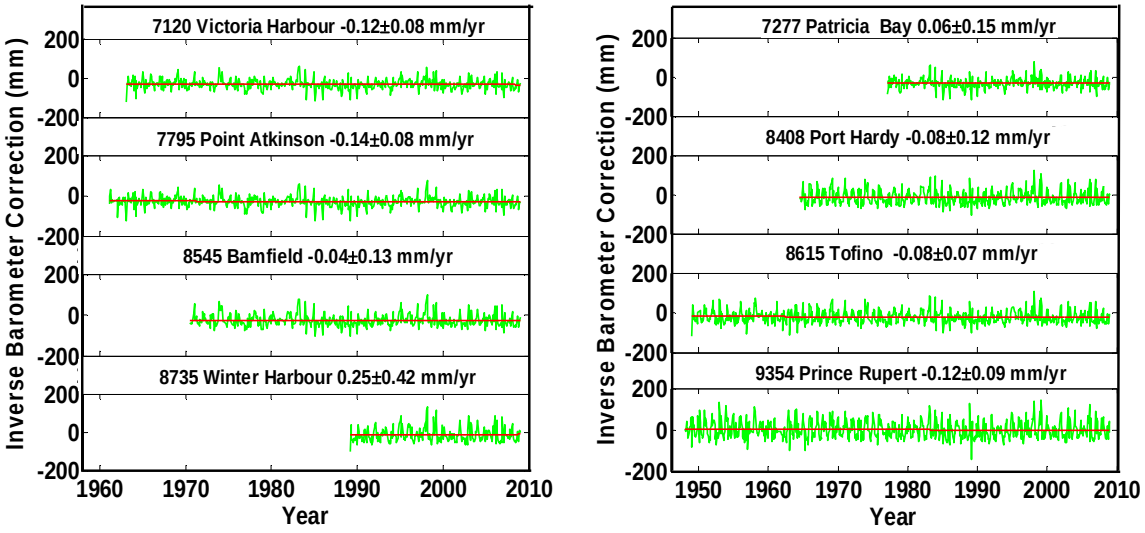

Figure 6.1: Inverse barometer corrections for 8 tide gauge sites in the west coast of Canada. Green lines are the inverse barometer corrections and red lines indicate the trends included in the inverse barometer corrections.

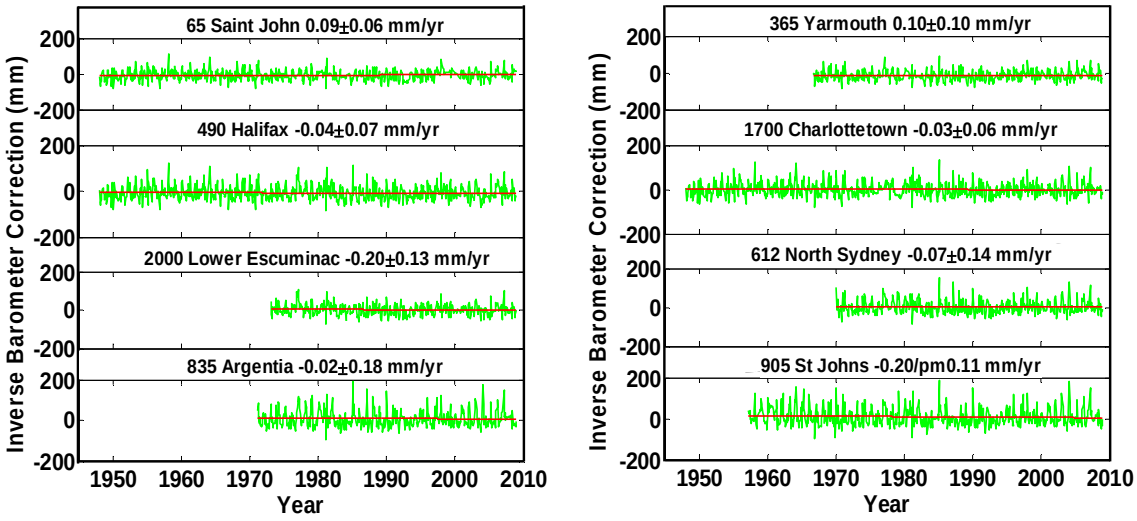

Figure 6.2: Inverse barometer corrections for 8 tide gauge sites in the east coast of Canada. Green lines are the inverse barometer corrections and red lines indicate the trends included in the inverse barometer corrections.

All inverse barometer time series show a small trend which affects the estimated trends of RSL.

For example, at Victoria Harbour the inverse barometer trend leads to a RSL fall of about 0.12

mm/yr and at St. Johns the trend of inverse barometer corrections leads to a RSL falls of about 0.2 mm/yr. So in order to avoid a bias of the RSL rate estimation, we detrend the inverse barometer correction time series before applying the corrections. On average, the sea level pressure correction reduces the data variance by 29%.

6.2.2 Empirical annual seasonal correction

Strong annual seasonal signals are removed from MMSL by Equations (3.8) and (3.9). Monthly average sea levels are shown in Figure 6.3 (the west coast of Canada) and Figure 6.4 (the east coast of Canada). All stations show 100 – 150 mm peak-to-peak variations in average monthly anomalies. Victoria Harbour, Bamfield, Winter Harbour and Prince Rupert in the west coast of Canada and Halifax, Argentia, Charlottetown and St Johns have the lowest water levels during summer months while the other stations have the opposite situations. This may be due to the effects of seasonally varying alongshore winds and associated alongshore surface currents.

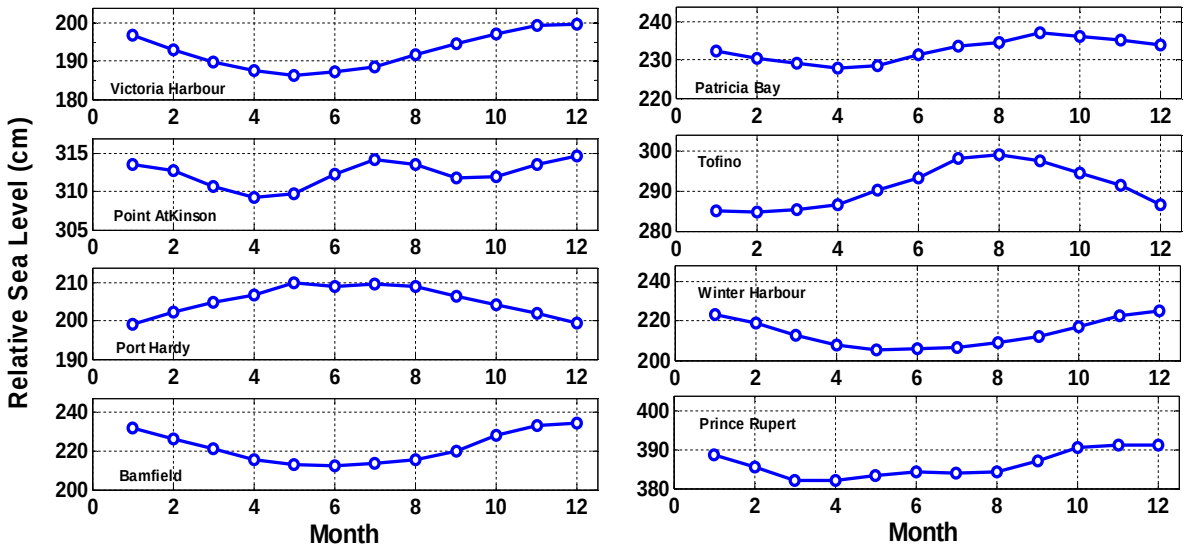

Figure 6.3: Monthly average sea level for 8 tide gauge stations in the west coast of Canada.

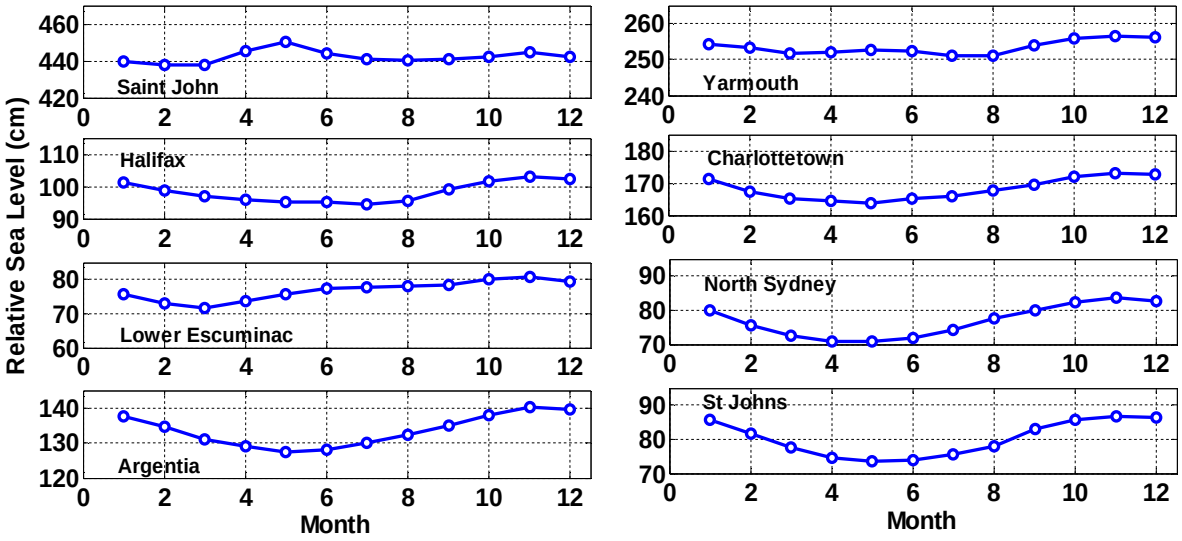

Figure 6.4: Monthly average sea level for 8 tide gauge stations in the east coast of Canada.

6.2.3 Regional common mode noise correction

The regional common mode noise corrections were applied to MSL tide series. Such corrections are calculated by Equations (3.10) and (3.11). In the west coast of Canada, 9 tide gauge stations were categorized into two groups according to their correlation coefficients (shown in Table 6.2). In the east coast of Canada, 8 tide gauge stations were divided into three groups (shown in Table 6.2). Those stations whose correlation coefficient is greater than 0.6 should be categorized into one group. MMSL time series in each group were first corrected for the inverse barometer and annual seasonal variations and then detrended. The residual series were then stacked within each group to form the regional common model corrections, which were then removed from the original MMSL series.

Table 6.2. Regional common mode tide gauge stations categorization.

	Regions	Sites
Pacific Coast	Dixon Entrance, Hecate Strait	9354, 9850
	Pacific coast of Vancouver Island	7120, 7277, 7795, 8408, 8545, 8615, 8735
Atlantic Coast	Bay of Fundy	65, 365
	Atlantic coast of Nova Scotia and Gulf of St. Lawrence	490, 612, 1700, 2000
	Atlantic coast of Newfoundland	612, 835, 905

6.2.4 Corrected monthly mean sea level time series

Figure 6.5 (A to I) shows the original (plot a) and corrected (plot c) MMSL time series and the associated spectrums (plots b and d) of 9 tide gauge stations in the west coast of Canada. Figure 6.6 (A to D) is for the east coast of Canada. As shown in Figure 6.5 (A to I) and Figure 6.6 (A to D) plot b, the original MMSL power spectra of all sites show a very strong peak in amplitude at 1-year. There are also obvious signals in semi-annual periods of all sites except for Halifax and St Johns. There are also relative large variations at periods longer than 1 year (up to 10-year). After applying the annual seasonal variations correction, as shown in Figure 6.5 (A to I) and Figure 6.6 (A to D) plot d, the two peaks at 1-year and semi-annual periods have been removed. The regional common mode noise correction decreases the significant coherent signal at periods longer than 1-year. The above three procedures decrease the RMS of MMSL from 15.6 cm to 2.5 cm and remove 84% of the variations in average for the sites in the west coast of Canada. In the east coast of Canada the RMS of the MMSL decreases from 13.3 cm to 4.4 cm and 66% of the variations are removed.

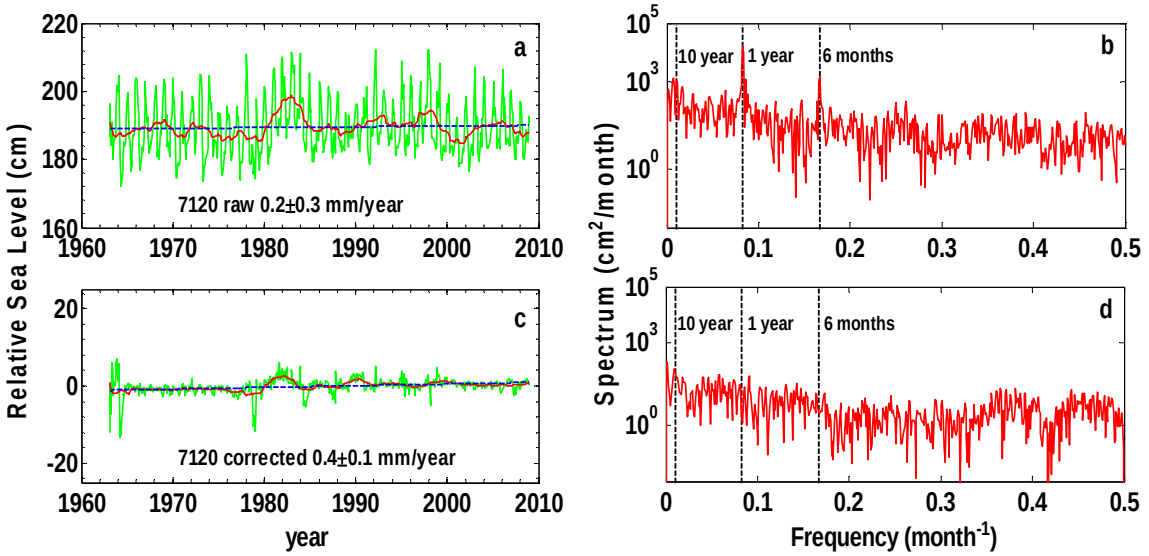

Figure 6.5 A: Monthly mean sea level data for Victoria (7120) MMSL time series. (Figures a and c) Green lines show raw (Figure a) and corrected (Figure c) MMSL. Red lines show 1-year moving averages. Blue lines show linear RSL trends. (Figures b and d) Power spectra of raw (Figure b) and corrected (Figure d) detrended MMSL data. Dashed vertical line indicate 1-year period.

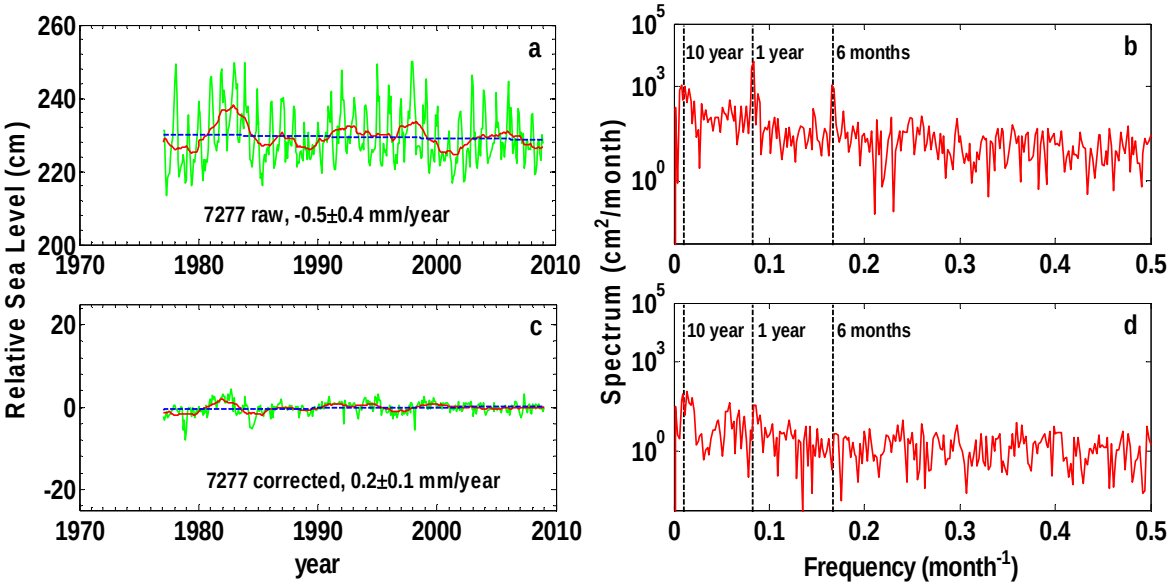

Figure 6.5 B: Monthly mean sea level data for Patricia Bay (7277) MMSL time series.

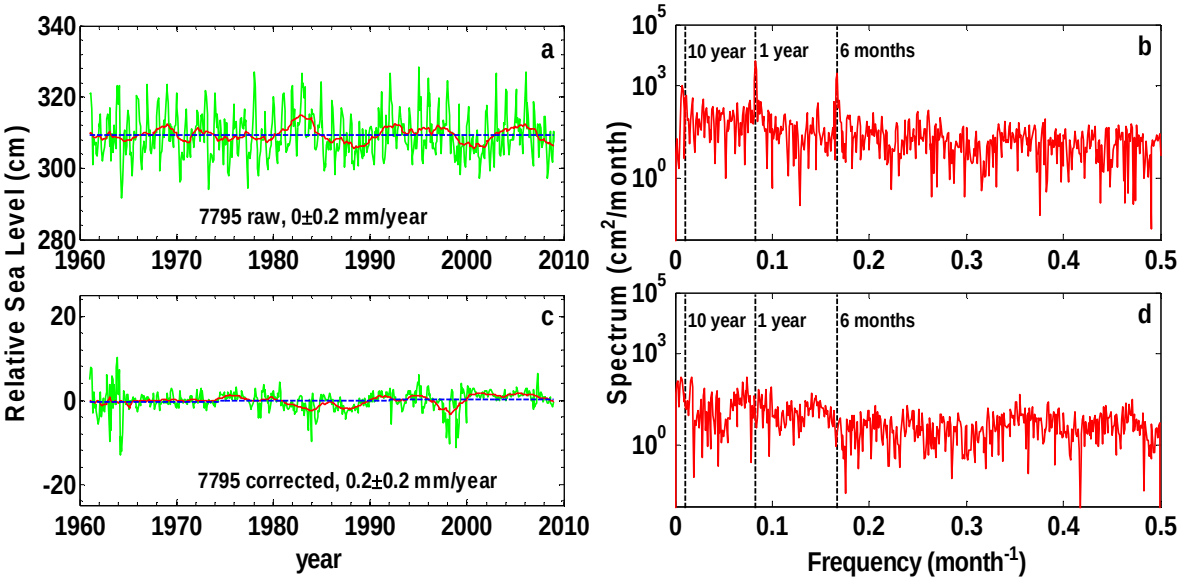

Figure 6.5 C: Monthly mean sea level data for Point Atkinson (7795) MMSL time series.

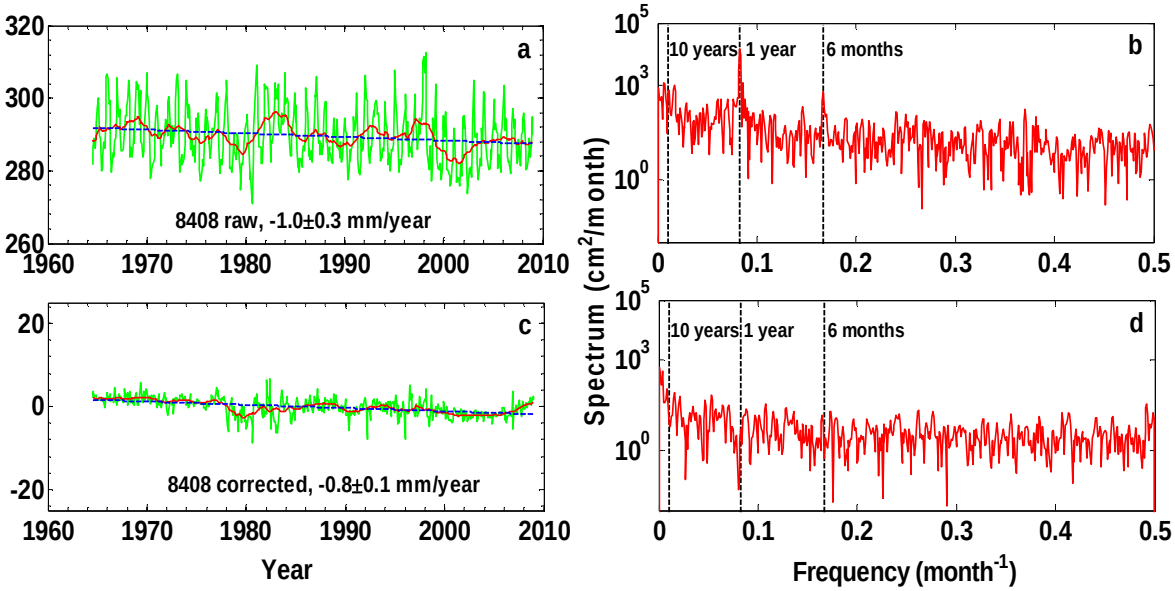

Figure 6.5 D: Monthly mean sea level data for Port Hardy (8408) MMSL time series.

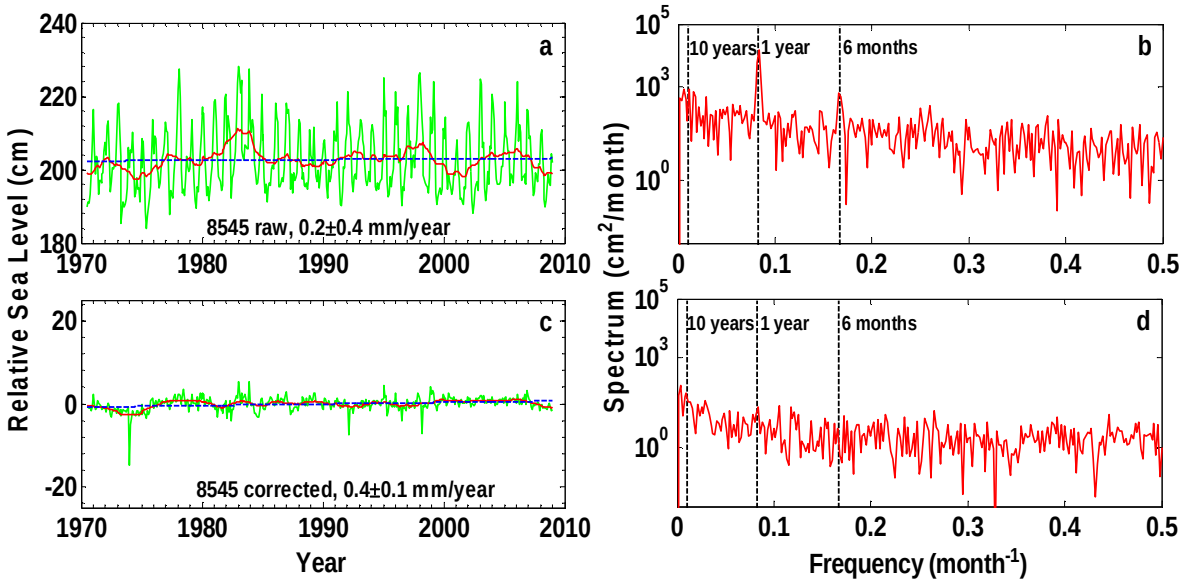

Figure 6.5 E: Monthly mean sea level data for Bamfield (8545) MMSL time series.

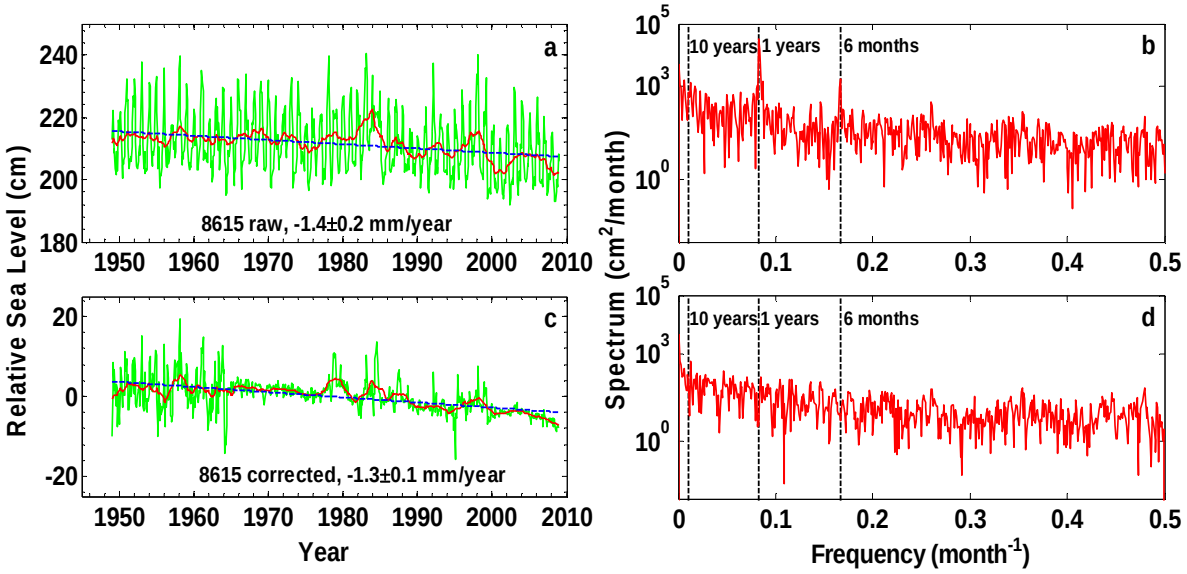

Figure 6.5 F: Monthly mean sea level data for Tofino (8615) MMSL time series.

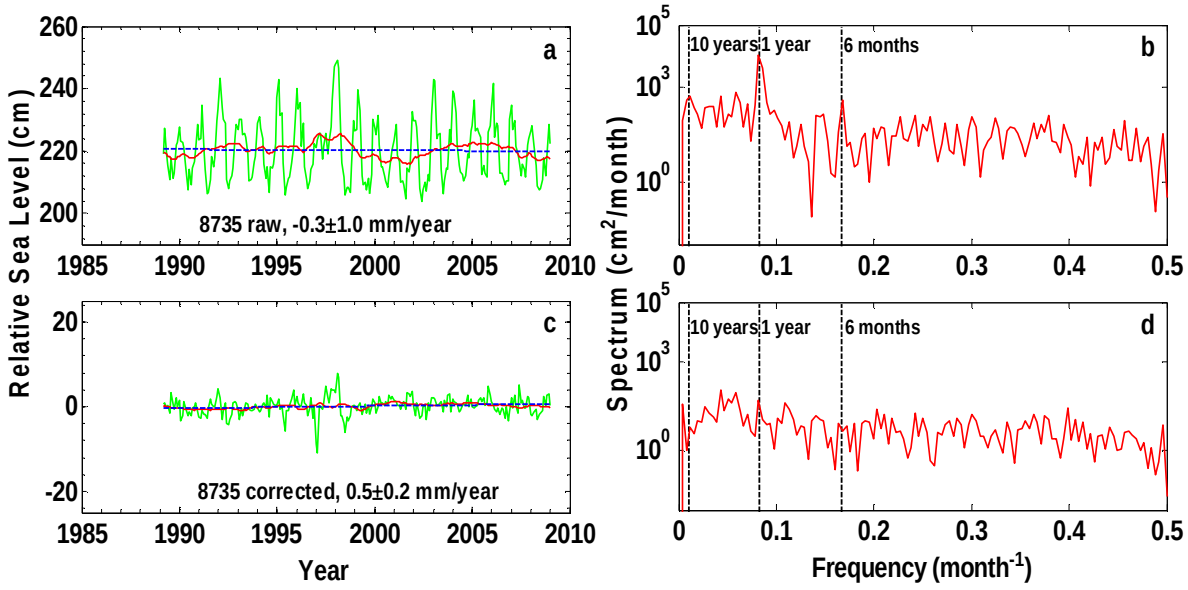

Figure 6.5 G: Monthly mean sea level data for Winter Harbour (8735) MMSL time series.

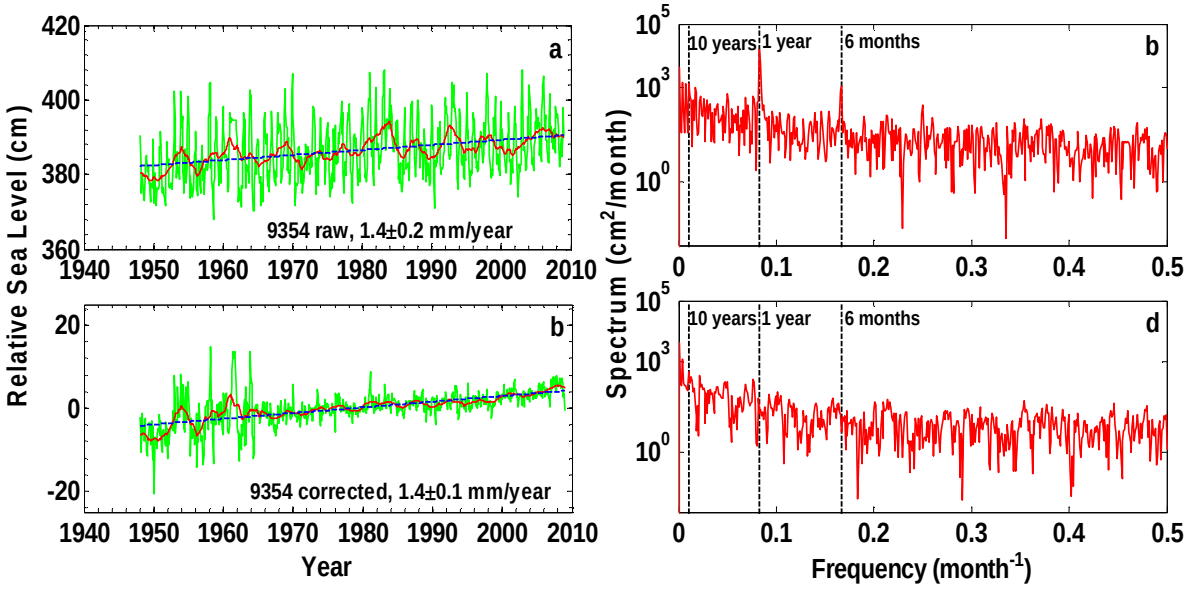

Figure 6.5 H: Monthly mean sea level data for Prince Rupert (9354) MMSL time series.

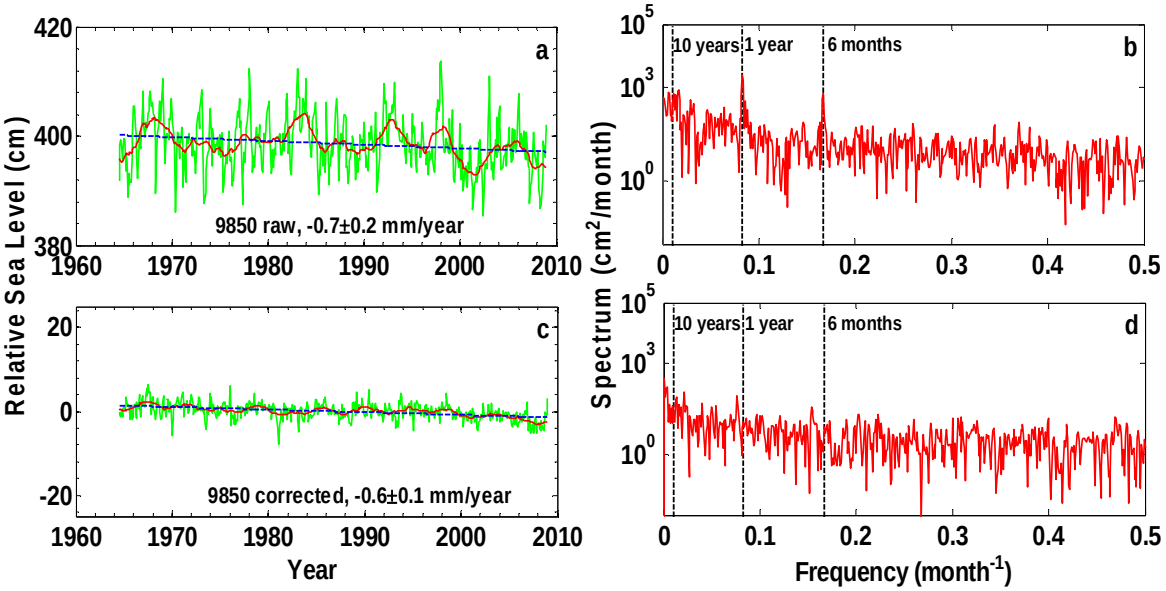

Figure 6.5 I: Monthly mean sea level data for Queen Charlotte City (9850) MMSL time series.

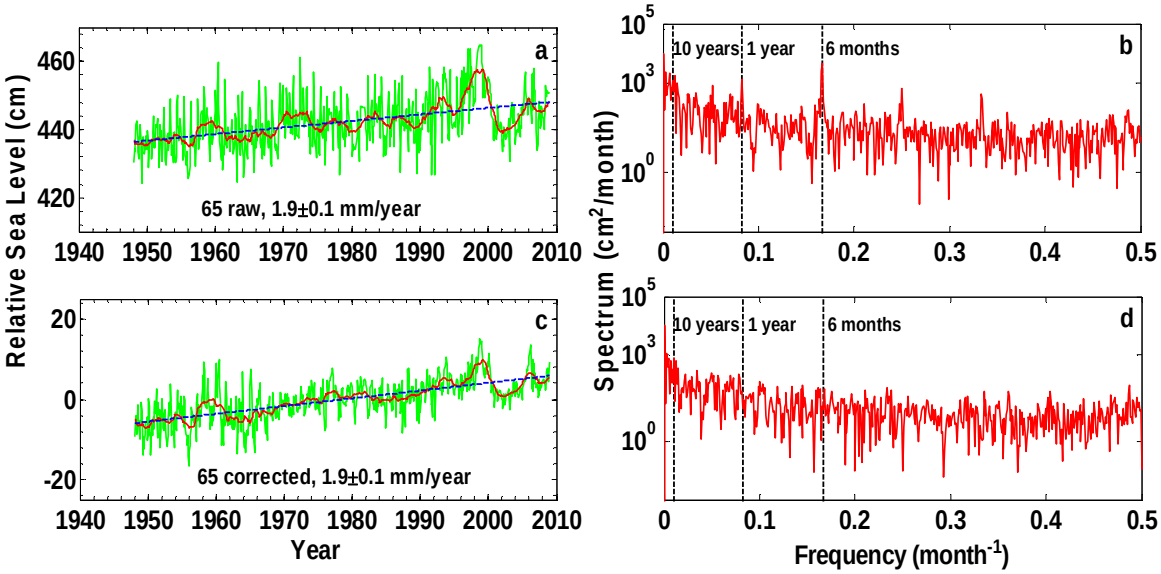

Figure 6.6 A: Monthly mean sea level data for Saint John (65) MMSL time series. (Figures a and c) Green lines show raw (Figure a) and corrected (Figure c) MMSL. Red lines show 1-year moving averages. Blue lines show linear RSL trends. (Figures b and d) Power spectra of raw (Figure b) and corrected (Figure d) detrended MMSL data. Dashed vertical line indicate 1-year period.

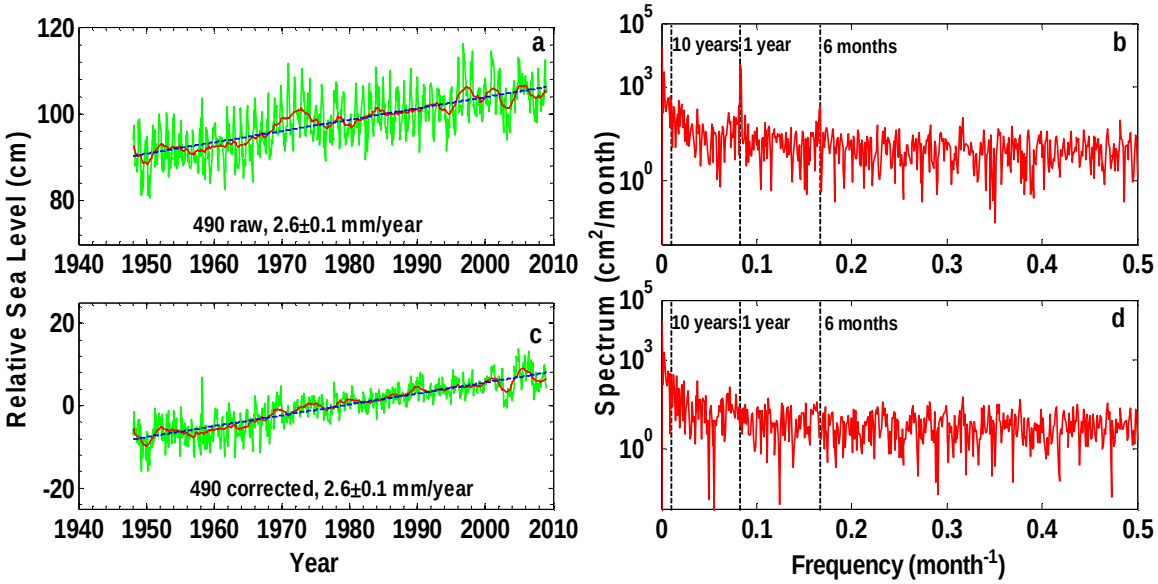

Figure 6.6 B: Monthly mean sea level data for Halifax (490) MMSL time series.

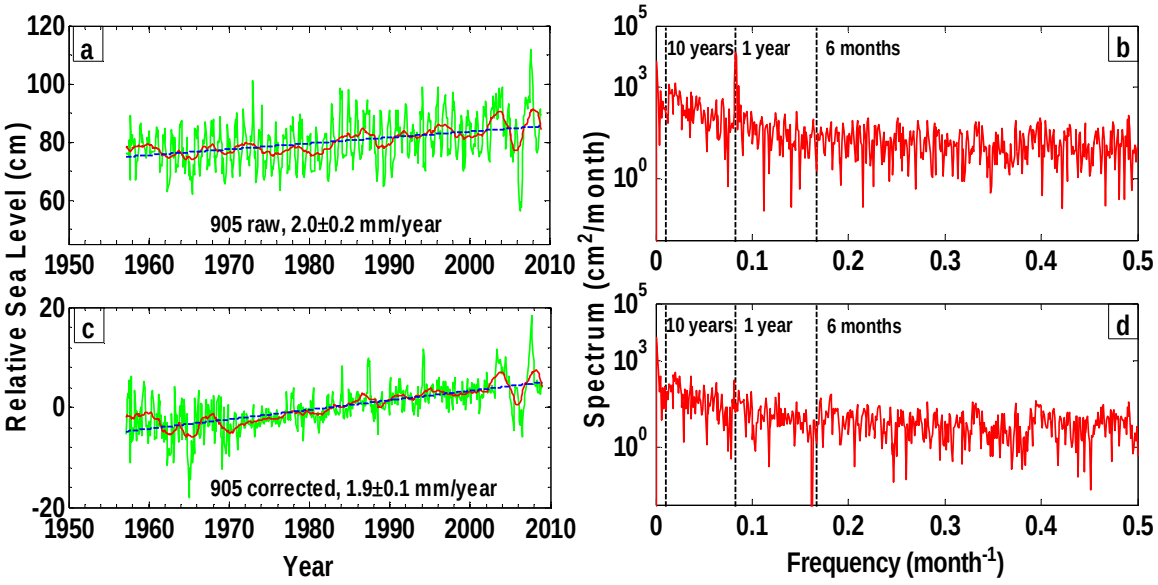

Figure 6.6 C: Monthly mean sea level data for St Jones (905) MMSL time series.

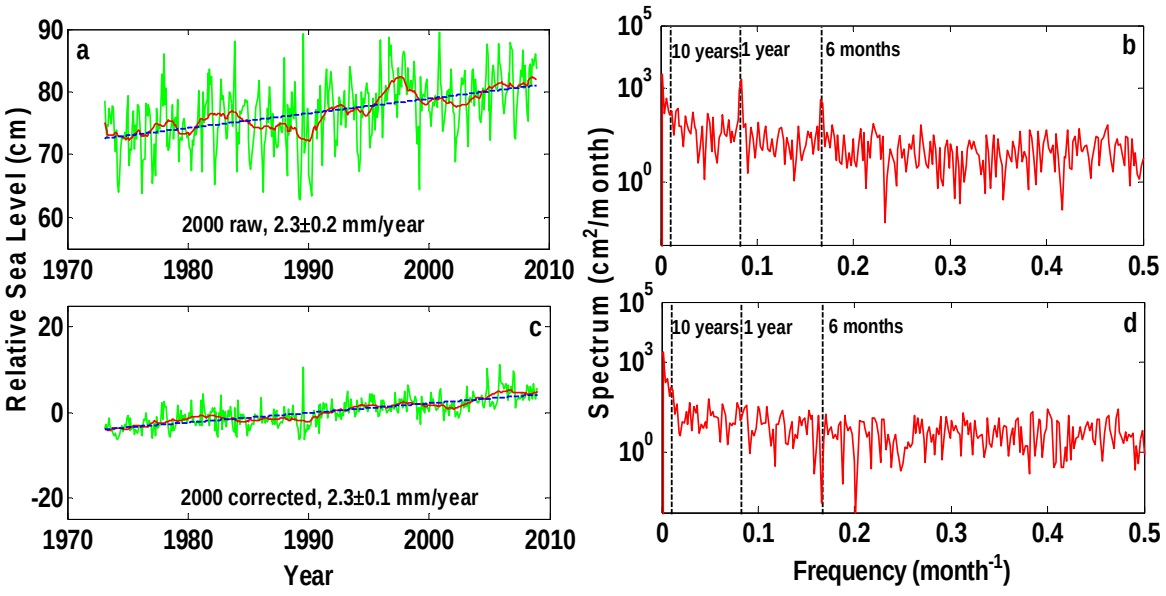

Figure 6.6 D: Monthly mean sea level data for Lower Escuminac (2000) MMSL time series.

6.3 Relative sea level change

The rate of RSL and its uncertainty at every tide gauge site are estimated by the linear regression model

$$MMSL(t_i) = a_{RSL} t_i + b + \varepsilon_i , \qquad 6.1$$

Equation (5.1) is in the exact same form as Equation (3.1) but has the parameter a_{RSL} specific for the rate of the RSL. As discussed in Chapter Three, in order to solve this model, an appropriate noise model for MMSL should be found. Before testing the noise model, a least-squares processing is applied to the MMSL with an identity weight matrix to derive the residuals. We also get the estimated rate of RSL and associated uncertainty at every tide gauge site which are shown on Figure 6.5 and Figure 6.6. Blunders in the MMSL are detected by the method described in Chapter Three using the residuals. The number of blunders and the blunder

ratio for every tide gauge site are listed in Table 6.3 and Table 6.4. 2.4% and 1.0% of MMSL data in the west and east coast of Canada, respectively, are discarded after blunder detection. After blunder detection, the MMSL series are processed by the linear regression again to create the post-fit residuals which are used to test the noise model.

Table 6.3 Number of monthly mean sea level records, number of blunders and the blunder ratio for 9 tide gauge sites in the west coast of Canada.

Site	7120	7277	7795	8408	8545	8615	8735	9354	9850
Number of MMSL	552	384	576	535	463	720	239	732	535
Number of blunders	26	4	18	10	5	31	3	28	2
Blunder rate (%)	4.7	1.0	3.1	1.9	1.1	4.3	1.3	3.8	0.4

Table 6.4 Number of monthly mean sea level records, number of blunders and the blunder ratio for 8 tide gauge sites in the east coast of Canada.

site	65	365	490	612	835	905	1700	2000
Number of MMSL	732	509	732	468	455	623	732	432
Number of Blunders	0	0	1	7	7	12	15	2
Blunder rate (%)	0	0	0.1	1.5	1.5	1.9	2.1	0.5

6.3.1 Noise model testing

As stated in Chapter Three, the noise model is testing by the power spectral density analysis and the maximum likelihood analysis.

6.3.1.1 Power spectral density analysis

The power spectra for the individual sites are calculated by analyzing the post-fit residuals using the formulas (3.22), (3.23) and (3.24) in Chapter Three. Figure 6.7 and Figure 6.8 are the spectra for the sites Victoria Harbour and Saint Johns, respectively. The power concentrates mostly at low frequencies. The associating spectral index κ is estimated and the results are listed in Table 6.5 and Table 6.6.

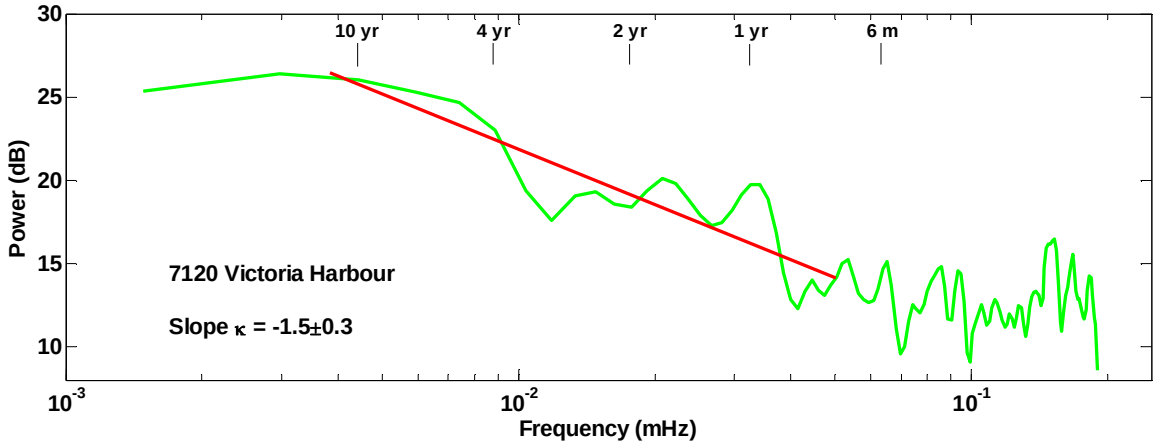

Figure 6.7: Power spectral density estimate at tide gauge site 7120 Victoria Harbour in units of dB relative to 1 cm^2 / Hz, is computed with section averaging of 8 windows. The best fit line (red) is computed in log-log space for the whole frequencies.

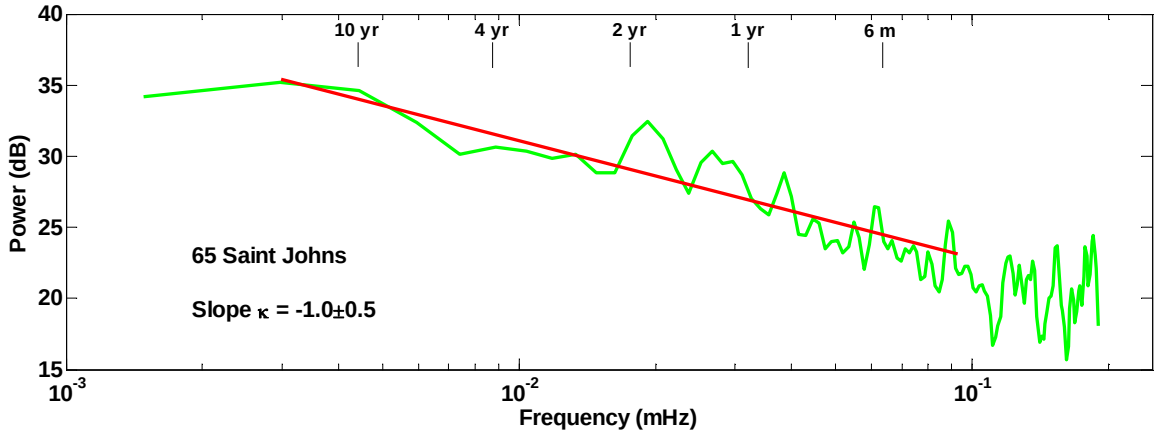

Figure 6.8: Power spectral density estimate at tide gauge site 65 Saint Johns in units of dB relative to 1 cm^2 / Hz, is computed with section averaging of 8 windows. The best fit line (red) is computed in log-log space for the whole frequencies.

In the west coast of Canada, all tide gauge sites except 7795, 9354 and 9850 have the values of κ close to -1 indicating that the predominant noise is probable the flicker noise. The values of κ for the other three sites are around -1.5, which make it hard to say if the predominant noise is flicker or random walk noise. In the east coast of Canada, the situation is very similar to that in

the west coast except at site 365 where the value of κ is equal to -2 indicating random walk noise.

There is a problem in the power spectral density analysis. The values of the standard deviations are relatively large. Take the site 7795 as an example. The estimated value of κ is -1.5 with a standard deviation of 0.3. It leads to the low limit of -1.8 which is close to the random walk noise and the high limit of -1.2 which is close to the flicker noise. So it is very hard to say if the predominant noise is the flicker or random walk or both. These large standard deviations may be due to the "unclean" residuals. Although we assume the residuals are purely composed of the measurement noise, this seldom happens in the actual measurements because there are still some long term signals (e.g., signals with period longer than 10 years) that we cannot remove. The spectral analysis is biased by these un-removed signals. So while power spectral density analysis can demonstrate the existence of time-correlated noise, it can only provide a rough estimate of the power level of this type of noise.

Table 6.5. Estimated spectral index and its uncertainty at 9 tide gauge site in the west coast of Canada

site	7120	7277	7795	8408	8545	8615	8735	9354	9850
Slope κ	-1.5	-1.3	-1.5	-1.4	-1.3	-1.3	-1.2	-1.5	-1.6
Standard deviation	0.3	0.3	0.3	0.4	0.3	0.4	0.4	0.5	0.4

Table 6.6. Estimated spectral index and its uncertainty at 8 tide gauge site in the east coast of Canada

site	65	365	490	612	835	905	1700	2000
Slope κ	-1.1	-2.0	-1.4	-1.3	-1.4	-1.2	-1.5	-1.5
Standard deviation	0.5	0.4	0.5	0.4	0.4	0.3	0.4	0.4

6.3.1.2 Maximum likelihood analysis

The values of a^2 and/or $d_{-\kappa}^2$ for different noise model are estimated by maximizing the probability function (Equation (3.25) using the downhill simplex method. The values of a^2 and/or $d_{-\kappa}^2$ for the tide gauge sites in the west and east coast of Canada are shown in Table 6.7. For the white and colored noise model, if $d_\kappa / a << 1$, the monthly mean sea level observations are temporally uncorrelated. When $d_\kappa / a \approx 1$, the temporal correlations may not be visually evident in the time series (especially for short series) but they nevertheless can have a significant detrimental effect on the uncertainties of the RSL velocities estimated from observations. As listed in Table 6.7, the ratio d_κ / a is greater than 1 at almost all the stations, which shows that the colored noise component is more dominant in the time series. It would bias the accuracy of the velocity estimation.

Substituting the a^2 and/or $d_{-\kappa}^2$ estimates to Equation (3.26), we can get the values of maximum log-likelihood which are listed in the second, third and fourth columns in Table 6.8 for the WN, WR and WF noise model. Based on the values of Λ-statistics (listed in the fifth, sixth and seventh column in Table 6.8) which is calculated by Equation (3.27), we can find that the combination noise models fit the data better than the white noise model. The WF fits the data better than the WR model for almost all sites except for sites 7795 and 365. So the WF model is chosen as the noise model used in the linear regression processing.

Table 6.7. Values of spectral amplitudes a^2 and/or $d_{-\kappa}^2$ for different noise model estimated by the maximum likelihood analysis.

Site	Data	White	White and Random Walk (WR)	White and Flicker (WF)

	length (year)	(WN)						
		a (cm)	a (cm)	d_{-2} (cm/yr$^{0.5}$)	d_{-2}/a	a (cm)	d_{-1} (cm)	d_{-1}/a
West coast of Canada								
7120	**47**	**1.32**	**0.74**	**2.14**	**1.70**	**0.96**	**2.28**	**2.37**
7277	**34**	**1.40**	**0.68**	**3.83**	**2.37**	**0.99**	**2.71**	**2.74**
7795	**49**	**1.85**	**1.38**	**7.01**	**2.25**	**1.38**	**3.73**	**2.70**
8408	**47**	**1.73**	**1.67**	**2.18**	**1.14**	**1.34**	**2.85**	**2.13**
8545	**40**	**1.31**	**0.77**	**2.13**	**1.66**	**0.96**	**2.42**	**2.51**
8615	**60**	**1.64**	**2.14**	**1.31**	**0.78**	**1.45**	**3.82**	**2.63**
8735	**22**	**1.91**	**2.08**	**6.78**	**1.81**	**1.61**	**3.67**	**2.28**
9354	**67**	**1.62**	**1.68**	**4.14**	**1.57**	**1.45**	**3.31**	**2.29**
9850	**46**	**1.77**	**1.87**	**3.53**	**1.37**	**1.44**	**3.25**	**2.26**
East coast of Canada								
65	**61**	**1.62**	**1.20**	**9.40**	**2.80**	**1.44**	**4.29**	**2.98**
365	**44**	**4.03**	**1.89**	**13.68**	**2.69**	**3.79**	**1.70**	**0.67**
490	**61**	**1.62**	**1.93**	**2.31**	**1.09**	**1.47**	**2.82**	**1.92**
612	**40**	**4.02**	**1.61**	**10.68**	**2.58**	**2.36**	**21.02**	**2.98**
835	**38**	**4.76**	**2.33**	**14.90**	**2.53**	**3.46**	**27.41**	**2.81**
905	**53**	**1.77**	**1.56**	**9.41**	**2.46**	**1.57**	**4.49**	**2.87**
1700	**61**	**2.64**	**1.48**	**6.16**	**2.04**	**2.07**	**14.72**	**2.67**
2000	**37**	**2.04**	**2.74**	**2.58**	**0.97**	**1.68**	**3.21**	**1.91**

The estimated rates of RSL at every tide gauge site using the white or white and flicker noise model are listed in Table 6.9. Rates estimate in units of millimeters per year and all uncertainties denote 95% confidence intervals. Ratio is defined as the WF uncertainties divided by WN uncertainties. An important factor found is that the velocity estimates themselves are not significantly affected by the assumed measurement noise model. For the WN model, velocity uncertainties (STD[1]) are less than 0.1 mm/yr for 14 sites and greater than 0.1 mm/yr for the other three at 95% confidence level. These uncertainties are consistent with the uncertainties estimated by Equation (3.41). Based on Equation (3.41) we can find that under the white noise assumption, rate uncertainty is inversely proportional to the total time interval and the square

root of the number of continuous measurements. The uncertainty estimated under the WF model is 7.6 (5.4 to 9.8) times greater than that by the WN model in the west coast of Canada and 7.9 (2.5 to 10.3) times greater in the east coast of Canada on average.

Table 6.8. Log-likelihood tests for stochastic models

Site	Log-likelihood			Λ -statistic		
	WN	WR+WN	WF+WN	WN over WR+WN	WN over WF+WN	WR+WN over WF+WN
			West coast of Canada			
7120	923.47	932.77	934.86	0.00	0.00	0.12
7277	660.04	671.15	673.52	0.00	0.00	0.09
7795	1172.30	1180.65	1174.83	0.00	0.08	336.97
8408	1033.76	1046.15	1052.33	0.00	0.00	0.00
8545	765.36	775.95	781.74	0.00	0.00	0.00
8615	2119.67	2128.83	2136.27	0.00	0.00	0.00
8735	480.78	488.17	493.70	0.00	0.00	0.00
9354	1903.11	1915.55	1919.47	0.00	0.00	0.02
9850	1053.44	1061.70	1064.75	0.00	0.00	0.05
			East coast of Canada			
65	2349.89	2356.59	2361.94	0.00	0.00	0.00
365	1258.90	1269.37	1265.47	0.00	0.00	49.40
490	1765.04	1782.76	1788.41	0.00	0.00	0.00
612	1633.27	1646.98	1648.54	0.00	0.00	0.21
835	872.30	880.13	890.97	0.00	0.00	0.00
905	929.75	937.75	945.30	0.00	0.00	0.00
1700	962.26	994.29	1001.54	0.00	0.00	0.00
2000	1562.38	1573.33	1574.66	0.00	0.00	0.26

Table 6.9 RSL velocity estimates

site	Data Length (Year)	WN			WF			Ratio
		Rate	STD[1]	STD[2]	Rate	STD[1]	STD[3]	(WF STD[1]/WN STD[1])
West coast of Canada								
7120	47	0.33	0.04	0.04	0.24	0.30	0.37	7.5
7277	34	0.20	0.08	0.08	0.32	0.52	0.64	6.5
7795	49	0.15	0.06	0.06	0.05	0.48	0.58	8.0
8408	47	-0.77	0.06	0.06	-0.63	0.40	0.48	6.7
8545	40	0.36	0.05	0.05	0.25	0.39	0.47	7.8
8615	60	-1.34	0.06	0.04	-1.47	0.59	0.48	9.8
8735	22	0.49	0.21	0.21	0.38	1.14	1.39	5.4
9354	61	1.45	0.05	0.03	1.55	0.46	0.41	9.2
9850	46	-0.64	0.06	0.06	-0.57	0.46	0.55	7.7
		East coast of Canada						
65	61	1.93	0.08	0.03	1.96	0.82	0.53	10.3
365	43	3.13	0.12	0.07	3.07	0.30	0.24	2.5
490	61	2.65	0.05	0.03	2.50	0.42	0.35	8.4
612	39	3.33	0.08	0.03	3.23	0.72	0.47	9.0
835	38	1.45	0.11	0.09	1.45	0.85	0.67	7.7
905	52	1.90	0.08	0.08	1.71	0.74	0.88	9.3
1700	61	2.93	0.05	0.09	2.94	0.50	1.04	10
2000	36	2.24	0.09	0.05	2.32	0.55	0.65	6.1

STD^1 indicates the uncertainty is estimated by the linear regression progress.

STD^2 indicates the uncertainty is calculated by Equation (3.41).

STD^3 indicates the uncertainty is calculated by Equation (3.53).

6.4 Vertical land motion and absolute sea level change

Tide gauge data are required to be corrected for vertical land motion so that they can be used to derive the absolute sea level change. Glacial isostatic adjustment (GIA) is one of the most significant sources of vertical land movement in Canada. GIA is the gradual springing back of the Earth's crust in response to the removal of the ice loads of the last glacial maximum, which

were at their maximum around 21000 years ago (Douglas and Peltier, 2002). In nearly all previous studies, vertical motion corrections are the corrections for GIA. In order to predict the GIA values, two kinds of data are required: a rheological model for the Earth's viscoelastic response and the space-time history of the late Pleistocene and early Holocene ice cover. So every GIA model is composed of an earth viscosity model and a deglaciation model which is used to describe the ice history. Church et al. (2004) discussed three major GIA models: the Mitrovica model, the Lambeck model and the ICE-4G VM2 model. They reconstructed the global sea level for 1950 to 2000 by tide gauge measurements and estimated that the global mean rate of sea level rise using the Lambeck, Mitrovica, and Peltier GIA corrections are 1.75, 1.89, and 1.91 mm/year, respectively. Differences between these three estimates are a result of the different Earth models used, different ice models, and possibly differences in the numerical solutions of the glacio-hydro-isostatic sea level equations used by the three GIA models (Church et al., 2004). They also compared the global mean rate of absolute sea level rise estimated by satellite altimetry for 1993 to 2000 with the rate of RSL rise by tide gauges and found a 0.3 mm/year discrepancy, with the RSL rate being higher. If we assume that the GIA dominates the vertical land motion, such a difference would range from 0.2 to 0.5 mm/yr depending on the adopted GIA model (Church et al., 2004). Hence the ASL rate estimated by tide gauge data would vary depending on the chosen GIA model. Besides PGR, the vertical land motion maybe also be due to other processes such as active tectonics. Mzaaotti et al. (2008) stated that for western Canada and northwestern United States, postglacial rebound and tectonics are particularly significant. Global postglacial rebound models overpredict rebound velocities by 1 to 2 mm/year due to not accounting for the low viscosity of western North America upper mantle. Active tectonics lead to vertical velocities that are typically between -1

to 4 mm/yr. In conclusion, using a global GIA model to correct vertical land motion leads to two main issues: first, GIA corrections vary depending on the GIA model used; and second, GIA corrections do not account for other processes such as active tectonics.

The disagreement between GIA corrections and real vertical land motion can partly be reduced by measuring vertical land motion using Global Positioning System (GPS) at or near tide gauges. In the forth meeting in Toulouse France alongside the Sixth Meeting of the GLOSS Group of tide gauge experts and geodesists held in 1999 plans were made for the initiation of an international study group on operating GPS at tide gauge sties continuously rather than in campaigns (episodic). A combined PSMSL/GLOSS/IGS/IAG/IAPSO working group was set up called CGPS@TG. More than 300 CGPS stations near tide gauges are installed and their continuous measurements are processed by different agencies. The "GPS Tide Gauge Benchmark Monitoring – Pilot Project" (TIGA-PP) is one of the CGPS@TG projects. To date, only a few studies have used GPS data at tide gauge sites to estimate ASL changes on a global or regional scale. Some of published results were reviewed in Chapter Two. Mazzotti et al. (2003) used data from 92 GPS stations to study the tectonics of Northern Cascadia and Mazzotti (2007) estimated a local ASL rate in northern Cascadia of 1.7 ± 0.5 mm/yr based on seven local stations. On the basis of a subset of twenty eight global sites, Wöppelmann et al. (2007) derive a 20^{th} century global mean ASL rate of 1.3 ± 0.3 mm/yr.

In this thesis, the rates of vertical land motion for 9 tide gauge sites in the west coast of Canada are the published values of Mazzotti (2008). Mazzotti et al. (2008) updated the GPS results of Mazzotti et al. (2003) by using the ocean tide loading corrections from the FES95.2 global

model and the solid Earth tidal corrections from the International Earth Rotation Service 2003 model (IERS2003), by estimating the daily positions jointly with tropospheric delay models using Dry Niell mapping functions, by using antenna height changes and phase center values from IGS relative phase center calibrations and by estimating the velocity standard errors using a colored noise model. They utilized 24 GPS stations in the west coast of Canada with average 5.5 years of data between January 1996 and November 2006. The GPS data were processed using a double-difference phase solution to derive daily coordinates in a regional reference frame. Then they aligned their results with ITRF2000 reference frame by minimizing the velocity differences at a subset of nine common stations that span the whole network. The information about the GPS data can be found in

Table 6.1. The locations of tide gauge sites and associated GPS stations are shown in Figure 6.9. The smallest distance between a tide gauge site and a GPS station is at the tide gauge site 8545 with the value of 0.1 km. The second smallest is at site 7277 with the value of 1 km. The largest distance is at site 8615 with the value of 37 km.

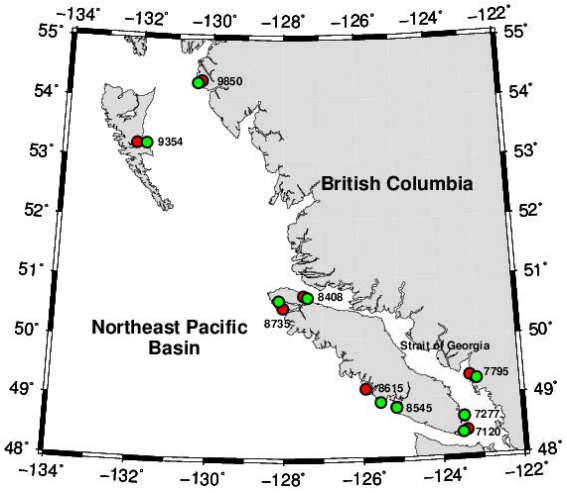

Figure 6.9: Western Canada tide gauge and GPS locations. Red circles and green circles show locations of 9 tide gauge stations and their associated 9 continuous GPS stations.

In the east coast of Canada, the rate of vertical land motion used is the mean value of the results provided by three agencies. The three data sources are: JPL, Scripps Orbit and Permanent Array Center (SOPAC) and Système d′Observation du Niveau des Eaux Littorals (SONEL). JPL analyzes GPS data for 747 geodetic stations in the CORS, IGS and other networks by their own software GIPSY/OASIS II. The JPL methodology for processing GPS data is described at ftp://igscb.jpl.nasa.gov/igscb/center/analysis/jpl.acn and their results can be downloaded from http://sideshow.jpl.nasa.gov/mbh/series.html. JPL velocity is referring to ITRF2005. SOPAC analyze GPS data for 1935 geodetic stations in the CORS, IGS, CACS (Canadian Active Control System) and other networks. They use the GAMIT-GLOBK software developed by MIT. SOPAC's methodology for estimating crustal velocities is described in Nikolaidis (2002). The SOPAC solution of vertical velocity can be downloaded from http://sopac.ucsd.edu/cgi-bin/refinedModelVelocities.cgi. Their results are referring to ITRF2005. SONEL solution is the latest ULR solution, ULR4. Their database covered the period from January 1996 to December 2008 and included 316 stations among which 216 stations were co-located with a corresponding tide gauge. The data are also analyzed by the GAMIT/GLOBK software. The description about their products can be found at http://www.sonel.org/-Solutions-.html and their products can be downloaded from http://www.sonel.org/IMG/txt/ULR4_Vertical-Velocities_Table.txt. The velocities are referring to ITRF2005.

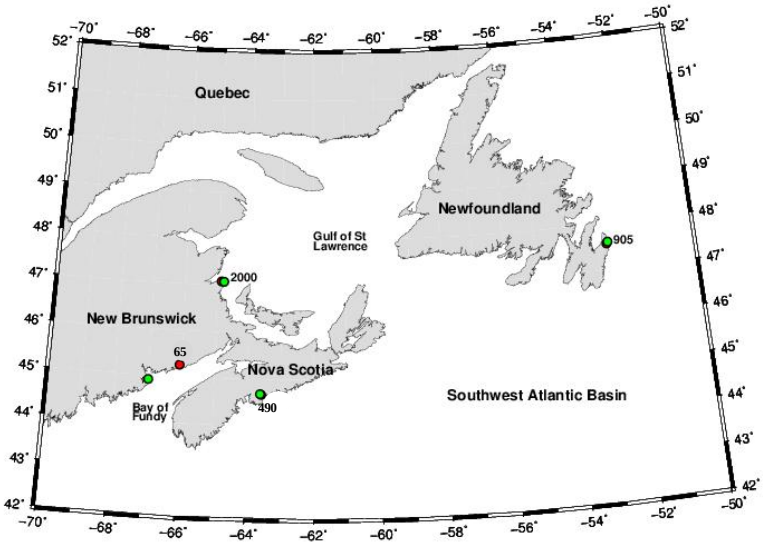

Figure 6.10: Eastern Canada tide gauge and GPS locations. Red circles and green circles show locations of 4 tide gauge stations and their associated 4 continuous GPS stations.

Vertical velocities from these three sources for four GPS stations which are very close to four tide gauge sites in the east coast of Atlantic are found. The positions of the tide gauge sites and the corresponding GPS stations can be seen at Figure 6.10. Tide gauge sites 490, 905 and 2000 have distances to the GPS stations within 5 km. The maximum distance happens at the tide gauge site 65 with the value of 56 km. The combined solution for a particular station is calculated by the weighted mean of the individual values and the corresponding standard error is determined by the law of error propagation.

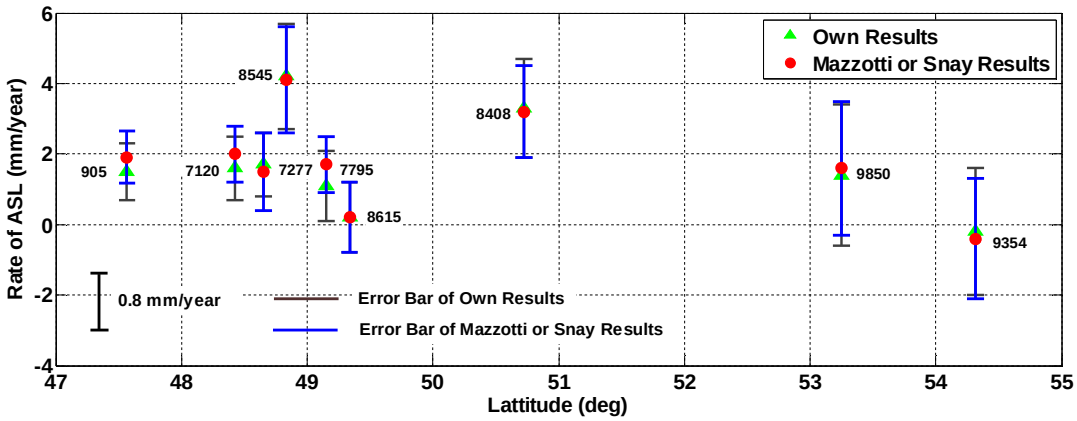

Figure 6.11: Comparison of tide-gauge-derived rate of ASL between the results of this study and the results of Mazzotti (2008) or Snay (2007). The error bar indicates the standard deviation of the rate. The rate and uncertainty for tide gauge 905 is from Snay (2007) and the results of other tide gauge sites are from Mazzotti (2008). The rate estimation in this comparison is derived by all tide gauge data.

The mean rates and standard errors of the vertical land motion determined by GPS data are listed in Table 6.10. The rate of ASL is then calculated by adding the rate of vertical land motion to the rate of RSL. The rate estimates of ASL for the west coast of Canada and for the east coast of Canada are listed in Table 6.10. For comparison purposes, the RSL rate and uncertainty estimated using the WN noise model is also listed in Table 6.10. Our results agree with the results of Mazzotti (2008) and of Snay (2007) very well (shown in Figure 6.11). For the period coinciding from the middle of the 20th century to 2008, the ASL rate for the west coast of Canada is 1.83±0.46 mm/year while the rate for the east coast of Canada is 2.3±0.47 mm/year. The rate for the west coast is very close to the mean global rate estimate from the Intergovernmental Panel on Climate Change (Bindoff, 2007), which is 1.8±0.5 mm/year for the period 1961 to 2003. If we narrow the data length to 1993 to 2008, the rate for the west coast of Canada is 1.37±0.44 mm/year, and the value for the east coast is 1.46±0.34 mm/year. The west

coast rate estimate is very close to Mazzotti's (2008) estimate of 1.5±0.4 mm/year, and is about half of the global average rate from satellite altimetry (about 3 mm/year).

Table 6.10. Rate and uncertainty of RSL and ASL estimated by tide gauge data using WN and WF noise model, Rate and uncertainty of vertical land motion monitored by GPS station nearby.

Site	Relative Sea Level			Vertical land motion	Absolute Sea Level	
	WN	WF				
	Rate and Std. (mm/year)	Rate and Std. (All Data) (mm/year)	Rate and Std. (1993-2008) (mm/year)	Rate and Std. (mm/year)	Rate and Std. (All Data) (mm/year)	Rate and Std. (1993-2008) (mm/year)
West coast of Canada						
7120	0.33 ± 0.04	0.24 ± 0.30	0.05 ± 0.50	1.40 ± 0.80	1.64 ± 0.85	1.45 ± 0.94
7277	0.20 ± 0.08	0.32 ± 0.52	-0.27 ± 0.68	1.40 ± 0.80	1.72 ± 0.95	1.13 ± 1.05
7795	0.15 ± 0.06	0.48 ± 0.05	0.38 ± 0.85	-0.30 ± 1.00	0.18 ± 1.00	0.08 ± 1.31
8408	-0.77 ± 0.06	-0.63 ± 0.40	-0.03 ± 0.70	3.90 ± 1.30	3.27 ± 1.36	3.87 ± 1.48
8545	0.36 ± 0.05	0.25 ± 0.39	-0.20 ± 0.58	3.90 ± 1.50	4.15 ± 1.55	3.70 ± 1.61
8615	-1.34 ± 0.06	-1.47 ± 0.59	-2.80 ± 0.73	2.60 ± 0.80	1.13 ± 0.99	-0.20 ± 1.08
8735	0.49 ± 0.21	0.38 ± 1.14	0.65 ± 1.27	2.40 ± 0.90	2.78 ± 1.45	3.05 ± 1.56
9354	1.45 ± 0.05	1.55 ± 0.46	1.84 ± 0.63	-1.70 ± 1.70	0.15 ± 1.76	0.14 ± 1.8
9850	-0.64 ± 0.06	-0.57 ± 0.46	-1.18 ± 0.73	2.00 ± 1.90	1.43 ± 1.95	0.82 ± 2.04
East coast of Canada						
65	1.93 ± 0.08	1.96 ± 0.82	0.41 ± 1.19	3.10 ± 1.20	5.1 ± 1.5	3.51 ± 1.69
490	2.65 ± 0.05	2.50 ± 0.42	1.80 ± 0.72	-1.70 ± 0.30	0.8 ± 0.5	0.10 ± 0.78
905	1.90 ± 0.08	1.71 ± 0.74	1.96 ± 1.12	-0.20 ± 0.20	1.5 ± 0.8	1.76 ± 1.14
2000	2.24 ± 0.09	2.32 ± 0.55	2.26 ± 0.80	-0.50 ± 0.02	1.8 ± 0.6	1.76 ± 0.80

6.5 Summary

There are three contributions in this chapter.

(1) We generated the cleaned MMSL time series from tide gauge data for the west and east coasts of Canada. In Chapter Two, daily tide gauge time series were constructed by corrected for the effects of atmospheric loading and converted from the chart datum to the mean sea level in the pre-processing steps. Then they were averaged to MMSL time series. Tide gauge MMSL time series were then corrected for the seasonal annual

(calculated by Equations (3.8) and (3.9)) and regional common mode effects (derived by Equations (3.8) and (3.9)). Outlier detection which is defined by Equation (3.12) was used to detect the suspicious MMSL data, which were removed afterward. The cleaned MMSL data vary between -5 cm and 5 cm.

(2) We tested WN, WR and WF models for tide gauge MMSL time series by power spectral density (Equations (3.22), (3.23) and (3.24)) and maximum likelihood analysis (Equations (3.26) and (3.27)), and found that WF model is appropriate for all of the time series in the west and east coasts of Canada. The covariance matrix of WF model for each tide gauge site was constructed by Equation (3.21).

(3) We derived the rate and uncertainty of RSL change at every tide gauge site. Cleaned MMSL time series were substituted to Equations (3.3), (3.4), (3.5) and (3.6) to solve the linear regression model using the generated covariance matrix.

(4) We derived the rate and uncertainty of ASL change at every tide gauge site. The effects of vertical land motion to the rate estimates were compensated by GPS data. The velocities of vertical land motion in the west coast of Canada were the published values in Mazzotti et al. (2008). And the velocities in the east coast of Canada were average values from published results by three agencies. These estimates of ASL trend will be the observations for computing the rate of coastal sea level change in Chapter Seven.

Chapter Seven: Regional ASL sea level change

7.1 Introduction

Regional sea level rates are calculated for the west and east coastal regions of Canada separately. Chapters Five and Six discussed the data processing method and the estimated of ASL rates for every satellite altimetry and tide gauge MMSL time series respectively. In this chapter, altimetry-derived rates and tide-gauge-derived rates will be averaged alone or together to obtain the mean regional sea level rate. The first section is about the research areas. The least-squares averaging method and resulting regional rate estimates for each type of data will be shown in Section 7.3 and 7.4, respectively. Section 7.5 will continue the results from combining altimetry and tide gauge data together. The last section will explain the error sources of the regional rate estimates by the combination method.

7.2 Research areas

The research areas of this thesis are the west and east coast of Canada, which were defined in Chapter Two. In order to estimate the distribution of local mean sea level rate, each coastal region is divided into four smaller areas according to geological boundaries. These sub-areas are listed in Table 7.1 and shown on Figure 7.1 and Figure 7.2.

7.3 Regional ASL rate determined by satellite altimetry data

Chapter Five introduced the linear regression model and the measurement noise model which are used to determine the rate and uncertainty of sea level change at each altimetry measuring point. The T/P and Jason1 MMSL time series, which are averaged from the raw 10-day SLA

data after applying the IB correction, are also corrected for the annual seasonal variation and the regional common mode corrections if necessary. Altimetry results are categorized into the sub-regions to estimate the regional sea level trend. The last columns of Table 7.1 show the passes and the number of altimetry time series within each region. In the west coast of Canada, three regions have altimetry data with time series number varying from 42 to 54. In the east coast of Canada, altimetry tracks exist in each sub-region and three sub-regions have more than 150 time series except for the Bay of Fundy sub-region.

Table 7.1 Sub-regions, number of tide gauge or satellite altimetry measuring locations

Region Index	Region Name	Tide Gauge	Satellite Altimetry	
			Pass	Time Series Number
		Western Coast of Canada		
1	Hecate Strait	9354, 9850	45, 104	45
2	Queen Charlotte Sound	--	104, 121, 197	54
3	Salish Sea	7120, 7277, 7795	--	0
4	West Coast of Vancouver Island	8408, 8545, 8615, 8735	104	42
Whole Region	1+2+3+4	9354, 9850, 7120, 7277, 7795, 8408, 8545, 8615, 8735	45, 104, 121, 197	141
		Eastern Coast of Canada		
5	Bay of Fundy	65	24, 65	21
6	East coast of Nova Stocia	490	24, 65, 100, 141, 176, 217, 252	165
7	East coast of Island of Newfoundland	905	39, 48, 115, 150, 217	230
8	Gulf of ST Lawrence	2000	65, 74, 141, 150, 243, 252	227
Whole Region	5+6+7+7	65, 490, 905, 2000	24, 39, 48, 65, 74, 100, 115, 141, 150, 176, 217, 143, 252	643

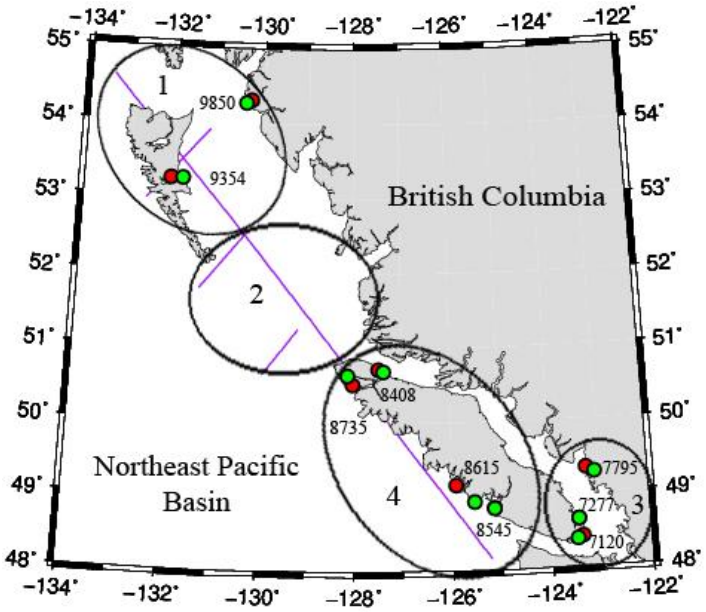

Figure 7.1: Satellite altimetry ground tracks, tide gauge and GPS locations for the west coast of Canada. The purple line is the altimetry ground track. The green and red circles are for the position of GPS and tide gauge stations, respectively.

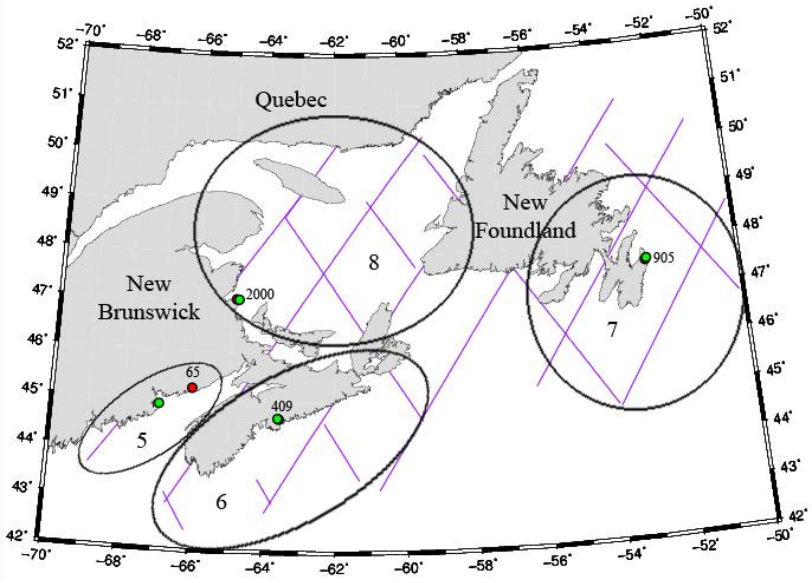

Figure 7.2: Satellite altimetry ground tracks, tide gauge and GPS locations for the east coast of Canada. The purple line is for the altimetry ground track. The green and red circles are for the position of GPS and tide gauge stations, respectively. .

The regional ASL trend denoted by θ is estimated by averaging the rate estimates derived from altimetry time series within the region. The averaging process is realized by a simple least-squares estimation using the equation:

$$b_{ASL}(\alpha,\beta) = \theta + \varepsilon(\alpha,\beta), \tag{7.1}$$

where $b_{ASL}(\alpha,\beta)$ is the rate of ASL at the location with the latitude α and longitude β, and $\varepsilon(\alpha,\beta)$ is the discrepancy between $b_{ASL}(\alpha,\beta)$ and the value of θ. For each altimetry time series, $b_{ASL}(\alpha,\beta)$ is considered as the observation with weight $w(\alpha,\beta)$ defined by the equation

$$w(\alpha,\beta) = 1/\sigma^2_{ASL}, \tag{7.2}$$

where σ^2_{ASL} denotes the standard error of $b_{ASL}(\alpha,\beta)$. Equation (7.1) is solved by the least-squares. The estimated regional sea level trends are listed in the fifth and sixth column of Table 7.2.

Table 7.2 Regional sea level trend.

Region Index	Tide Gauge Data Only (1993-2008)		Satellite Altimeter Data Only (1993-2008)		Combined Data (1993-2008)	
	Rate (mm/year)	Std. (mm/year)	Rate (mm/year)	Std. (mm/year)	Rate (mm/year)	Std. (mm/year)
West Coast of Canada						
1	0.44	1.35	-1.01	0.30	-0.99	0.30
2	--	--	-1.40	0.30	--	--
3	1.03	0.62	--	--	--	--
4	2.03	0.69	-1.46	0.28	-1.46	0.28
Whole Region	1.37	0.44	-1.27	0.28	-1.26	0.28
East Coast of Canada						
5	3.51	1.69	0.93	0.30	0.93	0.30
6	0.10	0.78	1.62	0.28	1.61	0.28
7	1.76	1.14	1.28	0.28	1.29	0.28
8	1.76	0.80	0.94	0.30	0.96	0.30
Whole Region	1.46	0.34	1.12	0.27	1.12	0.27

Under the assumption that the discrepancies $\varepsilon(\alpha,\beta)$ have a Gaussian distribution, the a-posteriori variance factor $\hat{\sigma}_0^2$ is

$$\hat{\sigma}_0^2 = \frac{\sum w(\alpha,\beta) \bullet \varepsilon(\alpha,\beta)^2}{v}, \tag{7.3}$$

where v is the degree of freedom. The yielded values of $\hat{\sigma}_0^2$ for each region (1 to 8, excluding region 3) are: 12.8, 12.1, 1.1, 7.6, 15.5, 24.7, 79.5. The fact that the value of $\hat{\sigma}_0^2$ is much greater than 1.00 suggests that the assigned weights $w(\alpha,\beta)$ may be too large, or equivalently, the values of σ_{ASL}^2 may be too small. This fact reminds us that the weights assigned as the reciprocal of σ_{ASL}^2 which are estimated by the distinct least-squares linear algorithm may not be appropriate. Mangiarotti (2007) proposes that the error budget for the estimate of sea level change using altimetry data is composed of the error of altimeter and radiometer calibrations, and least-squares estimated error. The estimate on the contribution of the altimeter and radiometer calibration error to the linear trend evaluation is 0.27 mm/year. The altimetry calibration (T/P) calibration error is common to all satellite data in the open ocean, as well as in the coastal areas. It is a systematic error. In order to assign the weights appropriately, the effects of this type of error estimated by Mangiarotti (2007) is added to σ_{ASL}^2 in this thesis. The yielded values of $\hat{\sigma}_0^2$ for each region (1 to 8 without the region 3) become: 2.51, 3.09, 0.60, 1.51, 2.26, 3.88, 10.83. A Chi-square test on the posteriori variance factor is used to modify the weights. The regional rates and uncertainties are listed in the fourth and fifth column of Table 7.2. In the west coast of Canada, the falling rate is increasing from -1.01 mm/year to -1.46 mm/year from the Hecate Strait to the West Coast of Vancouver Island. The rate for the whole area is -1.28±0.28 mm/year, which coincides with the rates obtained by Church et al. (2006) and

Mazzotti et al. (2008). In the east coast of Canada, the rate for each region indicates a small rising of sea level. The rate for the whole region is 1.12±0.27 mm/year.

7.4 Regional ASL rate determined by tide gauge data

Chapter Six described the MMSL tide gauge data processing and the linear regression method which is used to derive the RSL rate at each tide gauge location. The rate of vertical land motion estimated by GPS measurements helps to convert the RSL rate to the ASL rate. The RSL, vertical land motion and ASL estimates for 9 tide gauges in the west and 4 tide gauges in the east coast are listed in Table 6.10. Using the same processing method as for the altimetry data, regional ASL rates for each sub-area and the whole coastal area are derived by solving the equation

$$b_{RSL}(\alpha,\beta)+b_{VM}(\alpha',\beta')=\theta+\varepsilon(\alpha,\beta,\alpha',\beta'), \tag{7.4}$$

where $b_{RSL}(\alpha,\beta)$ is the rate of RSL, and $b_{VM}(\alpha',\beta')$ is the rate of vertical land motion which is monitored by the GPS station nearby. $\varepsilon(\alpha,\beta,\alpha',\beta')$ is the discrepancy between $b_{RSL}(\alpha,\beta)+b_{VM}(\alpha',\beta')$ and θ. The weight $w(\alpha,\beta,\alpha',\beta')$ for solving the model **(7.4** is defined as

$$w(\alpha,\beta)=1/(\sigma_{RSL}^2+\sigma_{VM}^2), \tag{7.5}$$

where σ_{RSL}^2 and σ_{VM}^2 is the standard error of $b_{RSL}(\alpha,\beta)$ and $b_{VM}(\alpha',\beta')$, respectively. σ_{RSL}^2 is the uncertainty of $b_{RSL}(\alpha,\beta)$ estimated by the distinct least-squares linear algorithm. The first and second columns of Table 7.2 show the estimated trend and uncertainty for each region. In the west coast of Canada, in contrast to the altimetry results, regional trends estimated by tide gauge data indicate an increase in sea level, with the rate ranging from 0.44 mm/year to 2.03 mm/year from the Hecate Strait to the West Coast of Vancouver Island. The mean rate for the whole

region is 1.37±0.44 mm/year. In the east coast of Canada, because one region has only one available tide gauge station, the regional trend is equal to the trend estimate at the tide gauge site. θ_{com} for the whole coastal area is equal to 1.46±0.34 mm/year which is slightly lower than 1.85±0.29 mm/year that was obtained by Snay et al. (2007). Actually, only 1 of the 15 Atlantic sites used by Snay et al. (2007) to estimate the rate for the Atlantic coast of North America is used in this thesis. The other 14 sites are located in the south of our 4 tide gauge sites. The rate for the whole area is also comparable to the altimetry result.

Figure 7.3 and Figure 7.4 show the temporal variation of the ASL rate for the west and east coast of Canada respectively. The time span of tide gauge data in the west coast of Canada is from 1964 to 2008 with a step of 5 years. For the period from 1999 to 2008, the estimate of ASL rate is less than 1 mm/year. Nevertheless, during the time span of 1994 or earlier to 2008, the ASL rate is greater than 1 mm/year. As the time span increasing, the ASL rate is approaching 1 mm/year. In the east coast of Canada, the ASL rate for time spans longer than 10 years is greater than 1 mm/year. The error bars at each rate estimate indicate the corresponding standard errors. Long data sets can greatly decrease the magnitude of the rate error, especially of the error which is caused by the long term signals existing in the data.

7.5 Regional ASL rate determined by combining satellite altimetry and tide gauge data

Our combination algorithm is introduced in detail in Chapter Three. As stated in last two sections, each type of data has its own averaging model (Equation (7.1) or Equation (7.4). When

combining them together, the general averaging model is in the same form as Equation (7.1), i.e.,

$$b_{ASL} = \theta_{com} + \varepsilon\,, \tag{7.6}$$

but b_{ASL} is composed of the rate estimates from both data set. For tide gauge data, Equation (7.6) reduces to Equation (7.4). The weight for altimetry or tide gauge data is still defined by Equation (7.2) or Equation (7.5). The regional trend for one specific area would be derived by solving the model (7.6).

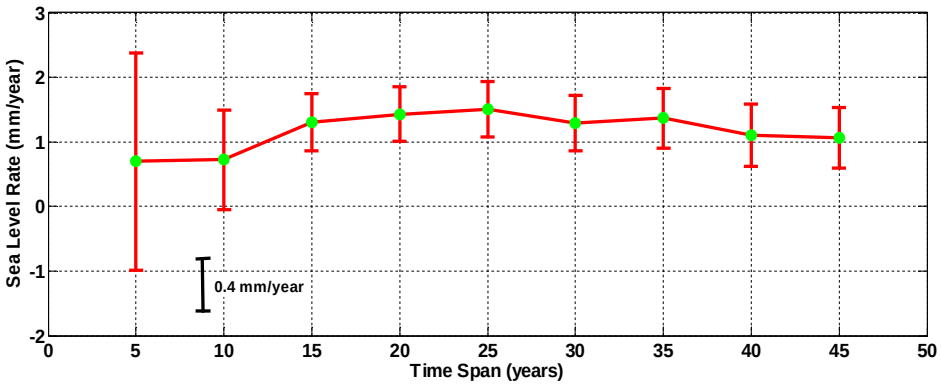

Figure 7.3: ASL rate for the west coast of Canada plotted as a function of the time span of the tide gauge data. The time span is from 2008 to 1964 with a step of 5 years.

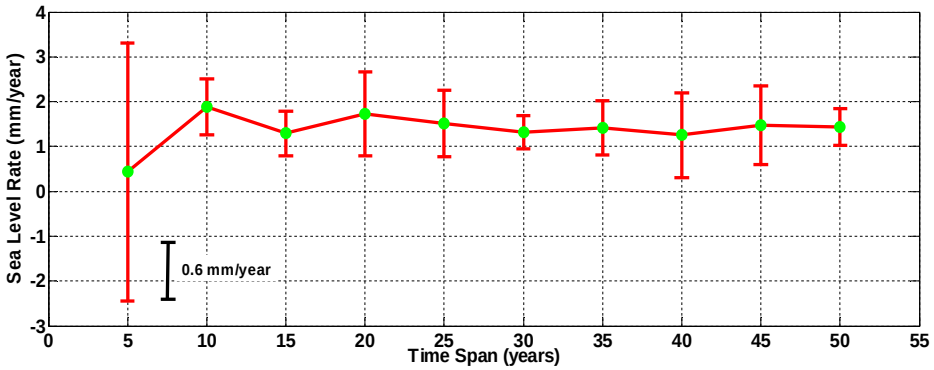

Figure 7.4: ASL rate for the east coast of Canada plotted as a function of the time span of the tide gauge data. The time span is from 2008 to 1959 with a step of 5 years.

When two types of measurements are used to solve the linear model under the least-squares criterion, variance component analysis (VCE) is generally applied to evaluate if the a-priori weights for the measurements are assumed appropriately. Among various VCE algorithms, the rigorous Helmert VCE method (Wang et al., 2009) is used in the current work. For two groups of measurements (altimetry and tide gauge), we first assume that their a-priori variance factors σ_0^2 are both equal to 1. The Helmert method would estimate the a-posteriori variance factor $\hat{\sigma}_0^2$ based on the measurement residuals in addition to achieving the least-squares solution of the parameters for each group of measurements. If the values of $\hat{\sigma}_0^2$ are not same, the weights of the measurements would be modified based on $\hat{\sigma}_0^2$ and least-squares processing would be applied to the measurements again to obtain the parameter estimates and the new values of $\hat{\sigma}_0^2$. This processing would be repeated until the value of $\hat{\sigma}_0^2$ for the altimetry measurement is equal that for the tide gauge data.

Table 7.3 lists the VCE results for each sub-region and for the whole area. In the west coast of Canada, only region 1 and region 4 have both altimetry and tide gauge data. The a-posteriori variance factor $\hat{\sigma}^2$ for satellite altimetry of value 2.51 is greater than the $\hat{\sigma}^2$ for tide gauges of value 0.58. This suggests that the a-priori weights assigned for tide gauge data are too small, whereas the a-priori weights for altimetry data are too large. The results in region 4 and the whole area are the opposite. After 5 iterations with modified weights, the difference between the $\hat{\sigma}^2$ for satellite altimetry and the $\hat{\sigma}^2$ for tide gauges decreased to less than 0.0000001.

In the east coast of Canada every sub-region has both altimetry and tide gauge data. In region 6, 7 and 8, the a-priori weights assigned, which are the standard deviation of ASL rate estimates at each point, for altimetry data are much larger than those for tide gauge data (especially in the region 8, 10.83 versus 1.30) which is contrary to the case in the region 5. The Helmert VCE method is used to modify the weights. After repeating the least-squares processing 4 to 8 times, the a-posteriori variance factors $\hat{\sigma}^2$ for both types of data are approaching 1.0, with a difference of less than 0.0000001.

Table 7.3 Results of Helmert variance component analysis

Region Index	Before Variance Component Analysis				After Variance Component Analysis			
	Posteriori Variance factor $\hat{\sigma}^2$		Rate (mm/year)	Std. (mm/year)	Posteriori Variance factor $\hat{\sigma}^2$	Iteration Number	Rate (mm/year)	Std. (mm/year)
	Satellite Altimetry	Tide Gauge						
West Coast of Canada								
1	2.51	0.58	-1.01	0.08	1.0000	5	-0.99	0.12
2	--	--	--	--	--		--	--
3	--	--	--	--	--		--	--
4	0.61	7.39	-1.39	0.29	1.0000	5	-1.46	0.28
Whole Region	2.27	4.55	-1.24	0.05	1.0000	5	-1.26	0.07
East Coast of Canada								
5	1.51	7.07	0.95	0.11	1.0000	4	0.93	0.14
6	2.26	1.46	1.61	0.04	1.0000	4	1.61	0.06
7	3.88	0.06	1.28	0.27	1.0000	8	1.29	0.06
8	10.83	1.30	0.95	0.04	1.0000	6	0.96	0.13
Whole Region	5.84	1.92	1.12	0.02	1.0000	4	1.12	0.05

Table 7.3 also lists the rate estimates before and after applying VCE analysis. When comparing them, we can find that modifying the weights for two types of data would affect both the rate and the uncertainty estimates in western Canada, while the difference is very small in Eastern Canada. This is because the number of tide gauge sites is very small compared with the number

of altimetry time series. The number ratio between tide gauge and altimetry data for region 1 to 8 except for 2 and 3 is 0.044, 0.095, 0.048, 0.006, 0.004 and 0.004. Hence the contribution of few tide gauge data to the rate estimate is overpowered by the more numerous altimetry data.

Table 7.2 lists the regional sea level rate estimated by the tide gauge, satellite altimetry and combined data. From the region 1 to 4, the tide-gauge-rate and the altimetry-rate indicate totally opposite spatial variation of sea level change. This may be explained by two possible reasons: (1) the location of tide gauge site and the altimetry time series; (2) the number ratio between tide gauge sites and altimetry series. Most tide gauge sites are installed at a harbor or at the mouth of a river or straits located exactly along the coastline or in the interior land close to the ocean. But for altimetry data, although many efforts have been made to obtain a data set approaching the coast as close as possible, the gaps between altimetry data and the coastline are still large. In other words, tide gauge measures the sea level change in the coastal area, while satellite altimetry works best in the quasi-coastal area. One of the motivations for combining tide gauge and altimetry data together is for extending the working area of satellite altimetry from the quasi to the real coastal area. In additional, compared to the dense spatial resolution of satellite altimetry data, the distribution of tide gauge sites is very sparse (it is worse in regions 5 to 8). So the limited tide gauge data cannot provide complete information about the sea level change for a large region. In the Atlantic coast of Canada, both altimetry- and tide-gauge-derived rates indicate a rising of sea level for each sub-region. The tide-gauge-derived rate is slightly larger than the altimetry-derived rate in every sub-region except in the east coast of Nova Scotia.

When we apply the combination procedure to the 141 altimetry-derived and 9 tide-gauge-estimated ASL rates in the west coast of Canada, we obtain $\theta_{com} = -1.26 \pm 0.30$ mm/year. In the east coast of Canada, θ_{com} is equal to 1.12±0.27 mm/year. These two values are almost the same as the respective estimates from satellite altimetry. This requires us to re-evaluate the contribution of tide gauge data to the rate estimate. Two factors affect the contribution of tide gauge, namely the number ratio between tide gauge and altimetry data, and the accuracy of the rate derived by tide gauge data.

The data and rate estimates for regions 7 and 1 are used to test the effect of the first factor. As shown in Table 7.3, the $\hat{\sigma}^2$ values for altimetry and tide gauge data after applying the least-squares combination processing for the first time are 3.88 and 0.06, respectively for region 7. The associated rate is 1.28±0.27 mm/year. Then the weights for altimetry data are reduced by 4 times (3.88 over 1.00) while the weights for tide gauge data are amplified by 17 times (1.00 over 0.06) before applying the least-squares processing for the second time. The new $\hat{\sigma}^2$ are 1.0 and 0.93 for altimetry and tide gauges, respectively. The new estimate of the rate is 1.29±0.28 mm/year. The change of the rate estimate is less than 0.8%. For region 1, after apply the least-squares processing for the first time, the weights for altimetry data are reduced 2.5 times while the weights for tide gauge data are magnified 1.7 times. The new $\hat{\sigma}^2$ values for these two types of data are 1.0 and 0.99, respectively, and the rate estimate changes from -1.01±0.28 mm/year to -0.99±0.30 mm/year. The changing of the rate estimate is approximate 2%. The weight reduction for altimetry data in region 7 is 1.6 times larger than that in region 1, and the weight magnification for tide gauge data in the region 7 is 10 times as larger as that in the region 1. The

change rate of the rate estimate in the region 7 is smaller than that in the region1. Considering the number ratios for regions 1 and 7, which are 0.044 and 0.004 respectively, we can conclude that the ratio number of tide gauge sites is a major factor limiting the contribution of tide gauge data in the combination method.

The data and rate estimates for region 4 are used to test the effect of the second factor. After applying the least-squares processing for the first time, the a-posteriori variance factor $\hat{\sigma}^2$ estimates indicate that the a-priori weights for the altimetry data are too small and the weights for the tide gauge data are too large. In other words, $\sigma_{RSL}^2 + \sigma_{VM}^2$ is larger than σ_{ASL}^2. After applying the least-squares processing repeatedly with modified weights, the rate estimate changes from -1.39±0.29 mm/year to -1.46±0.28 mm/year. The final result is the same as the value of the rate estimated by satellite altimetry data only. Considering the fact that tide gauge and altimetry results indicate opposite trends of sea level change, we can also conclude that the contribution of tide gauges to the rate estimate can be compensated by altimetry data if the ASL rate accuracy at every tide gauge site is less than that at every altimetry measuring point, even if the number of tide gauge sites is increasing.

7.6 Error sources contributing to the rate estimate

The error sources contributing to the rate estimate in our combination method are: (1) errors in the altimetry-derived ASL rate; (2) errors in the ASL sea level rates derived from tide gauge data; (3) errors associated with the assumption that all sites, in a particular region, experience the same rate of absolute sea level change.

Errors in the estimate of ASL rate for every altimetry time series are composed of the random error which is estimated by the distinct least-squares linear regression algorithm and the system error which is the radiometer and altimeter calibration error. The random error describes not only the random error in the altimetry measurements but also the discrepancy between the observation and the model (3.1). The magnitude of such error is ranging from 0.1 to 0.6 mm/year and from 0.1 to 0.3 mm/year in the west and east coast of Canada, respectively. The calibration error is generated during calibrating the radiometer and altimeter on board T/P and Jason-1 for possible instrument biases and drifts. The magnitude of this error is 0.27 mm/year, taken from the published value in Mangiarotti (2007).

Errors in the estimate of ASL rate for every tide gauge site are more complex to interprete. They are categorized into 4 groups, which are: (1) errors in the RSL rates derived from tide gauge data; (2) errors in the GPS-derived vertical land motion velocities; (3) errors due to the tide gauge and the GPS stations being situated at different locations; and (4) errors associated with the assumption that ITRF vertical velocities derived from a few years of continuous GPS observations have remained constant over the decades spanned by the tide gauge data.

Errors in the RSL rates are estimated directly from the least-squares linear regression processing. The errors of tide gauge measurements are verified to be white and flicker noises. The effect of temporally-dependent signals is reflected in the estimates of rate uncertainty. The magnitude of errors in the estimates of the RSL rate for the period from 1993 to 2008 is varying from 0.5 to 1.3 mm/year and 0.7 to 1.2 mm/year.

The GPS-derived velocities of vertical land motion are taken from the published values in Mazzotti et al. (2008) for tide gauge sites in the west coast of Canada. Standard errors of their estimates are based on the formal colored noise uncertainties and the uncertainties associated with the alignment to the ITRF 2000 frame. Errors range between 0.8 to 1.9 mm/year. In the Atlantic coast of Canada, the velocities of vertical land motion are derived by averaging the published GPS estimates from various agencies. Velocities for tide gauge 65, 490 and 905 are estimated by averaging the values provided by at least two agencies. But for site 2000, only one agency provides the velocity estimate from the GPS station nearby. The velocity uncertainty of 0.02 mm/year looks questionable.

Snay et al. (2007) quantifies the error associated with tide gauges and their associated GPS stations being situated at different locations. They divide their 30 sites into three bins, based on the distance between a tide gauge and its associated GPS station. Then for each bin, they calculate the weighted RMS of $\varepsilon(\alpha,\beta,\alpha',\beta')$ which is defined in Equation (7.4) over all sites. Their results indicate that these weighted RMS values do not differ significantly from one bin to another. They conclude that until a longer continuous GPS data exists, the magnitude of this type of error cannot effectively determined.

The third error source contributing to the rate estimate in our combination method relates to the approximation that all sites experience the same rate of absolute sea level change. This approximation or assumption is the basis for forming the combining model **(7.6**. The regional rate results in the west coast of Canada clearly reveal that this approximation is not always correct: the mean ASL rate estimated from tide gauge data (1.37±0.44 mm/year) differs

statistically from the mean ASL rate estimated from satellite altimetry data (-1.26±0.28 mm/year). Hence single type of data is insufficiently accurate to detect the complete spatial variations in the ASL rates.

In our study, the uncertainty of ASL trend estimated at each altimetry site accounts for both the random error, which is estimated by the distinct least-squares linear regression algorithm (e.g. Equations (3.3), (3.4) and (3.5)) using the selected noise model, and the system error, which is the radiometer and altimeter calibration error. The uncertainty of ASL trend from every tide gauge time series is determined by the uncertainty of RSL trend, which is estimated from least-squares linear regression processing (e.g. Equations (3.3), (3.4) and (3.5)) using the detected noise model, and the errors in the vertical land motion velocities, which are published along with the velocity estimates in Mazzotti et al. (2008) or by SOPAC, SONEL and JPL. Our estimates of ASL change from tide gauge data were derived under the assumption that the vertical velocities derived from a few years of continuous GPS data have remained constant over the decades spanned by the tide gauge data, and by ignoring the errors due to the tide gauge and the GPS stations being situated at different locations. We did not evaluate their effects on the trend estimates. In our combination method, coastal rate of ASL change is derived by under the assumption that all altimetry and tide gauge sites experience the same rate of ASL change for the same period. This assumption is not always correct, but we did not assess its effects on the coastal rate estimates in the current study.

7.7 Summary

In this chapter, we developed a combination method for estimating the coastal rates of ASL change using altimetry and tide gauge data together. Different from Mangiarotti's (2007) method, our method does not introduce any additional errors like the interpolation errors. However, our method has a problem similar to Church et al.'s (2008) method, that the benefits of long records of tide gauge data (generally more than 30 years) are limited by the short altimetry data. T/P and Jason-1 time series are as long as 16 years for the period from 1993 to 2008. Hence our coastal rate estimates are just for the period from 1993 to 2008.

We also estimated the coastal rates from altimetry and tide gauge data, separately, which are used to evaluate the contribution of tide gauge data to the rate estimates in the combination method. The coastal rates estimated by the combination method are very close to the estimates from altimetry data only, but different from the rates from tide gauge data. The comparison results indicate that the contribution of tide gauge data is greatly limited by the small number of tide gauge sites, and the accuracy of ASL trend estimates. Hence increasing the number of tide gauge sites and providing more accurate velocity estimates of vertical land motion from longer GPS data are two significant factors, which determine if our combination method can succeed in determine the coastal trend of ASL change.

Chapter Eight: Conclusions and Recommendations

The thesis proposed an innovative method to analyze the coastal sea level variations using combined tide gauge and satellite altimetry measurements. In order to obtain improved the sea level estimates at the coastal areas, improved processing techniques are carefully designed and implemented for both the tide gauge and satellite altimetry data processing. Furthermore, the optimum noise models for the satellite altimetry and tide gauge measurements are thoroughly evaluated for to improve the reliability of the estimated trend uncertainty. Given the results and findings presented in the previous chapters, Chapter Eight gives the conclusions and the possible recommendations for the future work.

8.1 Conclusions

Based on the results and analysis from the proposed method for the regional sea level estimate using the tide gauge and satellite altimetry data, major conclusions can be drawn as follows:

(1) Improved ocean tide corrections for the satellite altimetry was obtained using Webtide local tide model from Fisher and Oceans Canada instead of standard ocean tide models provided in the data products (CSR3.0 and FES95 for T/P, and GOT00 and FES2004 for Jason-1) for the coastal areas. Compared with the latest global tide models (e.g. FES2004, EOT11a and DTU10), the Webtide model provides improved ocean tide corrections using the constitute analysis of the regional tide gauge measurements as the performance metric. However, the large discrepancy at the M_2 constituent (up to 7 cm) between Webtide and the tide gauge data indicated the necessary to analyze the residual ocean tides in SLA.

(2) The residual ocean tide was analyzed using Least-squares spectral analysis to evaluate the efficiency of the ocean tide corrections for the satellite altimetry. Spectral results indicate that large residual ocean tide signals remain in SLA; average 68% (west coast of Canada) and 52% (east coast of Canada) of the SLA variations are due to the residual ocean tide. The long term constituents with periods greater than 6 months are the largest signals in the residual ocean tides. These signals must be removed from our data or they will affect the reliability of the trend uncertainty. The spectral results indicate that it is necessary to analyze and remove the residual ocean tide.

(4) The amplitudes and phases of the constituents in residual ocean tide were estimated by harmonic analysis. Then residual ocean tide for each altimetry time series was calculated and removed from the data. After corrected for the residual ocean tide, the variations of SLA reduce from 9.6 cm to 5.2 cm on average over the entire coastal area of west Canada. And in the east coast of Canada, the variations of SLA reduce from 8.7 to 5.1 cm on average. Applying this correction can greatly decrease the variation of SLA.

(3) Improved MMSL time series can be obtained using the annual seasonal and regional common mode corrections. For satellite altimetry, the MMSL time series were obtained by averaging 10-day SLA after the residual ocean tide correction. The annual seasonal corrections were applied only when noticeable annual or semiannual variations are observed in the area of interest. For the tide gauge data, the empirical annual seasonal

correction was always applied because of the existence of noticeable annual and semiannual variations.

(4) Proper noise models for satellite altimetry and tide gauge measurements were determined using the power spectral density and maximum likelihood analysis. Thus improved estimated accuracy of the liner trend of satellite altimetry tide gauge data can be obtained. Based on the results presented in Chapter Five, for satellite altimetry data, the measurement noise is dominated by white noise. But for tide gauge measurement noise, as shown in Chapter Six, it is dominated by white and flicker noise. The parameters of the noise (e.g. variance, c and d_{-1}) were determined by the MLE method.

(5) The ASL and RSL rate estimates for every satellite altimetry and tide gauge time series were invested using the linear regression model with determined proper noise model, respectively. The estimated ASL rate from satellite altimetry varies point by point but is generally in the range of -2 to 2 mm/year. For the period from 1993 to 2008, the ASL rate is -1.27±0.28 mm/year for the west coast, which agrees with results in Mazzotti et al. (2008) and CU SLRGroup, and 1.12±0.27 mm/year for the east coast, which coincides with the result published by CU SLRGroup. The RSL rate estimates from tide gauge vary between -2.80 ± 0.73 and 1.84 ± 0.63 mm/year in the west coast of Canada, which agree with the results in Mazzotti et al. (2008) and the RSL rates in the east coast of Canada change from 0.41 ± 1.19 to 2.26 ± 0.80 mm/year, which agree with results in Snay et al.

(2007). It is also noted that more practical estimated trend uncertainty for the tide gauge data was obtained using the WF model rather than the white noise model.

(6) The velocity of vertical land motion estimated by the continuous GPS data was used to convert the RSL trend from tide gauge to the ASL trend. GPS-derived velocities are published values in Mazzotti et al. (2008) or provided by SOPAC, SONEL and JPL. The estimated ASL trend for 9 tide gauge sites in the west coast of Canada in the thesis varies between -0.20 ± 1.08 and 3.87 ± 1.48 mm/year, which agrees with results from Mazzotti et al. (2008). In the east coast of Canada, the ASL trend for 4 tide gauge stations varies from 0.10 ± 0.78 to 3.51 ± 1.69 mm/year, which agrees with results from Snay et al. (2007).

(7) Improved coastal trend of the sea level change was obtained using the combination method. The least-squares fitting of a linear model was used for the rate estimates using both the satellite altimetry and tide gauge data. Helmert variance component analysis is used to adjust the weights for altimetry and tide gauge data during the least-squares adjustment. Compared with the rate estimates from the standalone satellite altimetry or tide gauge, the contribution of tide gauge data to the combined rate estimator is minor. It is expected due to the limited number of tide gauge sites. Furthermore, the large uncertainty of the vertical land motion estimates derived by the GPS velocity also limits the use of tide gauge date for the rate estimates.

8.2 Recommendations for future research

Based on the results presented in this thesis, several areas of future work have been identified in order to improve the coastal sea level trend estimation.

(1) Other altimetry missions, e.g., ERS1, ERS2 and Envisat, should be included in the research. Adding data from other altimetry missions to T/P and Jason-1 data could increase the inter-track spatial resolution, which could capture the ocean signals with shorter wavelengths.

(2) Radar pulse re-tracking and propagation of the open-ocean radiometer-derived wet troposphere correction to coastal area imposing a meteorological model as a constraint are two methods which can decrease the degradation of the altimeter and radiometer caused by the land contamination.

(3) More tide gauge sites should be added to the research. The number of tide gauge sites used in this thesis is very limited. The choice of tide gauges is following the criteria of long data record, small data gaps and accurate measurements. In addition, the use of the velocity estimate of vertical land motion from GPS requires that the tide gauge site should have a continuous GPS station no further than 20 km away (Mazzotti et al., 2008). It becomes another constraint on selecting the tide gauge sites. More tide gauge sites are required to increase the contribution of tide gauge data in our combination method. Under current conditions, other tide gauge sites which do not have nearby GPS stations but satisfy the other requirements may be also used by using GIA model accounting for the vertical land motion. In additional, GRACE data may also monitor the land motion. But the efficiency of GRACE in a small spatial scale needs to be evaluated.

Reference

Ardalan AA, and Hashemi H (2008) Empirical Global Ocean Tide and Mean Sea Level Modeling Using Satellite Altimetry Data Case Study: A New Empirical Global Ocean Tide and Mean Sea Level Model Based on Jason-1 Satellite Altimetry Observations. Lecture Notes in Earth Sciences, 112, Doi: 10.1007/978-3-540-78938-3_9, Springer Berlin.

Andersen OB (1999) Shallow water tides in the northwest European shelf region from TOPEX/POSEIDON altimetry. *J. Geophys. Res.*, 104(C4)15:7729-41.

Andersen OB, Vest AL, and Knudsen P (2004) The KMS-04 multi-mission mean sea surface. http://gocinascience.spacecenter.dk/publications/4_1_kmss04-lux.pdf.

Andersen OB, Egbert GD, Erofeeva SY, and Ray RD (2006) Mapping nonlinear shallow-water tides: a look at the past and future. Ocean Dynamics, 56:416-429, doi: 10.1007/s10236-006-0060-7.

Anzenhofer M, Shum CK, and Mathias R (1999) Coastal altimetry and applications. Tech. Rep. 464, Geodetic Science and Surveying, the Ohio State University Columbus, USA.

AVISO and PODAAC (2008) AVISO and PODAAC user handbook: IGDR and GDR Jason products, edition 4.1, AVISO SMM-MU-M5-OP-13184-CN, PODAAC JPL D-21352.

Ballantyne VA, Foreman MGG, Crawford WR, and Jacques R (1996) Three-dimensional model simulations for the north coast of British Columbia, Cont. Shelf Res., 16: 1655-1682.

Beckley BD, Lemoine FG, Lutchke SB, Ray RD, and Zelensky NP (2007) A reassessment of global and regional mean sea level trends from TOPEX and Jason-1 altimetry based on revised reference frame and orbits. *Geophys. Res. Lett.*, 34:L14608, doi: 10.1029/2007GL030002.

Benada JR (1997) Merged GDR (TOPEX/POSEIDON) generation B (MGDR-B) User's handbook. PO.DAAC, ftp://podaac.jpl.nasa.gov/allData/topex/L2/mgdrb/docs/uhmgdrb/html/usr _ toc.htm.

Berge-Nguyen M, Cazenave A, Lombard A, and Cretaux JF (2008) Reconstruction of past decades sea level using thermosteric sea level, tide gauge, and satellite altimetry and ocean reanalysis data. *Global Planet. Change* 62: 1-13.

Bindoff NL, Willebrand J, Artale V, Cazenave A, Gregory J, Gulev S, Hanawa K, Le Quéré C, Levitus S, Nojiri Y, Shum CK, Talley LD, and Unnikrishnan A (2007) Observations: Oceanic Climate Change and Sea Level. In: Climate Change 2007: The Physical Science Basis. Contribution of Working Group I to the Fourth Assessment Report of the Intergovernmental Panel on Climate Change [Solomon, S., D. Qin, M. Manning, Z. Chen, M. Marquis, K.B. Averyt, M. Tignor and H.L. Miller (eds.)]. Cambridge University Press, Cambridge, United Kingdom and New York, NY, USA.

Bosch, W (2003) Geodetic application of satellite altimetry. International Association of Geodesy Symposia, vol 126, editors: C. Hwang, C. K. Shum, and J. C. Li, Springer-Verlag.

Cartwright DE, and Tayler RJ (1971) New computations of the tide generating potential. *Geophys. JR Astr. Soc*., **23,** 45–74.

Cartwright DE and Edden AC (1973) Corrected tables of tidal harmonics. *Geophys. J.R. Astr. Soc*., 33**,** 253–264.

Cazenave A, Dominh K, Gennero MC, and Ferret B (1998) Global mean sea level changes observed by TOPEX-Poseidon and ERS-1. *Phys. Chem. Earth*, 23(9–10): 1069–1075.

Cazenave A, Bonnefond P, Mercier F, Dominh K, and Toumazou V (2002) Sea level variations in the Mediterranean Sea and Black Sea from satellite altimetry and tide gauges. Global and Planetary Change 34: 59-86.

Cazenave A, and Nerem RS (2004) Present-day sea level change: Observations and causes. *Rev. Geophys*., 42, RG3001, doi:10.1029/2003RG000139.

Chambers DP, Ries JC, and Urban TJ (2003) Calibration and verification of Jason-1 using global along-track residuals with TOPEX. *Mar. Geod*., 26(3–4):305–317.

Chelton DB, Ries JC, Haines BJ, Fu L-L, Nerem RS, and Tapley BD (2001) Satellite altimetry, in: Satellite altimetry and Earth sciences, a handbook of techniques and applications, Fu L-L and Cazenave A (eds.). Vol 69 Int. Geophys. Series, Academic Press, 1–131.

Chen JL, Wilson CR, Tapley BD, and Famiglietti JS (2005) Seasonal global mean sea level change from satellite altimeter, GRACE, and geophysical models. *J. Geod*., 79:532-539, doi: 10,1007/s00190-005-0005-9.

Cheng Y, Andersen OB (2010) Improvement in global ocean tide model in shallow water regions. Poster, SV.1-68 45, OSTST, Lisbon.

Cherniawsky JY, Foreman MGG, Crawford WR, Henry RF (2001) Ocean tides from TOPEX/Poseidon sea level data. Journal of Atmospheric and Oceanic Technology, 18(4): 649-664.

Cherniawsky JY, Foreman MGG, Crawford WR, and Beckley BD (2004) Altimeter observation of sea-level variability off the west coast of North America. INT. J. Remote Sensing, 25(7-8): 1303-1306.

Church JA, White NJ, Coleman R, Lambeck K, and Mitrovica J (2004) Estimates of the regional distribution of sea level rise over the 1950 – 2000 period. *J. Clim.*, 17, 2609 – 2625, doi:10.1175/1520-0442.

Church JA, and White NJ (2006) A 20th century acceleration in global sea-level rise. *Geophys. Res. Lett*., 33: L01602, doi: 10.1029/2005GL024826.

Church JA, White NJ, Aarup T, Wilson SW, Woodworth PL, Domingues PL, Hunter JR, and Lambeck K (2008) Understanding global sea levels: past present and future. *Sustain Sci*, 32, Doi: 10.1007/s11625-008-0042-4, Springer Japan.

Church JA, and White NJ (2011) Sea-level rise from the late 19th to early 21st century. *Surv Geophys*, 32:585-602, doi: 10.1007/s10712-011-9119-1.

CU SLRGroup, http://sealevel.colorado.edu/.

Deng W, Featherstone WE, Hwang C, and Berry PAM (2002) Estimation of contamination of ERS-2 and POSEIDON satellite radar altimetry close to the coasts of Australia. Marine Geodesy 25: 249-271.

Desportes C, Obligis E, and Eymard L (2007) On the wet tropospheric correction for altimetry in coastal regions. IEEE Trans. Geosci. Remote Sens. 45(7): 2139–2149.

Douglas BC (1991) Global sea level rise. *J. Geophys. Res*., 96: 6981–6992.

Douglas BC (1997) Global sea rise: a redetermination. Surveys in Geophysics, 18, 279-292.

Douglas BC (2001) An introduction to sea level, in Sea Level Rise: History and Consequences. Editors: B. C. Douglas, M. S. Kearney, S. P. Leatherman, Academic, London.

Douglas BC and Peltier WR (2002) The puzzle of global sea level rise. *Phys. Today*, 55(3), 35, doi: 10.1063/1.1472392.

Ducet N, and Le Traon PY (2000) Global high-resolution mapping of ocean circulation from Topex/Poseidon and ERS-1/2. *J. Geophys. Res*., 105, 19,477-19,498.

Dupont F, Hannah CG, Greenberg DA, Cherniawsky JY and Naimie CE (2002) Modelling System for Tides. *Can. Tech. Rep. Hydrogr. Ocean Sci*. 221: vii + 72pp.

Durand, F, Shankar D, Birol F, Shenoi SSC, Roblou L, Lyard F, and Menard Y (2006) Improved satellite altimetry for the observation of coastal ocean dynamics: a case for the Northern Indian Ocean. The international Society for Optical Engineering, 6406: 64060M.

Egbert GD and Erofeeva SY (2001) Efficient inverse modeling of barotropic ocean tides. Journal of Atmospheric and Oceanic Technology 19(2): 183-204.

Farrell WE (1972) Deformation of the Earth by surface loads. *Rev. Geophys. & Space Phys*. 10(3): 761-737.

Fenoglio-Marc L (2002), Long-term sea level change in the Mediterranean sea from multi-satellite altimetry and tide gauges, Physics and Chemistry of the Earth, 27, 1419-1431.

Foreman MGG, and Thomson RE (1997) Three-dimensional model simulations of tides and buoyancy currents along the west coast of Vancouver Island. *J. Phys. Oceanogr*., 27: 1300-1325.

Foreman MGG, Crawford WR, Cherniawsky JY, Gower JFR, Guypers L, and Ballantyne VA (1998) Tidal correction of TOPEX/POSEIDON altimetry for seasonal sea surface elevation and current determination off the Pacific coast of Canada. J. Geophys. Res., 103(C12): 27979-27998.

Foreman MGG, Crawford WR, Cherniawsky JY, Henry RF and Tarbottom MR (2000) A high-resolution assimilating tidal model for the northeast Pacific Ocean. *J. Geophys. Res.*, 105: 28,629-28,652.

Forrester WD (1983) Canadian Tidal Manual. Department of Fisheries and Oceans, Ottawa, 138pp.

Fu L-L, Christensen EJ, and Yamarone Jr CA (1994) TOPEX/POSIDEN mission overview. *J. Geophys. Res*., 99(C12): 24369-24381.

Gaspar P, Ogor F, Le Traon PY and Zanife OZ (1994) Estimating the sea state of the TOPEX and POSEIDON altimeters from crossover differences. *J. Geophys. Res.*, 99, 24981-24994.

Gaspar P, Labroue S, Ogor F, Lafitte G, Marchal L and Rafanel M (2002) Improving nonparametric estimates of the sea state bias in radar altimeter measurements of sea level. *J. Atmos. Oceanic Technol*., 19, 1690-1707.

Gysen HV, Coleman R, Morrow R, Hirsch B, and Rizos C (1992) Analysis of collinear passes of satellite altimeter data. *J. Geophys. Res.*, 97(C2): 2265-2277.

Hernandez F, and Schaeffer P (2001) The CLS01 Mean Sea Surface: a validation with the GSFC00.1surface. available at http://www.aviso.oceanobs.com/fileadmin/documents/data/produits/auxiliaires/cls01_valid_mss.pdf.

Holgate SJ, and PL Woodworth (2004) Evidence for enhanced coastal sea level rise during the 1990s. *Geophys. Res. Lett.*, 31, L07305, doi:10.1029/2004GL019626.

Hosking JRM (1981) Fractional differencing. Biometrika 68(1): 165 – 176.

Hwang C, Hsu HY, and Jang RJ (2002) Global mean sea surface and marine gravity anomaly from multi-satellite altimetry: applications of deflection-geoid and inverse Vening Meinesz formulae. *J. Geodesy*., 76: 407-418, doi: 10.1007/s00190-002-0265-6.

Jiang WP, Li JC, and Wang ZT (2003) Determination of global mean sea surface using multi-satellite altimetric data. International Association of Geodesy Symposia, VOL 126, editors: C. Hwang, C. K. Shum, and J. C. Li, Springer-Verlag.

Kahlouche SAR, and Benhamed Daho SA (2003) TOPEX altimetric mean sea level and gravimetric geoid in the North of Algeria. International Association of Geodesy Symposia, VOL 126, editors: C. Hwang, C. K. Shum, and J. C. Li, Springer-Verlag.

Kantha LH (1995) Barotropic tides in the global oceans from a nonlinear tidal model assimilating altimetric tides 1: Model description and results. *J. Geophys. Res*., 100(C12): 25283-25308.

Koblinsky CJ, Ray RD, Beckeley BD, Wang YM, Tsaoussi L, Brenner A, and Williamson R (1999) NASA ocean altimeter Pathfinder project report 1: Data processing handbook. NASA/TM-1998-208605.

Korotaev GK, Saenko OA, and Koblinsky CJ (2001) Satellite altimetry observations of the Black Sea Level. *J. Geophys. Res*., 106(C1): 917-933.

Labroue S, Gaspar P, Dorandeu J, Mertz F, Tran N, Zanife O, Vincent P, Picot N, and Femenias P (2006) Overview of the improvements made on the empirical determination of the sea state bias correction. http://earth.esa.int/workshops/venice06/participants/318/ paper_318_labroue.pdf.

Larsen CF, Echelmeyer KA, Freymueller JF, and Motyka RJ (2003) Tide gauge records of uplift along the northern Pacific-North America plate boundary, 1937 to 2001. *J. Geophys. Res*., 108(B4), 2216, doi:10.1029/2001JB001685.

Leuliette EW, Nerem RS and Mitchum GT (2004) Calibration of TOPEX/POSEIDON and Jason altimeter Data to construct a continuous record of mean sea level change. *Mar. Geod*., 27: 79-94, doi:10.1080/01490410490465193.

Le Provost C (1991) Generation of overtides and compound tides (review). In Tidal Hydrodynamics, Parker BB (eds.), John Wiley and Sons, New York, pp. 269-295.

Le Provost C, Genco ML, Lyard F, Vincent P, and Canceil P (1994) Spectroscopy of the world ocean tides from a finite element hydrodynamic model. *J. Geophys. Res*., 99: 24369-24381.

Le Provost C, Lyard F, Genco ML, Lyard F, Vincent P, and Canceil P (1995) Spectroscopy of the world ocean tides from a finite element hydrodynamic model. *J. Geophys. Res*., 99, 24777-24797.

Le Provost C, Lyard F, Molines JM, Genco ML, and Rabilloud F (1998) A hydrodynamic ocean tide model improved by assimilating a satellite altimeter-derived data set. *J. Geophys. Res*., 103(C3): 5513-5529.

Le Provost C (2001) Ocean tides, Satellite altimetry and earth sciences. Ed. Fu L-L and Cazenave A, pp. 267-303.

Lerch FJ, and Marsh JG (1982) Gravity model improvement for SEASAT. *J. Geophys. Res*., 87(C5): 3281-3296.

Lyard F, Lefevre F, Letellier T, and Francis O (2006) Modelling the global ocean tides: modern insights from FES2004. Ocean Dynamics, 56:394–415.

Madsen KS, Hoyer JL, and Tscherning CC (2007) Near-coastal satellite altimetry: Sea surface height variability in the North Sea-Baltic Sea area. *Geophys. Res. Lett*., 34: L14601, doi: 10.1029/2007GL029965.

Mangiarotti S (2007) Coastal sea level trends from TOPEX-Poseidon satellite altimetry and tide gauge data in the Mediterranean Sea during the 1990s. *Geophys. J. Int*. 170: 132-144, doi: 10.1111/j.1365-246X.2007.03424.x.

Mazzotti S, Dragert H, Henton JA, Schmidt M, Hyndman RD, James T, Lu Y, and Craymer M (2003) Current tectonics of northern Cascadia from a decade of GPS measurements. J. Geophys. Res., 108(B12): 2554, doi:10.1029/2003JB002653.

Mazzotti S, Lambert A, Courtier N, Nykolaishen L, and Dragert H (2007) Crustal uplift and sea level rise in northern Cascadia from GPS, absolute gravity, and tide gauge data. *Geophys. Res. Lett*., 34: L15306, doi: 10.1029/2007GL030283.

Mazzotti S, Jones C, and Thomson RE (2008) Relative and absolute sea level rise in western Canada and northwestern United States from a combined tide gauge-GPS analysis. *J. Geophys. Res*., 113, C11019, doi:10.1029/2008JC004835.

Macdonald RW, and Pedersen TF (1991) Geochemistry of sediments of the western Canadian continental shelf. *Continental Shelf Res*., 11, Nos 8-10., 7170735.

Mao A, Harrison CGA, and Dixon TH (1999) Noise in GPS coordinate time series. *J. Geophys. Res*. 104: 2797–2816.

Mitchum GT (2000) An improved calibration of satellite altimetric heights using tide gauge sea levels with adjustment for land motion. *Mar. Geod.* 23:145–166.

Munk WH, and MacDonald GJF (1960) The Rotation of the Earth. Cambridge University Press, 323 pp.

Nelder JA, and Mead R (1965) A simplex method for function minimization. *Computer Journal*, 7, 308-313.

Nerem RS (1995) Measuring global mean sea level variations using TOPEX/POSEIDON altimeter data. J. Geophys. Res. 100(C12): 25135-25151, doi:10.1029/95JC02303.

Nerem RS, Chambers DP, Leuliette EW, Mitchum GT, and Giese BS (1999) Variations in global mean sea level associated with the 1997–1998 ENSO event: Implications for measuring long term sea level change. *Geophys. Res. Lett*. 26(19): 3005–3008.

Nikolaidis R (2002) Observation of geodetic and seismic deformation with the global positioning system. PhD Thesis, University of California, San Diego.

Pagiataks SD (1990) The response of a realistic earth to ocean tide loading. *Geophys. J. Int*., 103: 541-560.

Peltier WR (2001) Global glacial isostatic adjustment and modern instrumental records of relative sea level history, In Sea Level Rise, pp. Douglas BC, Kearney MS, Leatherman SP (eds), Academic Press: San Diego; 65–95.

Peltier WR (2002) Global Glacial Isostatic Adjustment: Paleogeodetic and Space-Geodetic Tests of the ICE-4G (VM2) Model, *J. Quat. Sci*., 17, 491-510.

Pugh DT (1987) Chapter 4: Analysis and Prediction, in Tides, Surges and Mean Sea-Level. John Wiley & Sons Ltd.

Pugh DT (2004) Changing sea levels: effects of tides, weather and climate. pp 9-25, Cambridge University Press.

Ray RD (1999) A global ocean tide model from TOPEX/POSEIDON altimetry: GOT99.2, NASA Tech. Memorandum 1999-209478, Goddard Space Flight Center, Greenbelt, MD.

Sahagian D (2000) Global physical effects of anthropogenic hydrological alterations: sea level and water redistribution. *Global Planet. Change*, 25: 39-48.

Santamaría-Gómez A, Bouin M, Collilieux X (2011) Correlated errors in GPS position time series: Implications for velocity estimates. J. Geophys. Res. 116: B01405, doi:10.1029/2010JB007701.

Savcenko R, Bebler M, and Bosch W (2011) Validation of recent tide models by means of crossover differences and time series of bottom pressure and tide gauges. EGU General Assembly, poster: 8343, 2011.

Savcenko R and Bosch W (2011) EOT11a – a new tide model from multi-mission altimetry. OSTST 2011 meeting, poster. Available at http://www.aviso.oceanobs.com/fileadmin/documents/OSTST/2011/poster/savcenko_eot11a_sandiego%5B1%5D.pdf.

Scharroo R, Lillibridge JL, and Smith WHF (2004) Cross-calibration and long-term monitoring of the microwave radiometers of ERS, TOPEX, GFO, Jason, and Envisat. Marine Geodesy, 27: 279-297.

Schrama EJO, and Ray RD (1994) A preliminary tidal analysis of TOPEX/POSEIDON altimetry. *J. Geophys. Res*., 99: 24799-24808.

Schrama EJO (1997) Satellite altimetry, ocean dynamics and the marine geoid, In Geodetic Boundary Value Problems in View of the One Centimeter Geoid. Lecture Notes in Earth Sciences, 65: 405-454, Springer Berlin.

Scwharroo R, and Visser P (1998) Precise orbit determination and gravity field improvement for the ERS satellites. *J. Geophys. Res*., 103(C4): 8113-8127.

Scharroo R, and Miller L (2006) Global and regional sea level change from multi-satellite altimeter data. ESA SP, n614, Proceedings of the Symposium on 15 years of Progress in Radar Altimetry.

Shum CK (1997) Accuracy assessment of recent ocean tide models, *J Geophys. Res*., 102: 25173-25194.

Snay R, Cline M, Dillinger W, Foote R, Hilla S, Kass W, Ray J, Rohde J, Sella G, and Soler T (2007) Using global positioning system-derived crustal velocities to estimate rates of absolute sea level change from North America tide gauge records. J. Geophys. Res. 112 B04409, doi:10.1029/2006JB004606.

Tao WY (2008) Near real-time GPS PPP-inferred water vapor system development and evaluation, MSc thesis of University of Calgary.

Tapley BD, Ries JC, Davis GW, Eanes RJ, Schutz BE, Shum CK, and Watkins MM (1994) Precision orbit determination for TOPEX/POSEIDON. *J. Geophys. Res*., 99(C12): 24383-24404.

Tushingham AM, Peltier WR (1991) Ice-3G: A New Global Model of Late Pleistocene Deglaciation Based Upon Geophysical Predictions of Post-Glacial Relative Sea Level. Change. *J. Geophys. Res*., 96, 4497.

Vergos GS (2002) Sea surface topography, bathymetry and marine gravity field modelling, MSc Thesis, Department of Geomatics Engineering, University of Calgary.

Vignudelli S, Cipollini P, Roblou L, Lyard F, Gasparini GP (2005) Improved satellite altimetry in coastal systems: Case study of the Corsica Channel (Mediterranean Sea). *Geophys. Res. Lett*., 32: L07608, doi: 10.1029/2005GL022602.

Vignudelli S, Snaith HM, Lyard F, Cipollini P, Venuti F, Birol F, Bouffard J, and Roblou L. (2006) Satellite radar altimetry from open ocean to coasts: challenges and perspectives. Remote Sensing of the Marine Environment, 6406, p 64060L.

Wagner CA and Cheney RE (1992) Global sea level change from satellite altimetry. *J. Geophys. Res*., 97(C10): 15607-15615, doi: 10.1029/92JC01641.

Wagner CA, and Tai CK (1994) Degradation of ocean signals in satellite altimetry due to orbit error removal processes. *J. Geophys. Res*., 99(C8): 16255-16267.

Wahr JW (1985) Deformation induced by polar motion. *J. Geophys. Res*., 90(B11): 9363-9368.

Wang YM (2001) GSFC00 mean sea surface, gravity anomaly, and vertical gravity gradient from satellite altimeter data. *J. Geophys. Res*., 106(C12): 31167-31174.

Woodworth PL, Tsimplis MN, Flather RA, and Shennan I (1999) A review of the trends observed in British Isles mean sea level data measured by tide gauges. Geophys. J. Int, 136, 651-670.

Woodworth PL, and Gregory JM (2002) Benefits of GRACE and GOCE to sea level studies. Space Science Reviews, 108: 307-317.

Woodworth PL, White NJ, Jevrejeva S, Holgate SJ, Church JA, and Gehrels WR (2008) Review evidence for the accelerations of sea level on multi-decade and century timescales. *Int. J. Climatol.*, doi: 10.1002/joc.1771.

Wöppelmann G, Miguez BM, Bouin MN, and Altamimi Z (2007) Geocentric sea-level trend estimates from GPS analyses at relevant tide gauges world-wide. Global and Planetary Change 57: 396– 406, doi:10.1016/j.gloplacha.2007.02.002.

Zhang J, Bock Y, Johnson H, Fang P, Genrich JF, Williams S, Wdowinski S, and Behr J (1997) Southern California permanent GPS geodetic array: error analysis of daily position estimates and site velocities. *J. Geophys. Res* 102: 18 035–18 055.

$$J_{-2} = \begin{bmatrix} r_{11} & \cdots & r_{1n} \\ \vdots & \ddots & \vdots \\ r_{n1} & \cdots & r_{nn} \end{bmatrix}$$